NASA
Technical
Paper
2814

C. 2

June 1988

Aeropropulsive Characteristics
of Isolated Combined
Turbojet/Ramjet Nozzles at
Mach Numbers From 0 to 1.20

George T. Carson, Jr.,
and Milton Lamb

TECHNICAL REPORTS
FILE COPY

NASA

NASA
Technical
Paper
2814

1988

Aeropropulsive Characteristics
of Isolated Combined
Turbojet/Ramjet Nozzles at
Mach Numbers From 0 to 1.20

George T. Carson, Jr.,
and Milton Lamb
Langley Research Center
Hampton, Virginia

NASA

National Aeronautics
and Space Administration

Scientific and Technical
Information Division

Summary

An investigation was conducted in the Langley 16-Foot Transonic Tunnel to determine the aeropropulsive performance characteristics (the aerodynamic quantities affected by propulsion) of 13 isolated combined turbojet/ramjet nozzle configurations. These configurations simulated the variable-geometry features of two nozzle designs designated as the multiple-expansion ramp nozzle (MERN) and the composite contour nozzle (CCN). Test data were obtained at static conditions and at Mach numbers of 0.60, 0.90, and 1.20 while angle of attack was held constant at 0°. High-pressure air was used to simulate jet flow, and the nozzle pressure ratio of the simulated turbojet portion of the nozzle was varied from 1.0 (jet off) to approximately 20, depending on the configuration and free-stream Mach number. Since there was only a single air supply, the ramjet pressure ratio was a function of the turbojet pressure ratio and this function was varied by the use of choke plates with varying porosity. The results showed that the CCN had the higher performance over the Mach number range than the MERN, as indicated by the difference of thrust minus drag divided by ideal thrust. Increasing the ramjet throat area for the MERN resulted in an increase in performance that increased with Mach number. For the CCN at Mach numbers less than 1.20, increasing the ramjet throat area resulted in a loss in performance.

Introduction

Studies reported in references 1 through 7 indicate the feasibility of hypersonic, blended wing-body types of aircraft using turbojet and ramjet engines to provide propulsion over a widely diverse flight envelope (at Mach numbers from 0 to 5 and from sea level to an altitude of 100 000 ft). This combined propulsion system couples turbojets arranged in parallel above separate ramjets. Climb and acceleration to a flight Mach number of 0.80 are accomplished with only the turbojets operating because the ramjets produce little or no thrust below this Mach number. Both turbojets and ramjets operate from a flight Mach number of 0.80 to the point of turbojet shutdown. After turbojet shutdown, the turbojet subsonic duct is sealed and the vehicle accelerates to cruise with ramjets only. Figures 1 and 2 show a possible installation of the turbojet/ramjet propulsion system on the bottom aft portion of a hypersonic aircraft. These figures also indicate the appearance of the multiple-expansion ramp nozzle and the composite contour nozzle.

The purpose of this investigation was to determine the aeropropulsive performance character-istics (that is, the aerodynamic quantities affected by propulsion) such as thrust, drag, normal force, and pitching moment of two turbojet/ramjet nozzle concepts at flight Mach numbers up to 1.20. These concepts are referred to as the "multiple-expansion ramp nozzle" (MERN) (because both the turbojet and ramjet exhausts expand on ramp nozzles) and the "composite contour nozzle" (CCN) shown in reference 7 (because the nozzle is composed of both the turbojet nozzle and the ramjet nozzle), with the latter contoured to reduce expansion losses of the ramjet exhaust.

These nozzles were tested in the Langley 16-Foot Transonic Tunnel at static conditions and at free-stream Mach numbers of 0.60, 0.90, and 1.20. The simulated turbojet nozzle pressure ratio was varied from 1.0 (jet off) to approximately 20, and the angle of attack was maintained at 0°.

Symbols

Model forces and moments are referred to the body-axis system with the positive directions shown in figure 2 and the model moment reference center located at model station 32.950 in. on the model centerline.

$A_{c,k}$	increment of model cross-sectional area at metric break station 24.000 in. (see appendix), in^2
$A_{e,RJ}$	exit area of simulated ramjet nozzle (see figs. 5 and 9), in^2
$A_{e,TJ}$	exit area of simulated turbojet nozzle (see figs. 5 and 9), in^2
$A_{e,total}$	total exit area (see figs. 5 and 9), in^2
A_{max}	model cross-sectional area (maximum), 35.946 in^2
$A_{th,RJ}$	throat area of simulated ramjet nozzle (see figs. 5 and 9), 3.014 in^2 or 7.634 in^2
$A_{th,TJ}$	throat area of simulated turbojet nozzle (see figs. 5 and 9), 3.300 in^2
$A_{th,total}$	$= A_{th,RJ} + A_{th,TJ}$, in^2
A_{wet}	surface wetted area (see appendix), in^2
$C_{D,f}$	aerodynamic skin-friction drag coefficient (see appendix), $D_f/A_{max}q_\infty$

C_m pitching-moment coefficient, positive in nose-up direction for model as shown in figure 2, $M_Y/A_{\max}p_a l$ for $M = 0$ and $M_Y/A_{\max}q_\infty l$ for $M > 0$

C_N normal-force coefficient, positive in up direction for model as shown in figure 2, $N/A_{\max}p_a$ for $M = 0$ and $N/A_{\max}q_\infty$ for $M > 0$

C_p pressure coefficient, $\dfrac{p - p_\infty}{q_\infty}$

c chord, in.

D_f aerodynamic skin-friction drag

$D_{f,\mathrm{aft}}$ aerodynamic skin-friction drag on afterbody portion of model between stations 24.000 and 43.700 in., lbf

D_n total nozzle drag (aft of station 43.700 in.), lbf

F thrust along body axis, corrected as indicated in appendix, lbf

$F_{A,\mathrm{bal}}$ axial force measured by balance (see appendix), lbf

$F_{A,\mathrm{mom}}$ axial-momentum tare force due to bellows (see appendix), lbf

F_{cal} thrust of calibration nozzle (see appendix), lbf

F_g gross thrust, $(F^2 + N^2)^{1/2}$, lbf

F_i ideal isentropic thrust (see appendix), lbf

g standard acceleration of gravity $(1g \approx 32.174 \text{ ft/sec}^2)$

$h_{\mathrm{th,RJ}}$ throat height of simulated ramjet nozzle (see figs. 5 and 9), in.

k summation index (see appendix)

l model reference length, 6 in.

l_n nozzle reference length, distance from simulated turbojet nozzle throat to trailing edge of turbojet flap (see figs. 5 and 9), 6.580 in.

M free-stream Mach number

M_Y pitching moment

$\dot{m}$ measured mass-flow rate, lbm/sec

$\dot{m}_i$ ideal mass-flow rate, lbm/sec

N normal force measured by balance, positive in up direction for model as shown in figure 2, lbf

N_{Re} Reynolds number for characteristic length (see appendix)

$(\mathrm{NPR})_{\mathrm{RJ}}$ nozzle pressure ratio of simulated ramjet nozzle, $p_{t,j,\mathrm{RJ}}/p_a$ for $M = 0$ and $p_{t,j,\mathrm{RJ}}/p_\infty$ for $M > 0$

$(\mathrm{NPR})_{\mathrm{TJ}}$ nozzle pressure ratio of simulated turbojet nozzle, $p_{t,j,\mathrm{TJ}}/p_a$ for $M = 0$ and $p_{t,j,\mathrm{TJ}}/p_\infty$ for $M > 0$

p local static pressure, psia

p_a atmospheric pressure, psia

p_c local static pressure in metric break, station 24.000 in. (see appendix), psia

$p_{t,j,\mathrm{RJ}}$ jet total pressure of simulated ramjet nozzle, psia

$p_{t,j,\mathrm{TJ}}$ jet total pressure of simulated turbojet nozzle, psia

p_∞ free-stream static pressure, psia

q_∞ free-stream dynamic pressure, psia

R gas constant for air, 53.3 ft-lbf/lbm-°R

$T_{t,j,\mathrm{RJ}}$ jet total temperature of simulated ramjet nozzle (assumed to be same as $T_{t,j,\mathrm{TJ}}$), °R

$T_{t,j,\mathrm{TJ}}$ jet total temperature of simulated turbojet nozzle, °R

x axial distance from simulated turbojet nozzle throat (see figs. 5 and 9), positive downstream, in.

β boattail angle of simulated ramjet nozzle lower flap (see figs. 5 and 9), deg

γ ratio of specific heats, 1.3997 for air

δ effective jet-flow turning angle, positive in direction of positive normal force (downward jet-flow vector), $\tan^{-1}\frac{N}{F}$, deg

η	internal turning angle of simulated ramjet nozzle flap for MERN configurations (see fig. 5), deg
θ	internal turning angle of flow splitter of simulated ramjet nozzle for MERN configurations (see fig. 5), deg
σ	upstream divergence angle of flow splitter of simulated ramjet nozzle for CCN configurations (see fig. 9), deg
ϕ	downstream divergence angle of flow splitter of simulated ramjet nozzle for CCN configurations (see fig. 9), deg

Abbreviations:

CCN	composite contour nozzle
MERN	multiple-expansion ramp nozzle
RJ	ramjet
TJ	turbojet

Apparatus and Procedure

Wind Tunnel

This investigation was conducted in the Langley 16-Foot Transonic Tunnel, which is a single-return, continuous-flow, exchange-air-cooled, atmospheric-pressure wind tunnel with an octagonal, slotted-throat test section. The tunnel has a continuously variable airspeed up to a Mach number of 1.30. A detailed description of this wind tunnel is given in references 8 and 9.

Models

A possible proposed installation of an isolated combined turbojet/ramjet propulsion system on the bottom aft surface of a hypersonic aircraft is shown in figure 1. Both the multiple-expansion ramp nozzle and the composite contour nozzle are depicted in this figure and in figure 2, which shows the orientation of force and moment vectors. Figure 3 gives the general arrangement of the isolated nacelle model, support system, and the two families of nozzles tested. The nozzles were oriented on the support strut such that the ramjet lower flap was not in the wake of the strut. Since the Langley 16-Foot Transonic Tunnel has a floor-mounted support strut, it was necessary when testing for the nozzles to be rolled 180° (i.e., inverted) from the orientation indicated in figure 1, as shown in figure 3.

It is noted that the simulated turbojet portion of the nozzles was not changed for this investigation. Along with other geometric variables, the simulated ramjet nozzles had two throat sizes. The smaller throat size represented the case in which the air was flowing through the ramjet with or without combustion. The larger throat size represented the case in which a large volume of air without combustion was flowing through the ramjet in order to fill the nozzle region and thereby reduce base drag. Also, configurations were tested that represented no flow through the simulated ramjet nozzle.

Multiple-expansion ramp nozzle. A photograph of the MERN with minimum ramjet throat area installed in the tunnel is shown as figure 4. Figure 5 gives the dimensions of the two MERN configurations, that is, the minimum and maximum ramjet throat areas. These configurations represent the range of variable-geometry throat settings used during the acceleration, cruise, and deceleration modes of flight operations. Photographs of the two MERN configurations with their left sidewall removed are shown as figures 6 and 7.

Composite contour nozzle. A photograph of one of the 11 CCN configurations is shown as figure 8. Figure 9 gives the dimensions of the CCN configurations. In addition to the minimum and maximum ramjet throat areas as discussed for the MERN, the CCN also had variable ramjet flap positions in order to contour the exhaust for the reduction of overexpansion losses. The CCN was studied with two types of sidewalls. The original sidewall concept was designated as the V-notch sidewall, and a proposed lighter-weight concept was designated as the cutback sidewall. Photographs of the 11 CCN configurations with their left sidewall removed are shown as figures 10 through 20.

Jet-Exhaust Simulation

For jet-exhaust simulation, an external high-pressure air system provided a continuous flow of clean, dry air at a maximum pressure of 105 psia and a controlled temperature of nominally 540°R ahead of the nozzle throat. As shown in figure 3, this high-pressure air was brought through the support sting and strut into a high-pressure plenum and was then introduced, through eight sonic nozzles, radially into the metric portion of the model to minimize incoming axial momentum. Two flexible metal bellows provided an air seal between the metric and nonmetric portions of the nacelle. Finally, the air

traveled through choke plates into stagnation chambers and expanded through the nozzle configuration being tested.

Since only a single supply of compressed air was available, choke plates of differing porosity were used to regulate the airflows through the simulated turbojet and ramjet nozzles. Porosity refers to the percentage of flow area relative to the duct cross-sectional area. Only one choke plate was used for the simulated turbojet nozzle and it had a porosity of 49 percent. A choke plate with zero porosity was used in the ramjet nozzle, which represented the case of the ramjet being bypassed; a choke plate with 21-percent porosity was used in the ramjet nozzle having minimum throat area; and a choke plate with 40-percent porosity was used in the ramjet nozzle having maximum throat area.

Instrumentation

Metric model forces and moments were measured by a three-component strain-gauge balance. Jet total pressure and total temperature were measured by probes mounted in the instrumentation section as shown in figure 3. Rows of static-pressure orifices were on the centerline of the internal surfaces of the turbojet and ramjet nozzle flaps and on both the surfaces of the flow splitter. There was also a row of static-pressure orifices on the centerline of the external surface of the ramjet nozzle flap. Table I gives the pressure orifice locations for the MERN with minimum ramjet throat area, and table II gives the pressure orifice locations for the MERN with maximum ramjet throat area. The pressure orifice locations for all configurations of the CCN are given in table III. Static pressures in the gap at the metric break (station 24.000 in.) were obtained from 16 orifices distributed around the perimeter of the gap.

Test Conditions and Procedure

This investigation was conducted in the Langley 16-Foot Transonic Tunnel, where each nozzle configuration was tested at tunnel static conditions ($M = 0$) and at free-stream Mach numbers of 0.60, 0.90, and 1.20. Angle of attack was held constant at 0° for all tests. This angle was corrected for the 0.1° average upflow angle determined by previous experiments. Simulated turbojet nozzle pressure ratio was varied from 1.0 (jet off) to approximately 20 depending on free-stream Mach number and nozzle configuration.

In accordance with the criteria of reference 10, boundary-layer transition strips were used to ensure a turbulent boundary layer over the afterbody and the nozzle. A 0.10-in-wide strip of No. 100 silicon carbide grit, sparsely distributed in a lacquer film, was located 1.00 in. from the nose of the model. The average Reynolds number per foot varied from 3.25×10^6 at a Mach number of 0.60 to 3.90×10^6 at a Mach number of 1.20.

Figure 21 presents a representative schedule of nozzle pressure ratio with Mach number for a typical supersonic cruise turbojet engine operating at maximum thrust. This schedule, previously given in reference 11, was obtained from unpublished industry sources and is presented to indicate probable operating nozzle pressure ratio (NPR) versus Mach number values for use with the present data.

The data reduction used in this investigation is described in the appendix.

Presentation of Results

The results of this investigation are presented graphically in figures 22 through 44. Figures 24 through 31 show the force and moment data; figures 32 through 44 show the pressure distribution data. A list of data figures follows:

4

Discussion of Results

The flow through the simulated turbojet nozzle appeared to be choked throughout the test range. This condition represents a realistic simulation of flight operations in which the turbojet engine would be providing thrust in this Mach number range and the ramjet engine would be either in a noncombusting mode or a partial-combusting mode. For the simulated ramjet nozzles of this investigation, the flow passed through orifices in a choke plate. Although these orifices initiated discrete parallel jets, the distance from the orifice to the simulated ramjet nozzle throat divided by the orifice diameter, the result being approximately 57, implied uniform flow across the duct (ref. 12).

A review of the data indicated that variation of ramjet nozzle pressure ratio $(NPR)_{RJ}$ and total discharge coefficient $\dot{m}/\dot{m}_i$ with $(NPR)_{TJ}$ for the MERN and the CCN configurations of this test depended only on throat area. Therefore, $(NPR)_{RJ}$ and $\dot{m}/\dot{m}_i$ can be presented uniquely for the two throat areas at each Mach number representative of all configurations tested. Figure 22 gives the variation of $(NPR)_{RJ}$ as a function of turbojet nozzle pressure ratio $(NPR)_{TJ}$ for the two ramjet throat areas. The variation of $\dot{m}/\dot{m}_i$ (the discharge coefficient) for the two ramjet throat areas is shown in figure 23. This figure indicates that the discharge coefficient for the nozzles with the smaller simulated ramjet throat area was very high, near unity, whereas the discharge coefficient for the nozzles with the larger simulated

ramjet throat area was rather low, near 0.81 at all Mach numbers. Therefore, it can be concluded that the discharge coefficient for the NPR's investigated is independent of nozzle type tested, Mach number, and nozzle pressure ratio; and it varies inversely with ramjet nozzle throat area for the nozzles tested.

An estimate of mass-flow split between the turbojet and ramjet nozzles was calculated using the measured total mass-flow rate and the ideal mass-flow rate through the turbojet nozzle. These values are presented in table IV.

Force and Moment Data

The force and moment data are shown in figures 24 through 28 and in figures 30 and 31. These figures show the variation of axial-force ratio, normal-force coefficient, pitching-moment coefficient, gross thrust ratio, and effective turning angle, all as a function of simulated turbojet nozzle pressure ratio. Of primary importance is axial-force ratio $(F - D_n)/F_i$, which indicates performance at wind-on ($M > 0$) conditions. All data are displayed at Mach numbers of 0, 0.60, 0.90, and 1.20, except for gross thrust ratio and effective jet turning angle which could be measured only at static conditions. Figure 29 is a summary comparison of selected data.

Multiple-expansion ramp nozzle (MERN). The two test configurations of the MERN design (see fig. 5 and table V(a)) had different simulated ramjet throat areas. It is noted that since the turbojet nozzle throat area remains constant throughout the experiment, the term "throat area" refers to the ramjet nozzle throat area. The effects of throat area on the aeropropulsive performance characteristics (aerodynamic quantities affected by propulsion) of the MERN (see figs. 6 and 7) are shown in figure 24. The internal thrust performance F/F_i at $M = 0$ (fig. 24(a)) was essentially the same for both throat areas. However, a difference due to throat area can be seen for axial-force ratio $(F - D_n)/F_i$ (fig. 24(a)). This difference increases with increasing Mach number and is approximately 11 percent for $(NPR)_{TJ} = 7$ at $M = 1.20$. The MERN design of the current investigation is similar in geometry to typical single-expansion ramp nozzle designs (ref. 13) that have exhaust-flow containment on one side of the nozzle and free exhaust-flow expansion on the other side. The thrust performance of nozzles with free-expansion boundaries (single-expansion ramp, plug, and wedge nozzles) will be sensitive to external-flow effects at forward speeds. Thus, some of the axial-force-ratio differences shown in figure 24 for $M > 0$ may be caused by external-flow effects. However,

most of the axial-force-ratio variation with throat area is believed to be caused by differences in external drag on the two flap configurations tested. It is apparent that the nozzle with the smallest throat area (with the largest boattail angle β) has the lowest values of axial-force ratio at forward speeds.

The pressure data for the external surface of the ramjet flap, shown in figures 32 and 33, indicate that the external flow over both the minimum and maximum throat area flaps was separated. In addition, both flaps had nearly identical pressure distributions, particularly at $M = 0.90$ and 1.20. However, the axial projected area of the minimum throat area flap is approximately 60 percent larger than that of the maximum throat area flap. Thus, the external drag on the minimum throat area flap is also approximately 60 percent higher than that on the maximum throat area flap. This increased drag would partially account for the lower axial-force-ratio performance of the minimum throat area configuration at forward speeds.

The trends of normal-force coefficient C_N (fig. 24(b)) are very similar for both throat areas with the most negative value occurring at $(NPR)_{TJ} \approx 5$ for all Mach numbers, a result apparently due to the maximum δ occurring at this $(NPR)_{TJ}$. (See fig. 24(d).) Normal-force coefficient becomes less negative with increasing Mach number since C_N due to aerodynamics is overpowering C_N due to the normal component of thrust at increasing Mach number. Likewise, the trends of pitching-moment coefficients C_m are naturally similar with the largest value at $(NPR)_{TJ} \approx 5$, and this value decreases with increasing Mach number (fig. 24(c)). Since the projected normal area of the nozzle does not vary greatly with throat area, large changes in C_N and C_m would not be expected to occur. Although angle of attack α was held constant at $0°$, C_N and C_m were nonzero values because of the unsymmetrical design of the nozzles.

At static conditions ($M = 0$), two additional parameters were measured and given as follows: the ratio of gross thrust to ideal thrust F_g/F_i and the effective jet-flow turning angle δ. References 13 through 17 describe previous research conducted on unsymmetrical nozzles at static conditions. Figures 24(a) and 24(d) show that the value of F/F_i is approximately 4 percent less than F_g/F_i at $(NPR)_{TJ} \approx 5$ ($\delta = -17°$ highest turning angle achieved), which demonstrates that significant flow turning was developed and that a loss in thrust results from that flow turning. This level of performance loss agrees with the calculation in which this loss is expressed as $1 - \cos \delta$.

Composite contour nozzle (CCN). The test configurations of the CCN design involved two ramjet throat areas, three ramjet flap positions, and two types of sidewalls. (See fig. 9 and table V(b).)

The effects of ramjet flap geometry on the aeropropulsive characteristics of the CCN with minimum ramjet throat area and V-notch sidewalls (see figs. 9 through 12) are shown in figure 25. There is an effect of ramjet flap geometry on F/F_i with flap 3 generally having the highest level of static performance. Large fluctuations of δ occurred for all ramjet flap configurations (fig. 25(d)). The largest turning angles were measured for ramjet flap 2. The pressure data for the ramjet side of the flow splitter and internal surface of the ramjet flap shown in figures 34, 35, and 36 indicate shocks and regions of exhaust-flow separation in the CCN that vary in strength and location with $(NPR)_{TJ}$. Obviously, this unstable flow caused the erratic values of δ as shown in figure 25(d), and this turning of the flow from the body axis resulted in a substantial axial-thrust loss, as well as a substantial increase in the magnitude of normal force and pitching moment.

In addition to the effects of δ, both $A_{e,RJ}/A_{th,RJ}$ and $A_{e,total}/A_{th,total}$ also have an effect on the thrust. Since flap 2 has lower $A_{e,RJ}/A_{th,RJ}$ and $A_{e,total}/A_{th,total}$ than flaps 1 and 3, it could be expected to have a lower thrust loss due to less possible overexpansion than flaps 1 and 3 at low $(NPR)_{TJ}$. (See figs. 10, 11, and 12.) Even so, the configuration with flap 2 still generally had the lowest thrust performance throughout the Mach number test range. From the photograph shown in figure 11, it is obvious that use of flap 2 will result in turning the jet flow away from the body-axis direction. This observation is confirmed from the fact that this configuration produced the largest absolute values of δ, C_N, and C_m. Thus, large jet-flow turning losses were probably the cause for the low performance of this configuration. The axial-force ratio $(F - D_n)/F_i$ decreases with increasing Mach number for all configurations tested, a result probably due to the increasing drag on the lower surface flap of the ramjet.

The effects of ramjet flap geometry on the characteristics of the CCN with minimum ramjet throat area and cutback sidewalls (see figs. 13, 14, and 15) are shown in figure 26. The trends for these data are the same as those noted for this configuration with the V-notch sidewalls. Therefore, it can be concluded that there is no significant difference in aeropropulsive performance, and only minor differences in the other characteristics, resulting from substitution of the cutback sidewalls for the V-notch sidewalls.

Figure 27 is given as an example that illustrates data affected by sidewall geometry for all configurations tested.

The effects of ramjet flap geometry on the aeropropulsive characteristics of the CCN with maximum ramjet throat area and V-notch sidewalls (see figs. 16, 17, and 18) are shown in figure 28. At $M = 1.20$, the three flap geometries gave essentially the same thrust ratio results. Values of the normal-force coefficients and pitching-moment coefficients are similar to those of the minimum throat area configuration, except that they are smaller in magnitude. The lower magnitudes are probably caused by less jet-flow turning for the large $A_{th,RJ}$ configurations. (See fig. 28(d).) This lower jet turning angle is due to the reduced angle of the ramjet flap that is required to increase the ramjet throat angle. (Compare figs. 11 and 17.)

From a comparison of figures 25(a) and 28(a), it can be concluded that, generally, the configurations with the minimum throat area produce the higher aeropropulsive performance for the composite contour nozzle at Mach numbers less than or equal to 0.90. However, at a Mach number of 1.20, the configurations with the maximum throat area produced the higher performance.

A comparison of figures 25(a) and 28(a) leads to the conclusion that for the entire Mach numbers and nozzle pressure ratios tested, the highest aeropropulsive performance of the composite contour nozzle was obtained with the straight ramjet divergent flap (that is, RJ flap 3 as shown in figs. 9(b), 12, and 15).

From a comparison of figures 24(a), 25(a), and 28(a), it can be concluded that at $M < 1.20$, the performance of the composite contour nozzle was higher than that of the multiple-expansion ramp nozzle, especially for the minimum ramjet throat area configurations. At $M = 1.20$ the performance was essentially the same. This result is summarized in figure 29.

The aeropropulsive characteristics of the CCN with maximum ramjet throat area (RJ flap 2) and cutback sidewalls (see fig. 19) are shown in figure 30. As expected, these data are the same as those for the configuration with ramjet flap 2 and V-notch sidewalls. (See fig. 28.)

Figure 31 shows the aeropropulsive characteristics of the CCN with ramjet flap 3 (see figs. 12, 15, 18, and 20) and a blank plate in place of the choke plate at the entrance to the simulated ramjet nozzle. This arrangement simulated conditions in which the ramjet inlet would be bypassed for turbojet-only operation. The geometric variables for this set of configurations were minimum and maximum simulated ramjet throat area and V-notch and cutback sidewalls. Although there is no flow through the

simulated ramjet throat, the geometries of the nozzles are considerably different, as can be seen by comparing figures 12 and 18. The variation of axial-force ratios F/F_i and $(F - D_n)/F_i$ was only slightly affected by both ramjet throat area and the sidewall type. The variation of normal-force coefficient C_N and all the values related to this parameter, such as C_m, F_g/F_i, and δ, displayed somewhat more dependence on both the ramjet throat area and the sidewall type. It is noted that most variations occurred at wind-on conditions $(M > 0)$. Therefore, it appears that the boattail angle of the simulated ramjet nozzle ($\beta = 14.7°$ for the minimum ramjet throat area and $\beta = 7.2°$ for the maximum ramjet throat area) is the predominant geometric cause of data variation between these four nozzle configurations.

Pressure Data

The pressure data are presented in figures 32 and 33 for the MERN configurations and in figures 34 through 44 for the CCN configurations. Data are presented for Mach numbers of 0, 0.60, 0.90, and 1.20 over a $(NPR)_{TJ}$ range from 1.0 (jet off) to the maximum value depending on nozzle geometry and Mach number. The jet-off condition pertains only to the C_p plots of figures 32 through 43. Pressures on the external surface of the ramjet flap are presented as C_p versus x/l_n, where x is the distance downstream from the turbojet throat and l_n is the length of the turbojet flap from the throat to the trailing edge. (See figs. 5 and 9.) The internal pressures are presented as ratios of $p/p_{t,j}$ (where the jet total pressure $p_{t,j}$ is either for the ramjet or turbojet) versus x/l_n. For the MERN with minimum ramjet throat area, the turbojet throat is located at station 49.200 in. $(x/l_n = 0.000)$ and the ramjet throat is located at station 45.700 in. $(x/l_n = -0.532)$. For the MERN with maximum ramjet throat area, the turbojet throat is still located at station 49.200 in., but the ramjet throat is located at station 45.300 in. $(x/l_n = -0.593)$. (See fig. 5.) For all CCN configurations, the turbojet throat is located at station 48.700 in. $(x/l_n = 0.000)$ and the ramjet throat is located at station 47.000 in. $(x/l_n = 0.258)$. (See fig. 9.)

The pressure data in figure 44 are for the special cases of four CCN configurations when the ramjet portion of the nozzle was blanked off. The data are presented for Mach numbers of 0.60, 0.90, and 1.20 over a $(NPR)_{TJ}$ range from 1.0 to some maximum value depending on nozzle geometry and Mach number. Only the internal pressures for the turbojet are presented since the ramjet was blanked off for those cases.

Multiple-expansion ramp nozzle. As can be seen in figures 32 and 33, all the internal pressure orifices of the simulated turbojet portion of the nozzle are located downstream of the geometric throat (turbojet nozzle throat at $x/l_n = 0.000$). The pressure ratio $p/p_{t,j}$ at the first static orifice location is less than the ratio $p/p_{t,j} = 0.528$ (the choke condition at the turbojet throat) and indicates that the flow was choked at the turbojet throat for all $(NPR)_{TJ}$ values. However, for the MERN with minimum ramjet throat area, shock-induced separation occurs shortly downstream of the throat for $(NPR)_{TJ} = 2.89$ at $M = 0$, and this separation moves downstream as NPR is increased and becomes fully attached at $(NPR)_{TJ} = 18.73$ and $M = 1.20$. Comparing the data for the internal surfaces of the turbojet shows that there is very little effect of Mach number or ramjet throat area on these pressures when the flow is choked and attached.

All the pressure orifices on the ramjet side of the flow splitter and flap interior surface are located downstream of the ramjet throat $(x/l_n = -0.532$ and -0.593 for minimum and maximum ramjet throat area, respectively). On the ramjet side of the splitter, the flow was choked upstream of the first pressure measurement (probably near or slightly upstream of the geometric throat) and supersonic flow existed on the splitter. A series of exhaust-flow compressions and expansions occurred as the flow progressed down the duct. During the compression that occurred between $x/l_n = -0.20$ and $x/l_n = -0.04$ on the minimum ramjet throat area configuration, the exhaust flow became subsonic $(p/p_{t,j,RJ} > 0.528)$ for the lowest values of $(NPR)_{TJ}$ tested (e.g., $(NPR)_{TJ} < 5.74$ at $M = 0.60$). Except for $(NPR)_{TJ} = 2.87$ where the exhaust flow remained subsonic throughout the remainder of the duct at $M = 0.60$ and 0.90, the ensuing expansion generally caused supersonic exhaust flow on the downstream portion of the splitter.

Since subsonic flow does not occur on the internal side of the ramjet flap except at $(NPR)_{TJ} = 2.87$, a subsonic-flow bubble (surrounded by supersonic flow) exists on the ramjet splitter at some values of $(NPR)_{TJ}$. Reference 18 describes the formation of subsonic-flow bubbles in supersonic flow. A similar phenomenon is indicated on the splitter for the maximum ramjet throat area configuration, except that the subsonic-flow bubble has moved downstream and becomes smaller. From the pressure distributions shown on the internal surface of the minimum ramjet throat area flap (fig. 32), it is obvious that the exhaust flow did not choke at the geometric throat but at a downstream station near $x/l_n = -0.40$. Thus, the actual ramjet throat for the minimum throat area configuration did not coincide with the

geometric throat but was canted inside the duct. For the maximum throat area configuration (fig. 33), this was not the case since the exhaust flow is choked upstream of the first measured pressure. Once the flow was choked in the minimum ramjet throat area duct, the flow expanded supersonically until a shock-induced separation occurred near $x/l_n = -0.28$. On the flap of the maximum throat area ramjet duct (fig. 33), a single compression occurred downstream of the throat followed by a supersonic-flow expansion. For the maximum ramjet throat area configuration, exhaust flow remained attached to the ramjet flap for all values of $(NPR)_{TJ}$ above approximately 5.

Although the boattail angle of the ramjet flap was different for the MERN with minimum and maximum ramjet throat area ($42.5°$ and $26.1°$, respectively), the magnitude of the external-flap pressures remains nearly the same for both configurations at $M = 0.90$ and 1.20. Therefore, since previous experimentation (ref. 19) indicates that the largest possible boattail angle without separation (at the current test Mach numbers) is in the range from $18°$ to $20°$, it is expected that the flow over both flaps is totally separated. Even at $M = 0.60$, the flow along the exterior of the ramjet flap of the MERN with the minimum ramjet throat area ($\beta = 42.5°$) appears totally separated. At this Mach number, some pressure recovery (an increase in C_p with increasing x/l_n) should occur if the external flow were attached to the flap. At jet-on conditions, the external flow again appears to be separated from the flap. Therefore, it can be concluded that for both configurations of the MERN, flow separation was present on the external surface of the ramjet flap.

Composite contour nozzle. Figures 34 through 44 show internal pressure distributions on the CCN nozzle. As in the case of the MERN, all the internal pressure measurements for the turbojet portion of the CCN nozzle are downstream of the turbojet geometric throat. Also, the discussion of pressure distribution in the turbojet portion of the MERN configurations applies to the CCN configurations. All the pressure orifices on the ramjet side of the flow splitter and flap interior surface are located downstream of the ramjet geometric throat ($x/l_n = -0.258$). Two distinct pressure distribution profiles are evident for the ramjet side of the flow splitter. For the CCN configurations with the minimum ramjet throat area, there was a pressure rise near the trailing edge caused by a shock recompression that is characteristic of an over-expanded (too large $A_{e,RJ}/A_{th,RJ}$) nozzle operation. For the CCN configurations with the maximum ramjet throat area, the pressure distribution decreases throughout the ramjet duct, an indication of flow

expanding supersonically along the entire length of the flow splitter. For both throat areas, the exhaust flow appears to choke (become sonic) on the splitter at a location near or slightly downstream of the geometric throat location.

The pressure distributions on the internal surface of the CCN ramjet flap indicate that the exhaust flow chokes upstream of the first pressure measurement for both throat areas tested. Supersonic flow characterized by a series of flow expansions and compressions exists on the entire length of the internal ramjet flap. An exception to this result can be noted for the lowest values of $(NPR)_{TJ}$ tested for which subsonic flow existed over the aft portion of the flap ($(NPR)_{TJ} = 2.87$ in fig. 34(b)). Some of the ramjet flap distributions indicate shock-induced flow separation ($(NPR)_{TJ} = 3.82$ and 4.78 in fig. 34(b)) and subsonic-flow bubbles embedded in the supersonic-exhaust flow field ($(NPR)_{TJ} = 3.64$ in fig. 35(b), for example).

The external C_p distributions shown in figures 34 through 43 are typical. Some pressure recovery is evident at $M = 0.60$ and 0.90. Jet effects are small but feed relatively far forward in the separated flow over the ramjet flap for subsonic flow ($M = 0.60$ and 0.90). At $M = 1.20$, jet effects are small and limited to the areas of the flap trailing edge since pressure disturbances do not propagate upstream in supersonic flow. Large increases in C_p near the trailing edge of the flap (the farthest aft pressure measurement) could be caused by shock-induced separation or by slight movement of the terminal shock with NPR.

There was no significant difference in the pressure distributions between the CCN configurations with V-notch sidewalls and those with cutback sidewalls. This can be seen in the comparison of figure 34 with 37, 35 with 38, and 36 with 39 for minimum ramjet throat area and in figure 40 with 41 for maximum ramjet throat area.

The pressure distributions on the turbojet side of the flow splitter and the internal surface of the turbojet flap are shown in figure 44 for the special case in which the flow inlet to the ramjet nozzle is blanked off. This figure shows that the effects of both sidewalls (i.e., V-notch or cutback) and the ramjet throat area are insignificant.

Conclusions

An investigation has been conducted in the Langley 16-Foot Transonic Tunnel to determine the aero-propulsive performance characteristics of two families of isolated combined turbojet/ramjet nozzle configurations. This investigation was conducted at static conditions and at Mach numbers M of 0.60,

0.90, and 1.20 over a nozzle pressure ratio range from 1.0 (jet off) to approximately 20 while angle of attack was held constant at 0°. The results of this investigation indicated the following conclusions for the Mach number range tested:

1. The discharge coefficient was independent of the nozzle type tested, Mach number, and nozzle pressure ratio; and it varied inversely with the ramjet nozzle throat area for the nozzles investigated in this experiment.

2. Increasing the ramjet throat area of the multiple-expansion ramp nozzle (MERN) produced an aeropropulsive performance increase that increased with Mach number.

3. Some configurations of the composite contour nozzle (CCN) generated large values of effective jet-flow turning angle at static conditions. This turning of the flow from the body axis resulted in a substantial thrust loss, as well as substantial increases in the magnitude of normal force and pitching moment.

4. No significant difference in aeropropulsive performance of the CCN was observed by substituting the cutback sidewalls for the V-notch sidewalls.

5. Generally, the minimum ramjet throat area produced the higher aeropropulsive performance for the CCN at $M \leq 0.90$. However, at $M = 1.20$, the maximum ramjet throat area produced the higher performance.

6. Throughout the entire Mach number and nozzle pressure ratio regime, the highest aeropropulsive performance of the CCN was obtained with a straight ramjet divergent flap (position 3).

7. At $M < 1.20$, the performance of the CCN was higher than that of the MERN; but at $M = 1.20$, the performance was essentially the same.

Appendix

Data Reduction

All data from the instrumentation of the aircraft nozzle model and the wind-tunnel facility were recorded simultaneously on magnetic tape. For each data point, 50 frames of data were taken over a period of 5 sec and the average value was used for computation of standard force, moment, and pressure coefficients.

However, before experimental testing of the MERN and CCN configurations could begin, it was necessary to conduct a calibration to determine axial-momentum tare force. Axial-momentum tares were evaluated by statically ($M = 0$) testing several Stratford calibration nozzles (ref. 20) over the range of supply pressures, mass-flow rates, and throat areas intended for the test nozzles. Reference 12 shows the geometry of these calibration nozzles and gives their well-established values of F_{cal}/F_i and $\dot{m}/\dot{m}_i$. Therefore, this evaluation took the form

$$F_{A,\mathrm{mom}} = F_{A,\mathrm{bal}} - F_{\mathrm{cal}} \tag{1}$$

The value of $F_{A,\mathrm{mom}}$ determined was used to correct for axial-momentum and bellows tare forces caused by the high-pressure air flowing from the nonmetric high-pressure plenum into the instrumentation section through the eight small injection nozzles. (See fig. 3.) Although the air is injected radially and the flexible seals (metal bellows) are placed in tandem in an effort to eliminate such tares, small forces do arise in practice and must be taken into account. In the present investigation, these forces were generally less than 2 percent of ideal thrust. In equation (1), the term $F_{A,\mathrm{bal}}$ represents the raw-balance output corrected for interactions and model weight tares. (See ref. 8.) At static conditions ($M = 0$) during testing of the MERN and CCN configurations, the thrust along body axis (F) was determined as

$$F = F_{A,\mathrm{bal}} - F_{A,\mathrm{mom}} \tag{2}$$

In order to determine the thrust minus nozzle drag ($F - D_n$) during wind-on testing ($M > 0$) of the MERN and CCN, additional corrections were required to isolate the sum of external and internal forces on the nozzle alone (model portion aft of station 43.700 in.), since the model strain-gauge balance (fig. 3) measures the sum of pressure and viscous forces on the entire metric afterbody (model portions aft of station 24.000 in.). The nozzle body-axis thrust-minus-drag performance was computed from the relationship

$$F - D_n = F_{A,\mathrm{bal}} + \sum_{k=1}^{16} \left(p_{c,k} - p_\infty \right) A_{c,k} + D_{f,\mathrm{aft}} - F_{A,\mathrm{mom}} \tag{3}$$

The pressure-area term corrects for the force on the front face of the metric afterbody caused by differences between the cavity pressure p_c in the metric break and free-stream pressure p_∞. Even though experience with this model has shown cavity pressures to be extremely uniform, 16 orifices were used in these tests to determine this balance-correction term.

The term $D_{f,\mathrm{aft}}$ is the friction drag of the metric afterbody (stations 24.000 to 43.700 in.) ahead of the nozzle, which must be restored to the balance reading since this force is not associated with the nozzle. Aerodynamic skin-friction drag coefficients $C_{D,f}$ were computed from the flat-plate formula for the turbulent, compressible boundary layer given in reference 21 and modified by the factor $A_{\mathrm{wet}}/A_{\mathrm{max}}$. Thus,

$$C_{D,f} = \left[\frac{0.472}{(1 + 0.2M^2)^{0.467} \, (\log_{10} N_{\mathrm{Re}})^{2.58}} \right] \frac{A_{\mathrm{wet}}}{A_{\mathrm{max}}} \tag{4}$$

At each Mach number, $C_{D,f}$ was calculated for Reynolds number N_{Re} and wetted area A_{wet} corresponding to two different characteristic lengths on the model (fig. 3): (1) from the nose to the upstream end of the nozzle at station 43.700 in., and (2) from the nose to the metric-break station (24.000 in.). The difference between calculations (1) and (2) provided the estimated skin-friction drag coefficient of the metric afterbody ahead of the nozzle. The value $D_{f,\mathrm{aft}}$ used in the correction of the balance data was then computed as the product of the above coefficient, the model reference area at the corresponding test Mach number, and the free-stream dynamic pressure.

Ideal thrust, defined as the product of measured mass flow and the ideal isentropic velocity, was obtained from the relation

$$F_i = \dot{m} \left\{ \sqrt{\frac{2\gamma}{\gamma - 1} \frac{R}{g} T_{t,j,\mathrm{TJ}} \left[1 - \left(\frac{p_\infty}{p_{t,j,\mathrm{TJ}}} \right)^{\frac{\gamma-1}{\gamma+1}} \right]} \right.$$

$$\left. + \sqrt{\frac{2\gamma}{\gamma - 1} \frac{R}{g} T_{t,j,\mathrm{RJ}} \left[1 - \left(\frac{p_\infty}{p_{t,j,\mathrm{RJ}}} \right)^{\frac{\gamma-1}{\gamma}} \right]} \right\} \tag{5}$$

Measured mass-flow rate $\dot{m}$ was obtained by using the multiple critical venturi system described in reference 12.

The ideal mass-flow rates for the test configurations were computed from stagnation pressure and temperatures measured in the tailpipe by using the choked-flow equation

$$\dot{m}_i = p_{t,j,\mathrm{TJ}} A_{\mathrm{th,TJ}} \sqrt{\frac{\gamma g}{R T_{t,j,\mathrm{TJ}}} \left(\frac{2}{\gamma+1}\right)^{\frac{\gamma+1}{\gamma-1}}}$$

$$+ p_{t,j,\mathrm{RJ}} A_{\mathrm{th,RJ}} \sqrt{\frac{\gamma g}{R T_{t,j,\mathrm{RJ}}} \left(\frac{2}{\gamma+1}\right)^{\frac{\gamma+1}{\gamma-1}}} \qquad (6)$$

References

1. Gregory, Thomas J.; Petersen, Richard H.; and Wyss, John A.: Performance Tradeoffs and Research Problems for Hypersonic Transports. *J. Aircr.*, vol. 2, no. 4, July–Aug. 1965, pp. 266–271.

2. Jarlett, F. E.: *Performance Potential of Hydrogen Fueled, Airbreathing Cruise Aircraft.*
   Volume 1—Summary. NASA CR-73074, 1966.
   Volume 2—Studies, Phase I—Final Report. NASA CR-73075, 1966.
   Volume 2A, Phase I—Propulsion Studies. NASA CR-73076, 1966.
   Volume 3, Phase II—Studies. NASA CR-80501, 1966.
   Volume 4—Final Studies. NASA CR-73078, 1966.

3. Gregory, Thomas J.; Wilcox, Darrell E.; and Williams, Louis J.: The Effects of Propulsion System—Airframe Interactions on the Performance of Hypersonic Aircraft. AIAA Paper No. 67-493, July 1967.

4. Morris, R. E.; and Williams, N. B.: *Study of Air Breathing Launch Vehicles With Cruise Capability.*
   Volume I—Summary. NASA CR-73194, 1968.
   Volume II—Synthesis, Performance, Cost, and Evaluation. NASA CR-73195, 1968.
   Volume III—Aerodynamics, Propulsion, and Subsystems. NASA CR-73196, 1968.
   Volume IV—Thermodynamics, Structures, and Weights. NASA CR-73197, 1968.
   Volume V—Economics Model. NASA CR-73198, 1968.
   Volume VI—Technology. NASA CR-73199, 1968.

5. Apel, G. F.; and Hines, R. W.: *Estimated Performance of a Mach 8.0 Hydrogen Fueled Wrap-Around Turboramjet (SWAT-201B).* TDM-2001 (Contract AF33(615)-5153), Pratt & Whitney Aircraft, Jan. 4, 1967.

6. Waters, Mark H.: *Turbojet-Ramjet Propulsion System for All-Body Hypersonic Aircraft.* NASA TN D-5993, 1971.

7. Brewer, G. D.; Chirivella, J.; Boyd, J.; Peyton, R.; and Sherwood, D.: *High Altitude Configuration Technology.* U.S. Air Force, Oct. 1983.
   Volume I—Program Results. AFWAL-TR-83-3097-VOL-I. (Available from DTIC as AD B079 979L.)
   Volume II—Supporting Technology Data. AFWAL-TR-83-3097-VOL-II. (Available from DTIC as AD B079 980L.)

8. Peddrew, Kathryn H., compiler: *A User's Guide to the Langley 16-Foot Transonic Tunnel.* NASA TM-83186, 1981.

9. Corson, Blake W., Jr.; Runckel, Jack F.; and Igoe, William B.: *Calibration of the Langley 16-Foot Transonic Tunnel With Test Section Air Removal.* NASA TR R-423, 1974.

10. Braslow, Albert L.; Hicks, Raymond M.; and Harris, Roy V., Jr.: *Use of Grit-Type Boundary-Layer-Transition Trips on Wind-Tunnel Models.* NASA TN D-3579, 1966.

11. Carson, George T., Jr.; and Lee, Edwin E., Jr.: *Experimental and Analytical Investigation of Axisymmetric Supersonic Cruise Nozzle Geometry at Mach Numbers From 0.60 to 1.30.* NASA TP-1953, 1981.

12. Berrier, Bobby L.; Leavitt, Laurence D.; and Bangert, Linda S.: *Operating Characteristics of the Multiple Critical Venturi System and Secondary Calibration Nozzles Used for Weight-Flow Measurements in the Langley 16-Foot Transonic Tunnel.* NASA TM-86405, 1985.

13. Berrier, Bobby L.; and Re, Richard J.: *Effect of Several Geometric Parameters on the Static Internal Performance of Three Nonaxisymmetric Nozzle Concepts.* NASA TP-1468, 1979.

14. Capone, Francis J.: *Static Performance of Five Twin-Engine Nonaxisymmetric Nozzles With Vectoring and Reversing Capability.* NASA TP-1224, 1978.

15. Re, Richard J.; and Berrier, Bobby L.: *Static Internal Performance of Single Expansion-Ramp Nozzles With Thrust Vectoring and Reversing.* NASA TP-1962, 1982.

16. Re, Richard J.; and Leavitt, Laurence D.: *Static Internal Performance Including Thrust Vectoring and Reversing of Two-Dimensional Convergent-Divergent Nozzles.* NASA TP-2253, 1984.

17. Berrier, Bobby L.; and Leavitt, Laurence D.: *Static Internal Performance of Single-Expansion-Ramp Nozzles With Thrust-Vectoring Capability up to 60°.* NASA TP-2364, 1984.

18. Green, Robert S.; and Carson, George T., Jr.: *Measured Pressure Distributions Inside Nonaxisymmetric Nozzles With Partially Deployed Thrust Reversers.* NASA TM-89044, 1987.

19. Silhan, Frank V.; and Cubbage, James M., Jr.: *Drag of Conical and Circular-Arc Boattail Afterbodies at Mach Numbers From 0.6 to 1.3.* NACA RM L56K22, 1957.

20. Stratford, B. S.: The Calculation of the Discharge Coefficient of Profiled Choked Nozzles and the Optimum Profile for Absolute Air Flow Measurement. *J. Royal Aeronaut. Soc.*, vol. 68, no. 640, Apr. 1964, pp. 237–245.

21. Shapiro, Ascher H.: *The Dynamics and Thermodynamics of Compressible Fluid Flow, Volume II.* Ronald Press Co., c.1954.

Table I. Pressure Orifice Locations for the MERN With Minimum Throat Area
[Coordinate system is defined in figure 5]

TJ flap (internal surface)
x/ι_n
0.025
.099
.148
.198
.277
.331
.418
.505
.593
.790
.923

Flow splitter	
TJ side	RJ side
x/ι_n	x/ι_n
0.025	-0.508
.099	-.426
.148	-.380
.198	-.334
	-.274
	-.212
	-.137
	-.046
	.099
	.198

RJ flap	
Internal surface	External surface
x/ι_n	x/ι_n
-0.508	-0.501
-.426	-.401
-.380	-.365
-.334	-.319
-.274	-.274
-.213	-.228
-.137	-.182
	-.137

TJ throat

TJ flap (internal surface)
x/ι_n
0.025
.099
.148
.198
.277
.331
.418
.505
.593
.790
.923

Flow splitter	
TJ side	RJ side
x/ι_n	x/ι_n
0.025	-0.568
.099	-.502
.148	-.410
.198	-.331
	-.258
	-.167
	-.076
	-.046
	.099
	.198

RJ flap	
Internal surface	External surface
x/ι_n	x/ι_n
-0.568	-0.501
-.501	-.410
-.410	-.342
-.334	-.289
-.258	-.236
-.167	-.182
-.076	-.129
	-.076

TJ throat
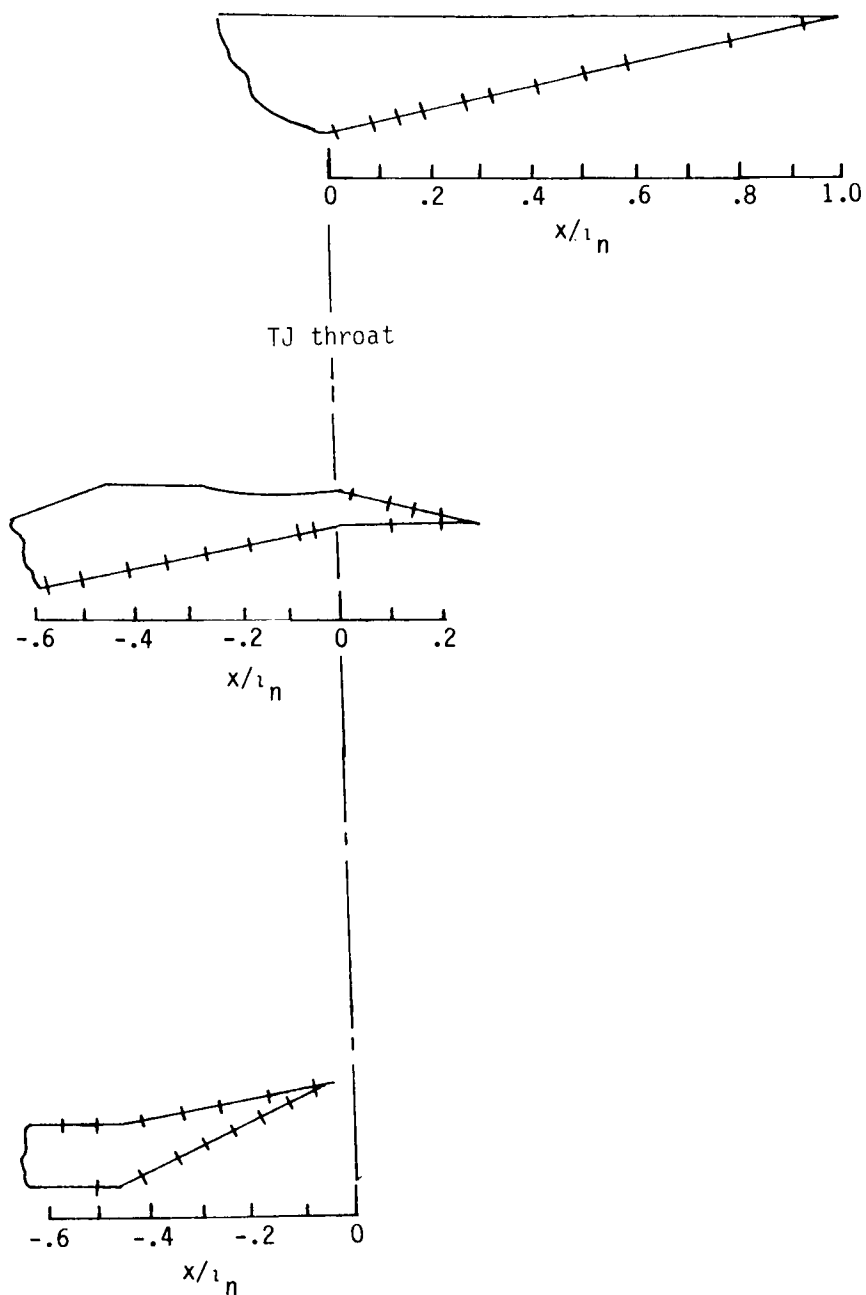
Table III. Pressure Orifice Locations for all Configurations of the CCN
[Coordinate system is defined in figure 9]

TJ flap (internal surface)
x/ι_n
0.025
.099
.148
.198
.277
.331
.418
.505
.593
.790
.923
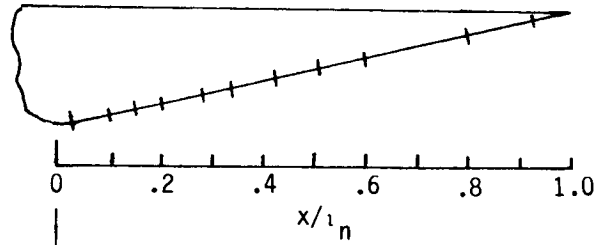
Flow splitter	
TJ side	RJ side
x/ι_n	x/ι_n
0.025	-0.227
.099	-.133
.148	-.007
.198	.099
	.198
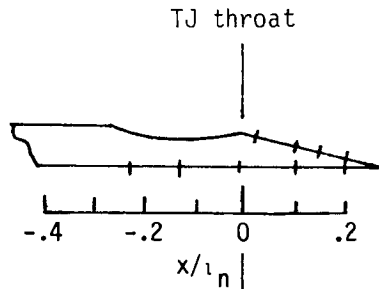
RJ flap	
Internal surface	External surface
x/ι_n	x/ι_n
-0.227	-0.471
-.133	-.297
-.007	-.106
.099	.091
.198	.280
.227	.496
.331	.712
.418	.927
.505	
.790	
.950	
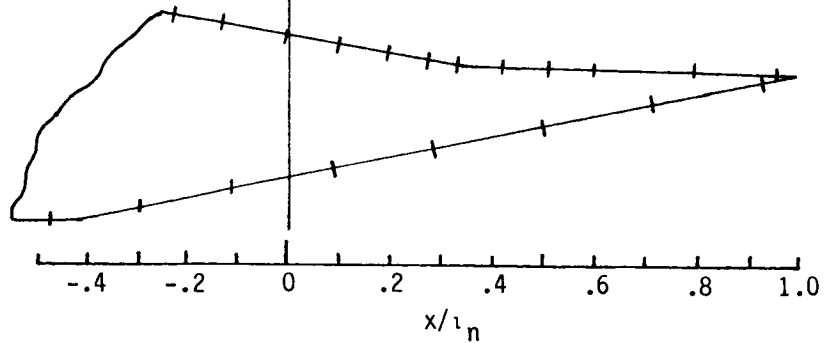
TJ throat

Table IV. Estimated Mass-Flow Split Between Turbojet and Ramjet Nozzles

(a) Configurations with minimum ramjet throat area

$(NPR)_{TJ}$	$\dot{m}_{i,TJ}/\dot{m}$	$(NPR)_{RJ}$	$\dot{m}_{RJ}/\dot{m}$
1.92	0.69	1.29	0.31
4.78	.68	2.92	.32
12.77	.68	7.83	.32

(b) Configurations with maximum ramjet throat area

$(NPR)_{TJ}$	$\dot{m}_{i,TJ}/\dot{m}$	$(NPR)_{RJ}$	$\dot{m}_{RJ}/\dot{m}$
2.69	0.53	1.33	0.47
6.89	.52	3.34	.48
12.44	.52	5.95	.48

Table V. Geometric Details of the MERN and CCN Configurations

(a) MERN configurations tested (see fig. 5)

Throat area mode	$A_{th,RJ}$, in^2	$h_{th,RJ}$, in.	$A_{e,RJ}$, in^2	$A_{e,total}$, in^2	β, deg	η, deg	θ, deg	Figure
Minimum	3.014	0.685	3.761	17.117	42.5	29.7	29.0	6
Maximum	7.634	1.735	8.573	20.567	26.1	11.0	11.6	7

(b) CCN configurations tested (see fig. 9)

Throat area mode	Sidewalls	RJ flap	$A_{th,RJ}$, in^2	$h_{th,RJ}$, in.	$A_{e,RJ}$, in^2	$A_{e,total}$, in^2	β, deg	σ, deg	ϕ, deg	Figure
Minimum	V-notch	1	3.014	0.685	5.835	18.090	11.3	-10.3	-1.1	10
Minimum	V-notch	2	→	→	3.318	10.399	21.0	-1.1	13.0	11
Minimum	V-notch	3			3.318	15.450	14.7	-1.1	-1.1	12
Minimum	Cutback	1			5.835	18.090	11.3	-10.3	-1.1	13
Minimum	Cutback	2	→		3.318	10.399	21.0	-1.1	13.0	14
Minimum	Cutback	3			3.318	15.450	14.7	-1.1	-1.1	15
Maximum	V-notch	1	7.634	1.735	11.199	24.448	3.2	-12.9	-2.8	16
Maximum	V-notch	2	→	→	8.405	18.916	10.2	-2.8	3.5	17
Maximum	V-notch	3	→	→	→	21.168	7.2	→	-2.8	18
Maximum	Cutback	2				18.916	10.2		3.5	19
Maximum	Cutback	3				21.168	7.2		-2.8	20

19
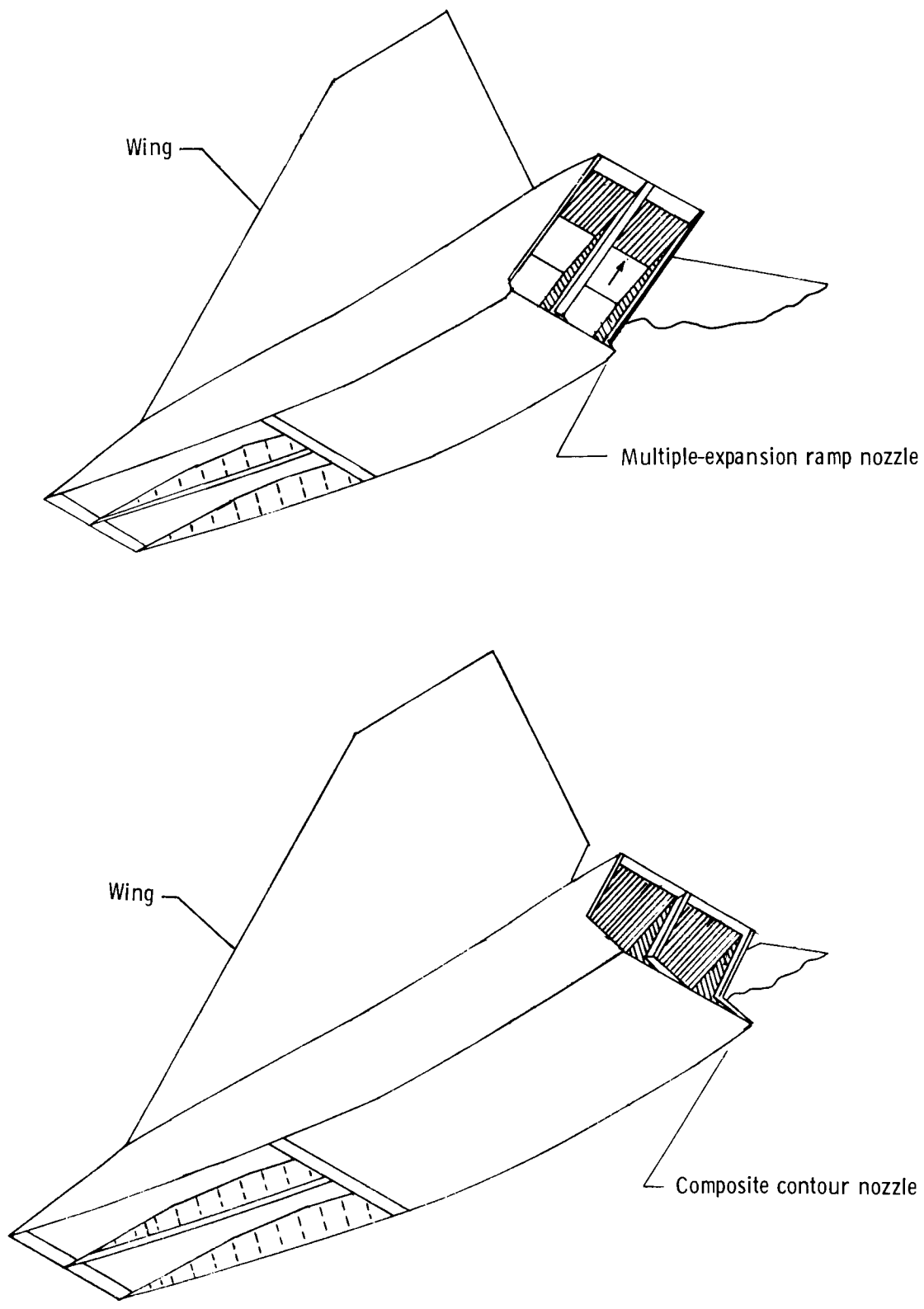
Figure 1. Possible installation of turbojets and ramjets on bottom aft portion of hypersonic aircraft.
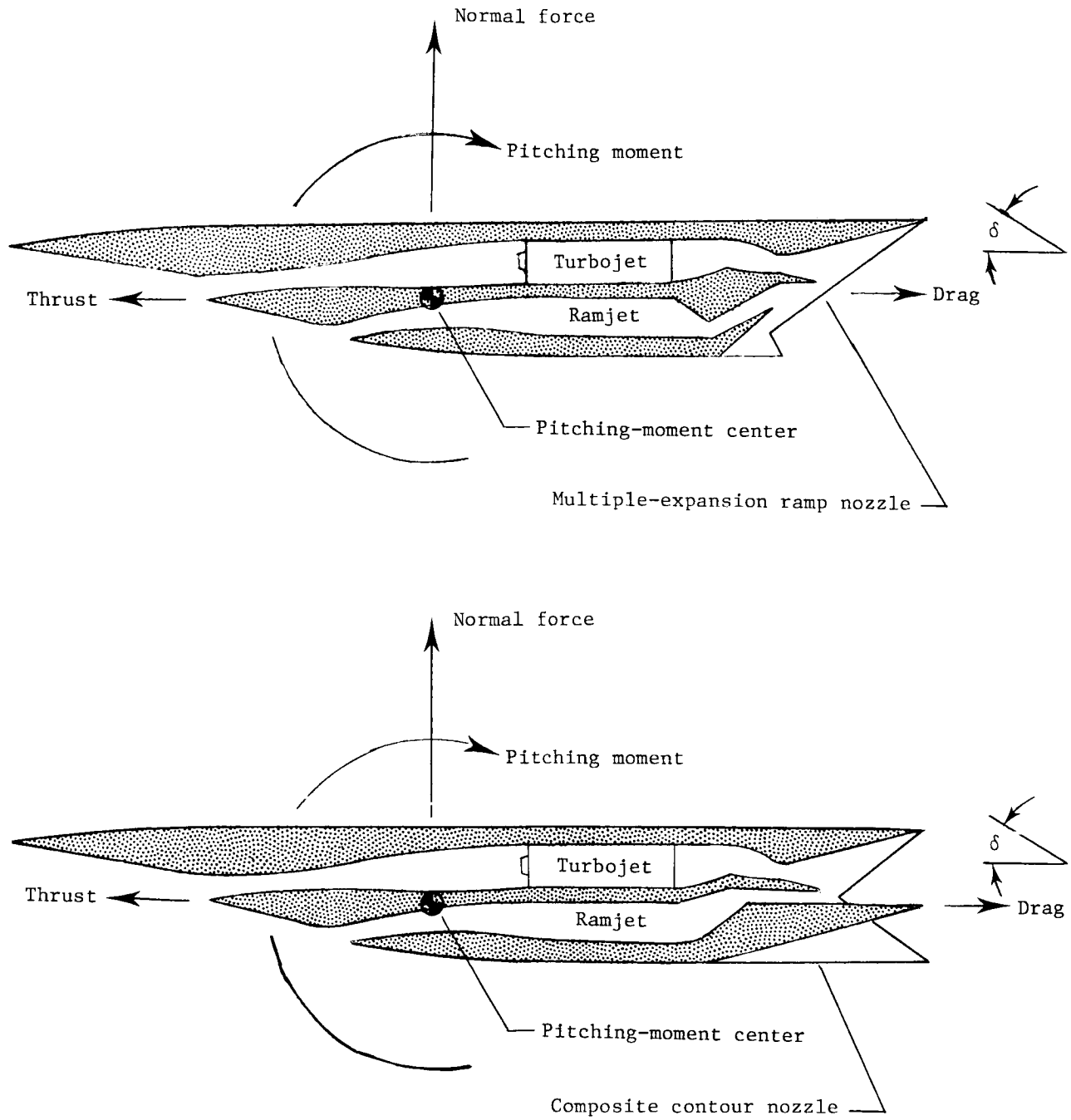
Figure 2. Aircraft-oriented positive direction of thrust, drag, normal force, and pitching moment used in data presentation of this report.
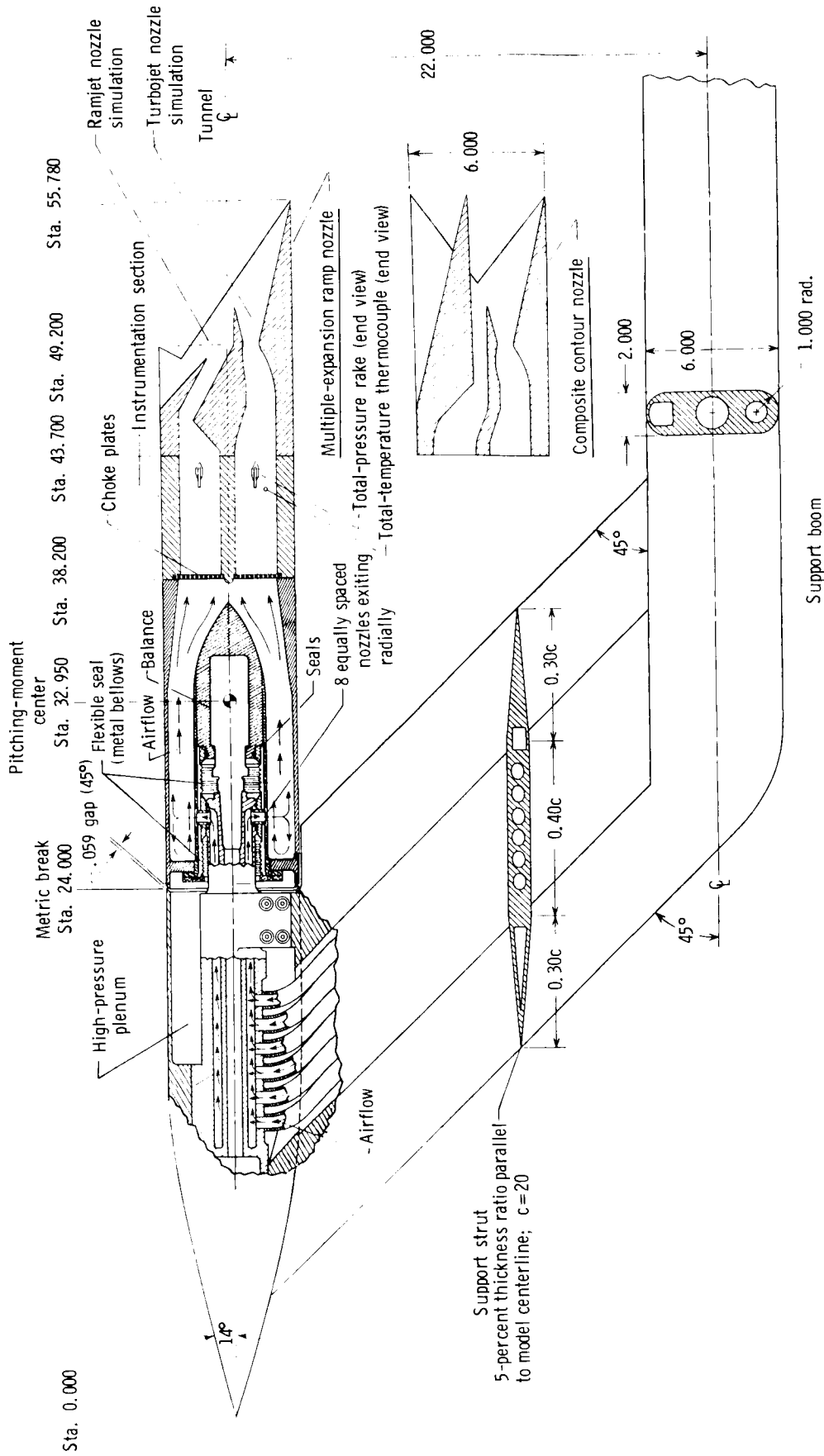
Figure 3. General arrangement of nacelle model and two families of nozzles tested. All linear dimensions are in inches. Model width is 6.000 in.
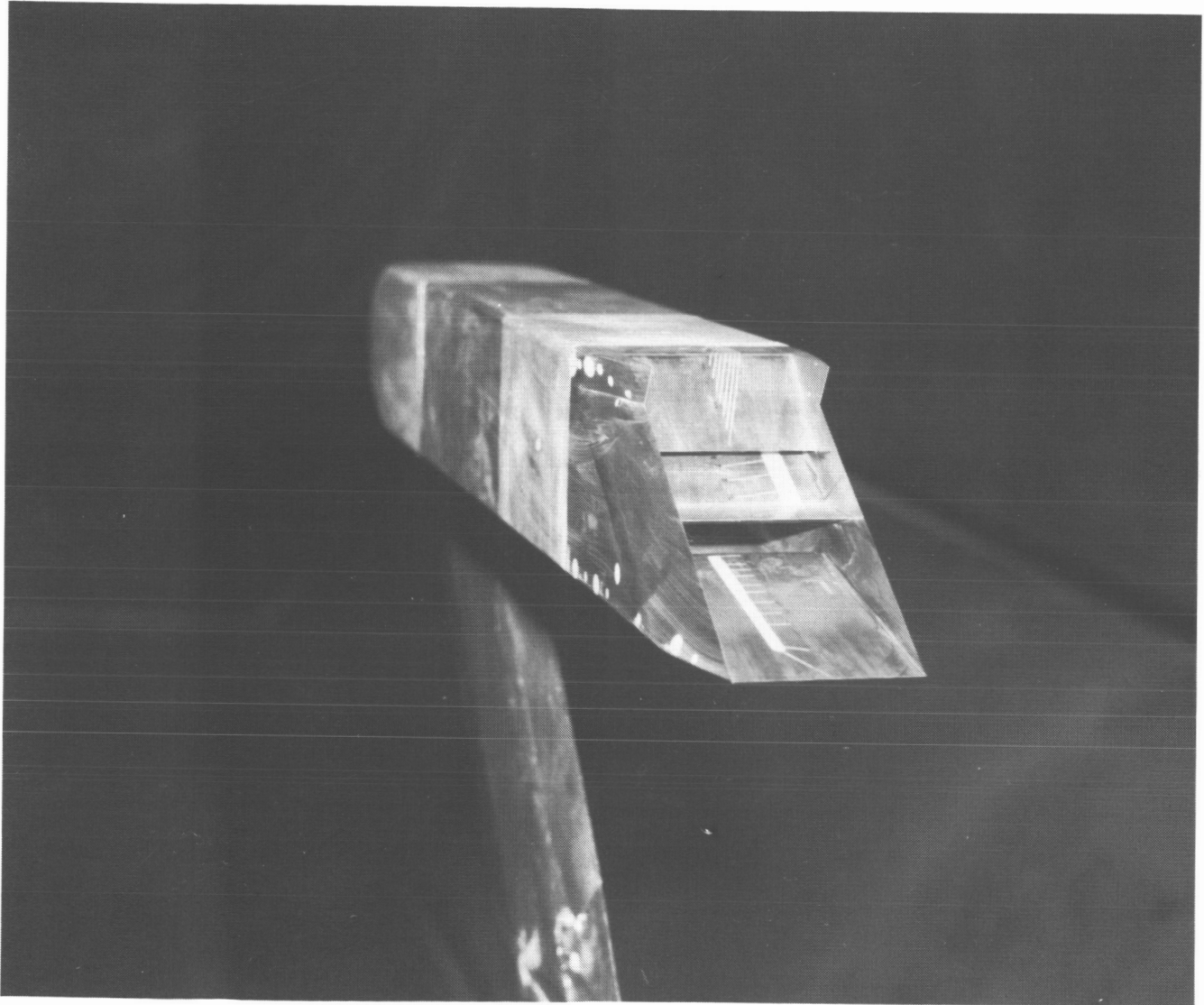
Figure 4. Installation of MERN with minimum ramjet throat area.
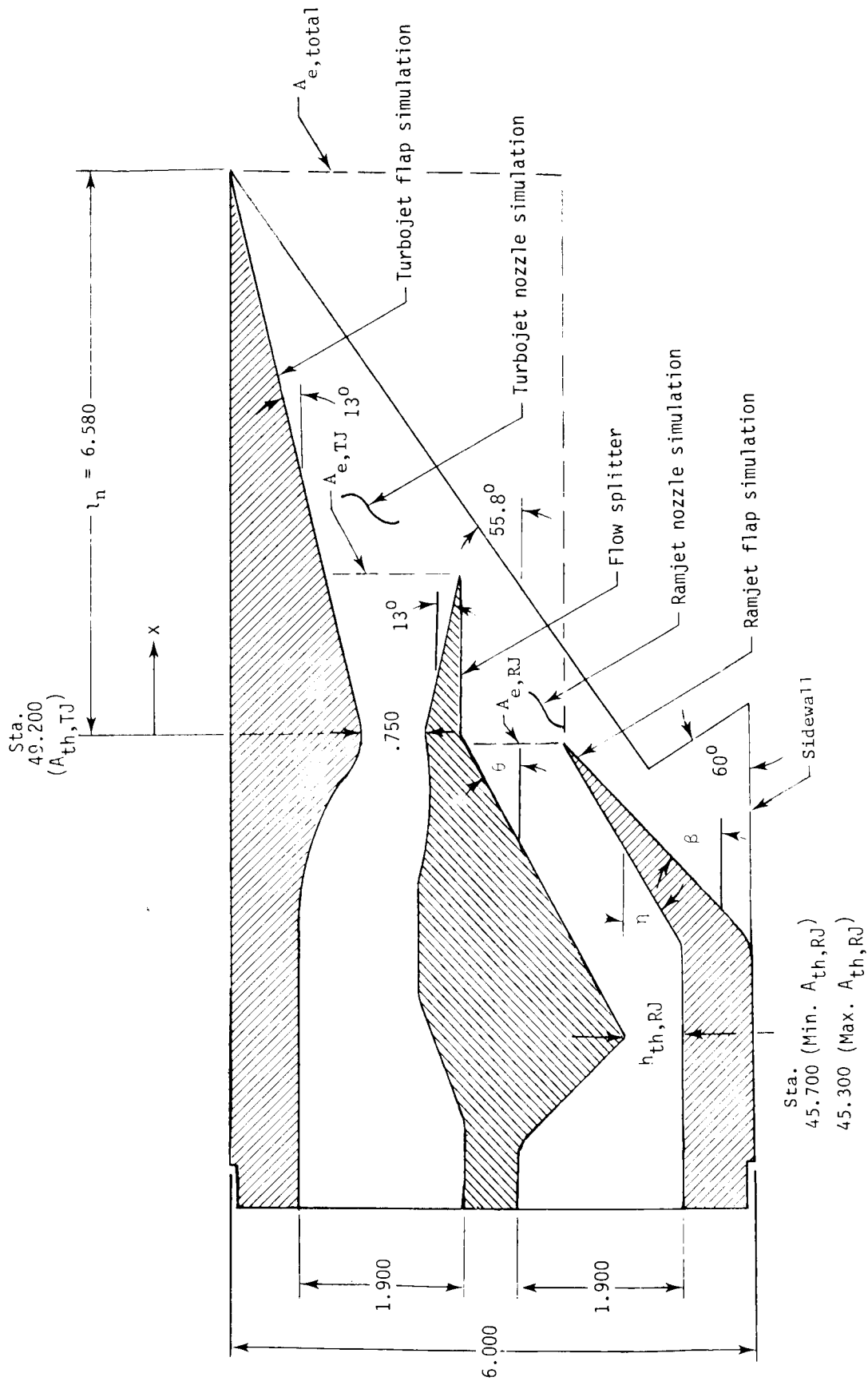
Figure 5. Geometric sketch of two MERN configurations. Nozzle width is 4.400 in., $A_{th,TJ} = 3.300$ in^2, and $A_{e,TJ} = 6.690$ in^2. Exit areas represent vertical projections between flaps. All linear dimensions are in inches. This figure shows the nozzle rolled 180° from the test orientation in order to match the aircraft installation shown in figure 1. For additional clarification, see table V(a) and figures 6 and 7.
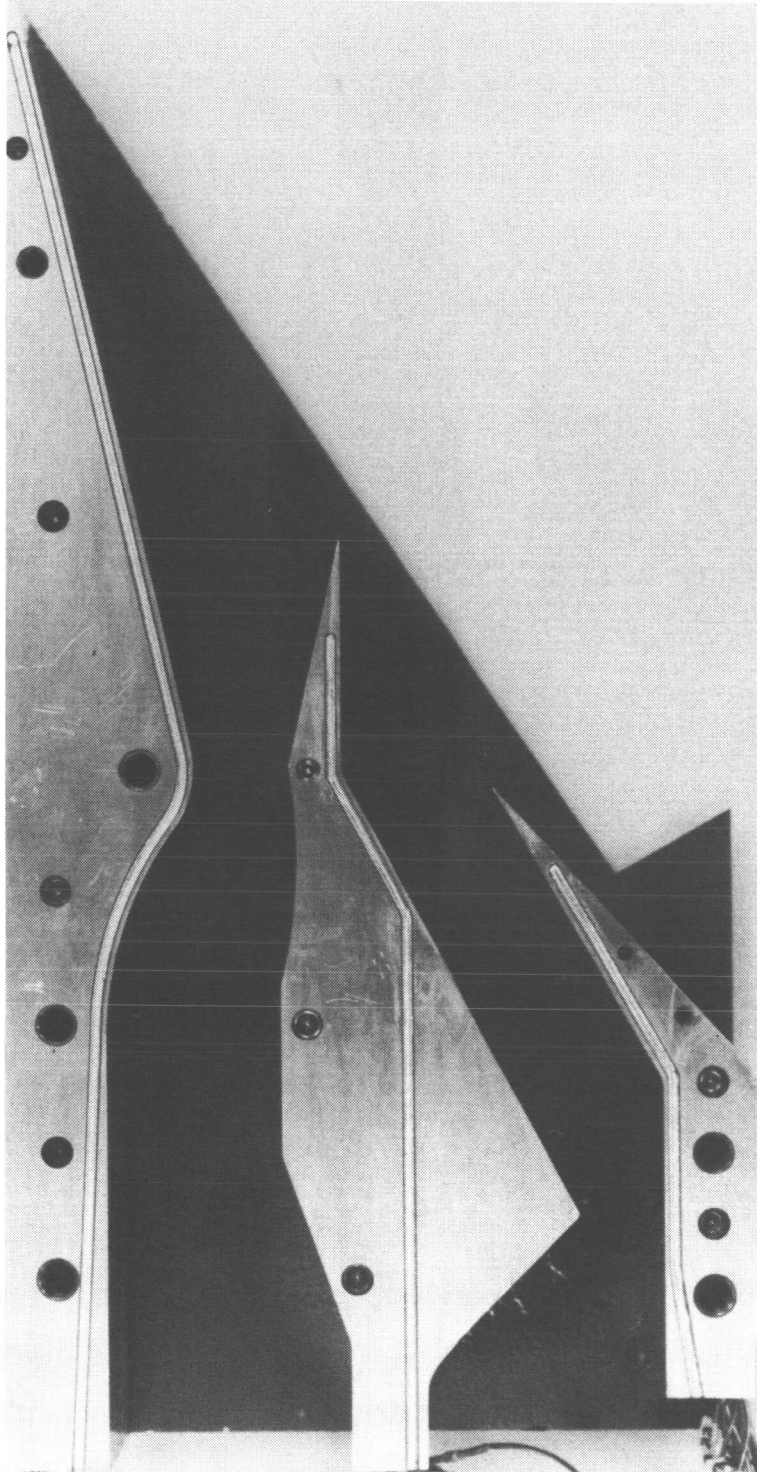
Figure 6. MERN with minimum ramjet throat area. $A_{e,\mathrm{RJ}}/A_{\mathrm{th,RJ}} = 1.248$; $A_{e,\mathrm{TJ}}/A_{\mathrm{th,TJ}} = 2.109$; $A_{e,\mathrm{total}}/A_{\mathrm{th,total}} = 2.711$.
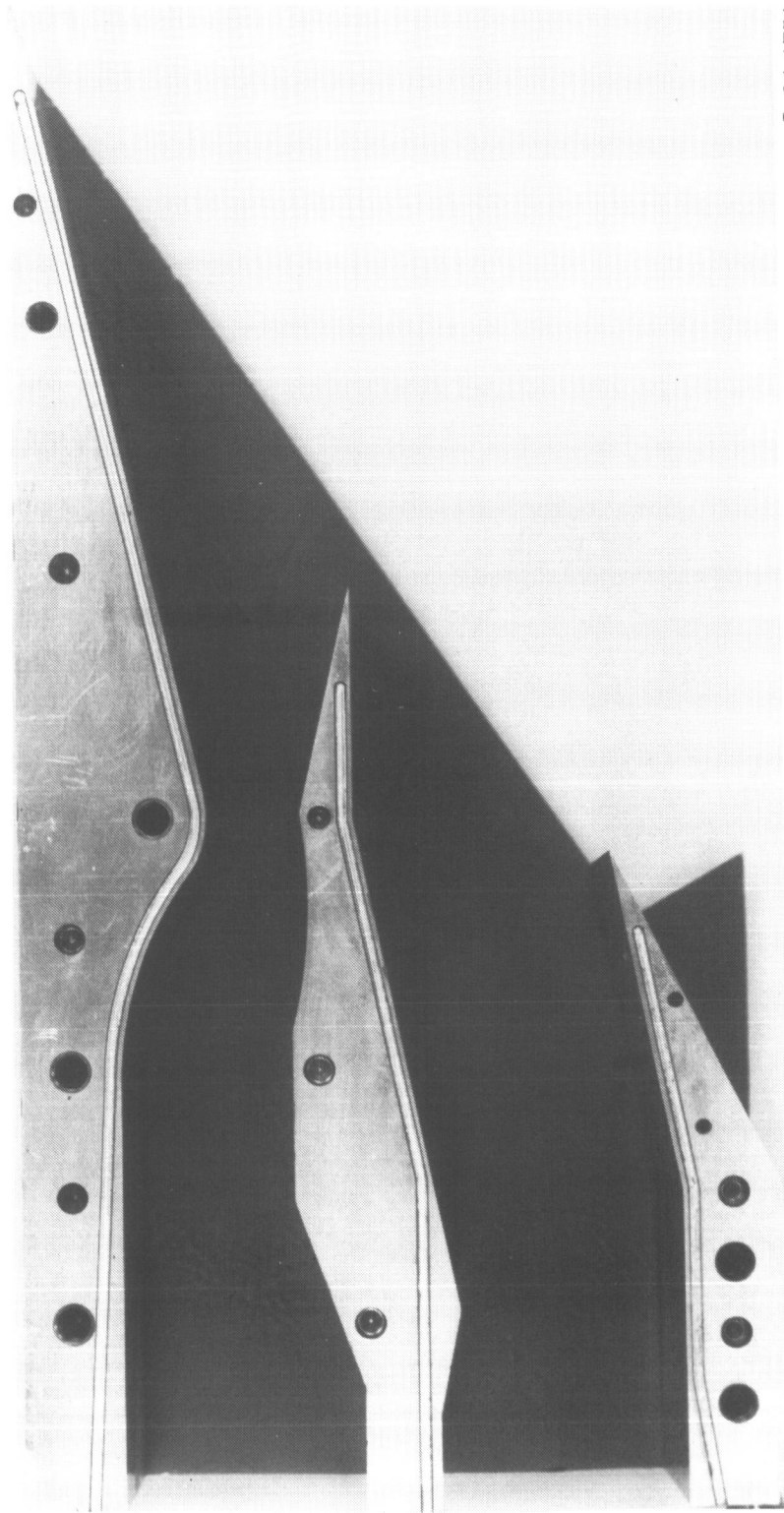
Figure 7. MERN with maximum ramjet throat area. $A_{e,\text{RJ}}/A_{\text{th,RJ}} = 1.123$; $A_{e,\text{TJ}}/A_{\text{th,TJ}} = 2.109$; $A_{e,\text{total}}/A_{\text{th,total}} = 1.881$.

L-84-1751

26
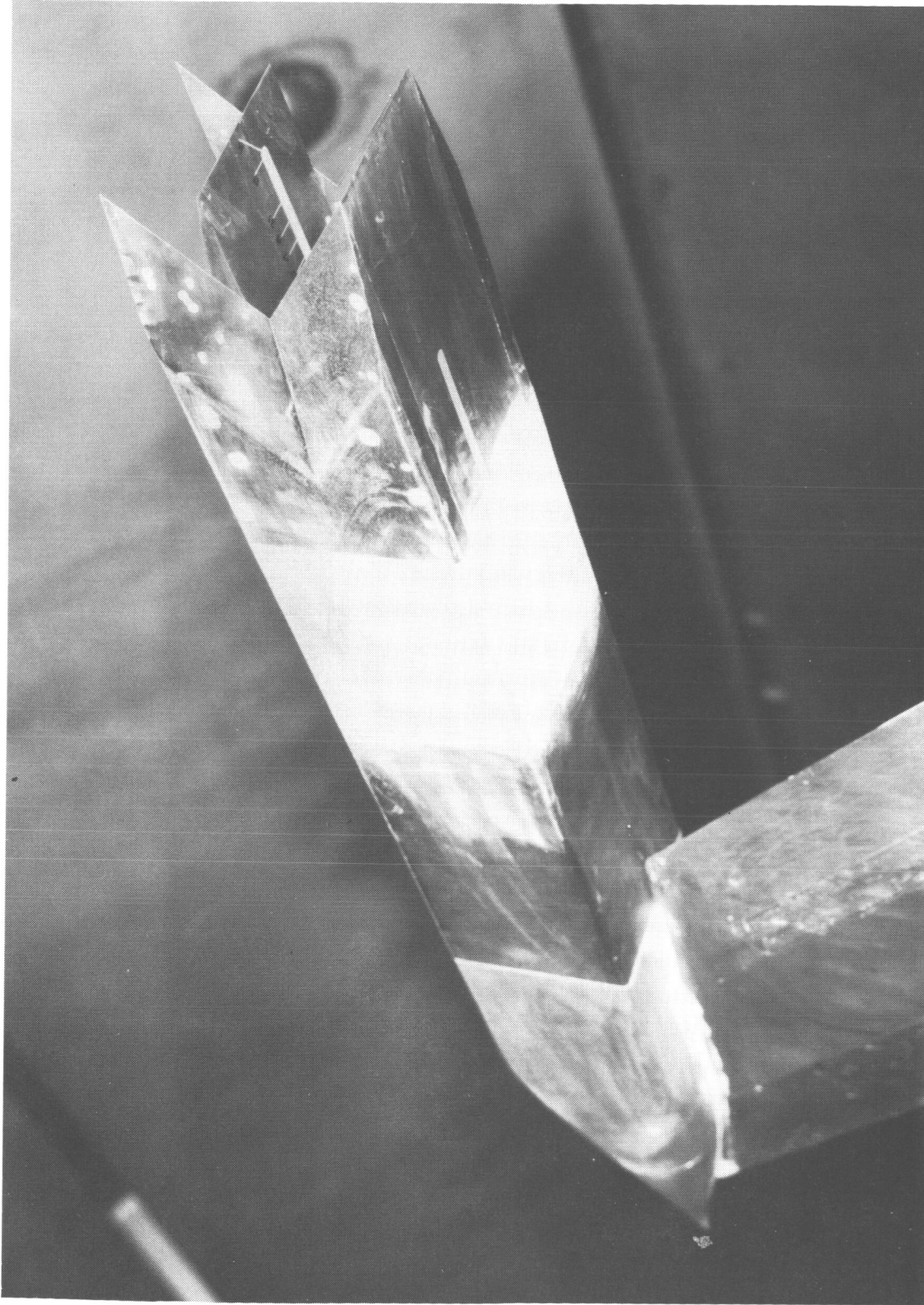
Figure 8. Installation of CCN with minimum ramjet throat area, V-notch sidewalls, and ramjet flap 3.
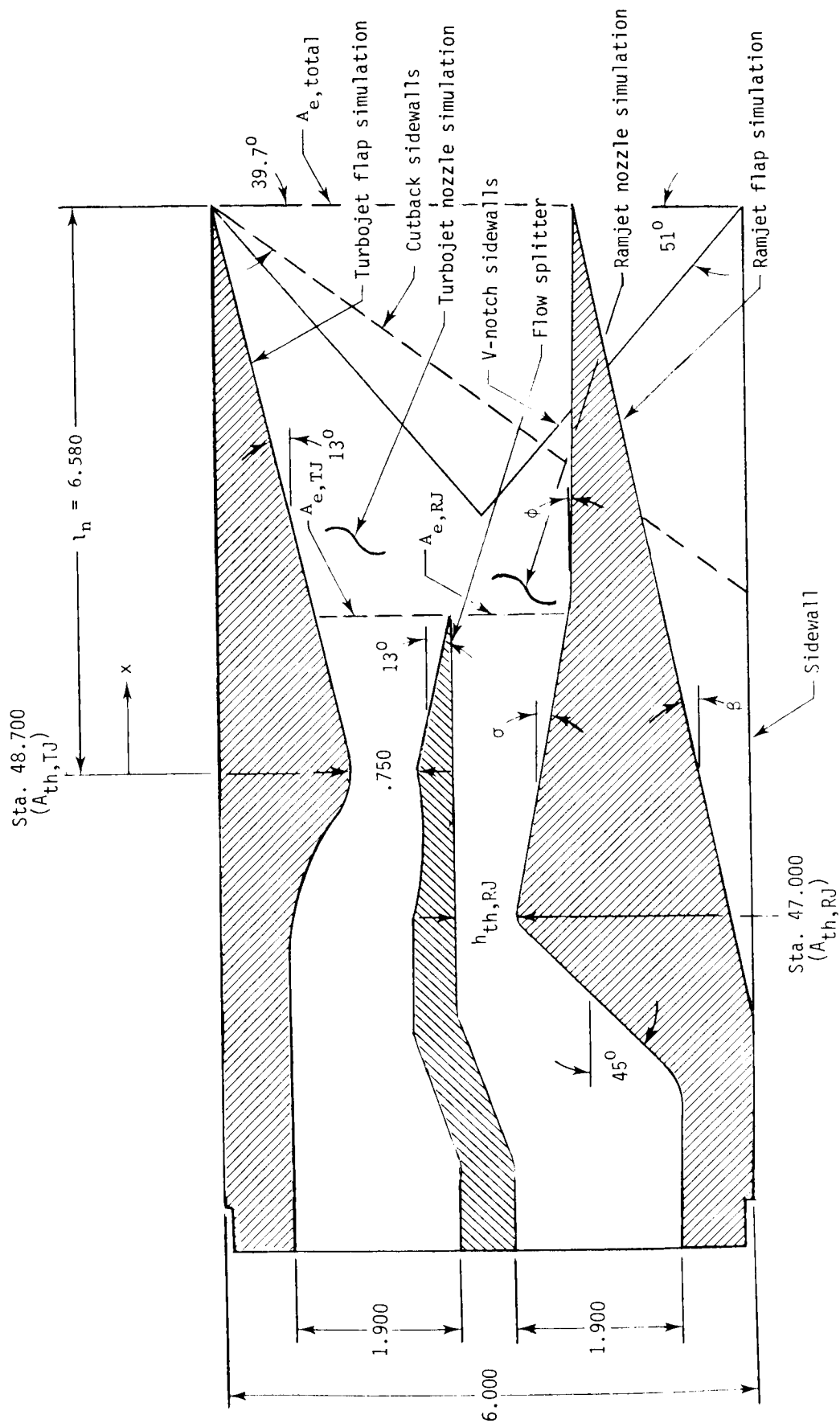
Figure 9. Geometric sketch of CCN configurations. Nozzle width is 4.400 in., $A_{th,TJ} = 3.300$ in^2, and $A_{e,TJ} = 6.690$ in^2. Exit areas represent vertical projections between flaps. All linear dimensions are in inches. This figure shows the nozzle rolled 180° from the test orientation in order to match the aircraft installation shown in figure 1. For additional clarification, see table V(b) and figures 10 through 20.
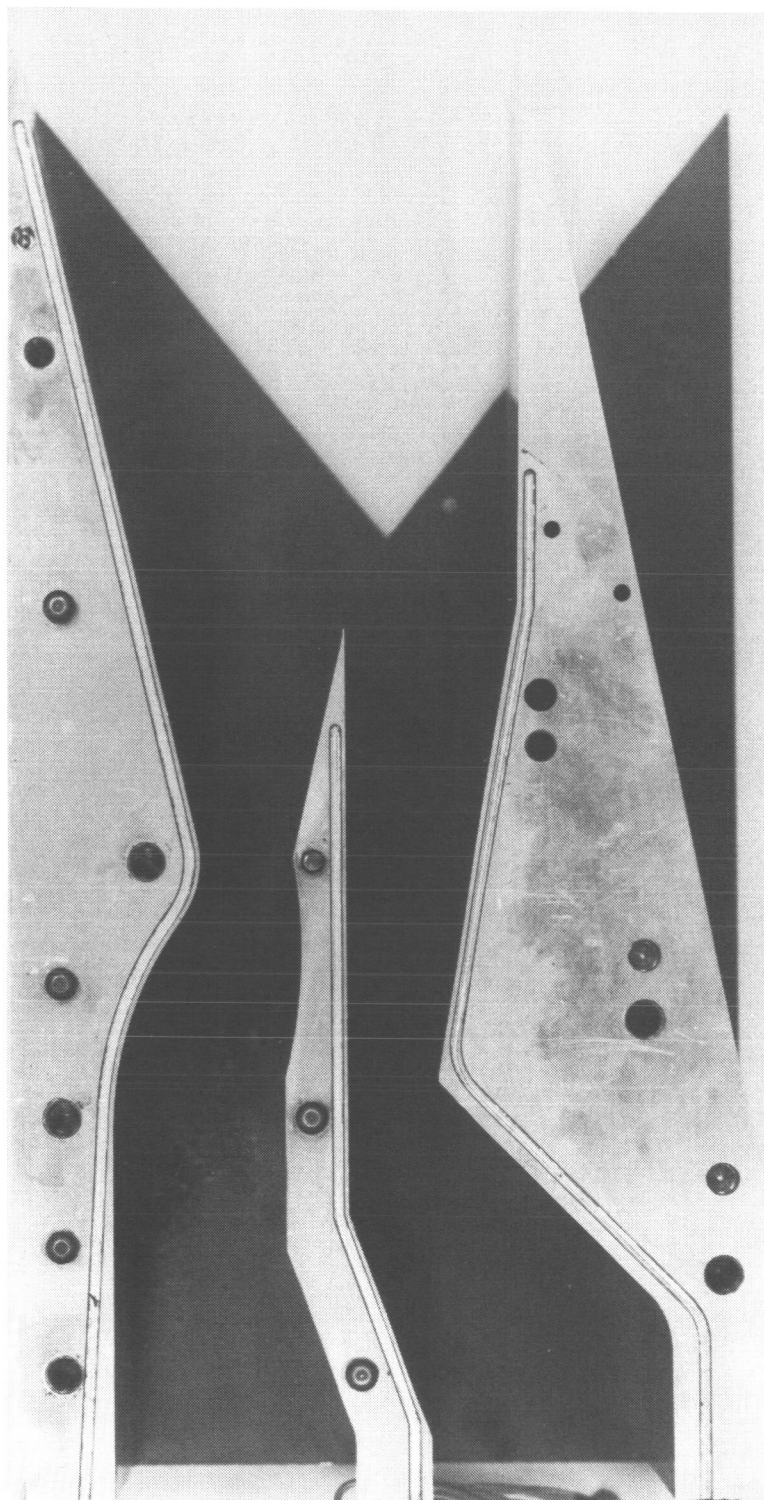
Figure 10. CCN with minimum ramjet throat area, V-notch sidewalls, and ramjet flap 1. $A_{e,\mathrm{RJ}}/A_{\mathrm{th,RJ}} = 1.936$; $A_{e,\mathrm{TJ}}/A_{\mathrm{th,TJ}} = 2.109$; $A_{e,\mathrm{total}}/A_{\mathrm{th,total}} = 2.865$.
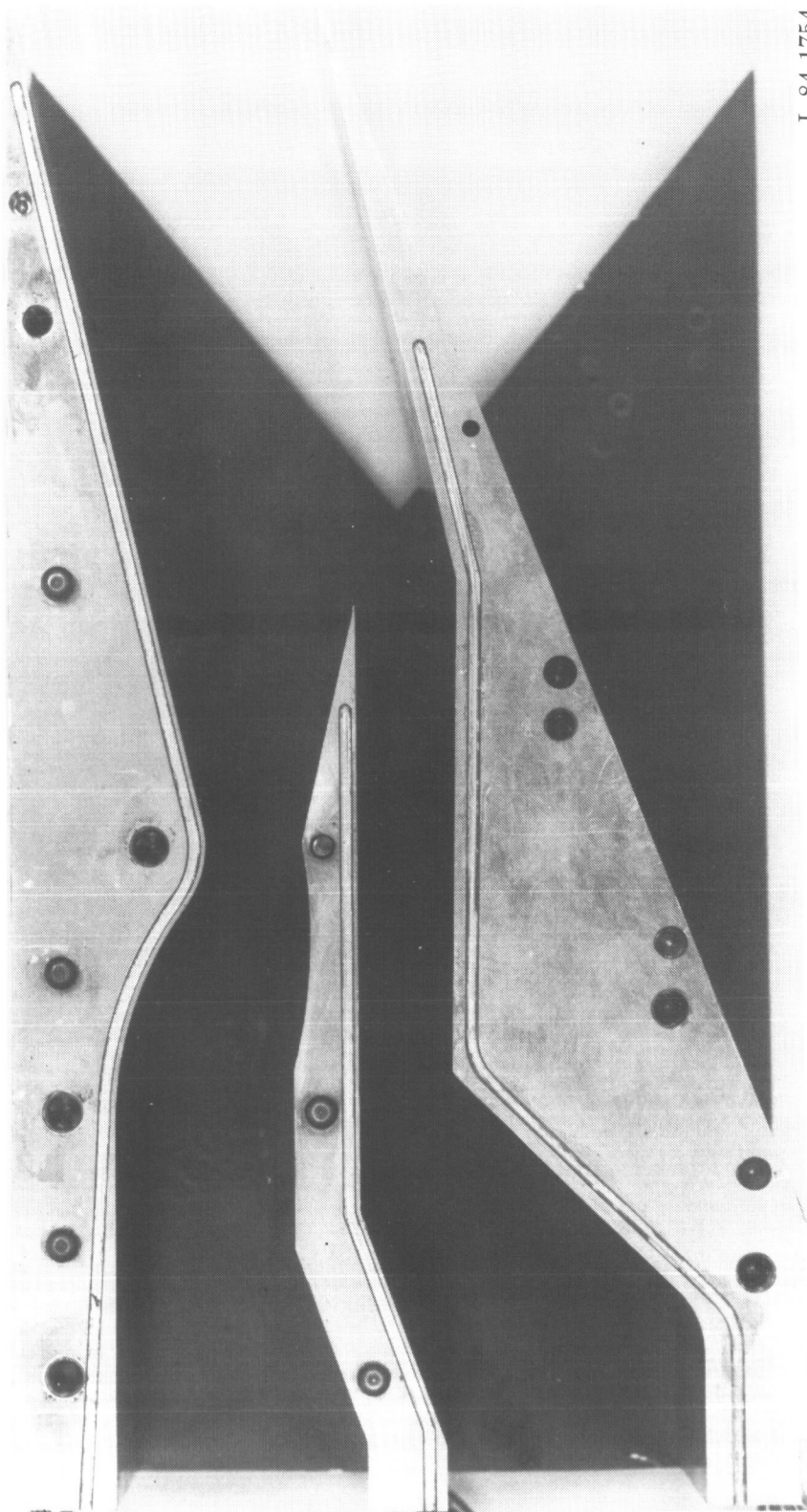
L-84-1752

Figure 11. CCN with minimum ramjet throat area, V-notch sidewalls, and ramjet flap 2. $A_{e,RJ}/A_{th,RJ} = 1.101$; $A_{e,TJ}/A_{th,TJ} = 2.109$; $A_{e,total}/A_{th,total} = 1.647$.

L-84-1754

30
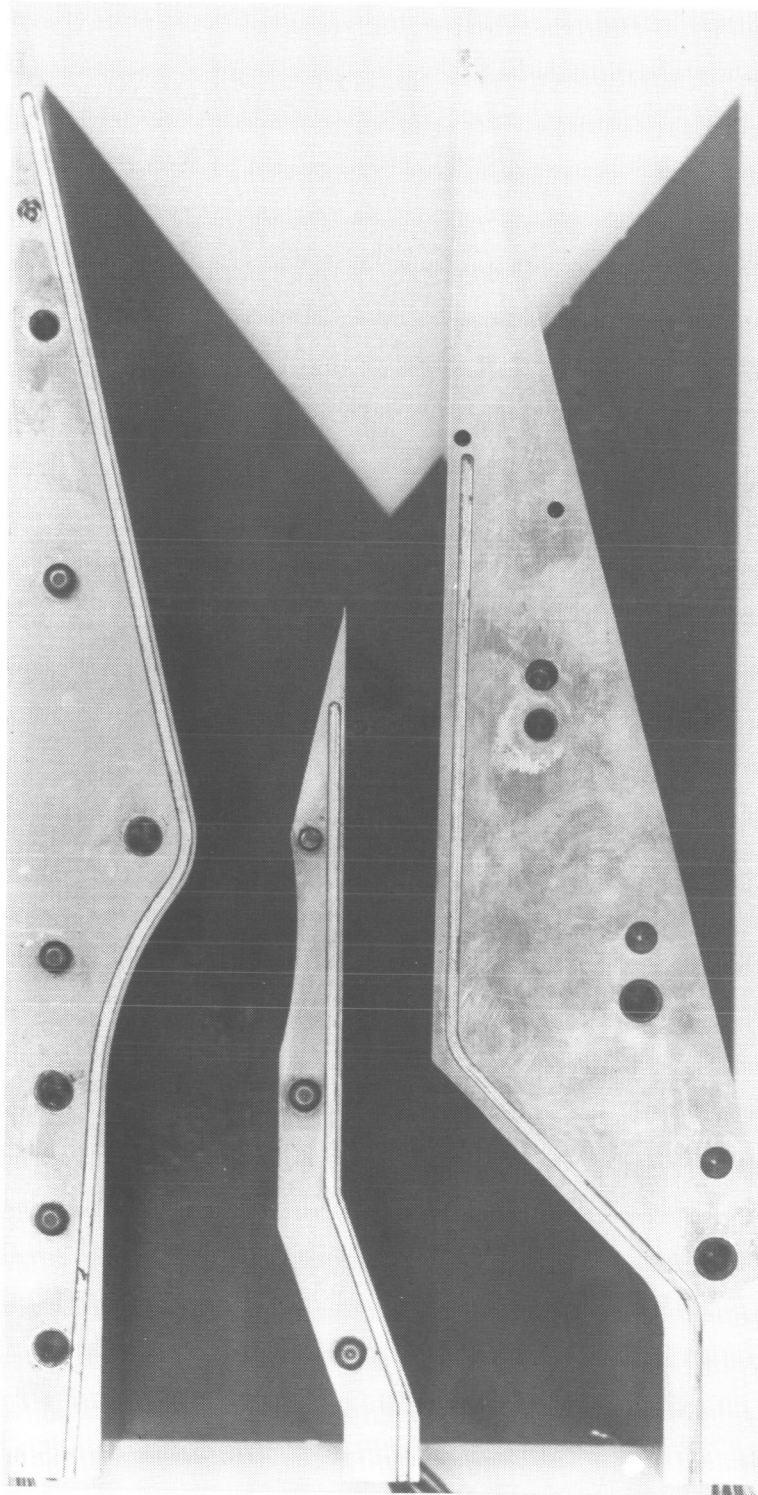
Figure 12. CCN with minimum ramjet throat area, V-notch sidewalls, and ramjet flap 3. $A_{e,\mathrm{RJ}}/A_{\mathrm{th,RJ}} = 1.101$; $A_{e,\mathrm{TJ}}/A_{\mathrm{th,TJ}} = 2.109$; $A_{e,\mathrm{total}}/A_{\mathrm{th,total}} = 2.447$.
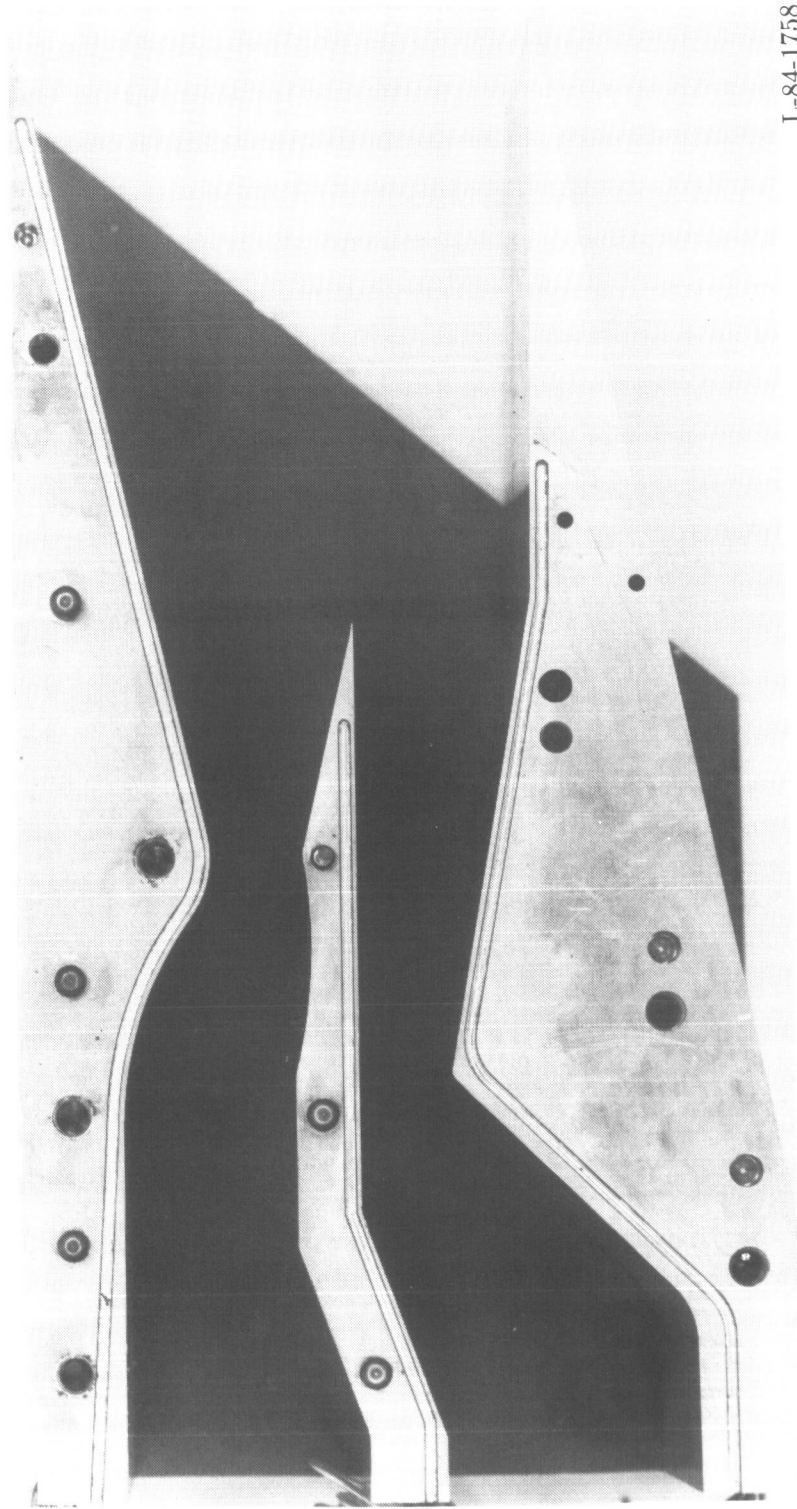
Figure 13. CCN with minimum ramjet throat area, cutback sidewalls, and ramjet flap 1. $A_{e,RJ}/A_{th,RJ} = 1.936$; $A_{e,TJ}/A_{th,TJ} = 2.109$; $A_{e,total}/A_{th,total} = 2.865$.
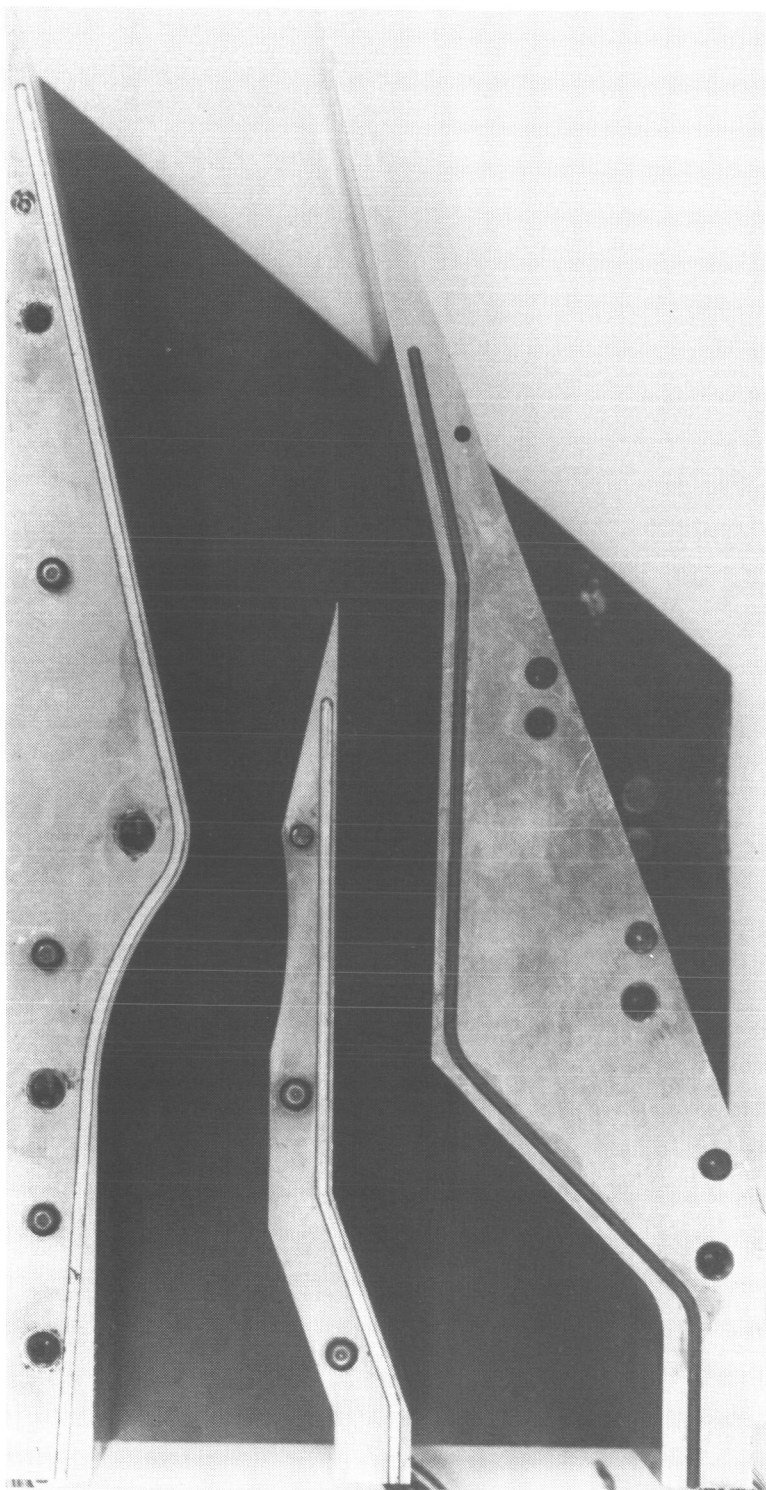
L-84-1758

Figure 14. CCN with minimum ramjet throat area, cutback sidewalls, and ramjet flap 2. $A_{e,\mathrm{RJ}}/A_{\mathrm{th,RJ}} = 1.101$; $A_{e,\mathrm{TJ}}/A_{\mathrm{th,TJ}} = 2.109$; $A_{e,\mathrm{total}}/A_{\mathrm{th,total}} = 1.647$.
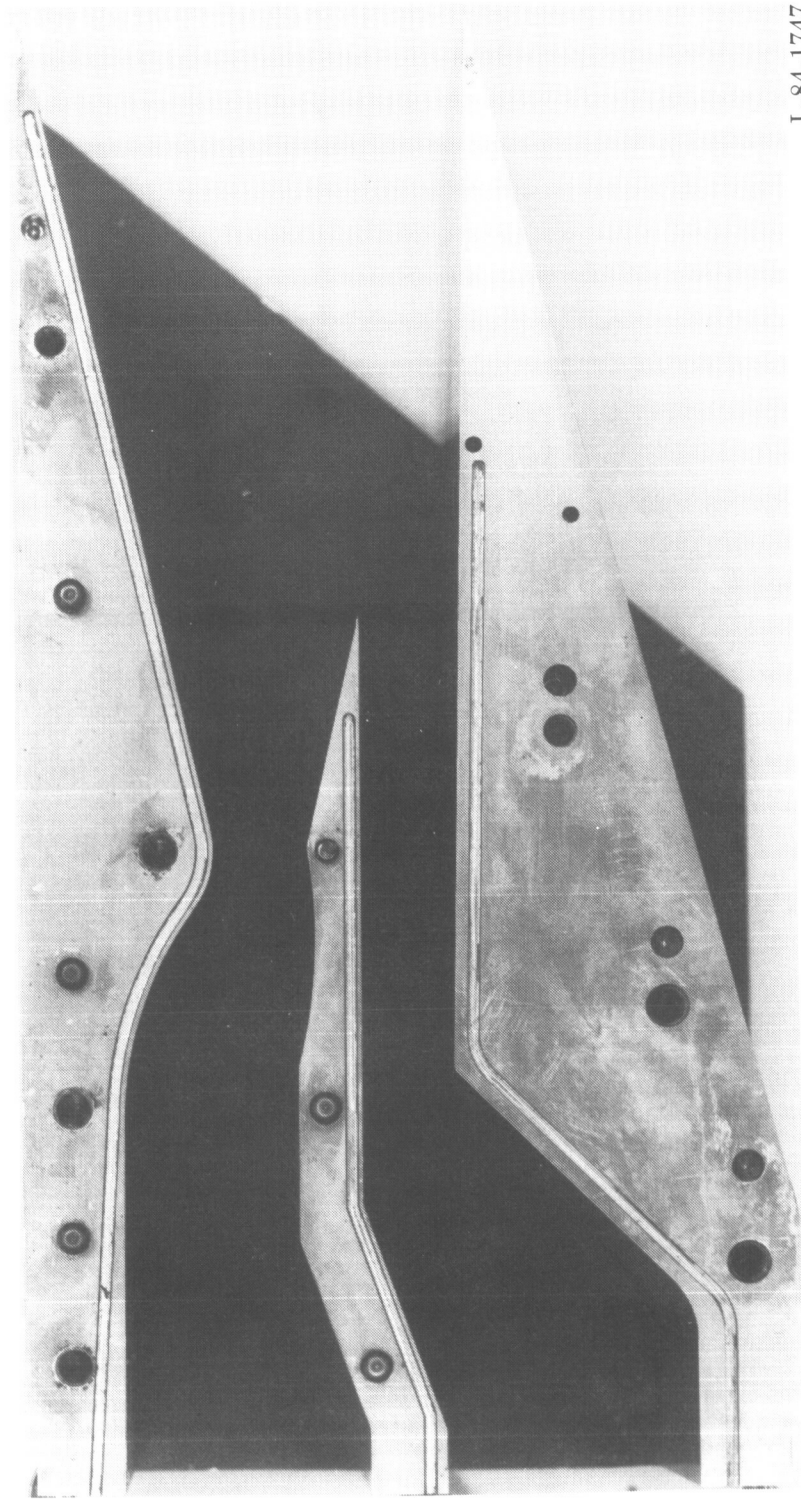
Figure 15. CCN with minimum ramjet throat area, cutback sidewalls, and ramjet flap 3. $A_{e,RJ}/A_{th,RJ} = 1.101$; $A_{e,TJ}/A_{th,TJ} = 2.109$; $A_{e,total}/A_{th,total} = 2.447$.
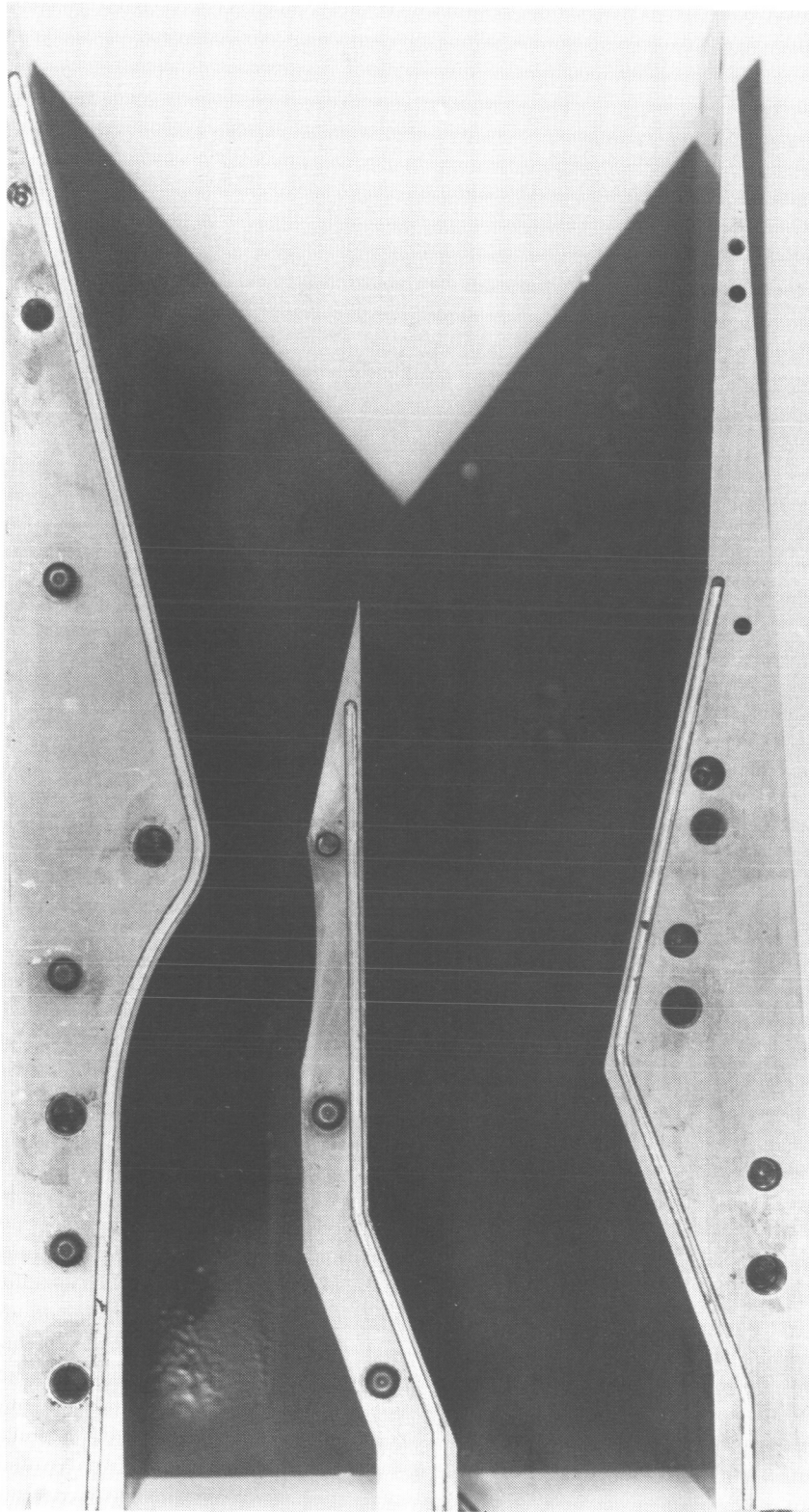
L-84-1747

Figure 16. CCN with maximum ramjet throat area, V-notch sidewalls, and ramjet flap 1. $A_{e,RJ}/A_{th,RJ} = 1.467$; $A_{e,TJ}/A_{th,TJ} = 2.109$; $A_{e,total}/A_{th,total} = 2.236$.
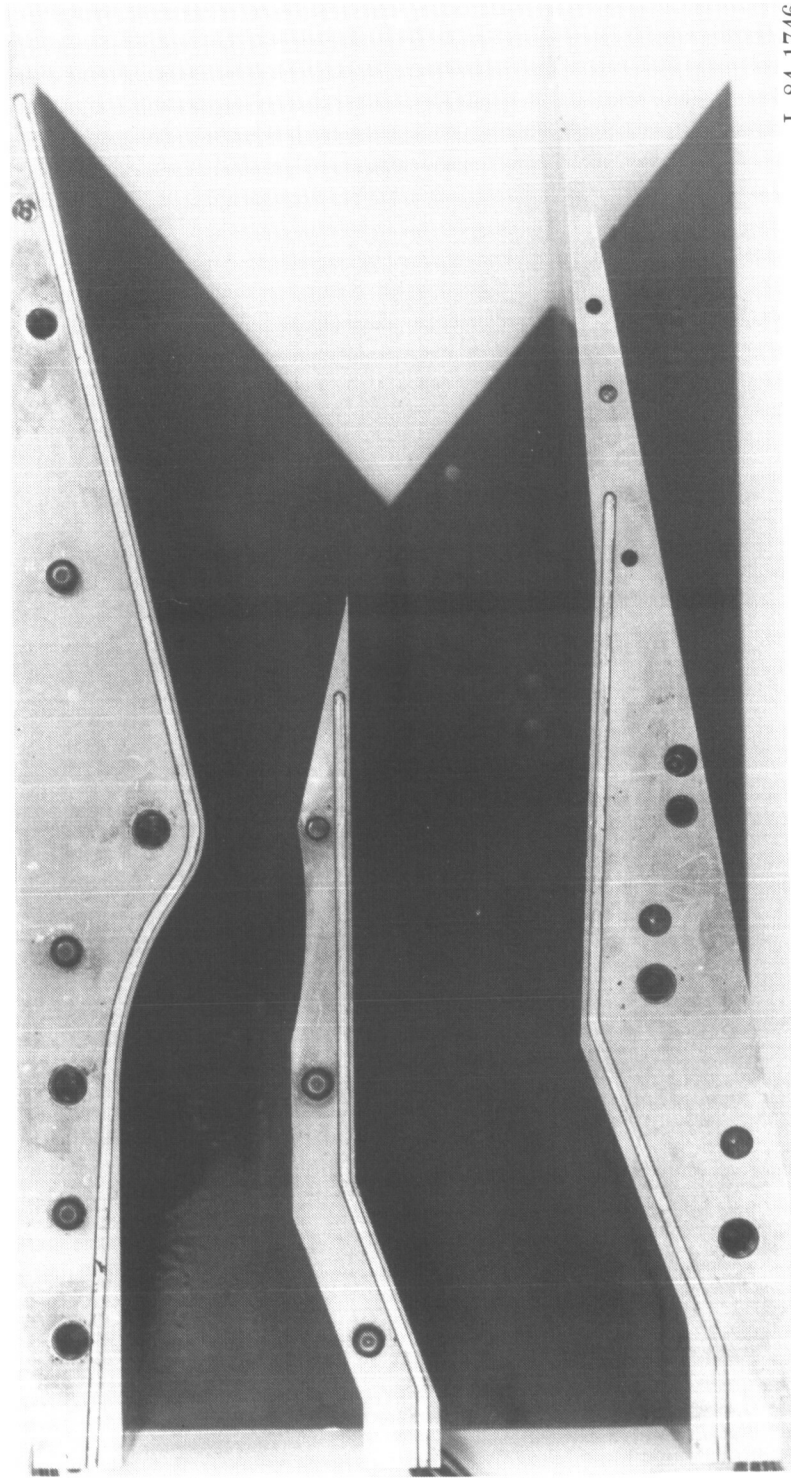
Figure 17. CCN with maximum ramjet throat area, V-notch sidewalls, and ramjet flap 2. $A_{e,RJ}/A_{th,RJ} = 1.101$; $A_{e,TJ}/A_{th,TJ} = 2.109$; $A_{e,total}/A_{th,total} = 1.730$.

L-84-1746

36
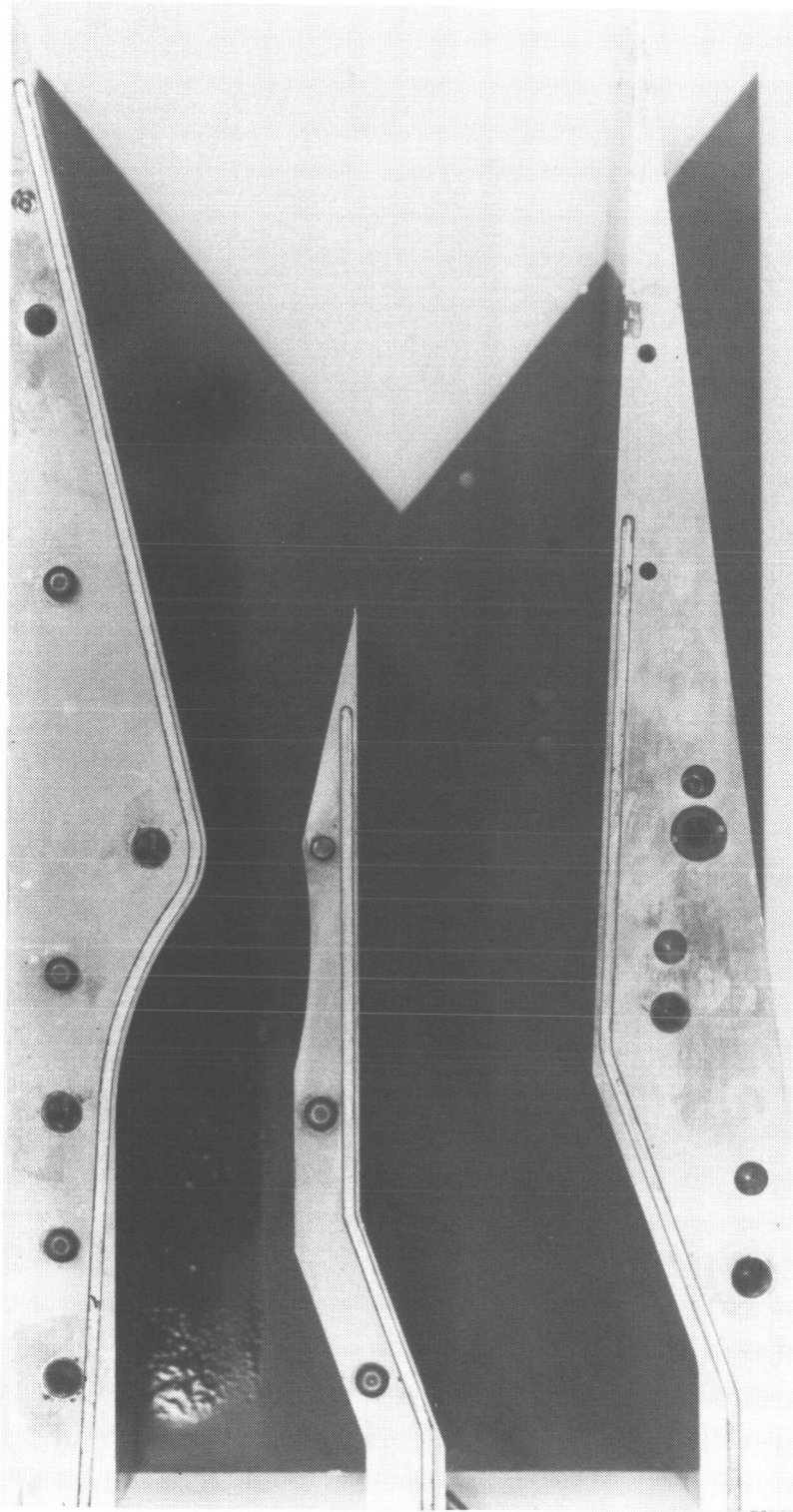
Figure 18. CCN with maximum ramjet throat area, V-notch sidewalls, and ramjet flap 3. $A_{e,RJ}/A_{th,RJ} = 1.101$; $A_{e,TJ}/A_{th,TJ} = 2.109$; $A_{e,total}/A_{th,total} = 1.936$.

L-84-1750

37
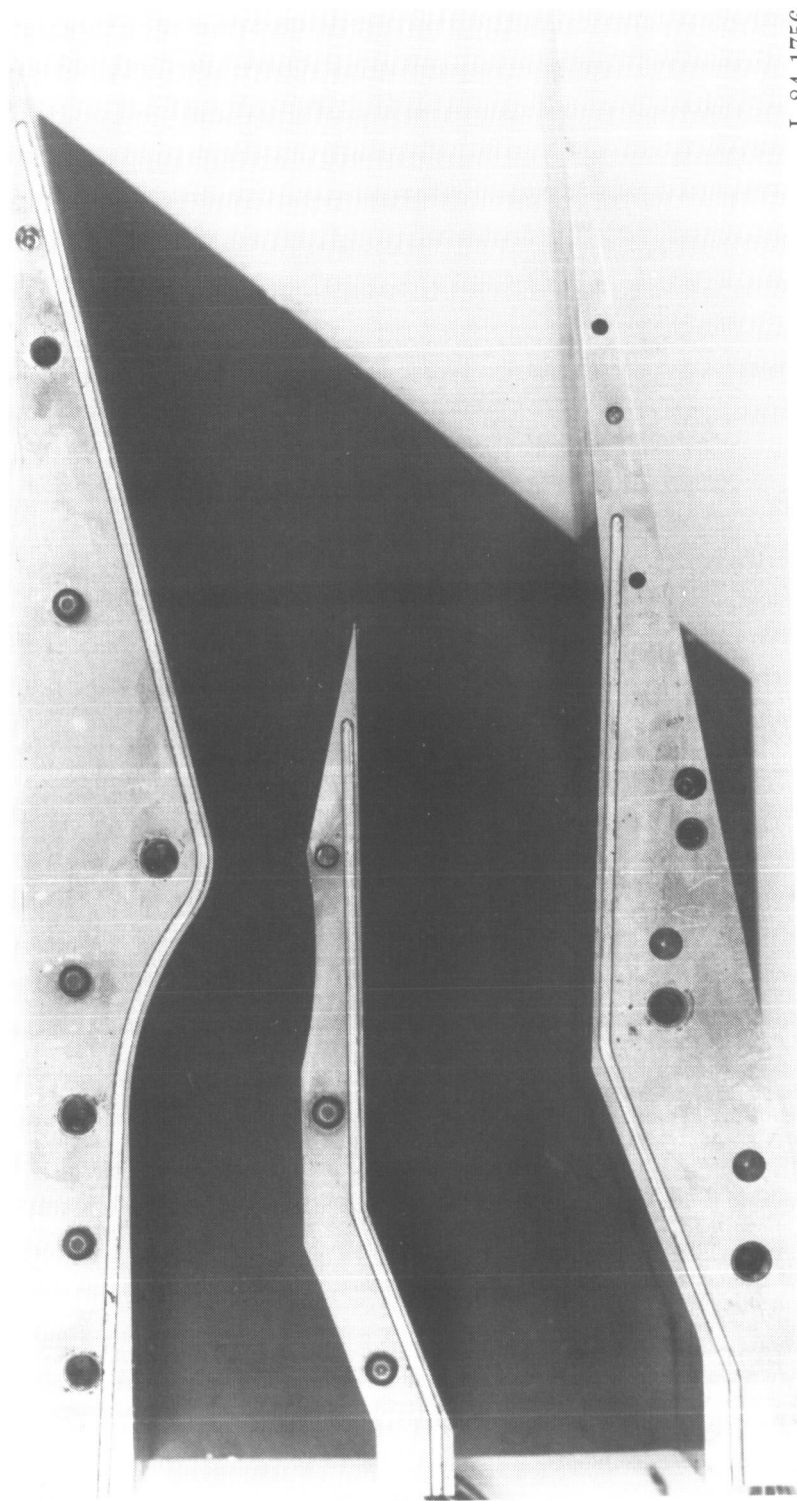
Figure 19. CCN with maximum ramjet throat area, cutback sidewalls, and ramjet flap 2. $A_{e,\mathrm{RJ}}/A_{\mathrm{th,RJ}} = 1.101$; $A_{e,\mathrm{TJ}}/A_{\mathrm{th,TJ}} = 2.109$; $A_{e,\mathrm{total}}/A_{\mathrm{th,total}} = 1.730$.

Figure 20. CCN with maximum ramjet throat area, cutback sidewalls, and ramjet flap 3. $A_{e,RJ}/A_{th,RJ} = 1.101$; $A_{e,TJ}/A_{th,TJ} = 2.109$; $A_{e,total}/A_{th,total} = 1.936$.

L-84-1753

Figure 21. Representative schedule of nozzle pressure ratio with Mach number for typical supersonic cruise turbojet engine at maximum thrust. .

Figure 22. Variation of $(NPR)_{RJ}$ with $(NPR)_{TJ}$.

Figure 23. Variation of total discharge coefficient with $(NPR)_{TJ}$.

Throat area
○   Minimum
□   Maximum

M = 0

M = 0.60

M = 0.90

M = 1.20

(a) Variation of axial-force ratio with $(NPR)_{TJ}$.

Figure 24. Effect of ramjet throat area on characteristics of MERN.

Throat area
○ Minimum
□ Maximum

M = 0

M = 0.60

M = 0.90

M = 1.20

C_N

C_N

$(NPR)_{TJ}$

$(NPR)_{TJ}$

(b) Variation of normal-force coefficient with $(NPR)_{TJ}$.

Figure 24. Continued.

44

Throat area
O Minimum
□ Maximum

M = 0

M = 0.60

M = 0.90

M = 1.20
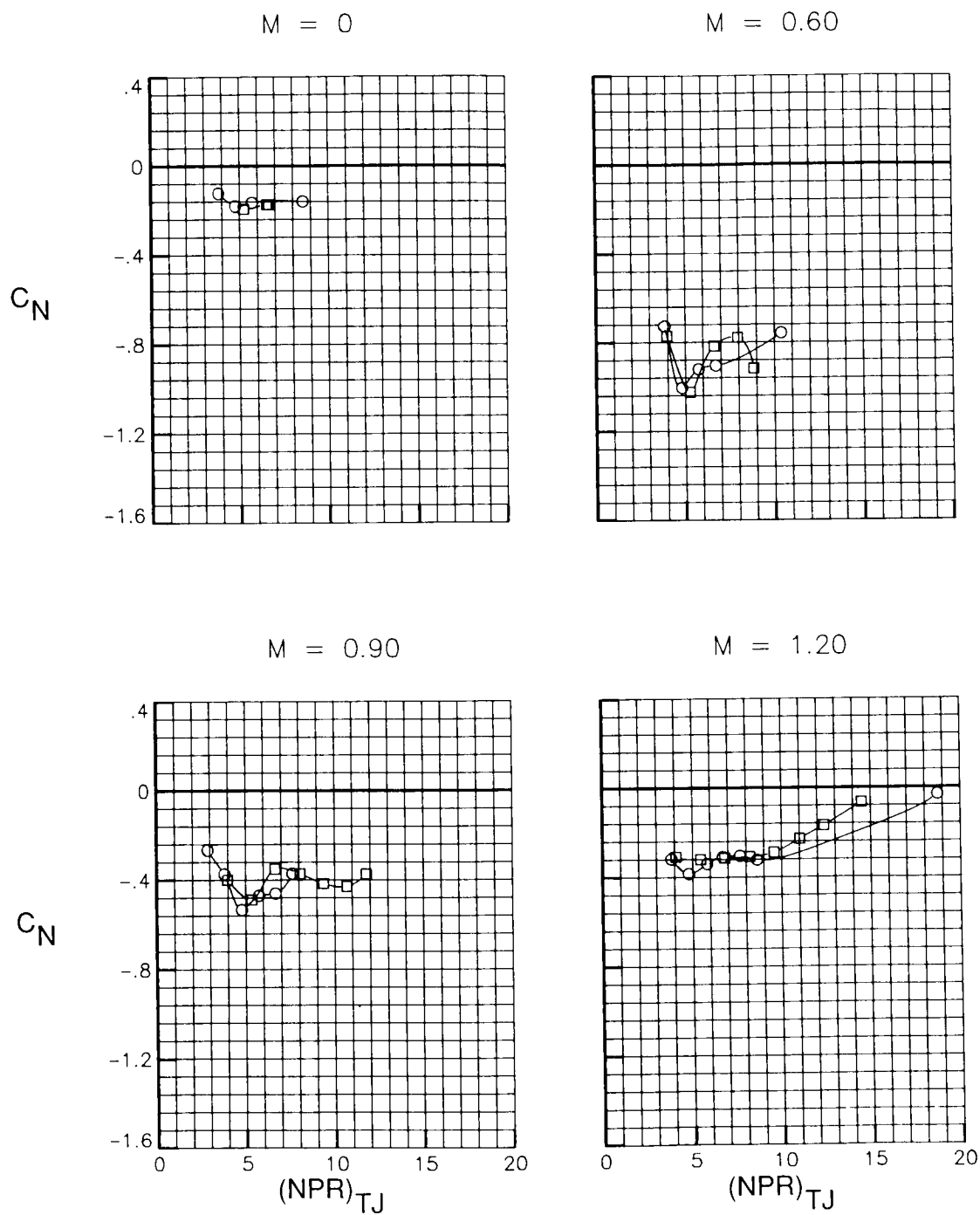
(c) Variation of pitching-moment coefficient with $(NPR)_{TJ}$.

Figure 24. Continued.

Throat area

○ Minimum
□ Maximum
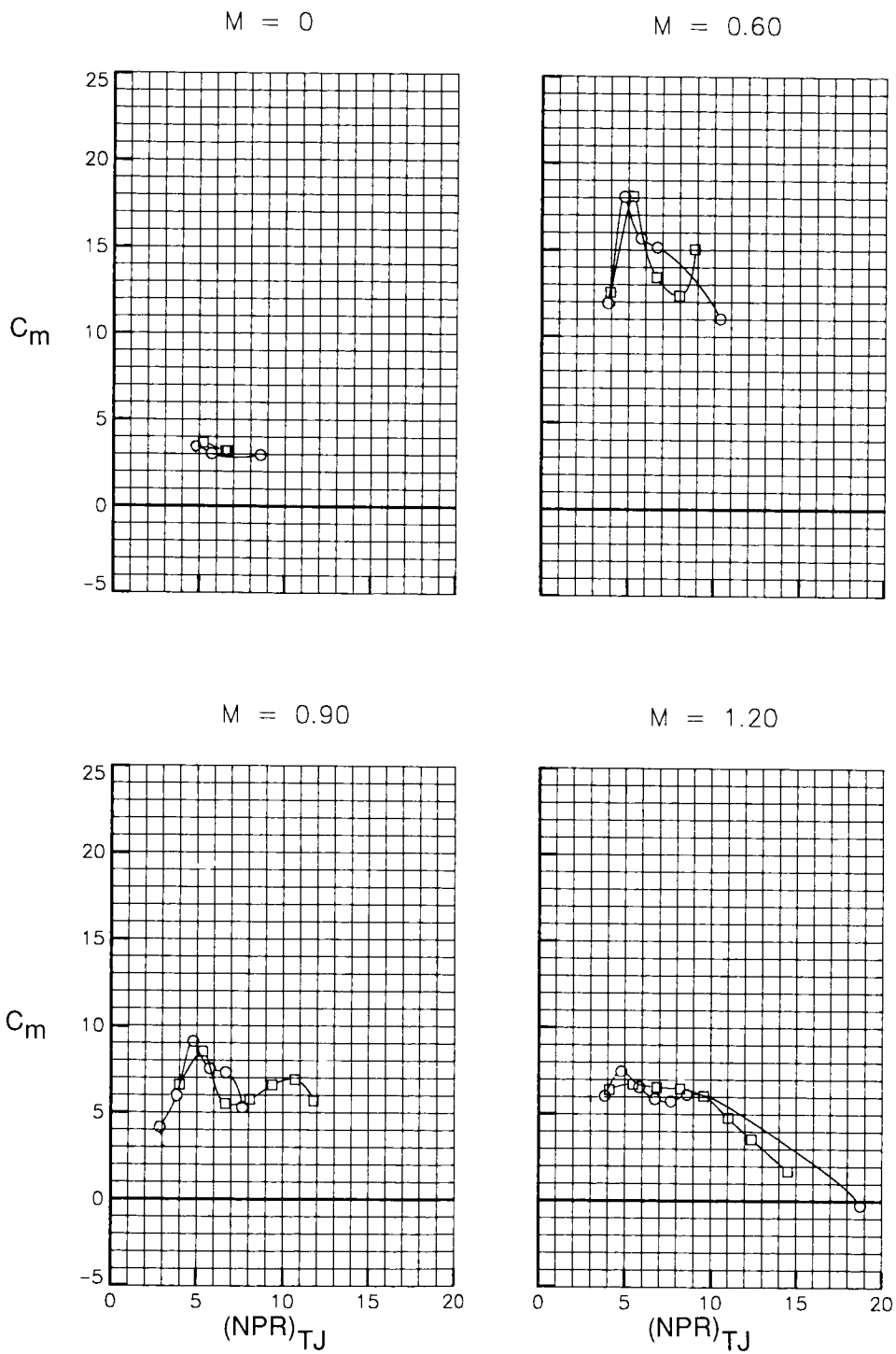
M = 0
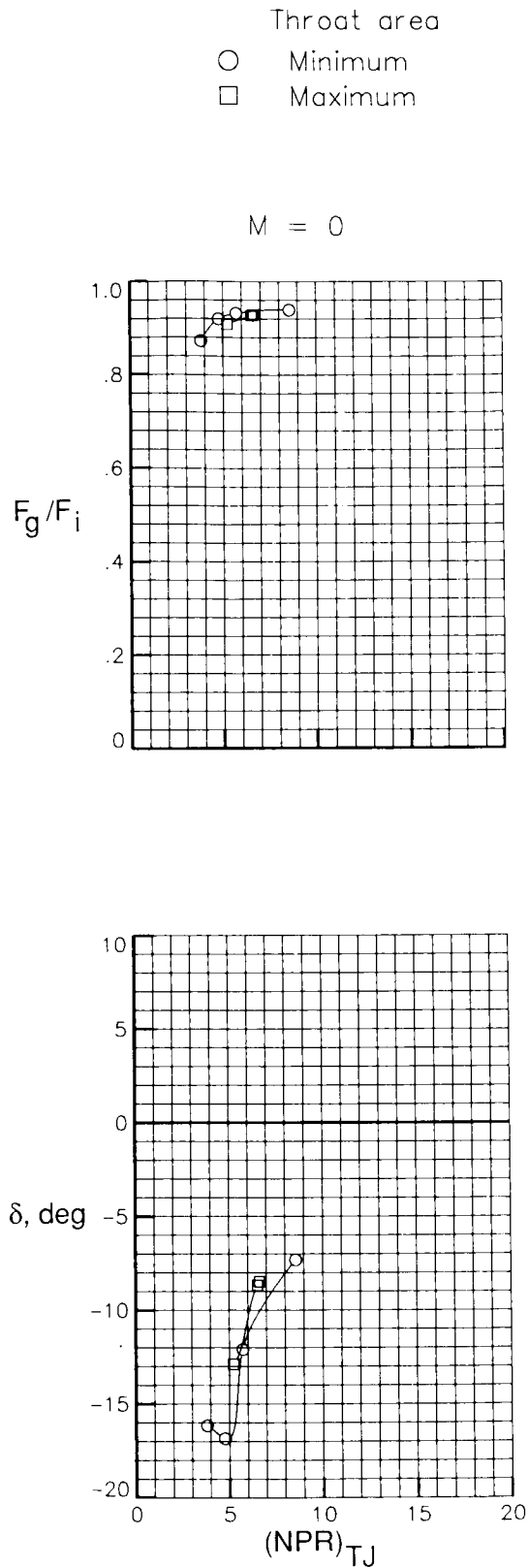
(d) Variation of gross thrust ratio and effective jet turning angle with $(NPR)_{TJ}$.

Figure 24. Concluded.

RJ flap
position
○   1
□   2
◇   3

M = 0

M = 0.60

M = 0.90

M = 1.20
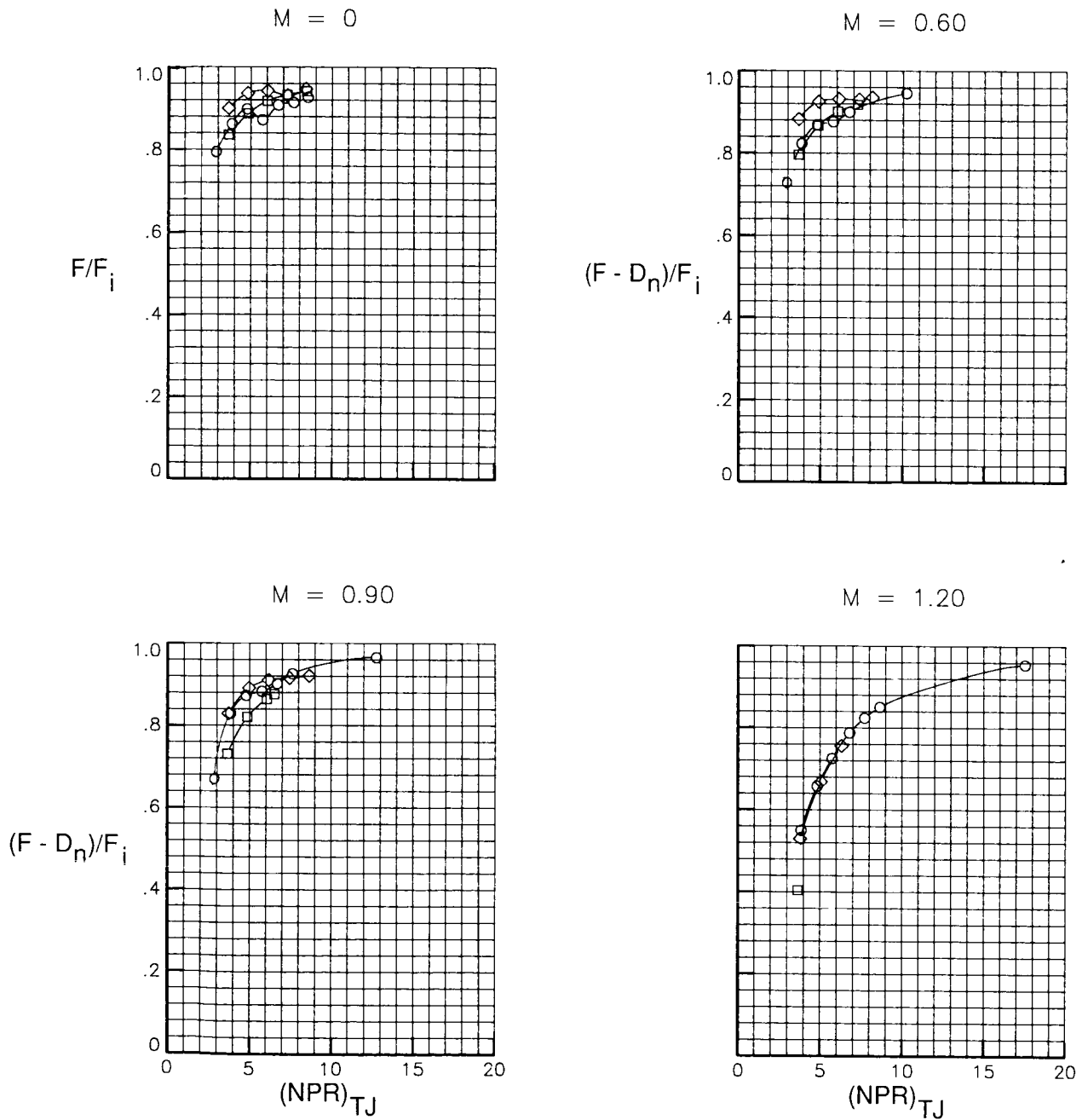
(a) Variation of axial-force ratio with $(NPR)_{TJ}$.

Figure 25. Effect of ramjet flap position on characteristics of CCN with minimum ramjet throat area and V-notch sidewalls.

RJ flap
position

○   1
□   2
◇   3

M = 0

M = 0.60

C_N

M = 0.90

M = 1.20

$(NPR)_{TJ}$

$(NPR)_{TJ}$

(b) Variation of normal-force coefficient with $(NPR)_{TJ}$.

Figure 25. Continued.
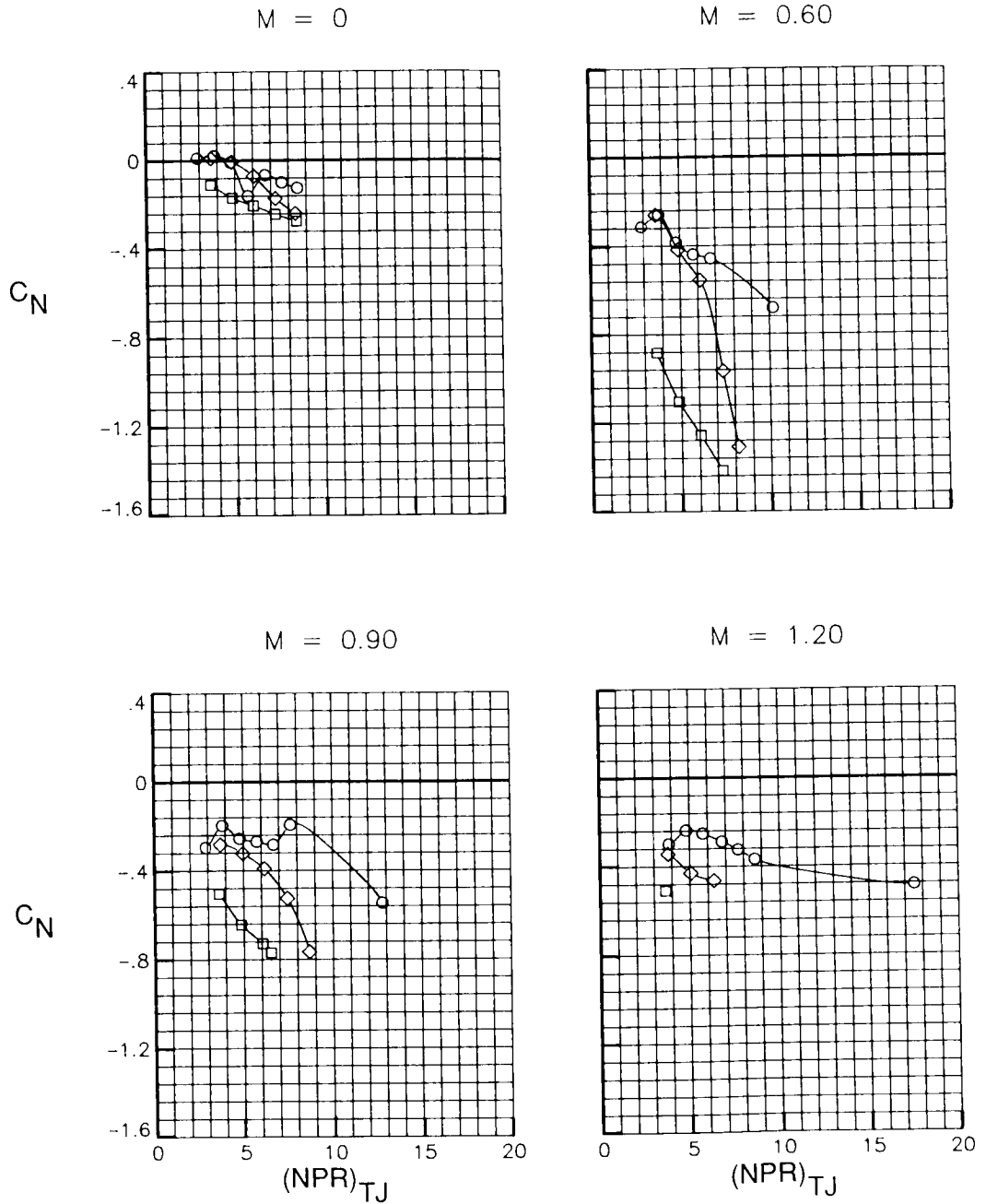
(c) Variation of pitching-moment coefficient with $(NPR)_{TJ}$.

Figure 25. Continued.

RJ flap
position
○ 1
□ 2
◇ 3

M = 0
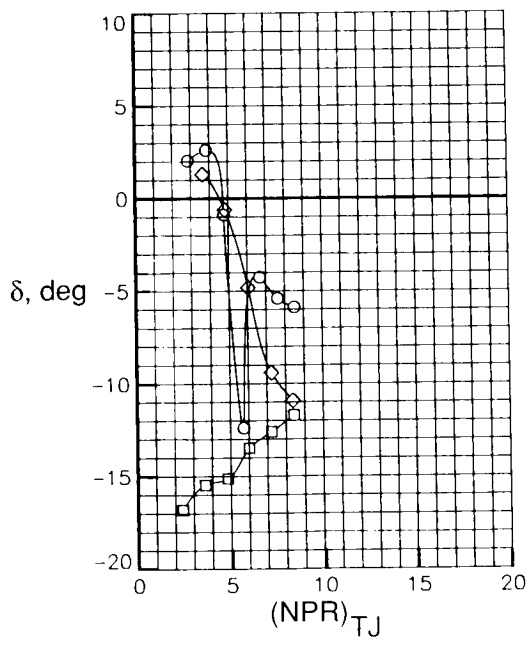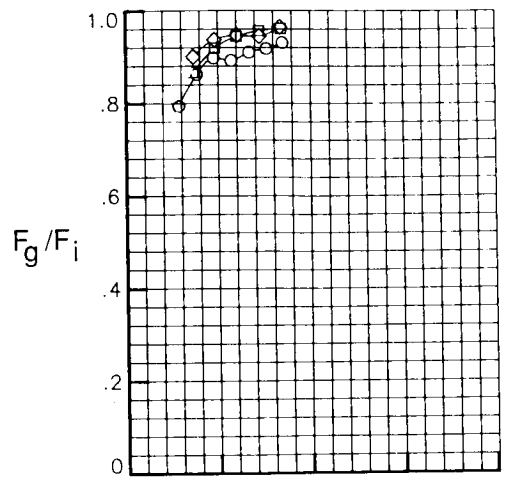
(d) Variation of gross thrust ratio and effective jet turning angle with $(NPR)_{TJ}$.

Figure 25. Concluded.

50

(a) Variation of axial-force ratio with $(NPR)_{TJ}$.

Figure 26. Effect of ramjet flap position on characteristics of CCN with minimum ramjet throat area and cutback sidewalls.

RJ flap
position
○ 1
□ 2
◇ 3
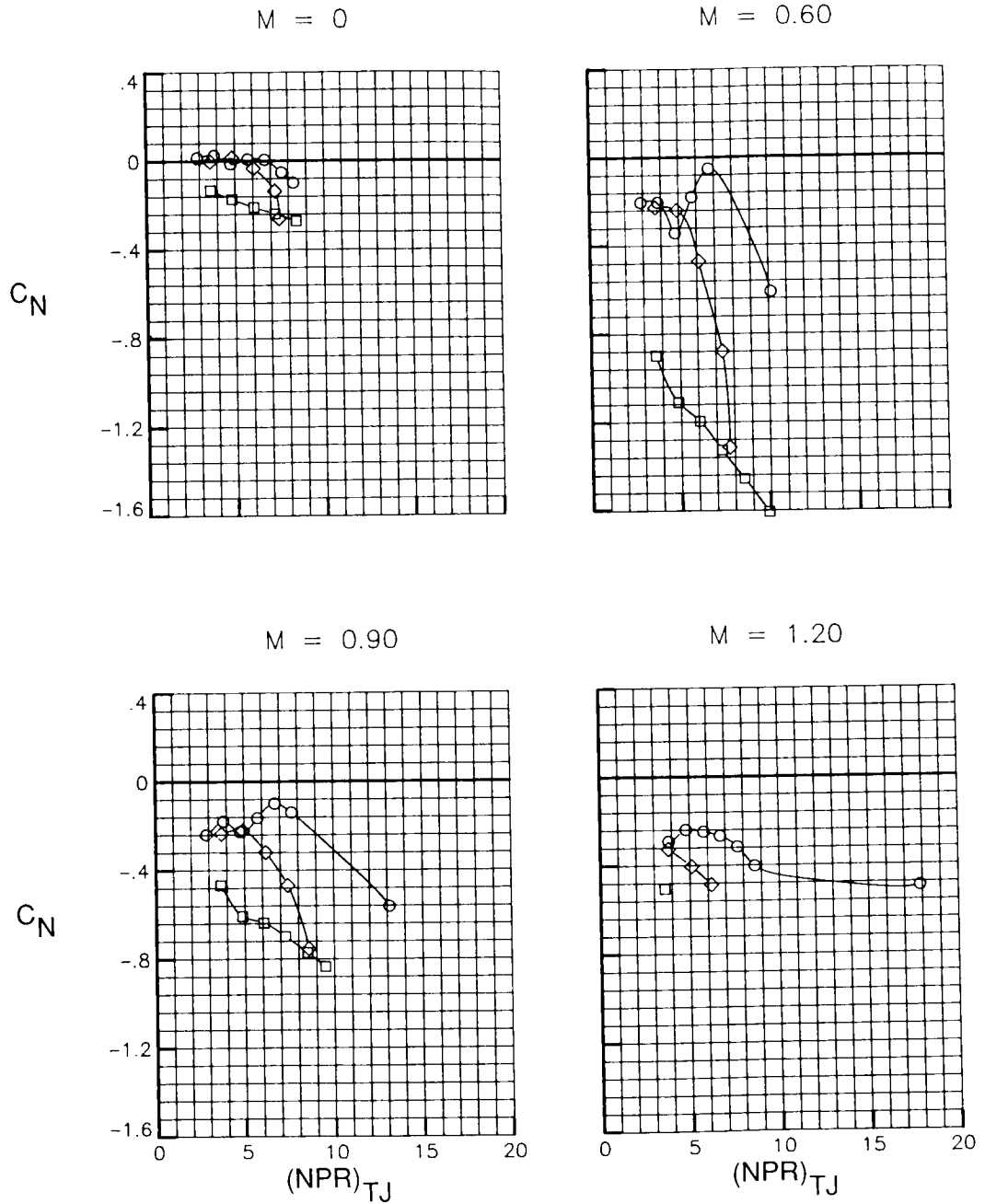
M = 0

M = 0.60

M = 0.90

M = 1.20

C_N

C_N

$(NPR)_{TJ}$

$(NPR)_{TJ}$

(b) Variation of normal-force coefficient with $(NPR)_{TJ}$.

Figure 26. Continued.

RJ flap
position
○   1
□   2
◇   3

M = 0

M = 0.60

M = 0.90

M = 1.20

C_m

C_m

$(NPR)_{TJ}$

$(NPR)_{TJ}$

(c) Variation of pitching-moment coefficient with $(NPR)_{TJ}$.

Figure 26. Continued.

RJ flap
position

○   1
□   2
◇   3

M = 0
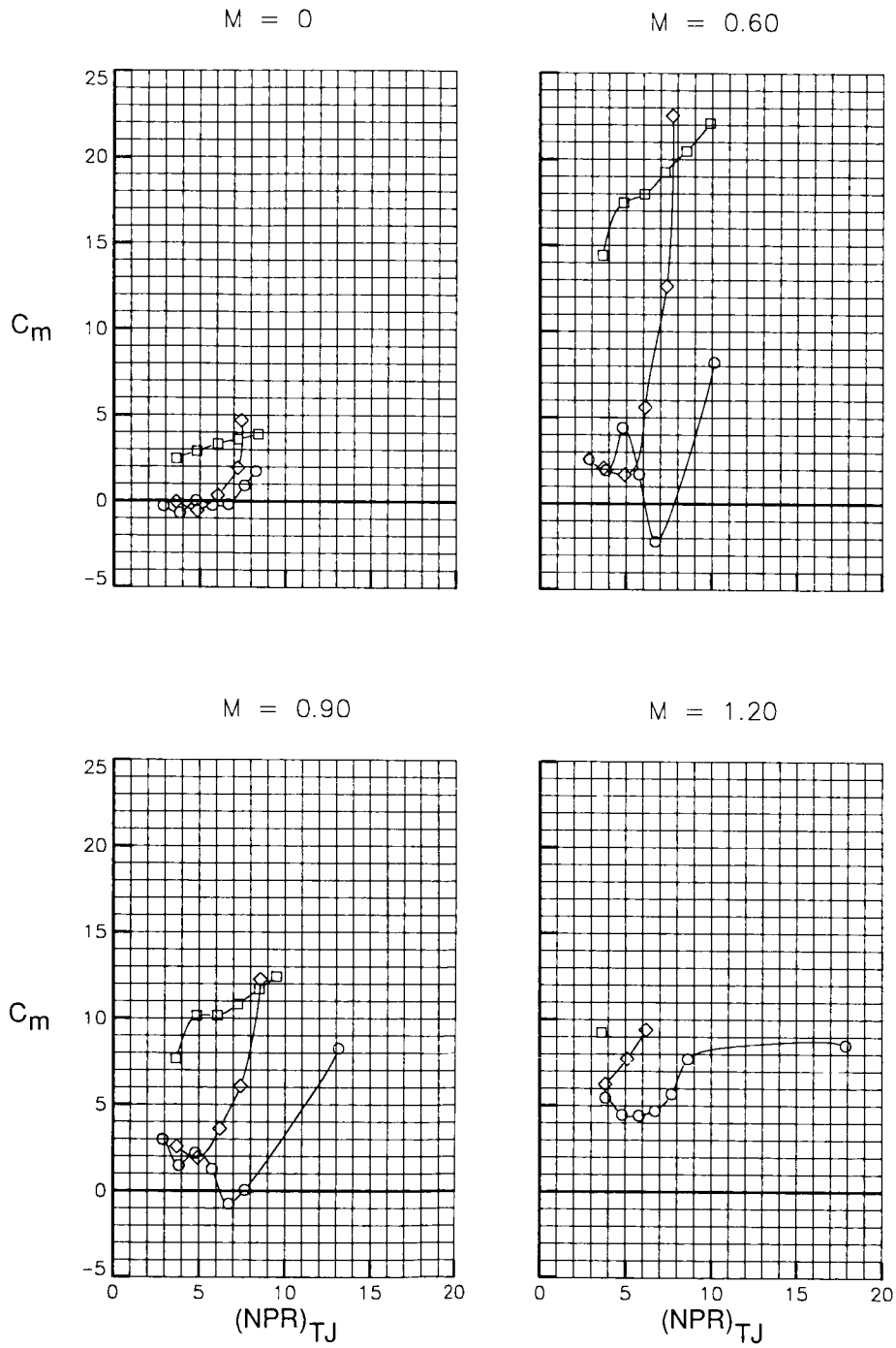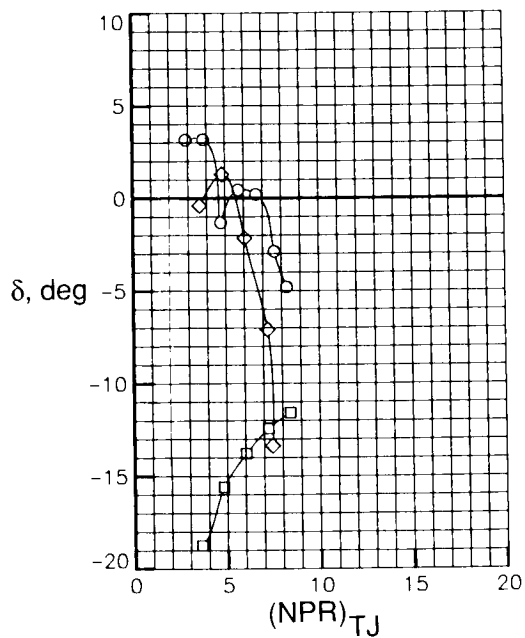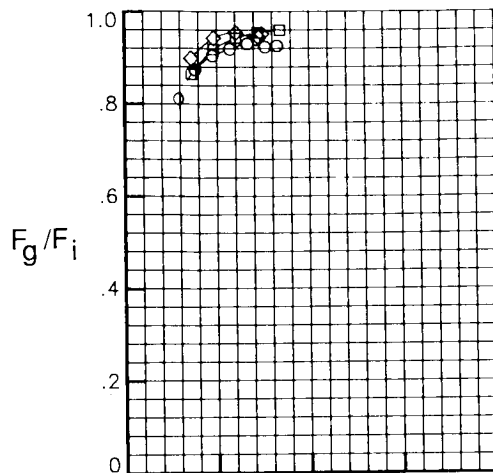
(d) Variation of gross thrust ratio and effective jet turning angle with $(NPR)_{TJ}$.

Figure 26. Concluded.

Sidewalls
○ V-notch
☐ Cutback
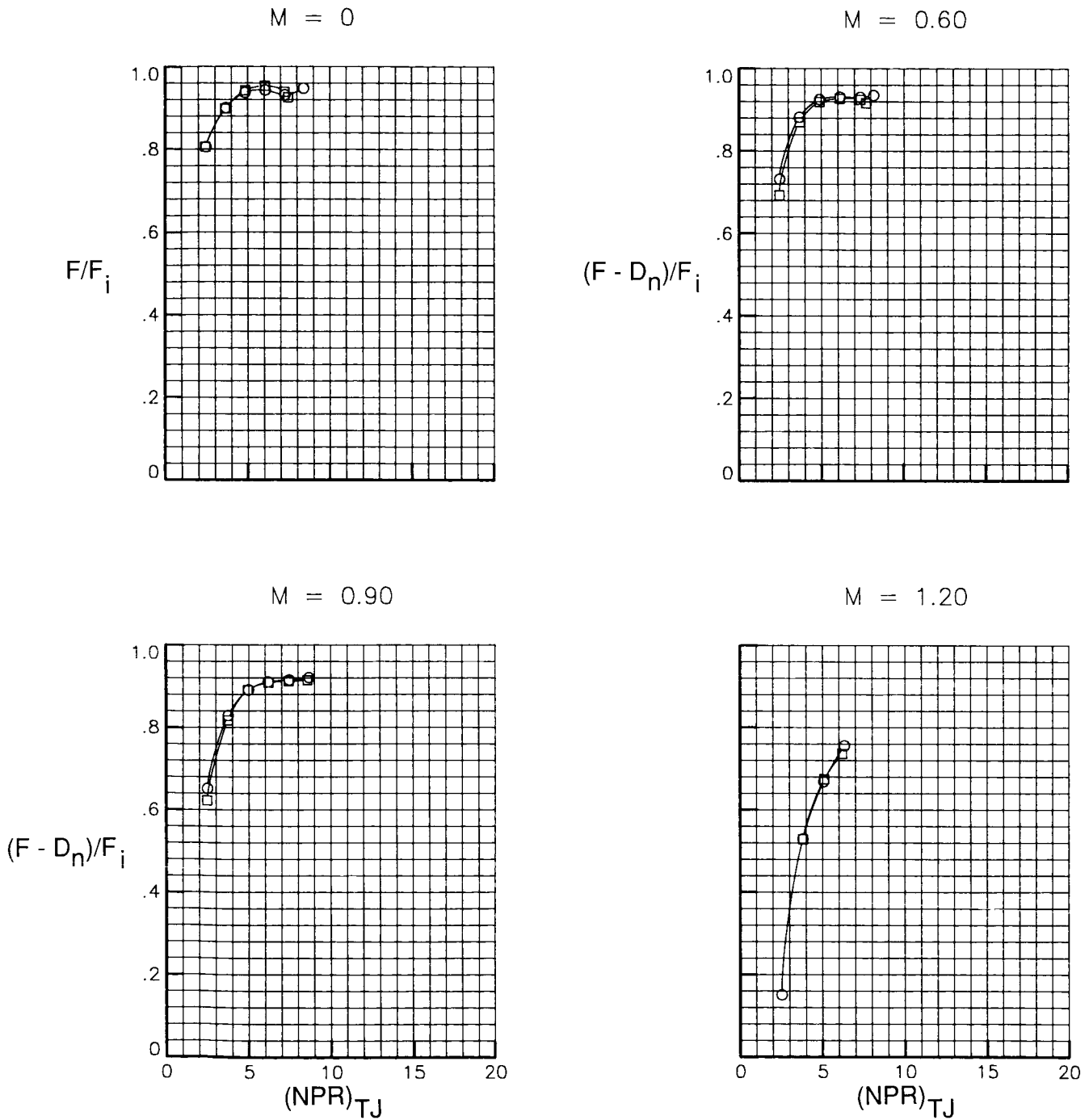
(a) Variation of axial-force ratio with $(NPR)_{TJ}$.

Figure 27. Effect of sidewalls on characteristics of CCN with minimum ramjet throat area and ramjet flap 3.

Sidewalls
○ V-notch
□ Cutback
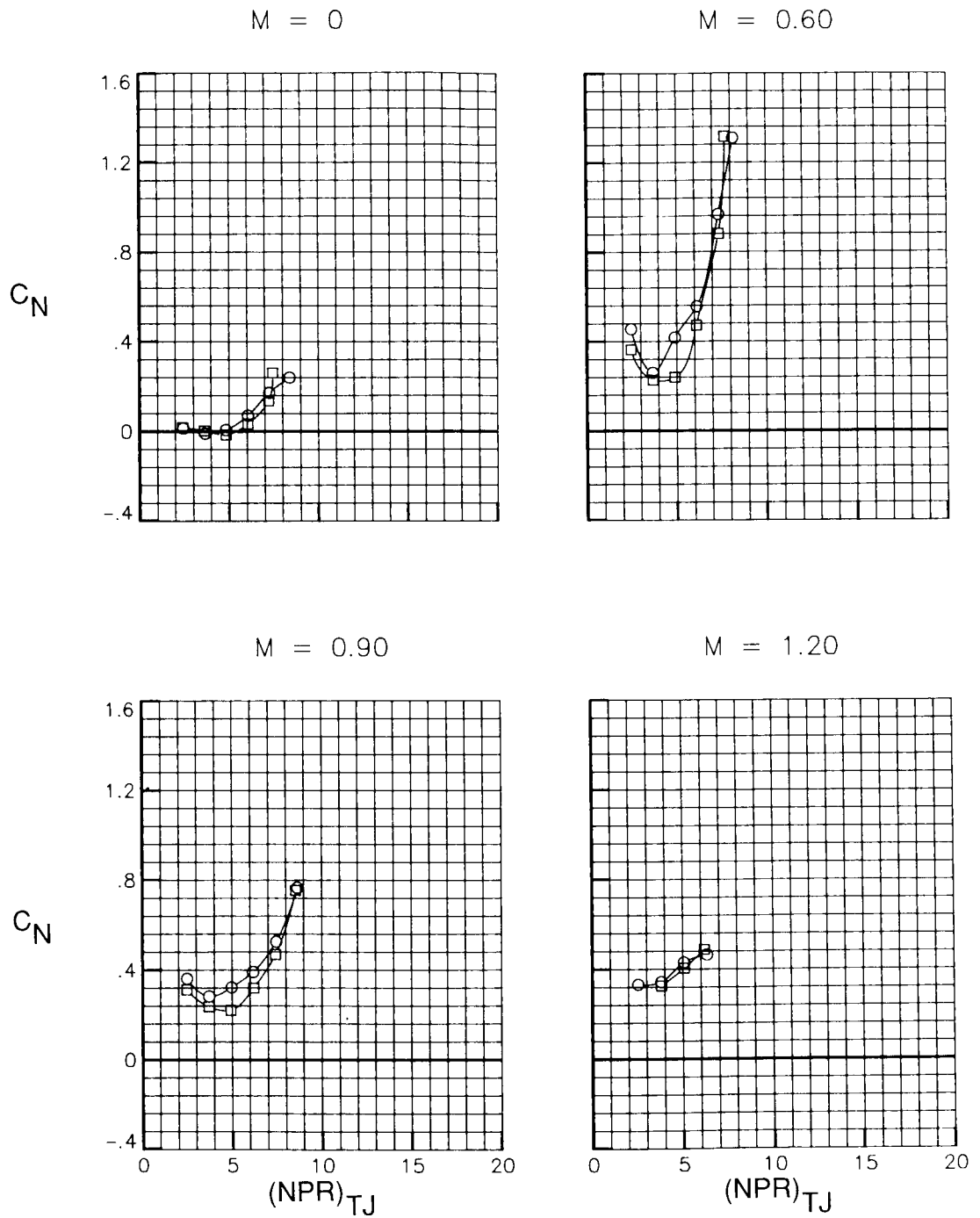
M = 0

M = 0.60

M = 0.90

M = 1.20

(b) Variation of normal-force coefficient with $(NPR)_{TJ}$.

Figure 27. Continued.

Sidewalls
○ V-notch
□ Cutback

M = 0

M = 0.60

M = 0.90

M = 1.20

C_m
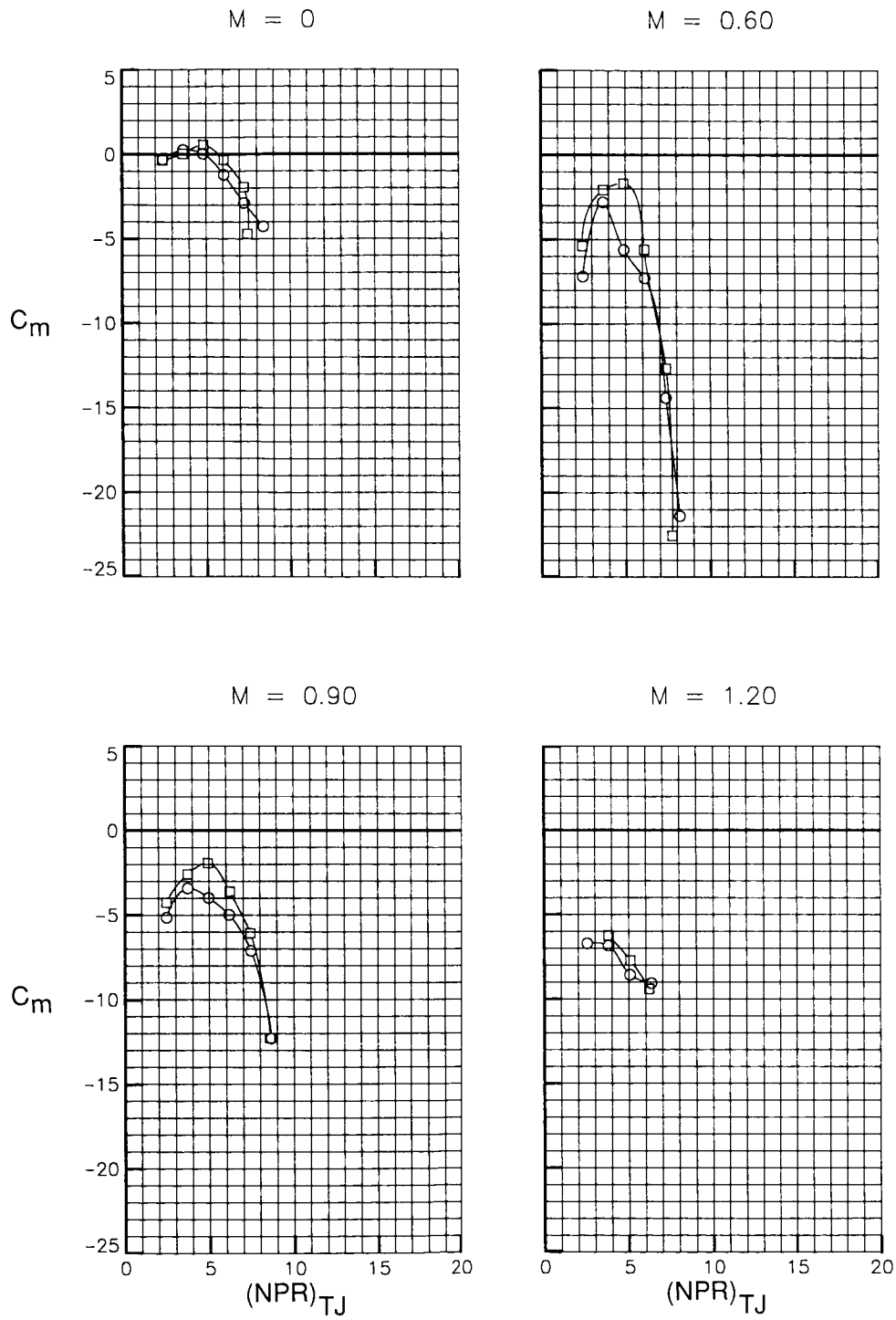
$(NPR)_{TJ}$

$(NPR)_{TJ}$

(c) Variation of pitching-moment coefficient with $(NPR)_{TJ}$.

Figure 27. Continued.

Sidewalls
○ V-notch
□ Cutback

M = 0
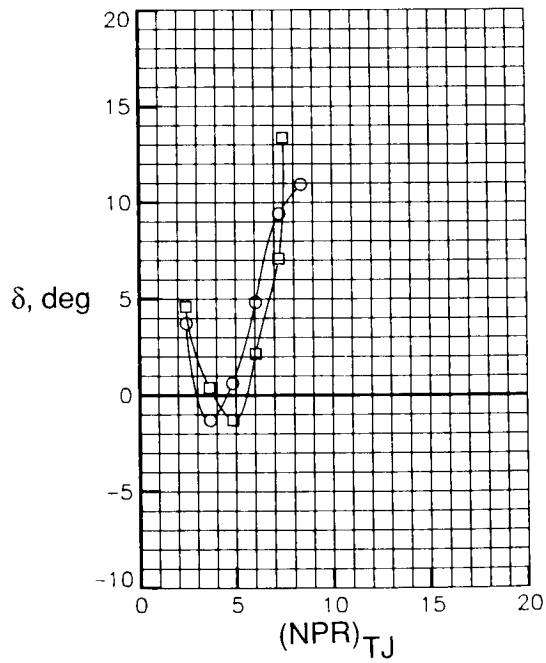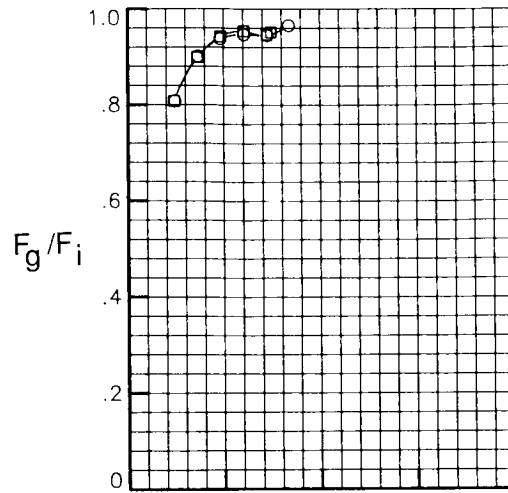
(d) Variation of gross thrust ratio and effective jet turning angle with $(NPR)_{TJ}$.

Figure 27. Concluded.

(a) Variation of axial-force ratio with $(NPR)_{TJ}$.

Figure 28. Effect of ramjet flap position on characteristics of CCN with maximum ramjet throat area and V-notch sidewalls.

(b) Variation of normal-force coefficient with $(NPR)_{TJ}$.

Figure 28. Continued.

(c) Variation of pitching-moment coefficient with $(NPR)_{TJ}$.

Figure 28. Continued.

(d) Variation of gross thrust ratio and effective jet turning angle with $(NPR)_{TJ}$.

Figure 28. Concluded.

○   MERN with minimum RJ throat area

☐   MERN with maximum RJ throat area

◇   CCN with minimum RJ throat area, RJ flap 3, and V-notch sidewalls

△   CCN with maximum RJ throat area, RJ flap 3, and V-notch sidewalls

M = 0

M = 0.60

F/F_i

$(F - D_n)/F_i$

M = 0.90

M = 1.20

$(F - D_n)/F_i$
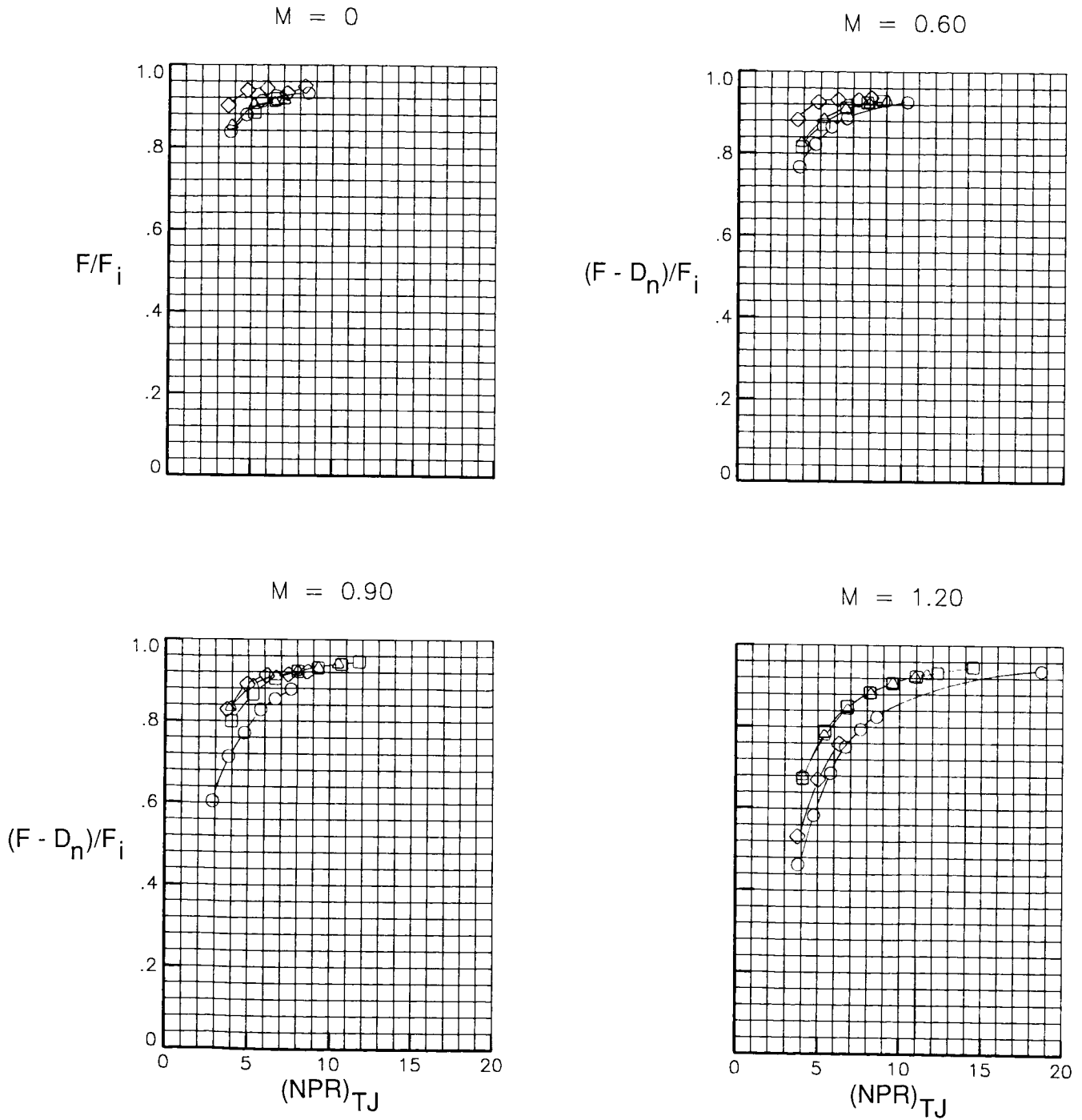
$(NPR)_{TJ}$

$(NPR)_{TJ}$

Figure 29. Summary of performance comparisons for selected configurations.

M = 0

M = 0.60

F/F_i

$(F - D_n)/F_i$

M = 0.90

M = 1.20

$(F - D_n)/F_i$
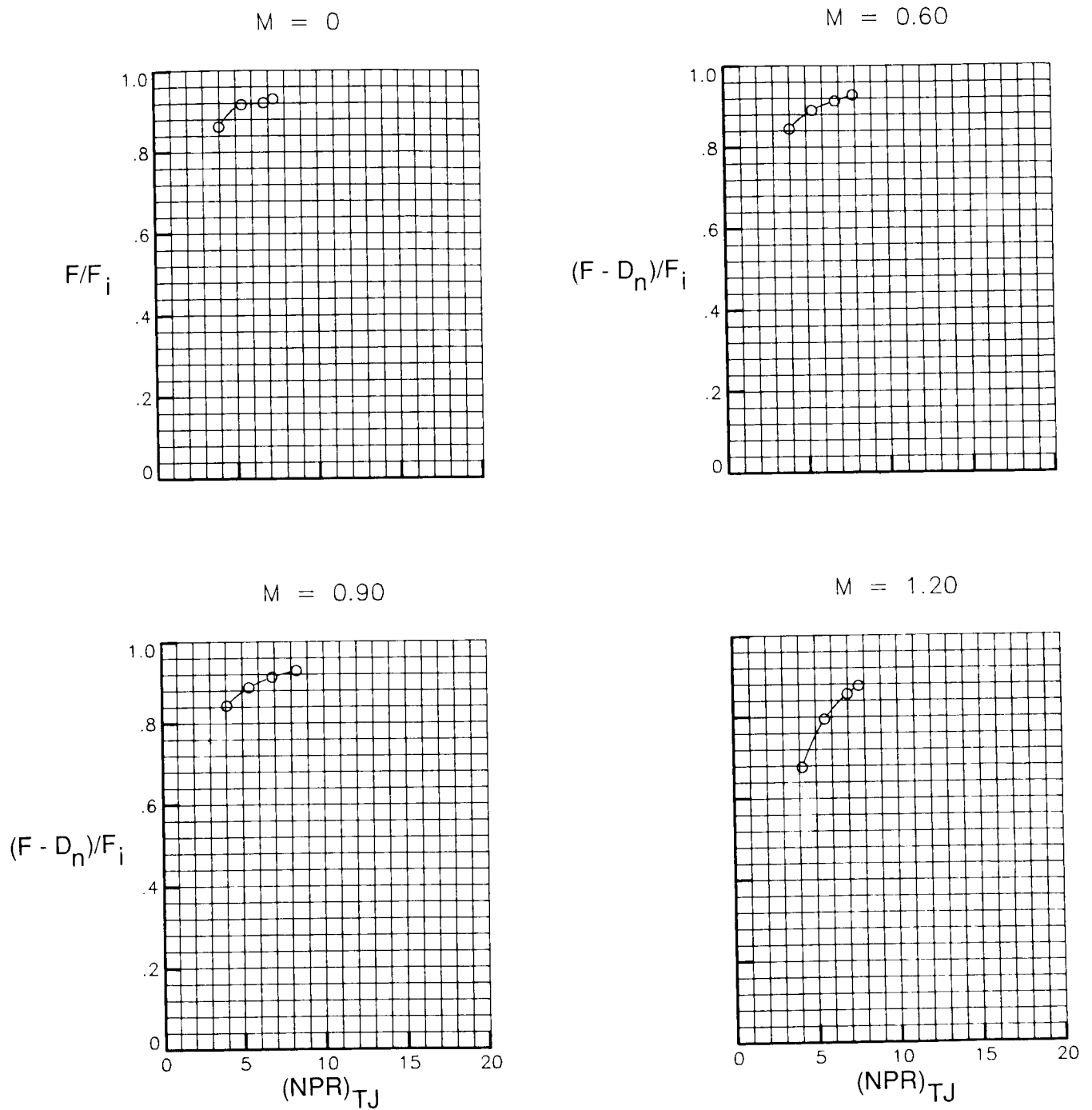
(NPR)$_{TJ}$

(NPR)$_{TJ}$

(a) Variation of axial-force ratio with (NPR)$_{TJ}$.

Figure 30. Characteristics of CCN with maximum ramjet throat area, ramjet flap 2, and cutback sidewalls.
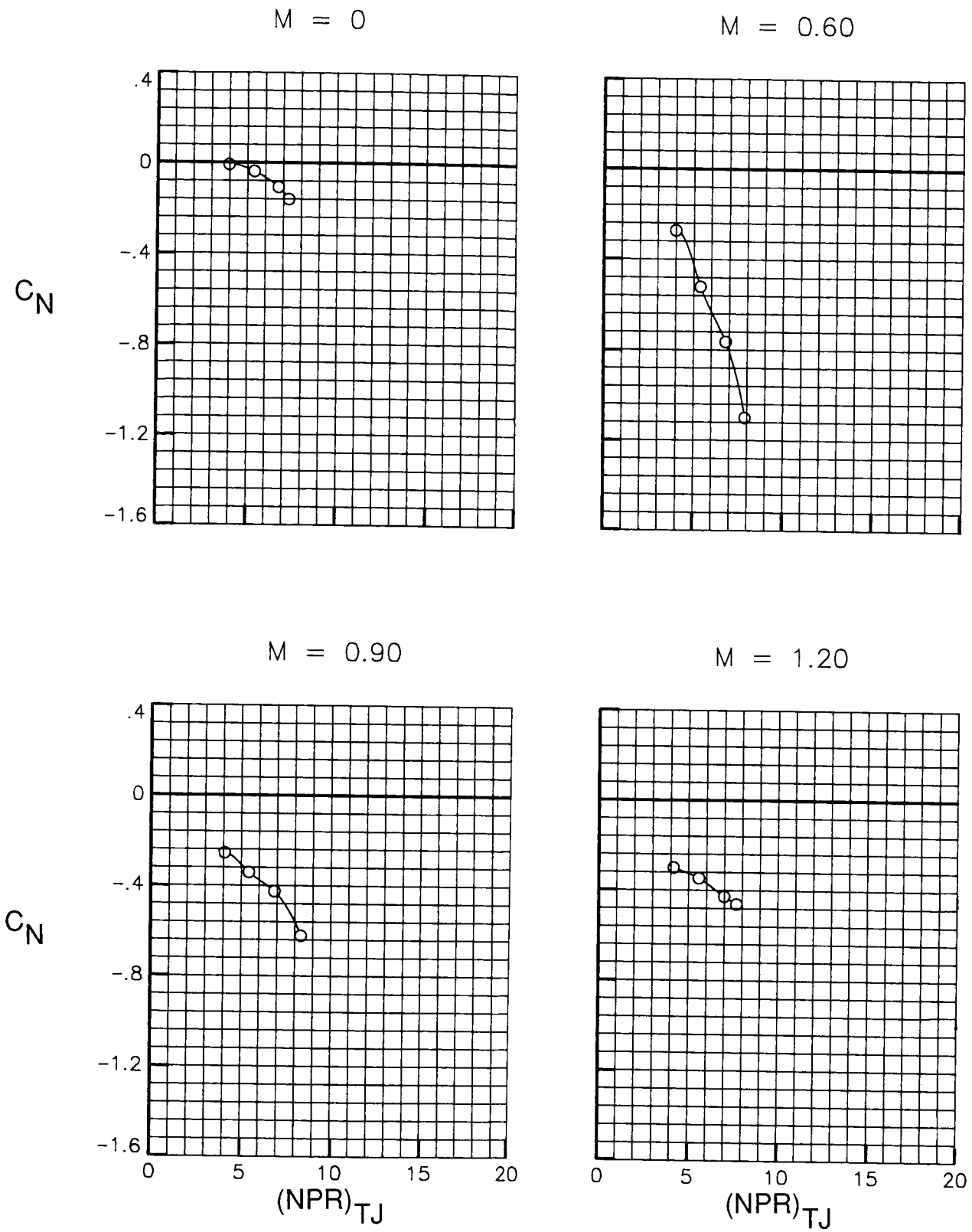
(b) Variation of normal-force coefficient with $(NPR)_{TJ}$.

Figure 30. Continued.
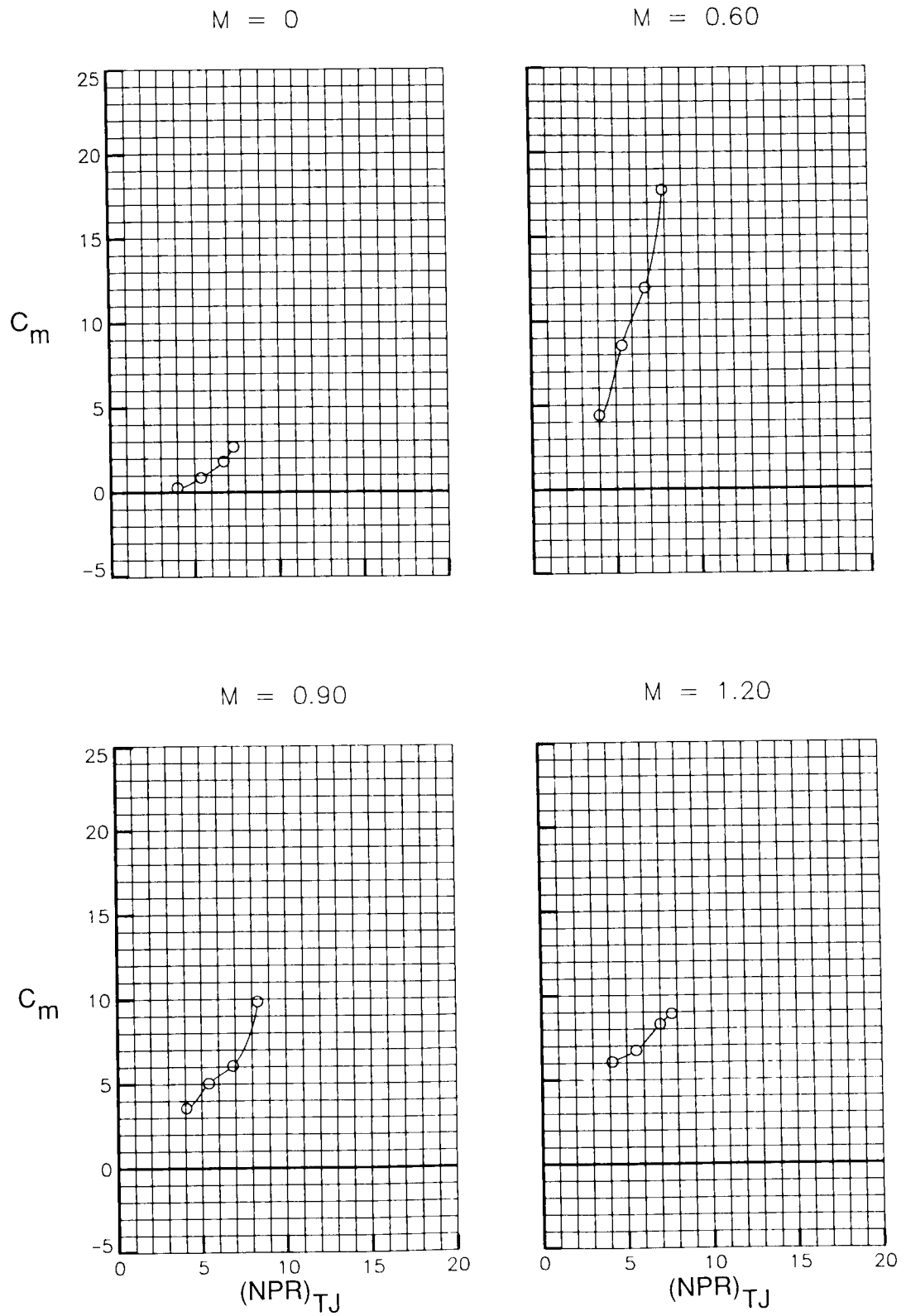
(c) Variation of pitching-moment coefficient with $(NPR)_{TJ}$.

Figure 30. Continued.

M = 0
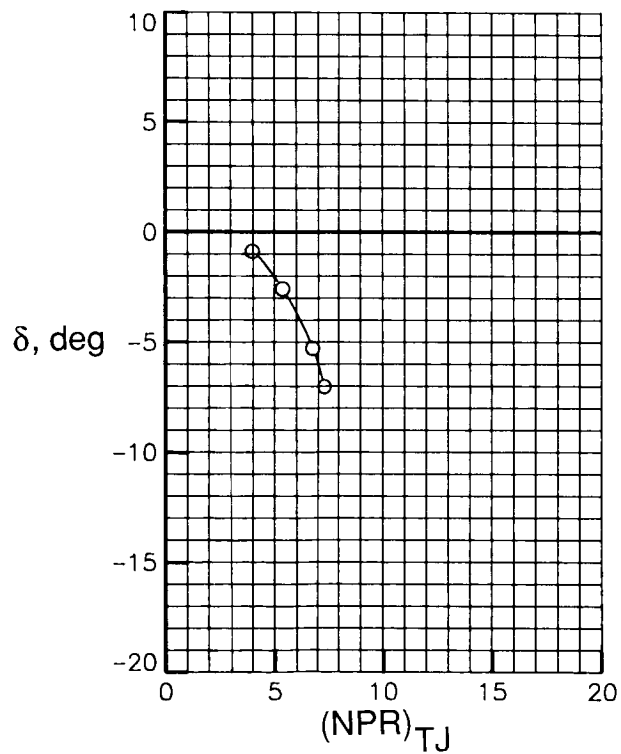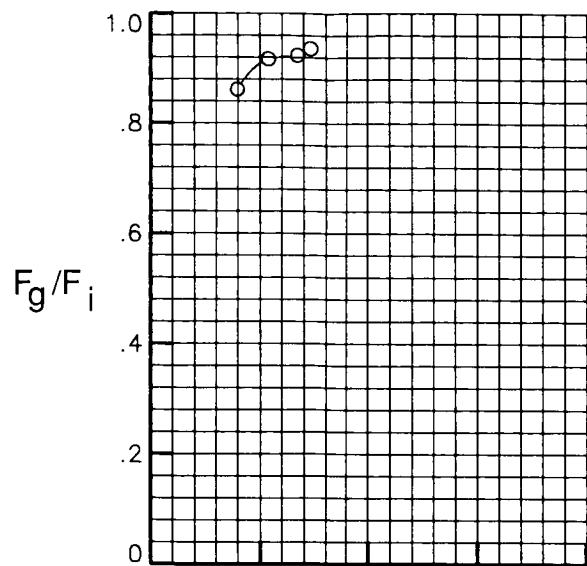
(d) Variation of gross thrust ratio and effective jet turning angle with $(NPR)_{TJ}$.

Figure 30. Concluded.
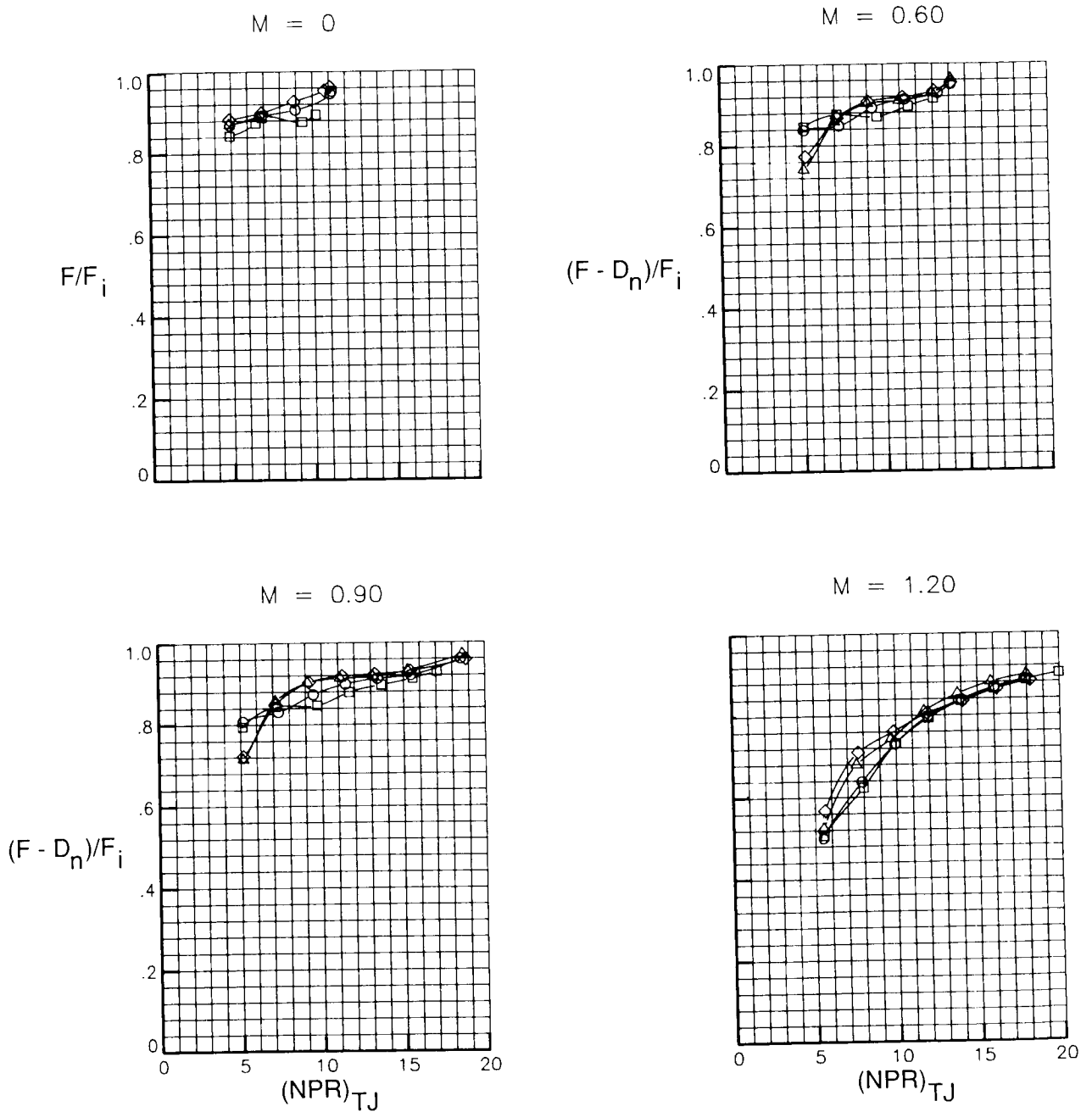
(a) Variation of axial-force ratio with $(NPR)_{TJ}$.

Figure 31. Effect of throat area and sidewalls on characteristics of CCN with blanked-off ramjet and ramjet flap 3.

Throat area | Sidewalls
$\bigcirc$ Minimum   V-notch
$\square$ Minimum   Cutback
$\diamondsuit$ Maximum   V-notch
$\triangle$ Maximum   Cutback

M = 0

M = 0.60

M = 0.90

M = 1.20

C_N
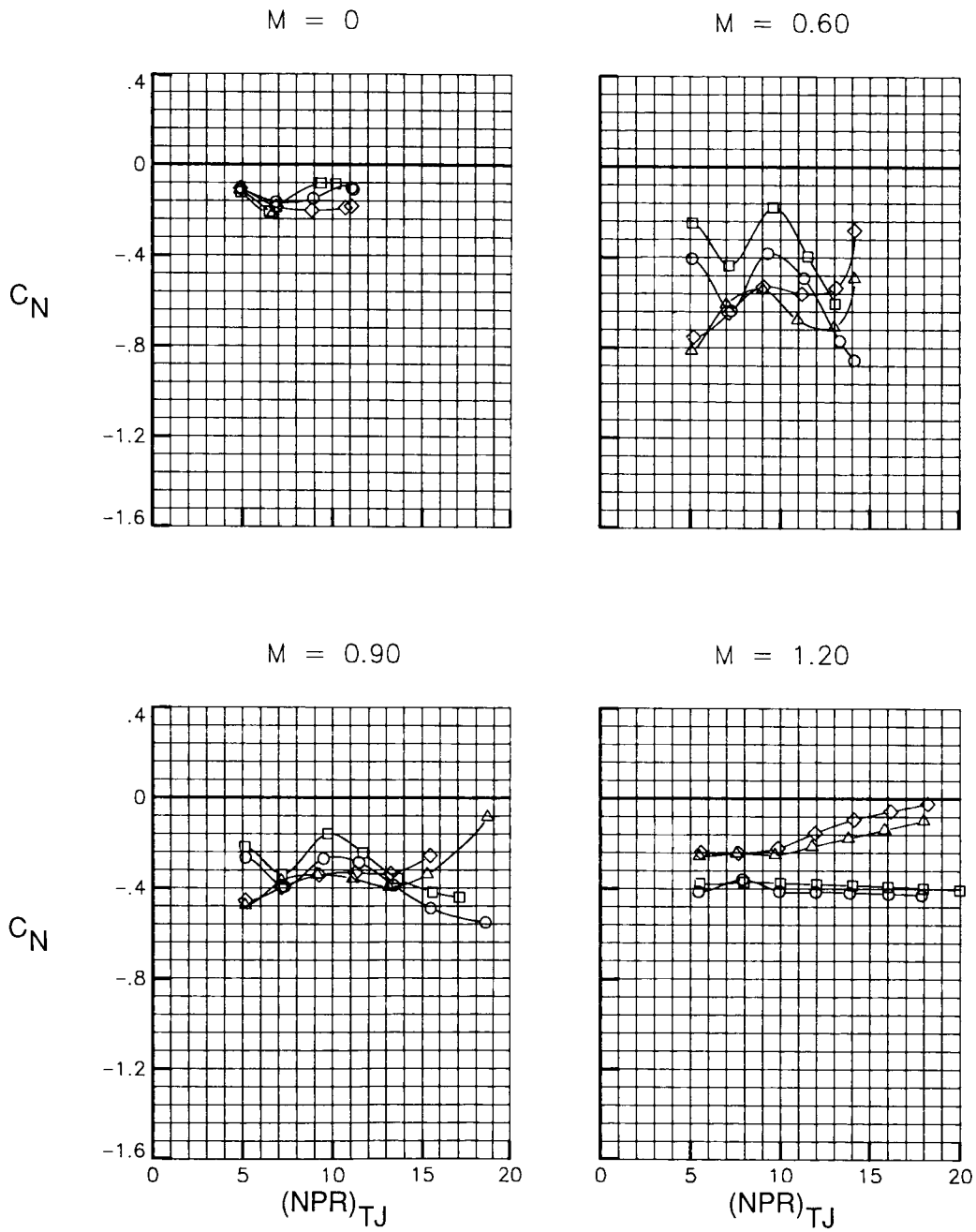
$(NPR)_{TJ}$

(b) Variation of normal-force coefficient with $(NPR)_{TJ}$.

Figure 31. Continued.

Throat area | Sidewalls
○ Minimum V-notch
□ Minimum Cutback
◇ Maximum V-notch
△ Maximum Cutback

M = 0

M = 0.60

C_m

M = 0.90

M = 1.20

C_m

$(NPR)_{TJ}$

$(NPR)_{TJ}$

(c) Variation of pitching-moment coefficient with $(NPR)_{TJ}$.

Figure 31. Continued.
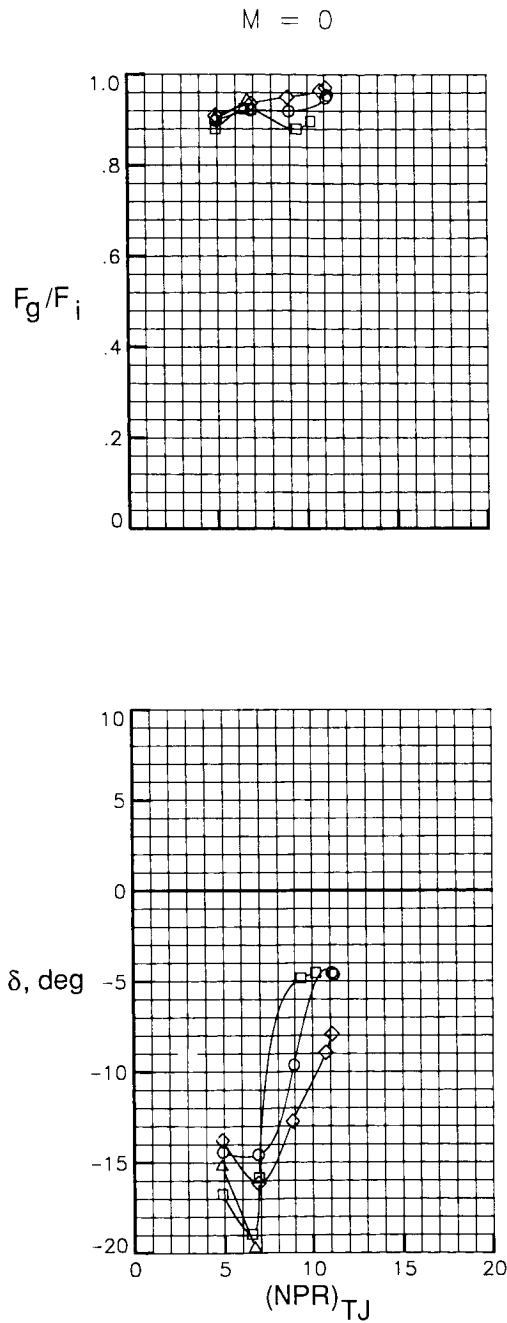
(d) Variation of gross thrust ratio and effective jet turning angle with $(NPR)_{TJ}$.
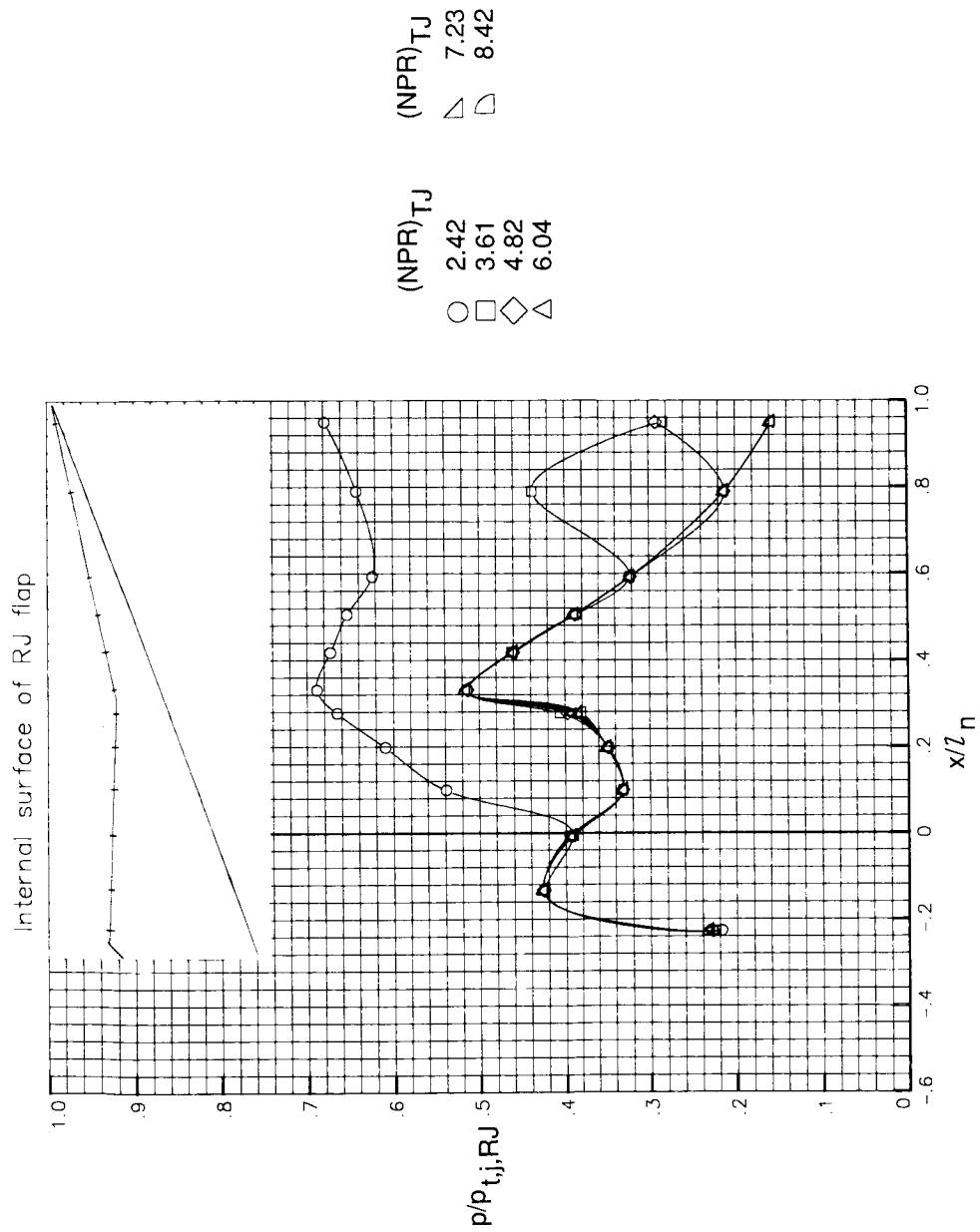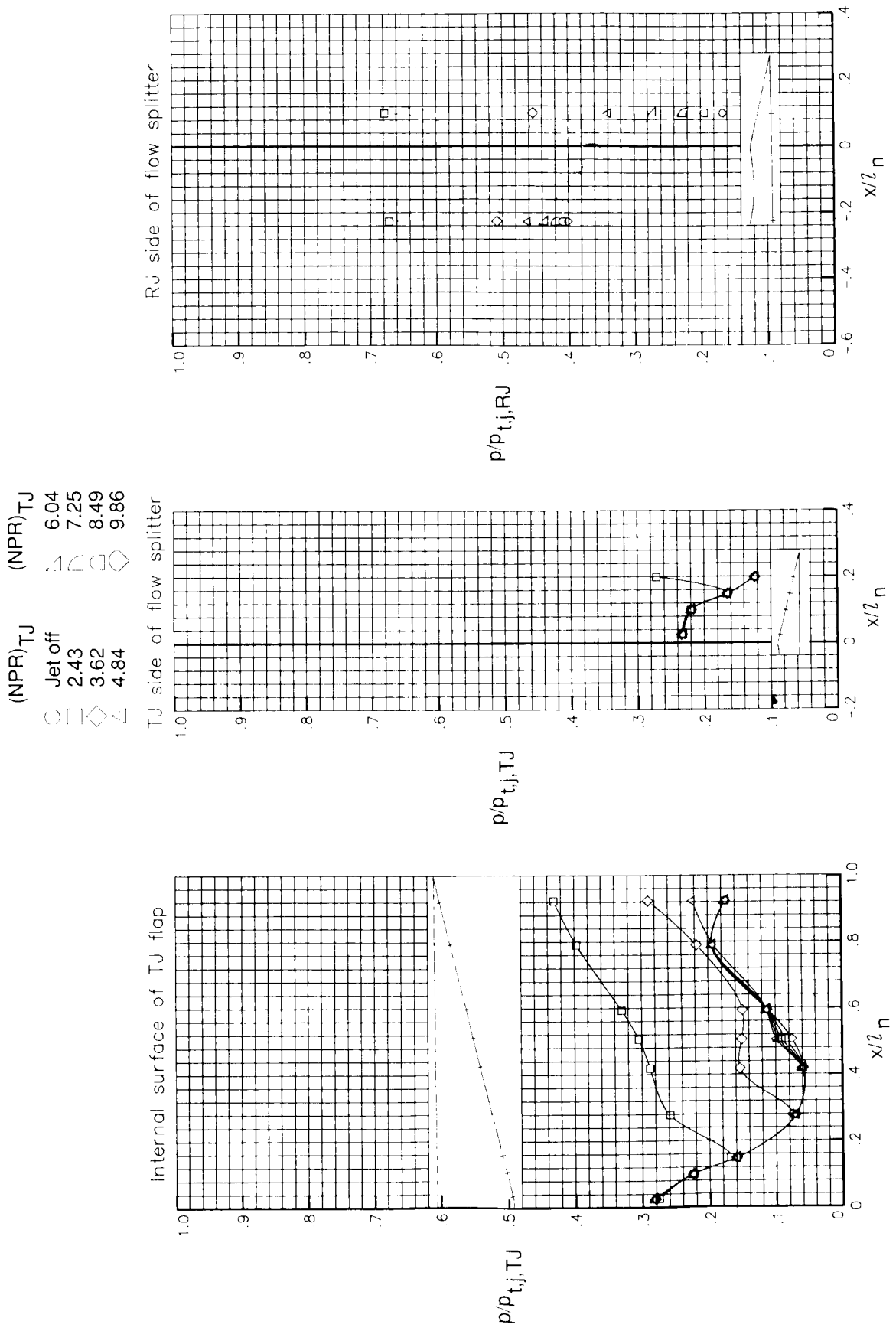
Figure 31. Concluded.
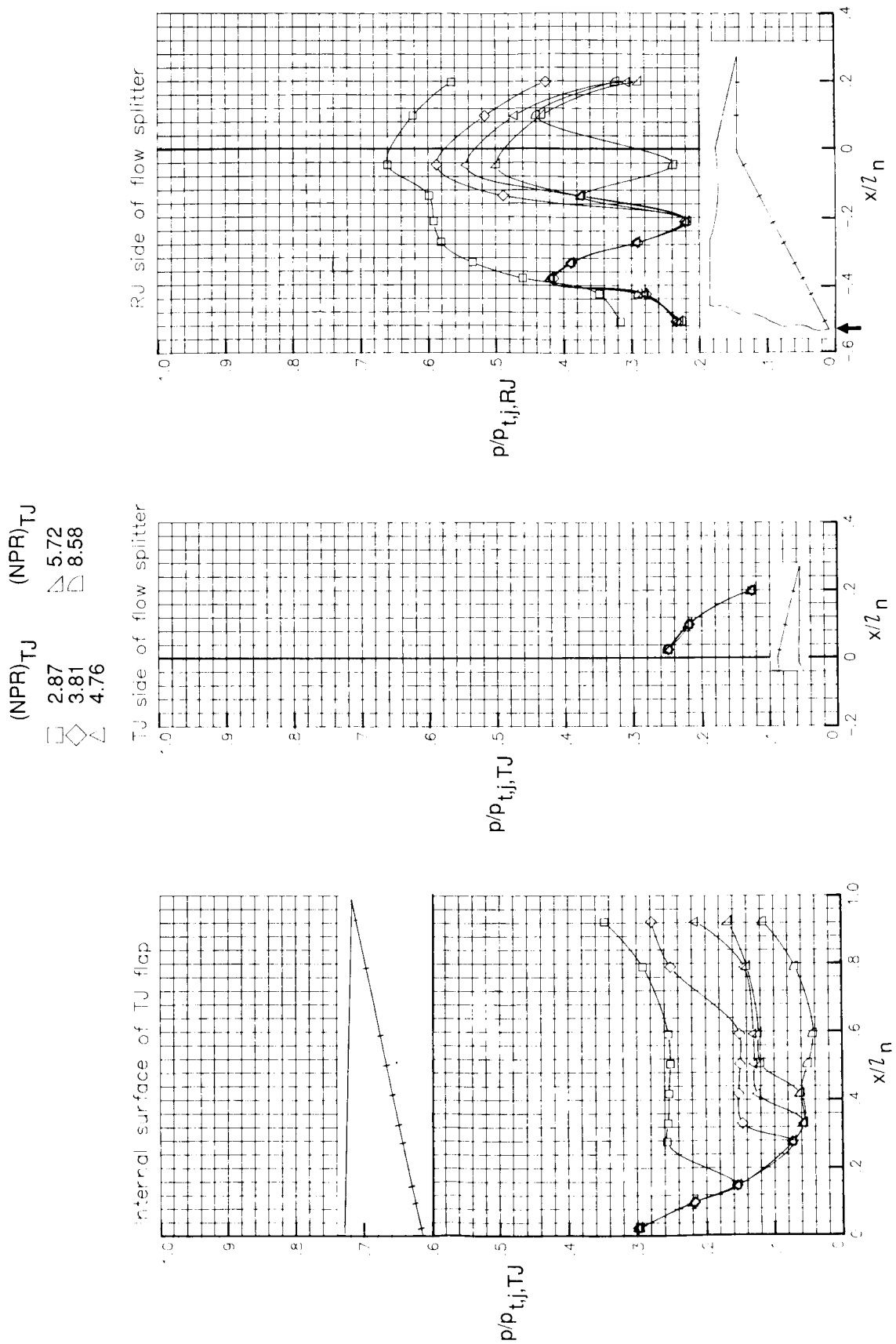
(a) $M = 0$. Arrow indicates RJ throat location.

Figure 32. Pressure ratio and pressure coefficient distributions of MERN with minimum ramjet throat area.

Internal surface of RJ flap

$p/p_{tj,RJ}$

x/l_n

(NPR)$_{TJ}$		(NPR)$_{TJ}$
☐ 2.87		△ 5.72
◇ 3.81		⬠ 8.58
△ 4.76		

(a) Concluded.

Figure 32. Continued.

73

Internal surface of TJ flap

$p/p_{t,j,TJ}$

x/l_n

TJ side of flow splitter

$p/p_{t,j,TJ}$

x/l_n

RJ side of flow splitter

$p/p_{t,j,RJ}$

x/l_n
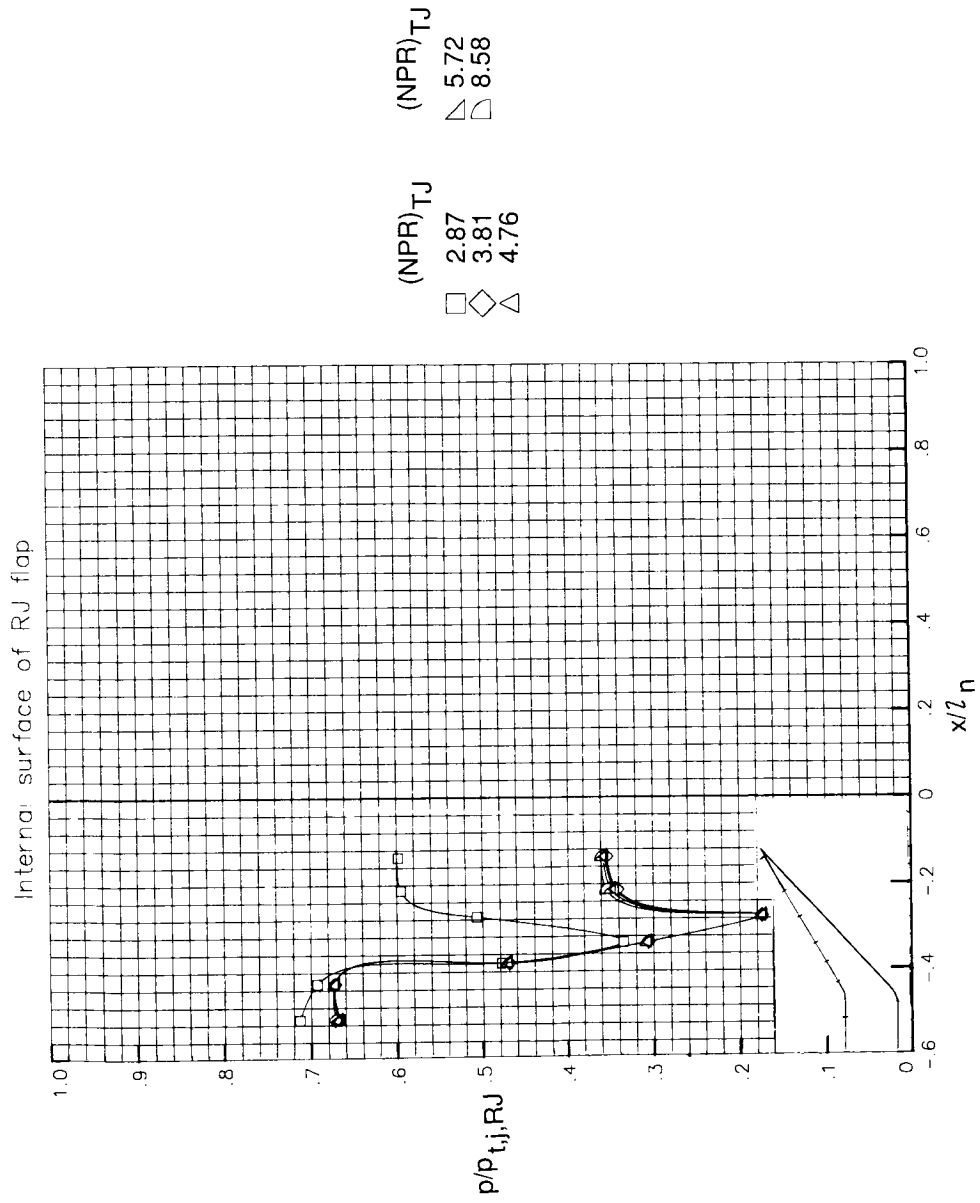
$(NPR)_{TJ}$		$(NPR)_{TJ}$	
	2.87		5.74
	3.83		6.69
	4.78		10.38
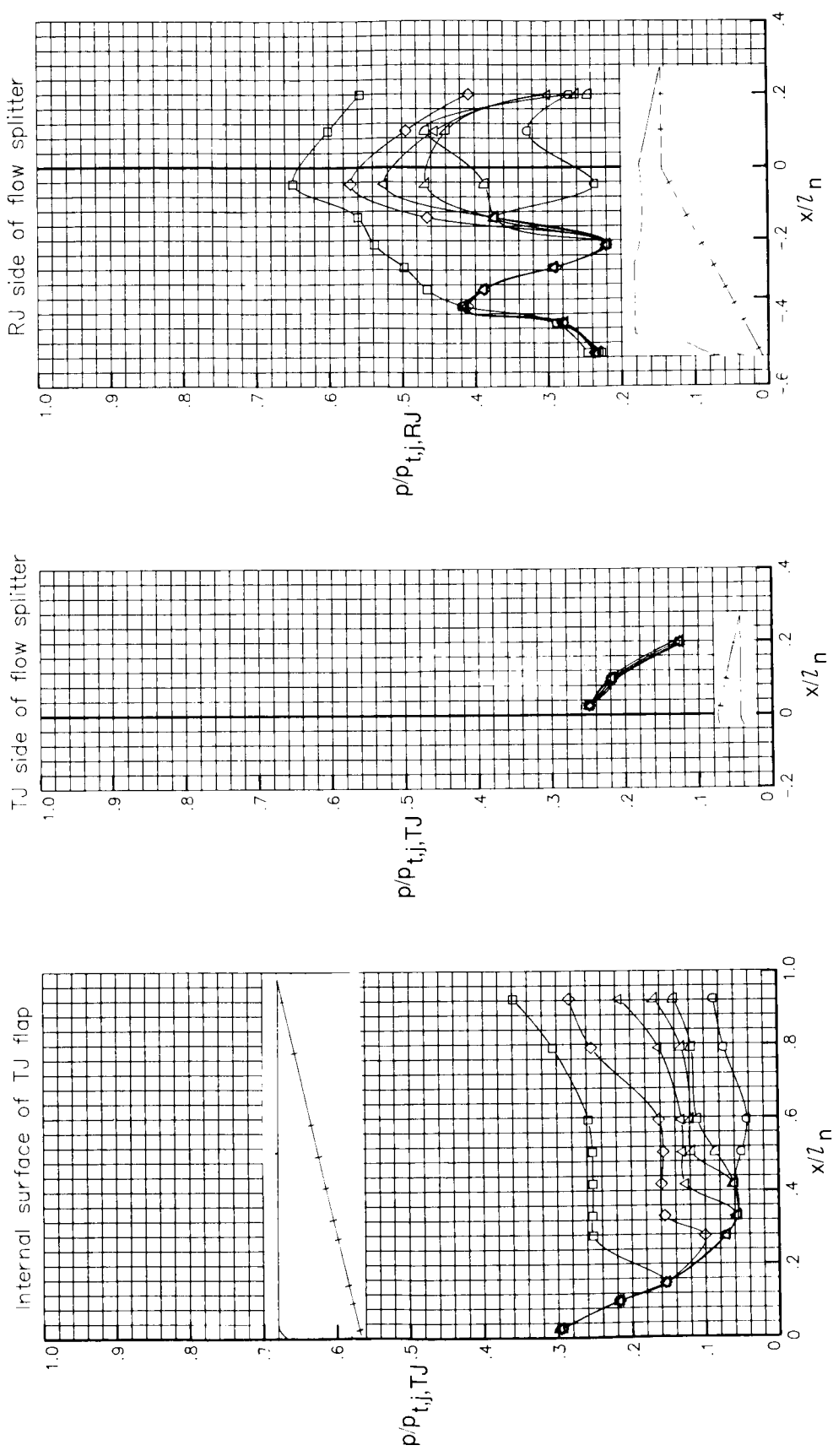
(b) $M = 0.60$.

Figure 32. Continued.

(b) Concluded.

Figure 32. Continued.
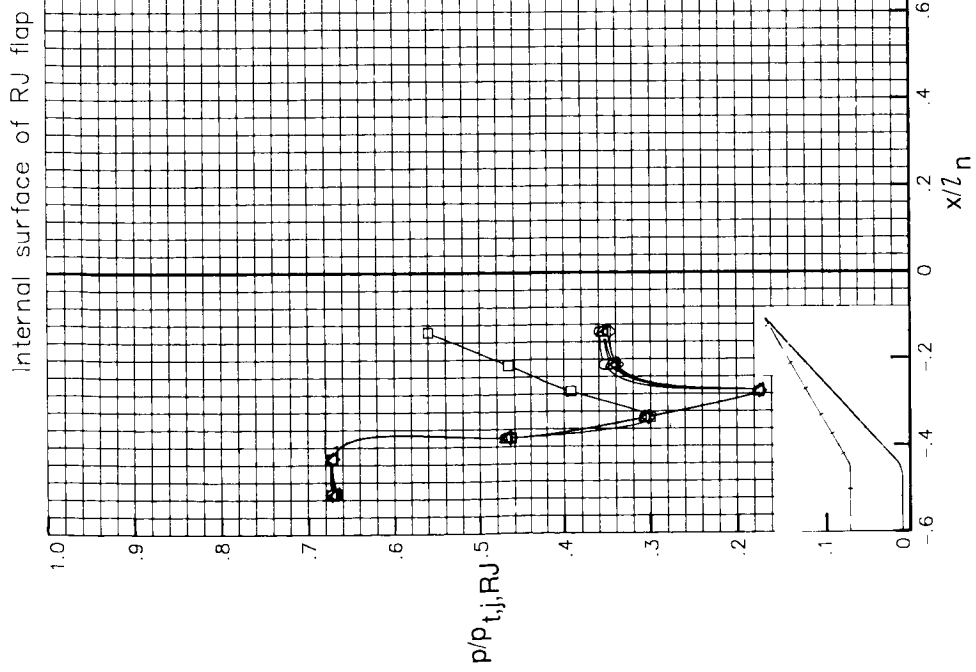
(c) $M = 0.90$.
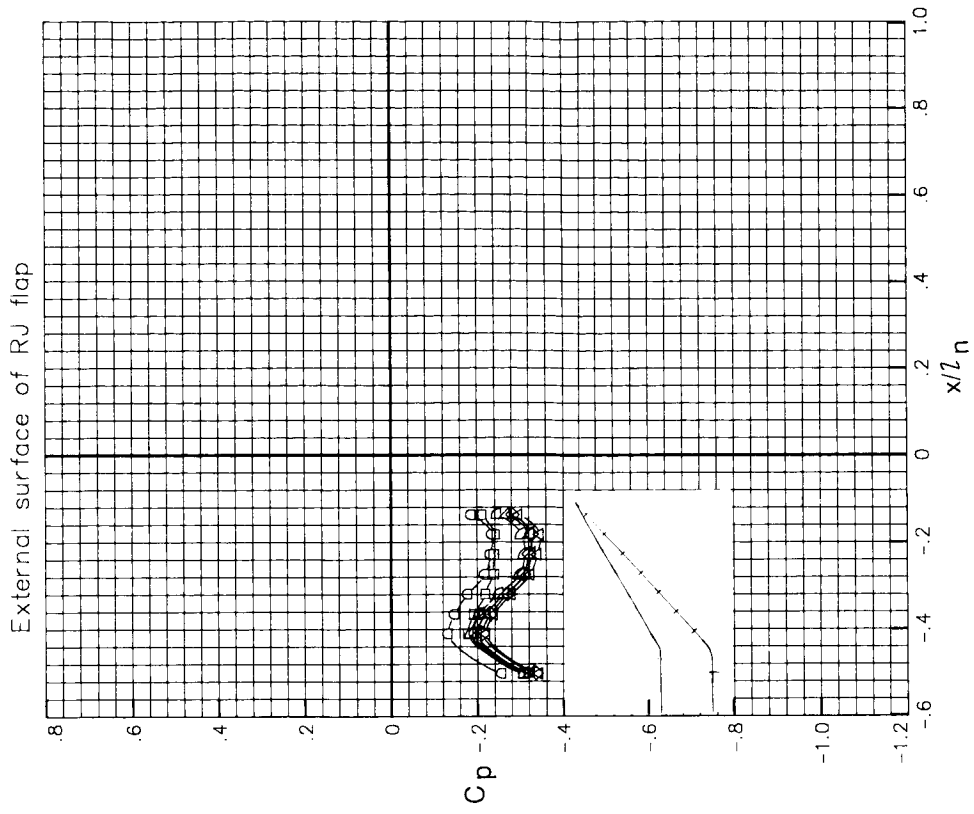
Figure 32. Continued.

External surface of RJ flap

$(NPR)_{TJ}$

$(NPR)_{TJ}$

○ Jet off   ◻ 5.76
◇ 2.87   ◻ 6.69
△ 3.82   ⬠ 7.63
△ 4.78

C_p

x/l_n

Internal surface of RJ flap

$p/p_{t,j,RJ}$

x/l_n
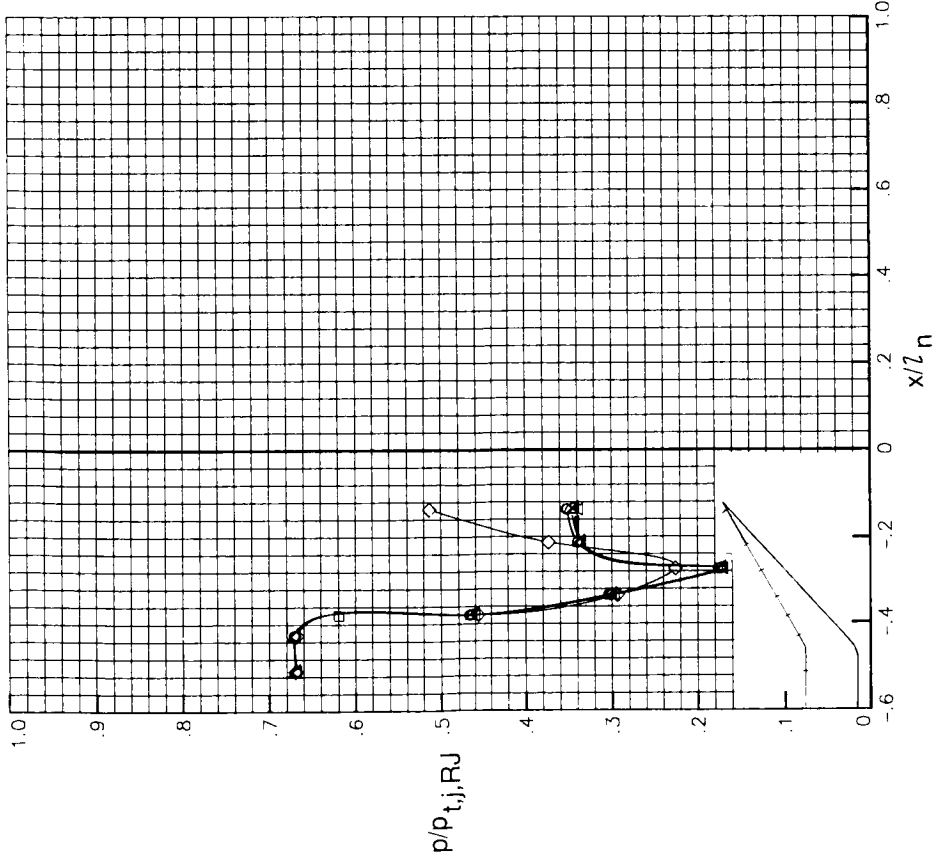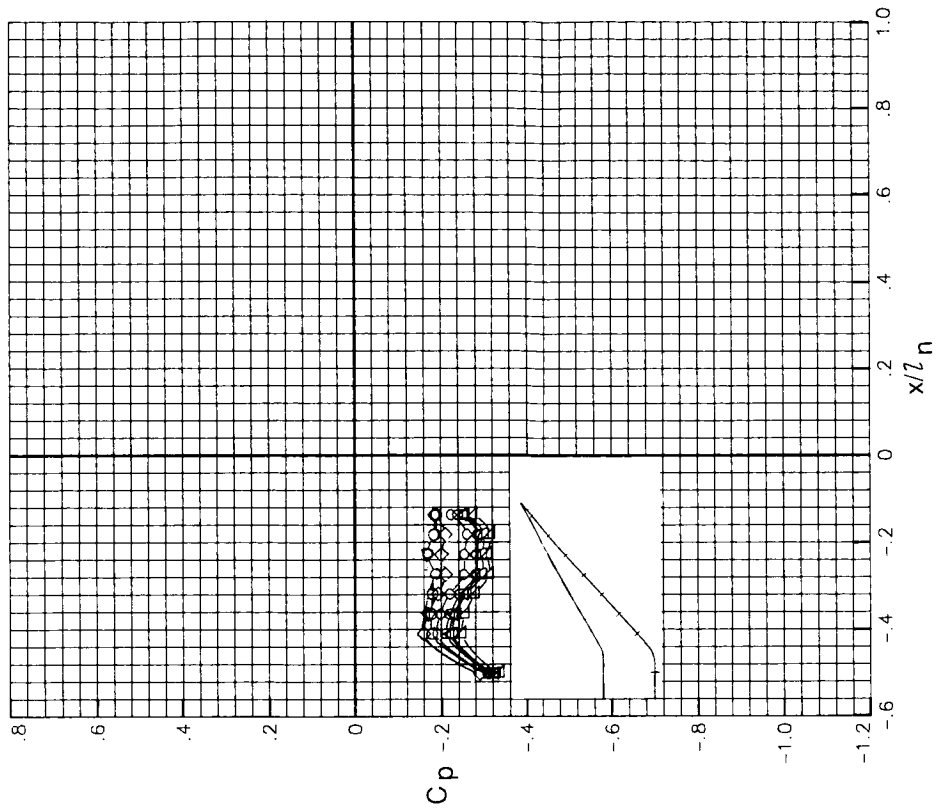
(c) Concluded.

Figure 32. Continued.
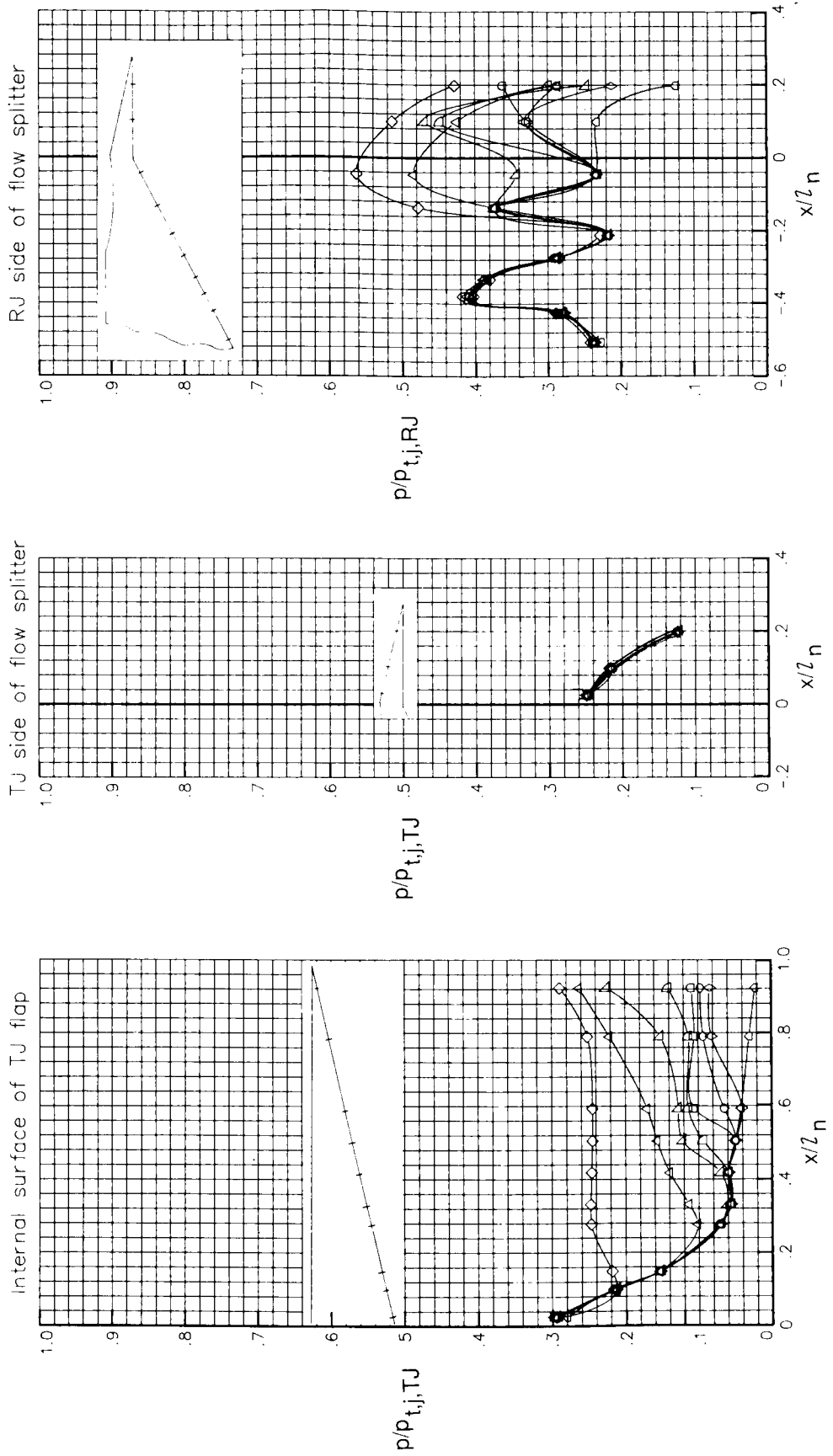
(d) $M = 1.20$.

Figure 32. Continued.

(d) Concluded.

Figure 32. Concluded.

(a) $M = 0$. Arrow indicates RJ throat location.

Figure 33. Pressure ratio and pressure coefficient distributions of MERN with maximum ramjet throat area.

80

Internal surface of RJ flap

x/l_n

$p/p_{t,j,RJ}$

$(NPR)_{TJ}$		$(NPR)_{TJ}$	
□	3.94	◁	6.53
◇	5.23	◿	6.64
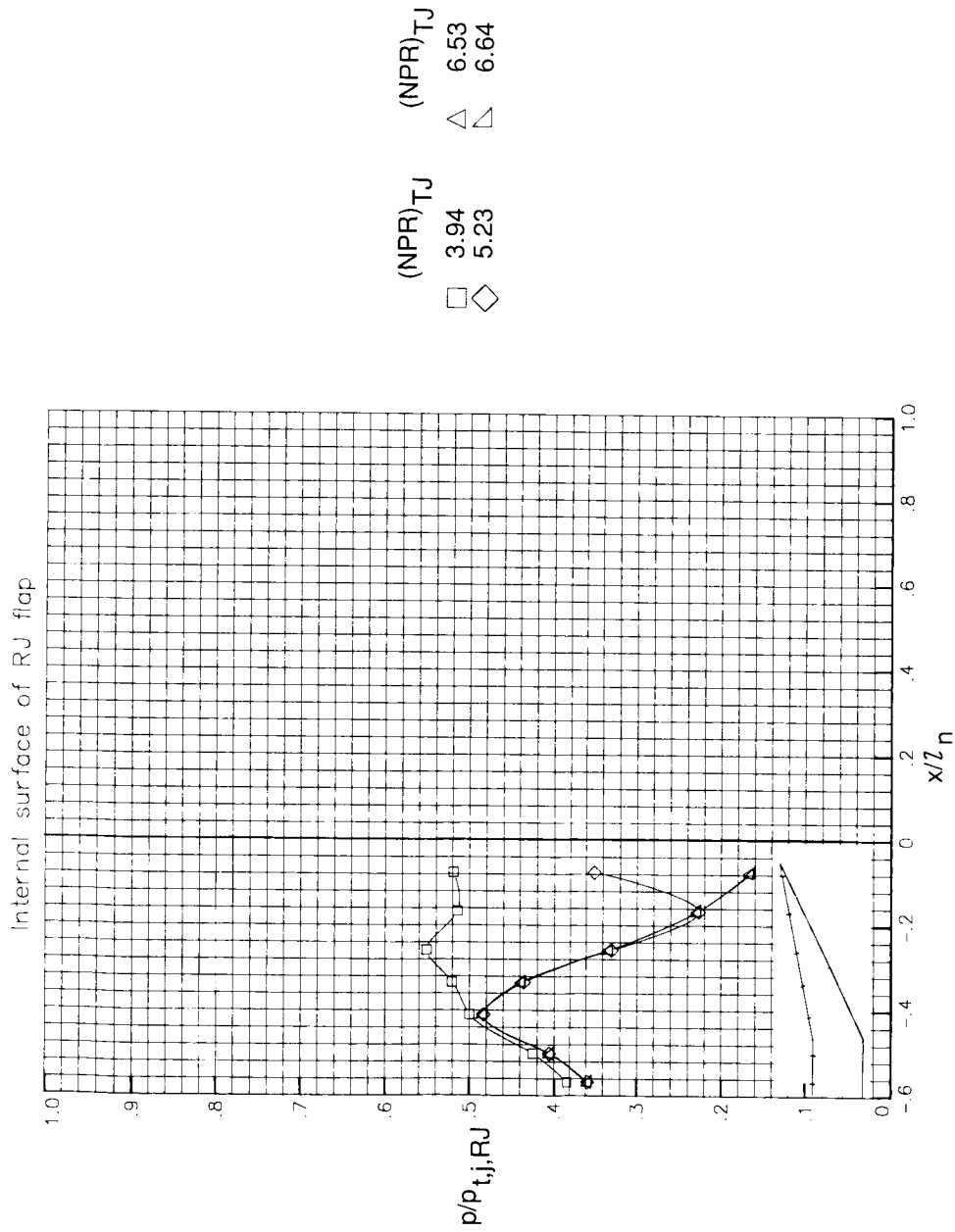
(a) Concluded.

Figure 33. Continued.

(b) $M = 0.60$.

Figure 33. Continued.

(b) Concluded.

Figure 33. Continued.

(c) $M = 0.90$.
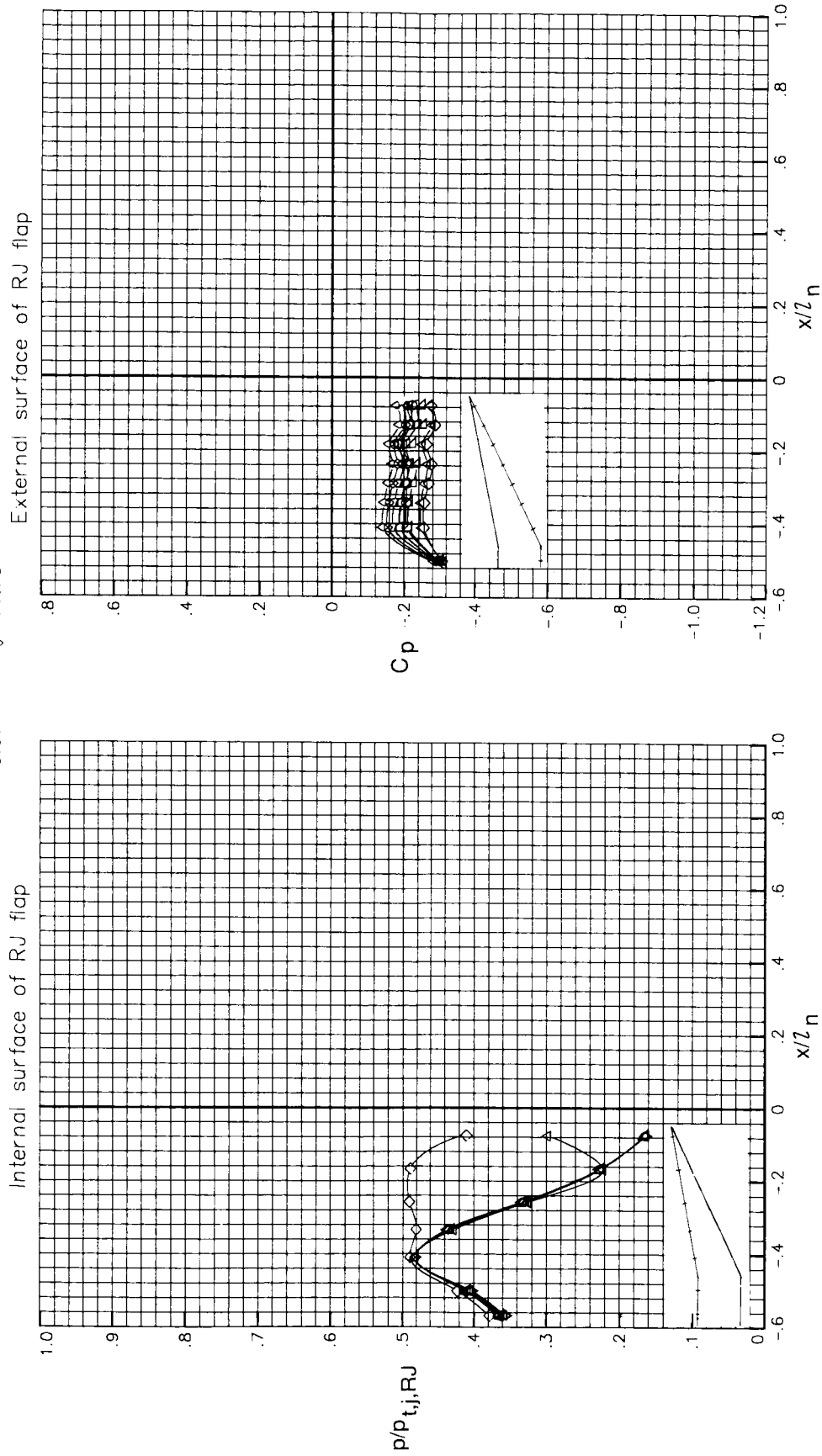
Figure 33. Continued.

(c) Concluded.

Figure 33. Continued.

(d) $M = 1.20.$

Figure 33. Continued.

(d) Concluded.

Figure 33. Concluded.
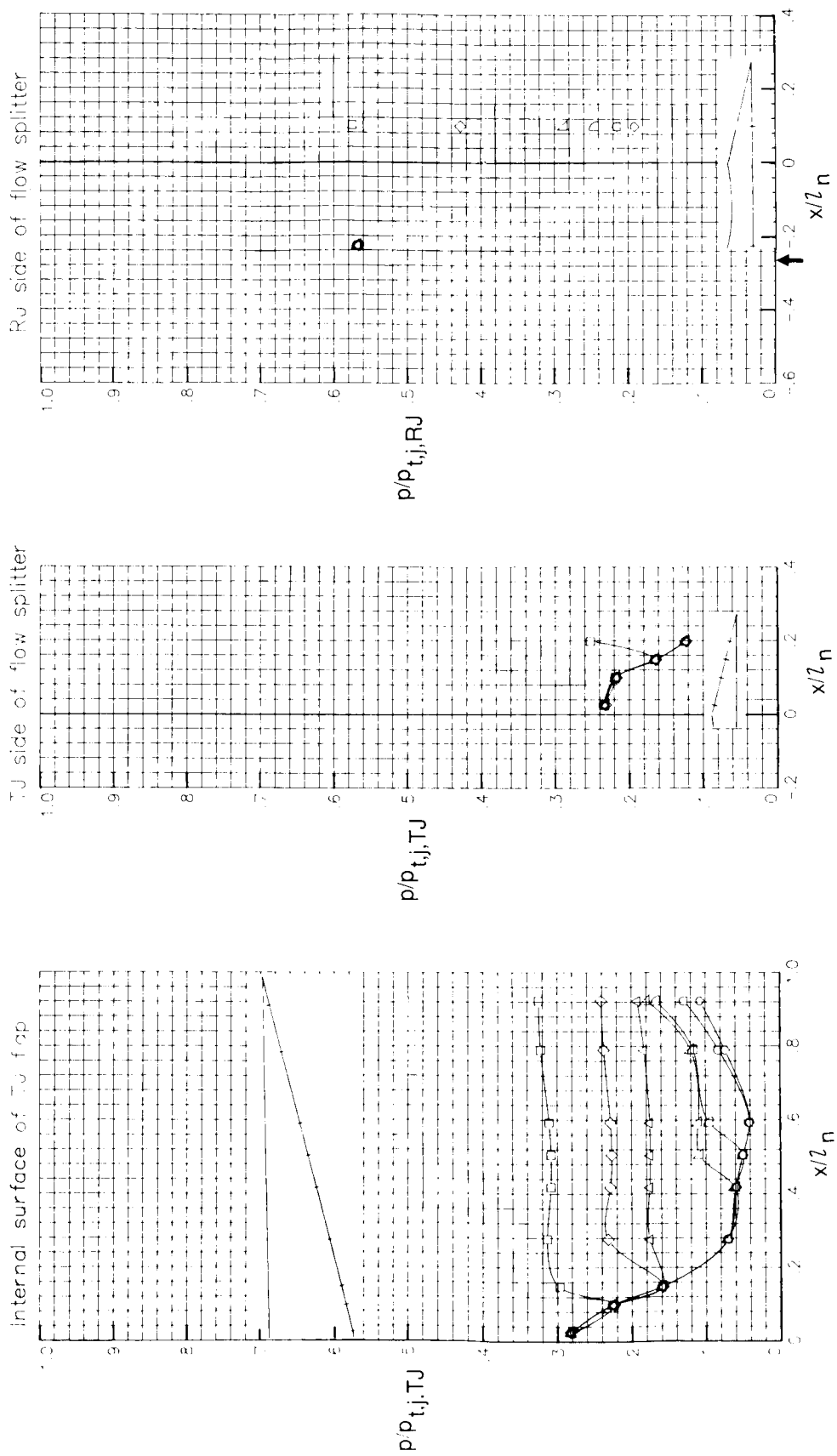
(a) $M = 0$. Arrow indicates RJ throat location.

Figure 34. Pressure ratio and pressure coefficient distributions of CCN with minimum ramjet throat area. V-notch sidewalls. and ramjet flap 1.
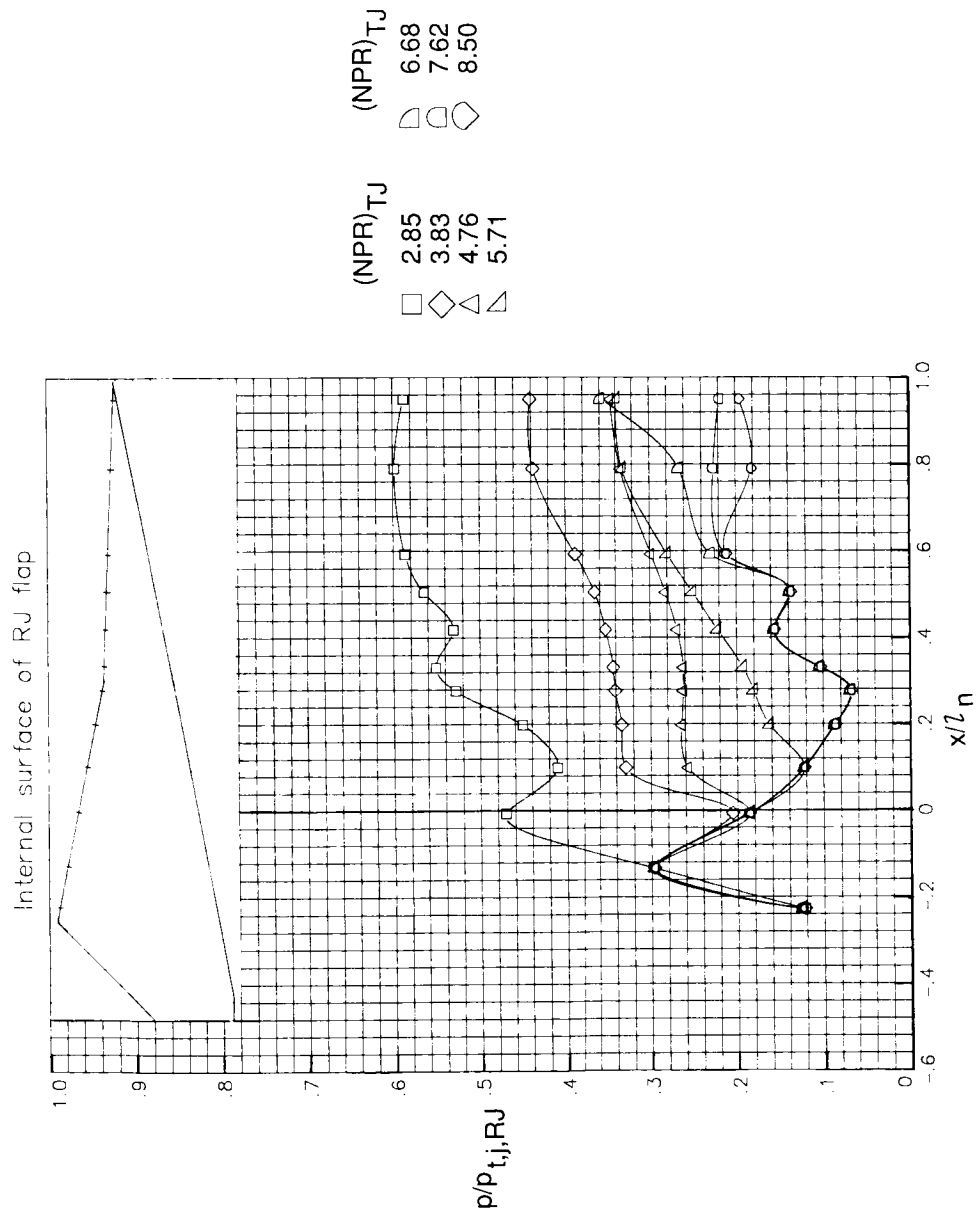
(a) Concluded.

Figure 34. Continued.

(b) $M = 0.60$.

Figure 34. Continued.

(b) Concluded.

Figure 34. Continued.
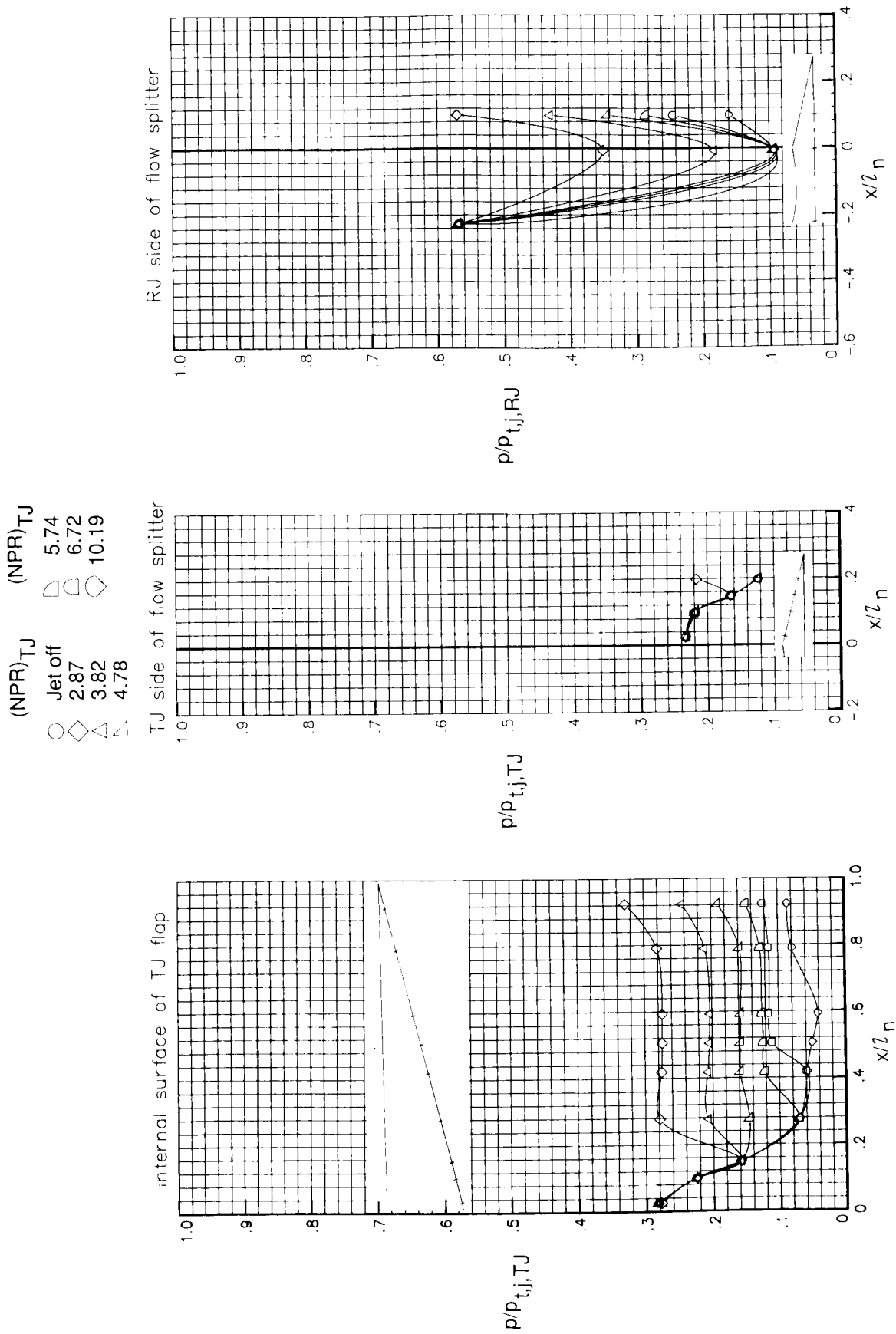
(c) $M = 0.90$.

Figure 34. Continued.

$(NPR)_{TJ}$

○	Jet off
◇	2.87
△	3.83
◁	4.78
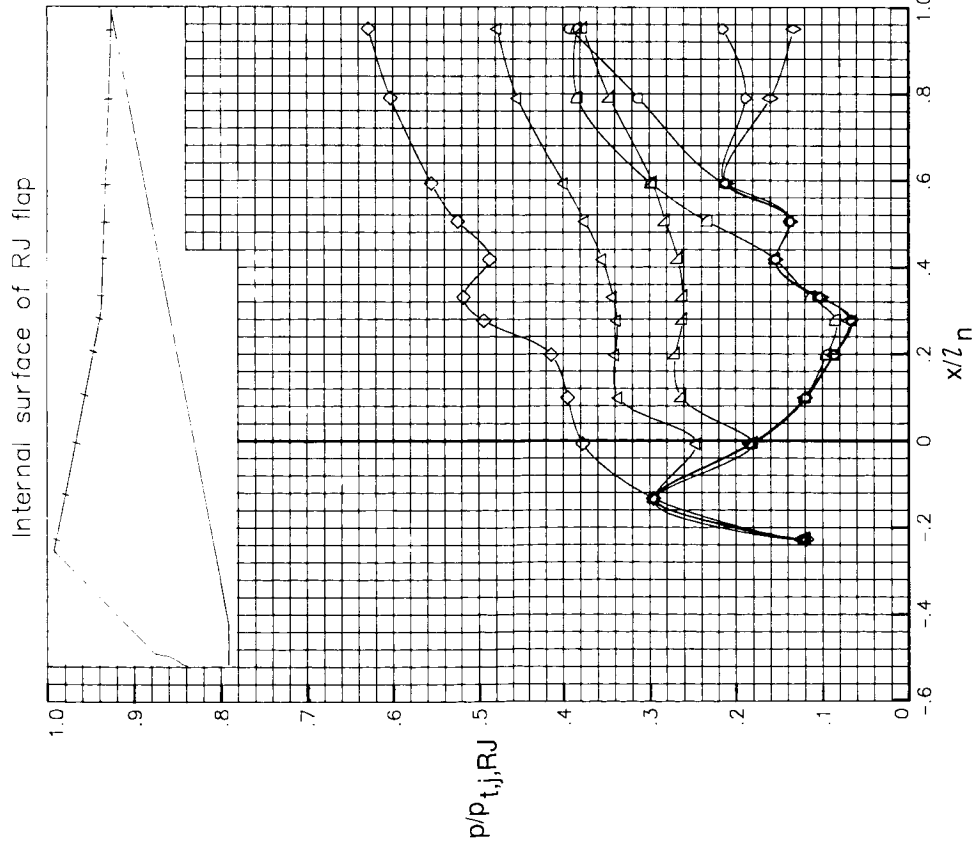
$(NPR)_{TJ}$

△	5.74
◻	6.68
⬠	7.63
◇	12.77

(c) Concluded.

Figure 34. Continued.
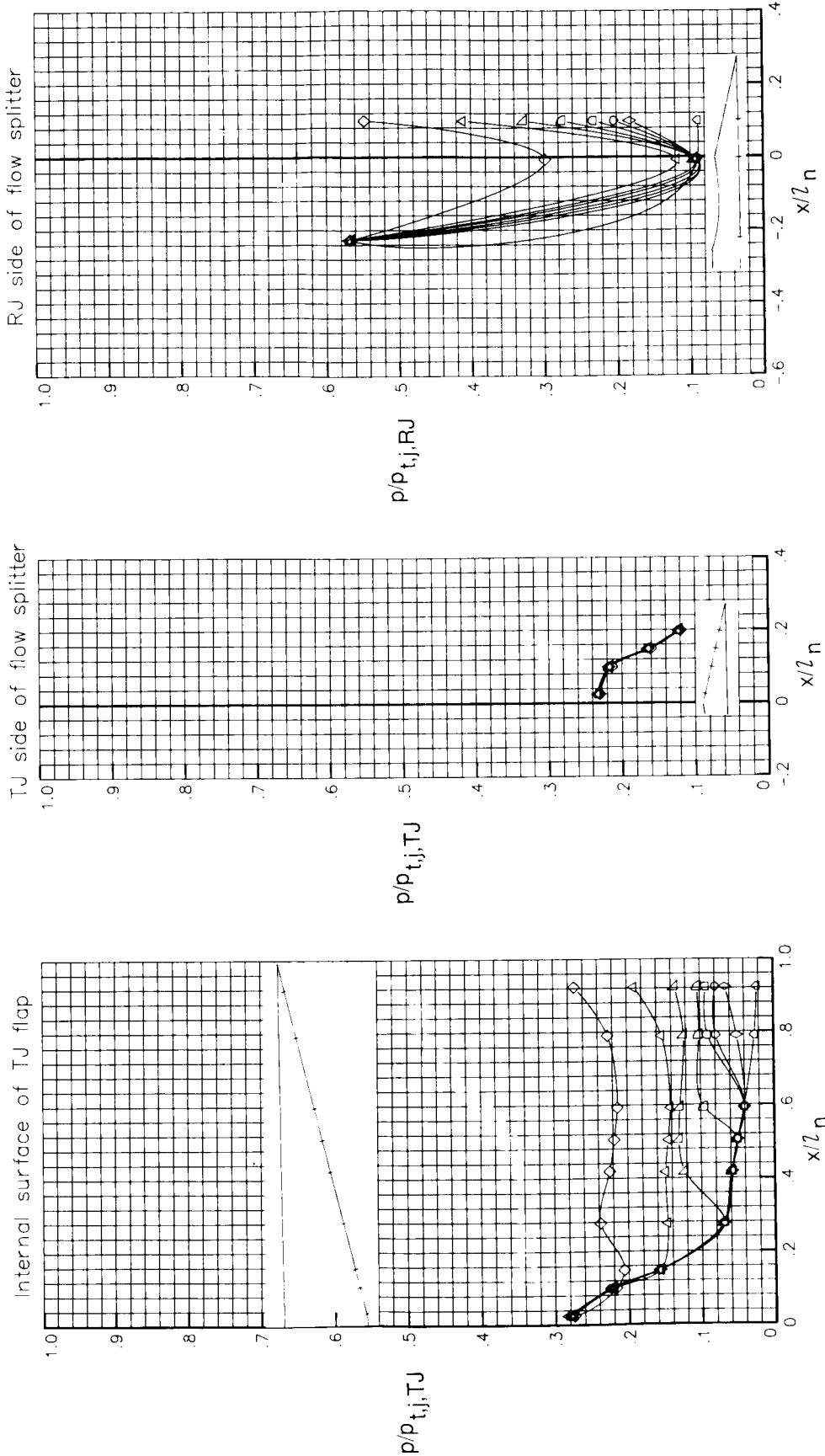
(d) $M = 1.20$.

Figure 34. Continued.
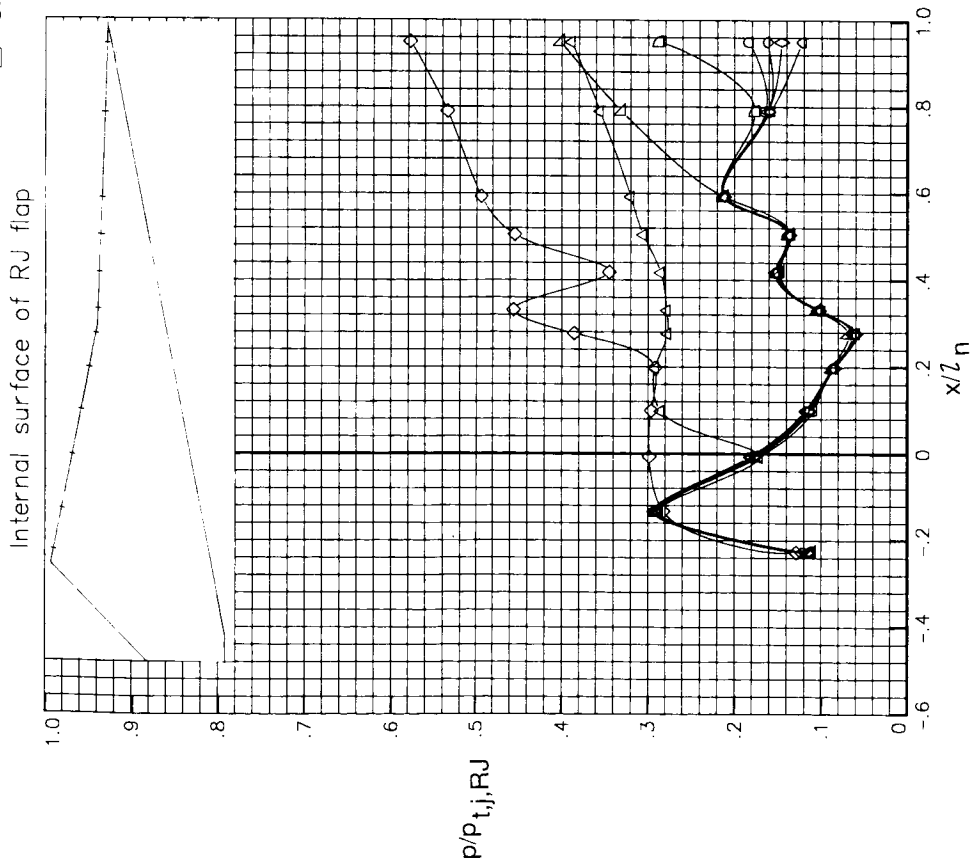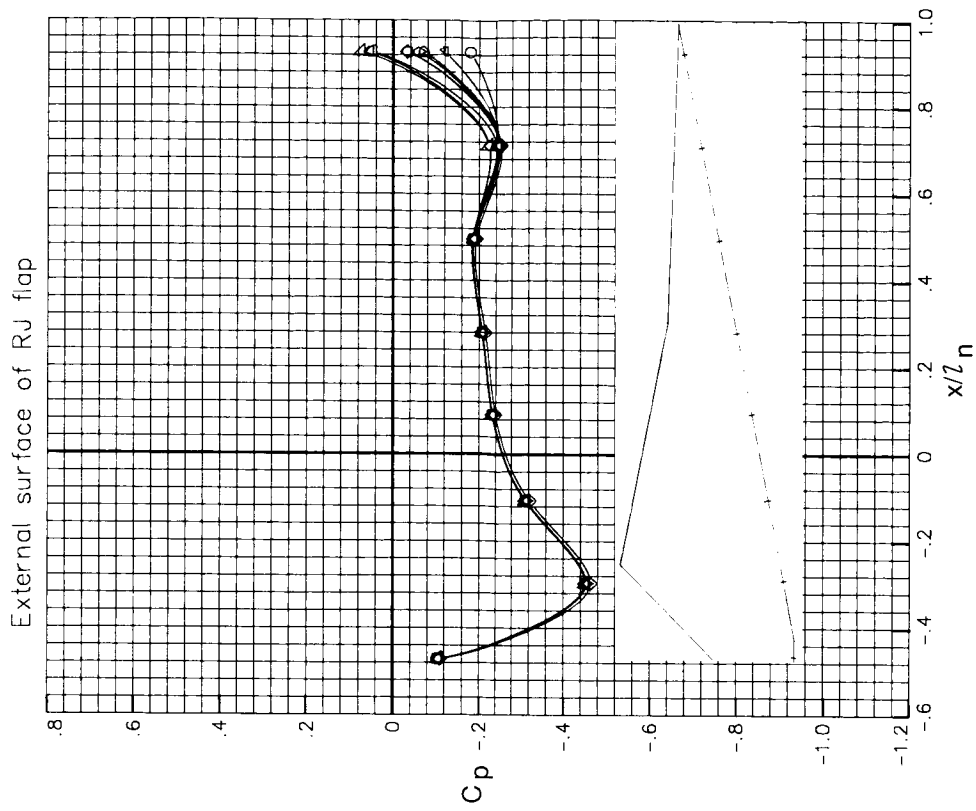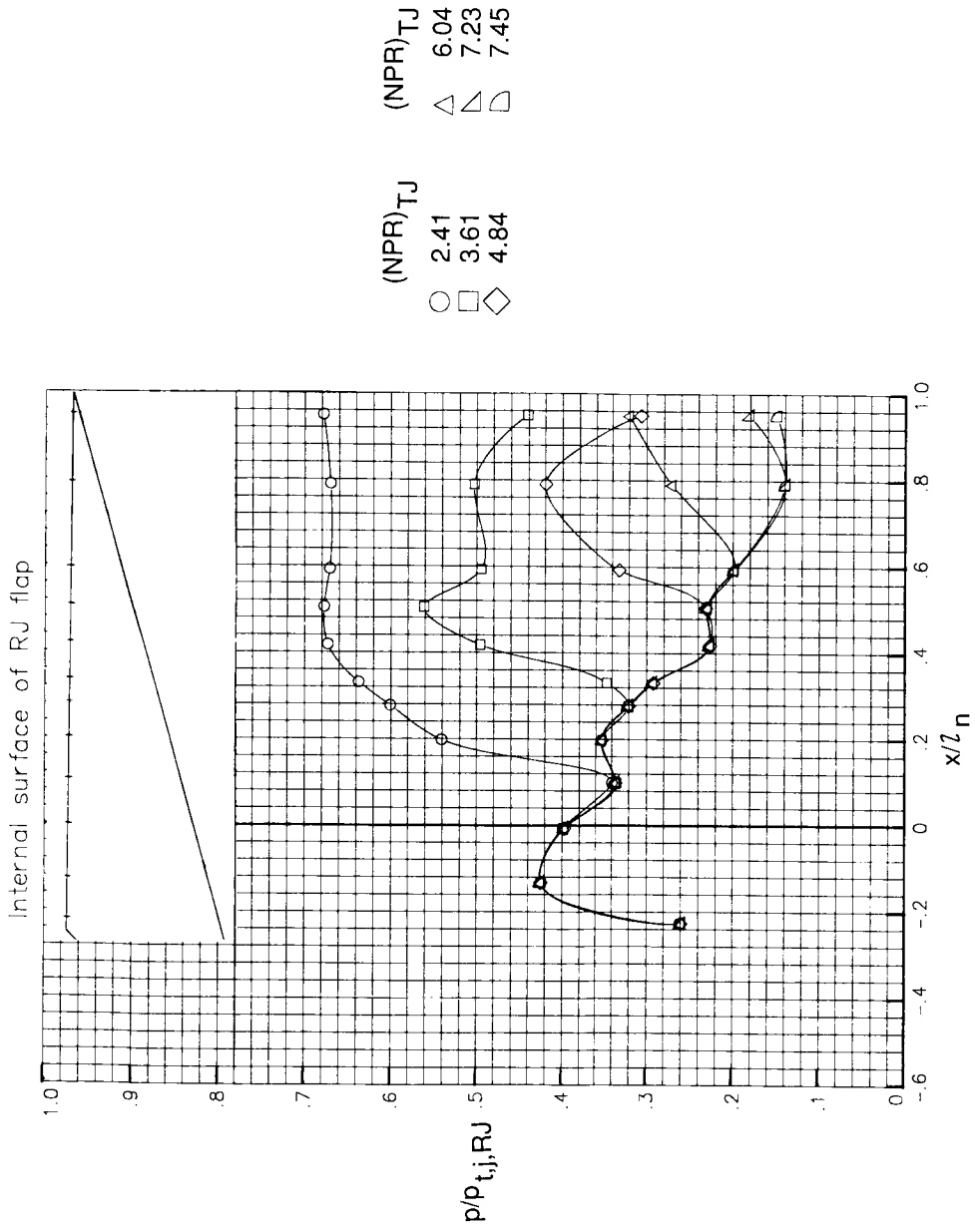
(d) Concluded.

Figure 34. Concluded.
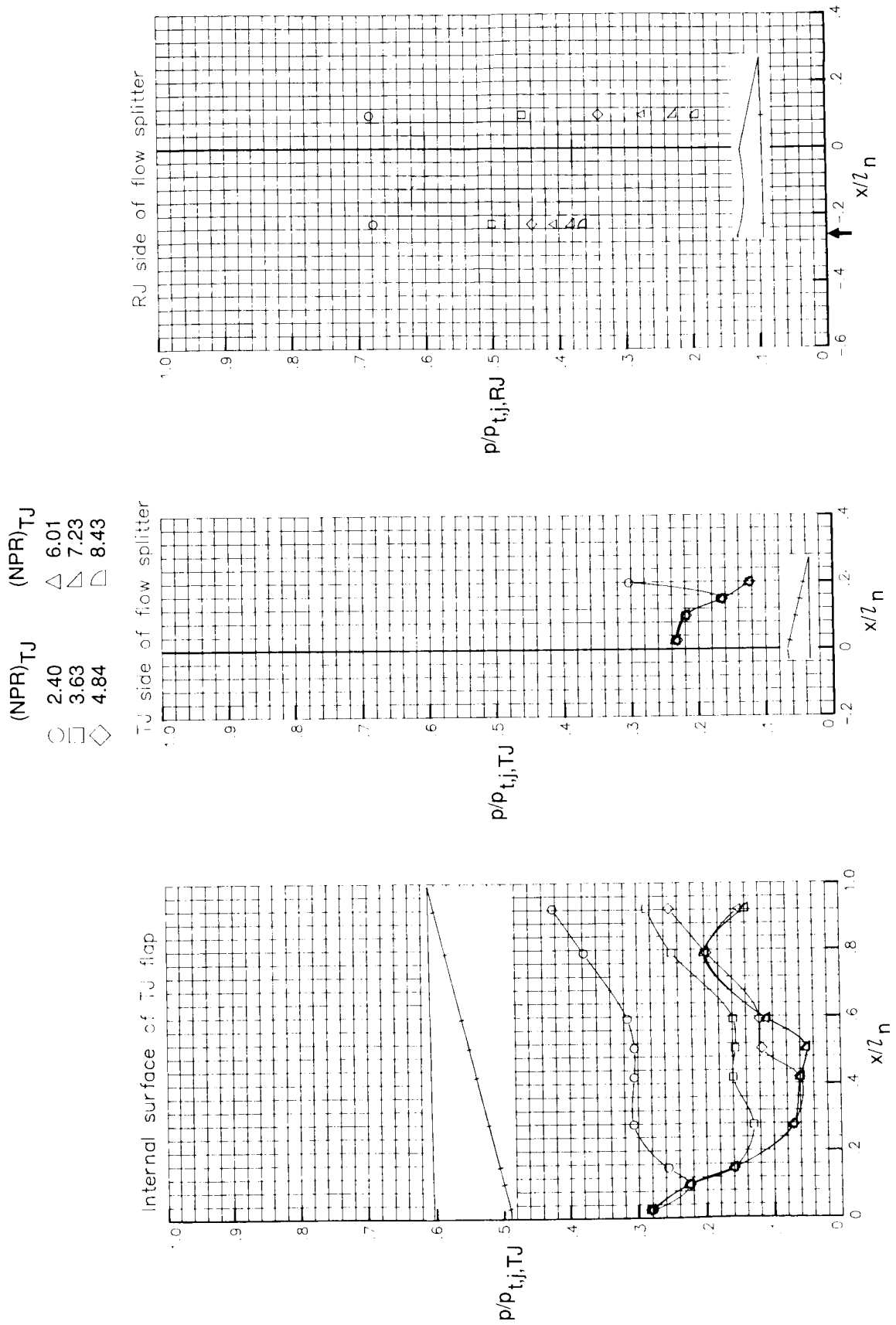
(a) $M = 0$. Arrow indicates RJ throat location.

Figure 35. Pressure ratio and pressure coefficient distributions of CCN with minimum ramjet throat area, V-notch sidewalls and ramjet flap 2.

Internal surface of RJ flap

(NPR)$_{TJ}$		(NPR)$_{TJ}$	
○	2.40	△	6.01
□	3.63	△	7.23
◇	4.84	◻	8.43

$p/p_{tj,RJ}$

x/l_n
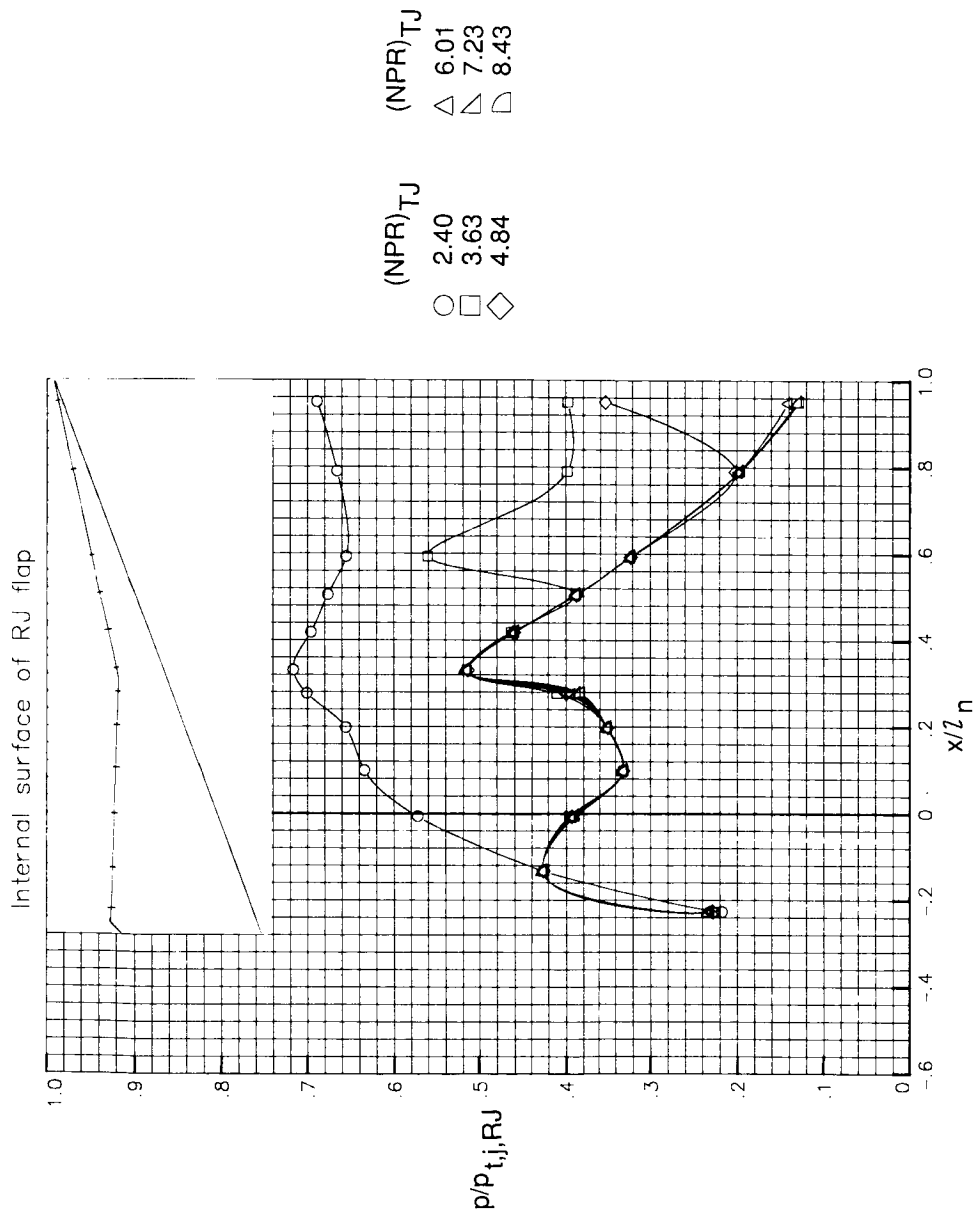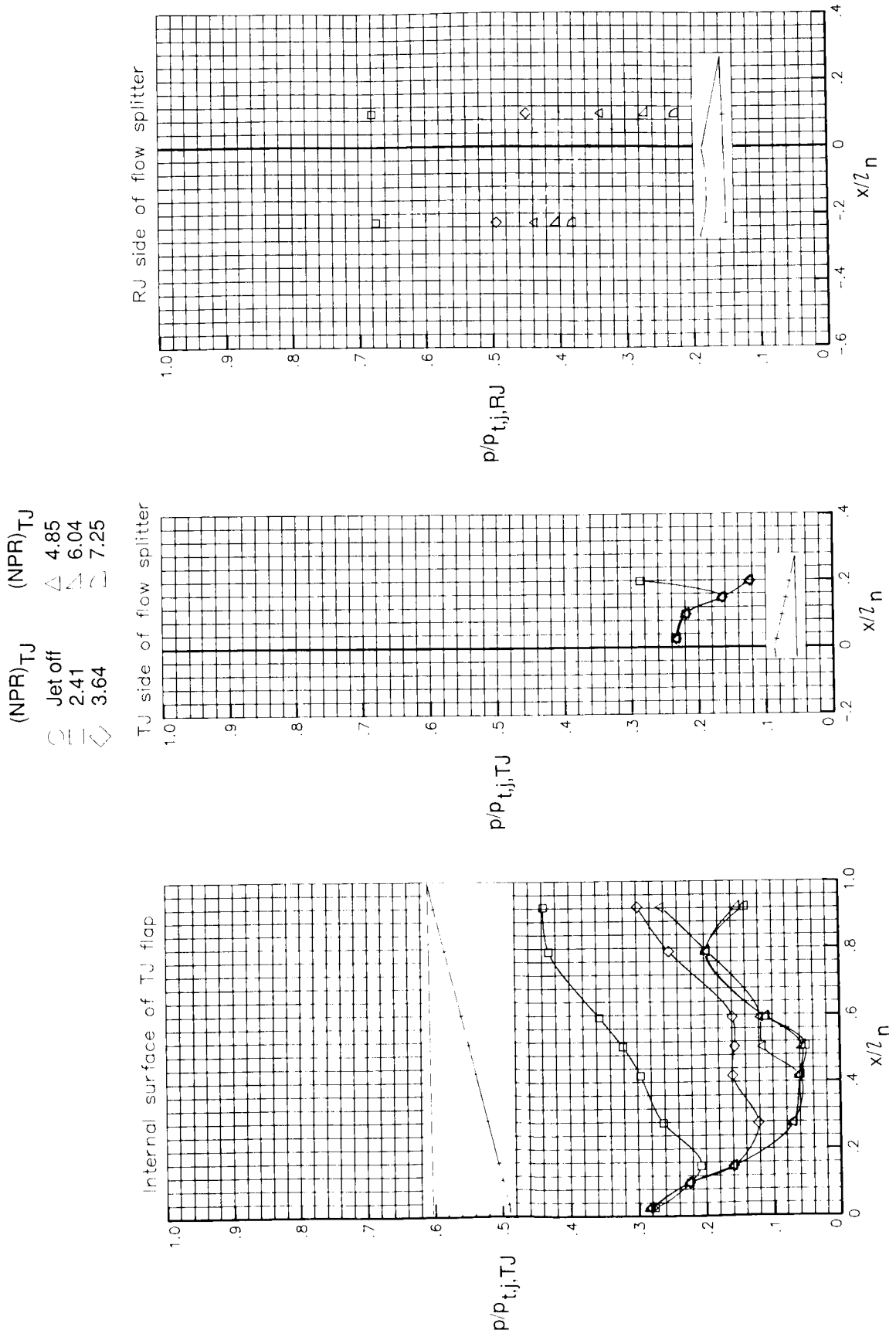
(a) Concluded.

Figure 35. Continued.

(b) $M = 0.60$.

Figure 35. Continued.
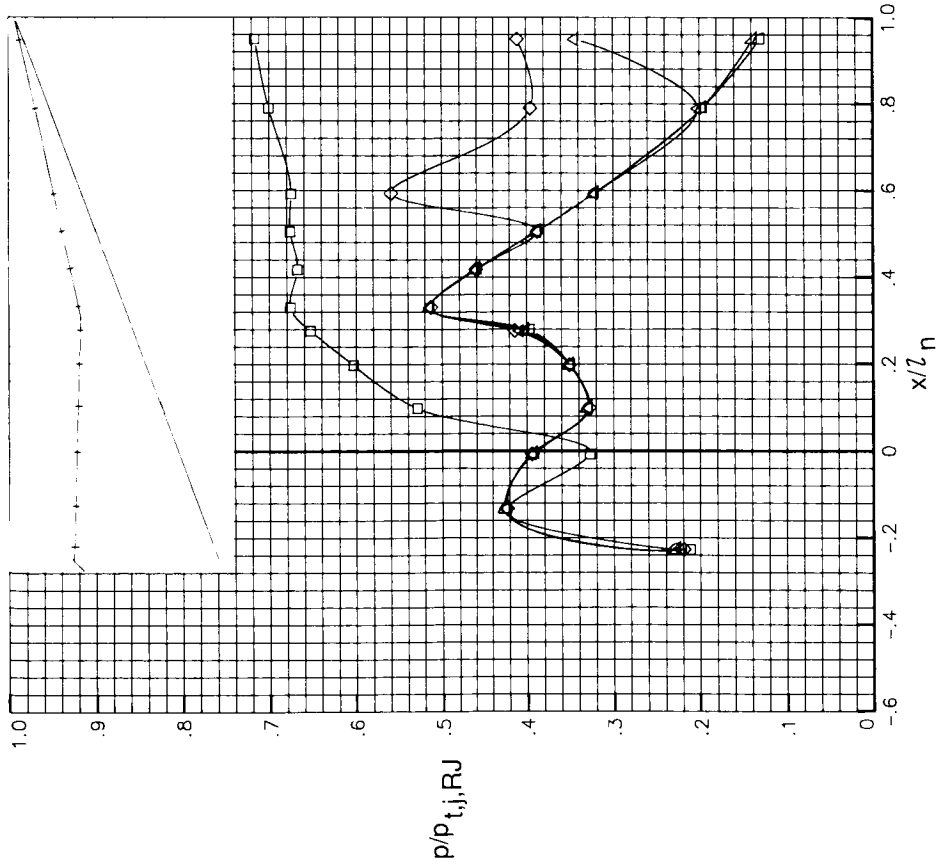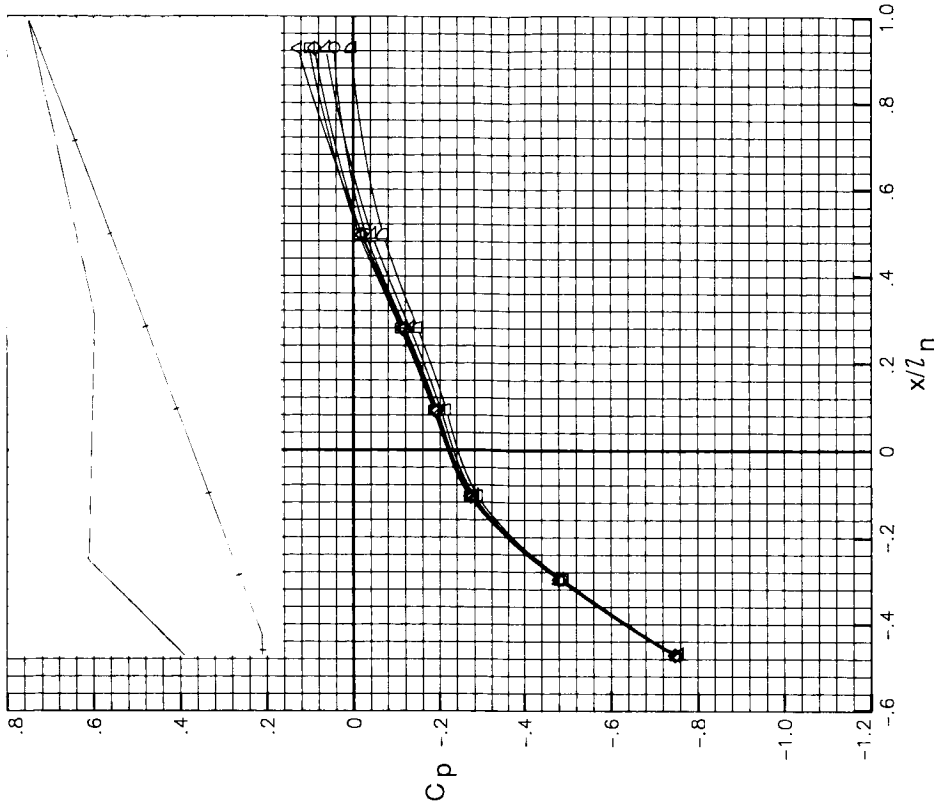
(b) Concluded.

Figure 35. Continued.
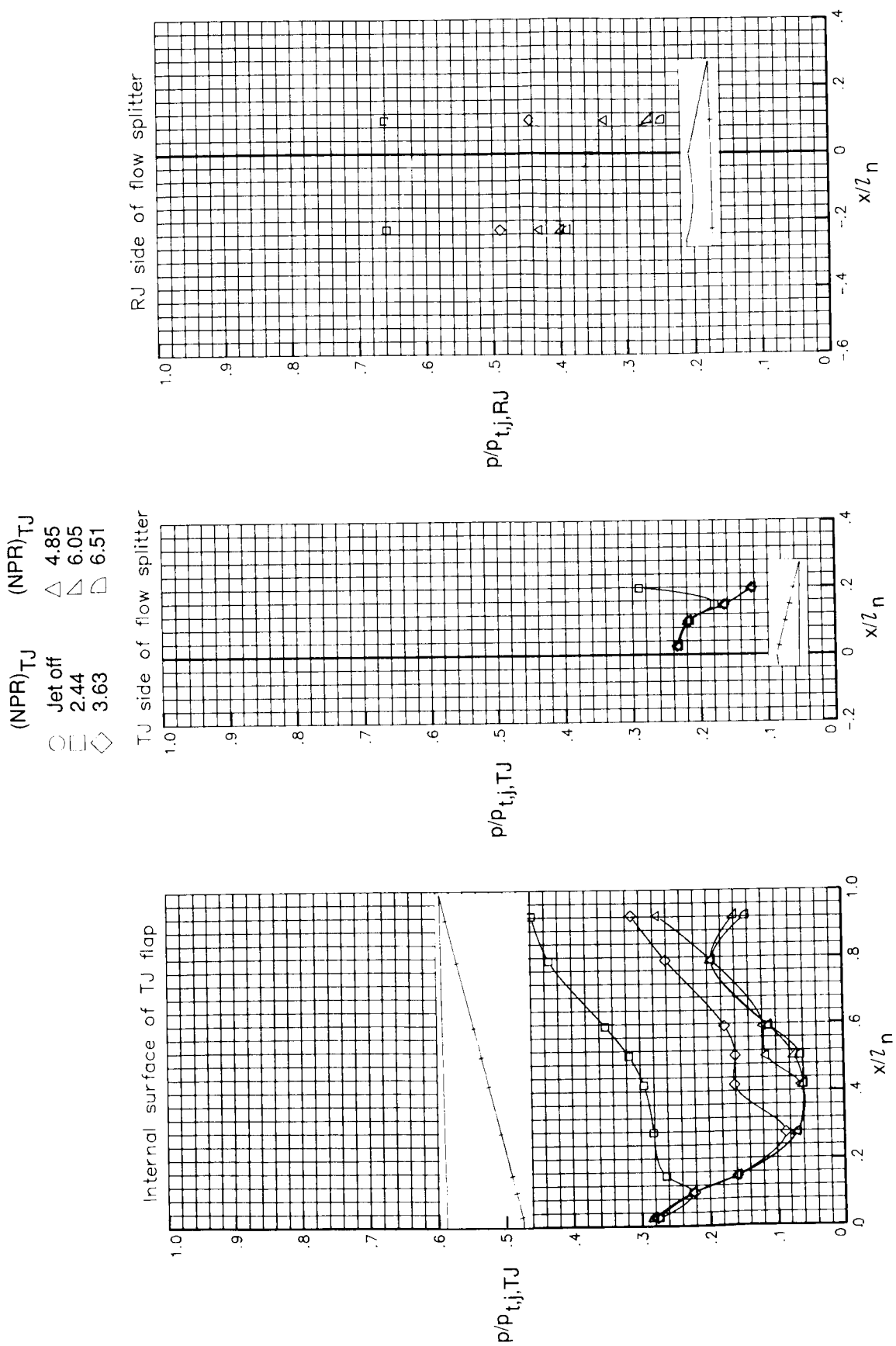
(c) $M = 0.90$.

Figure 35. Continued.
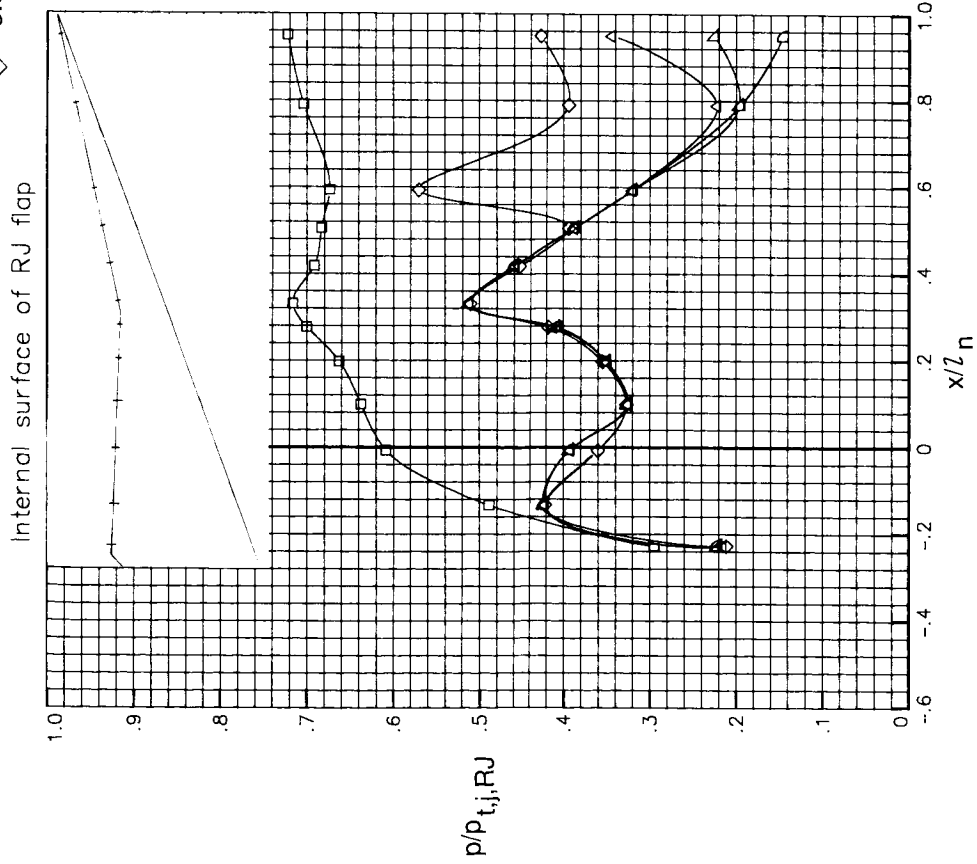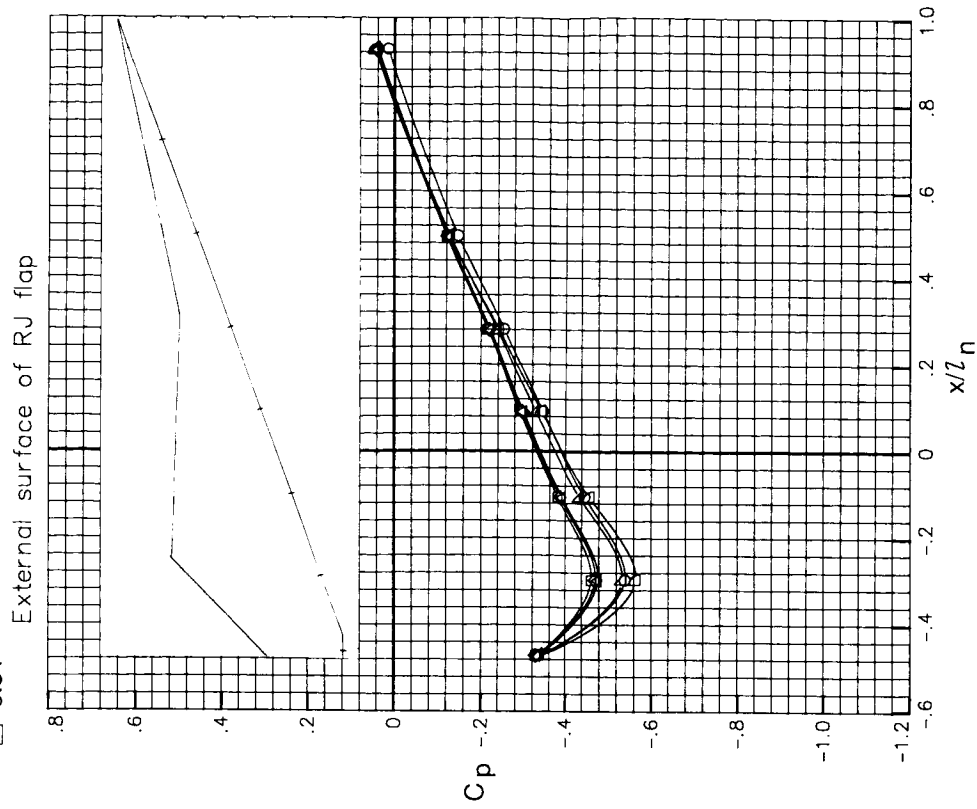
(c) Concluded.

Figure 35. Continued.

(d) $M = 1.20$.

Figure 35. Continued.

External surface of RJ flap

Internal surface of RJ flap

$(NPR)_{TJ}$

○ Jet off
□ 2.46
◇ 3.63
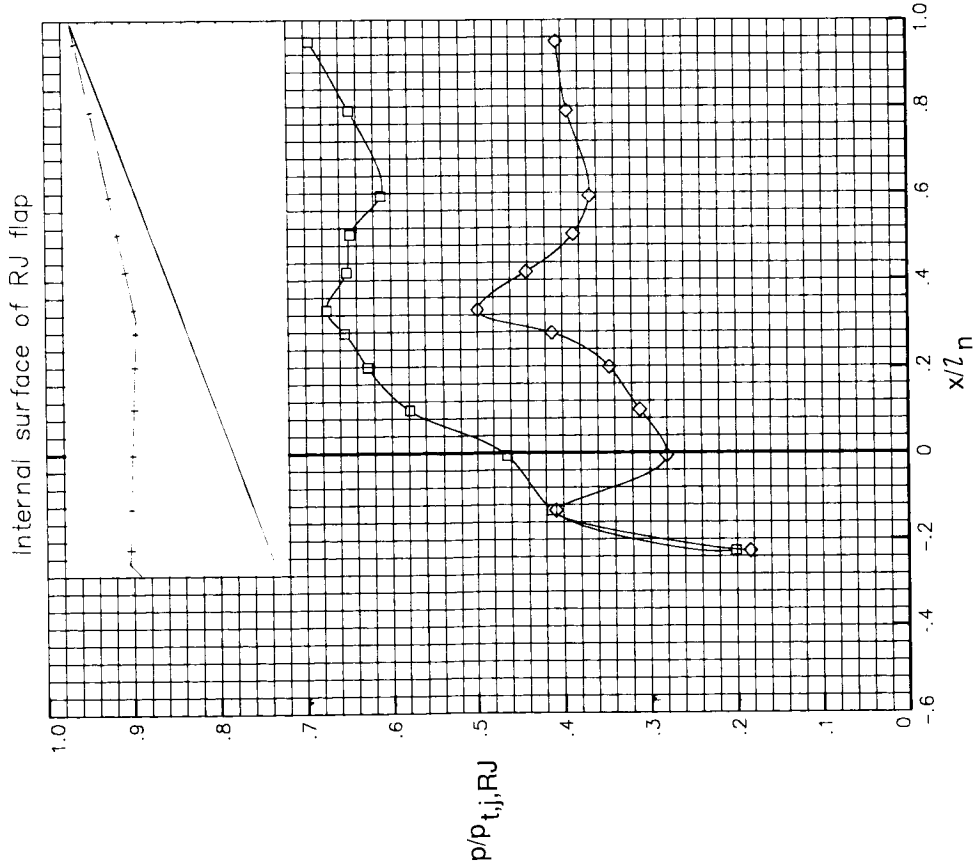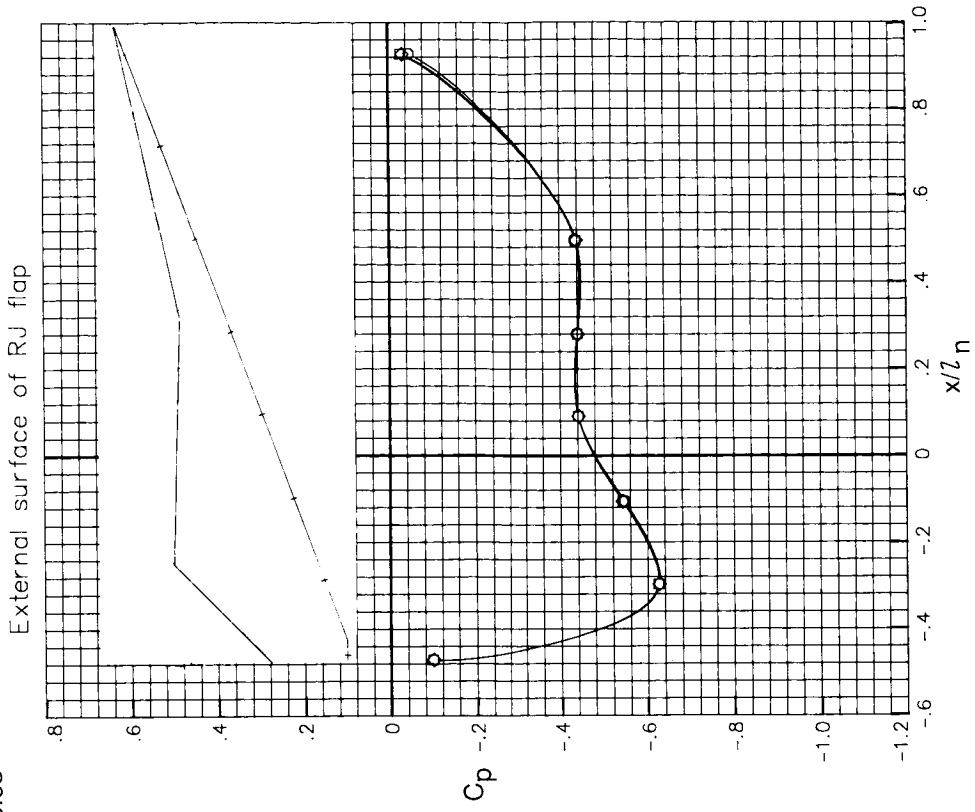
(d) Concluded.

Figure 35. Concluded.
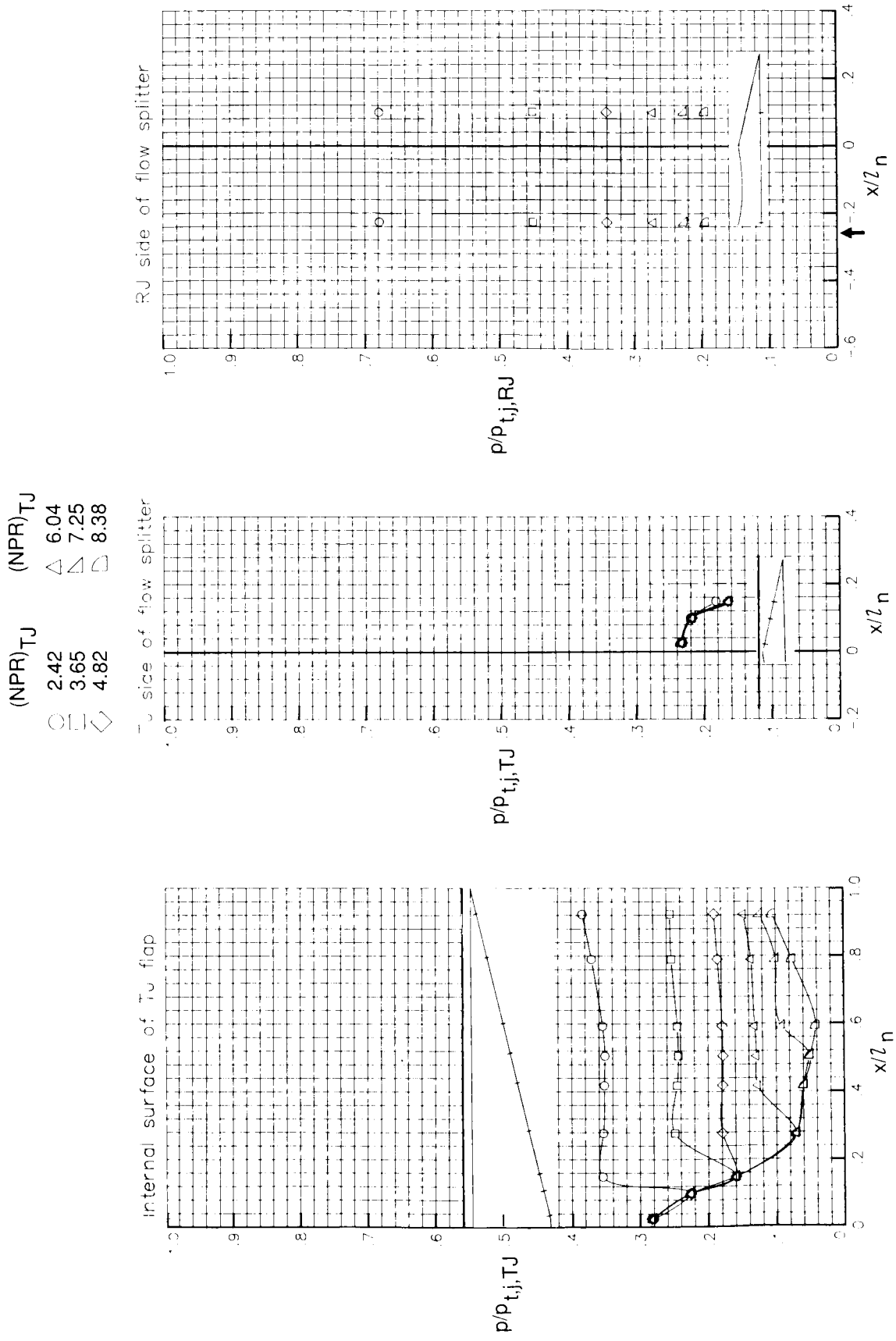
Figure 36. Pressure ratio and pressure coefficient distributions of CCN with minimum ramjet throat area, V-notch sidewalls, and ramjet flap 3.

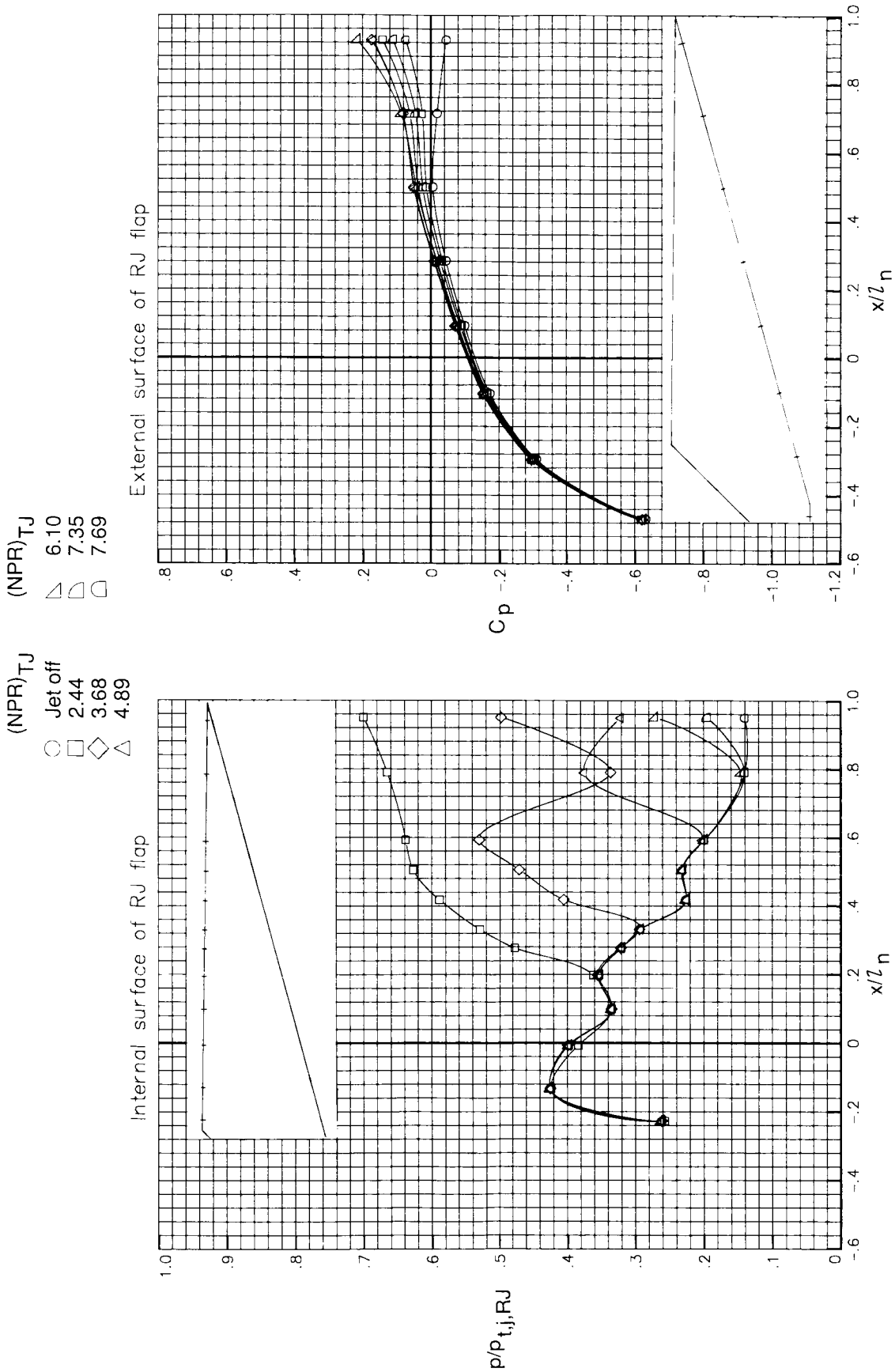(a) $M = 0$. Arrow indicates RJ throat location.
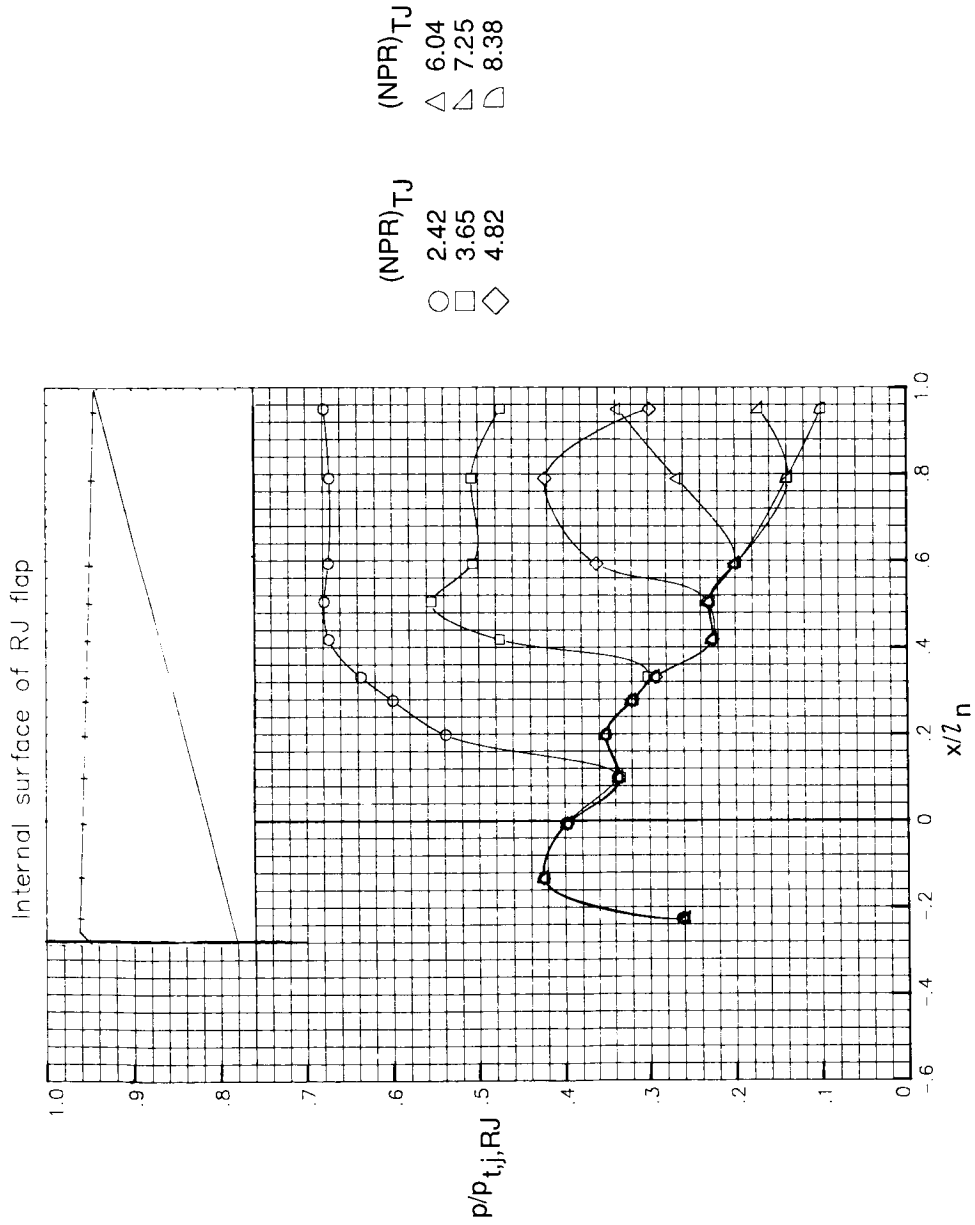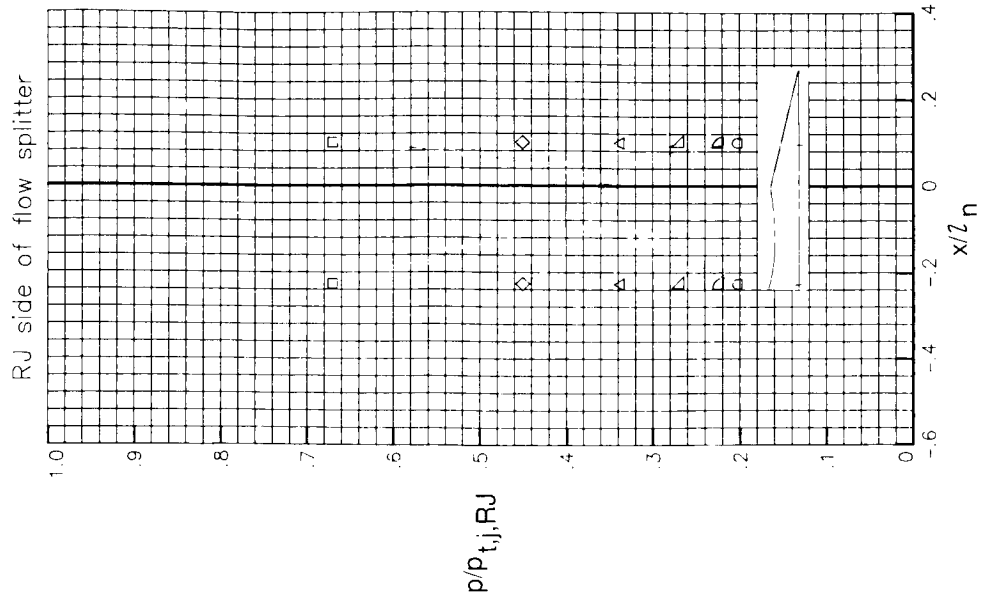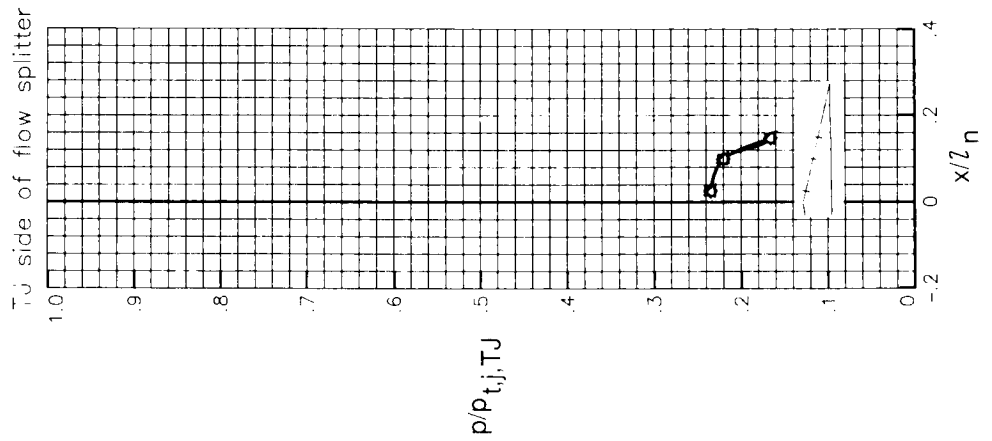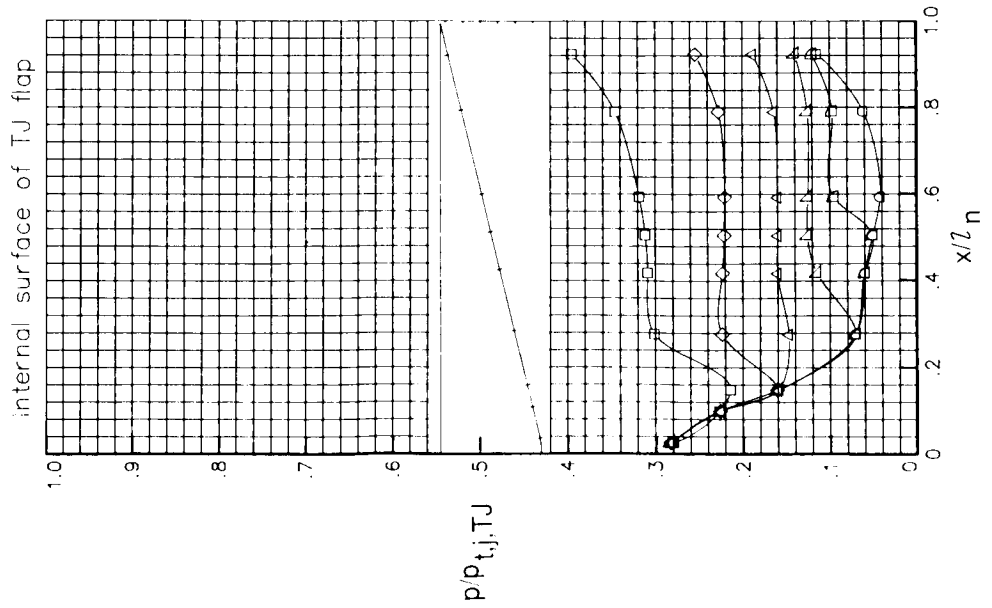
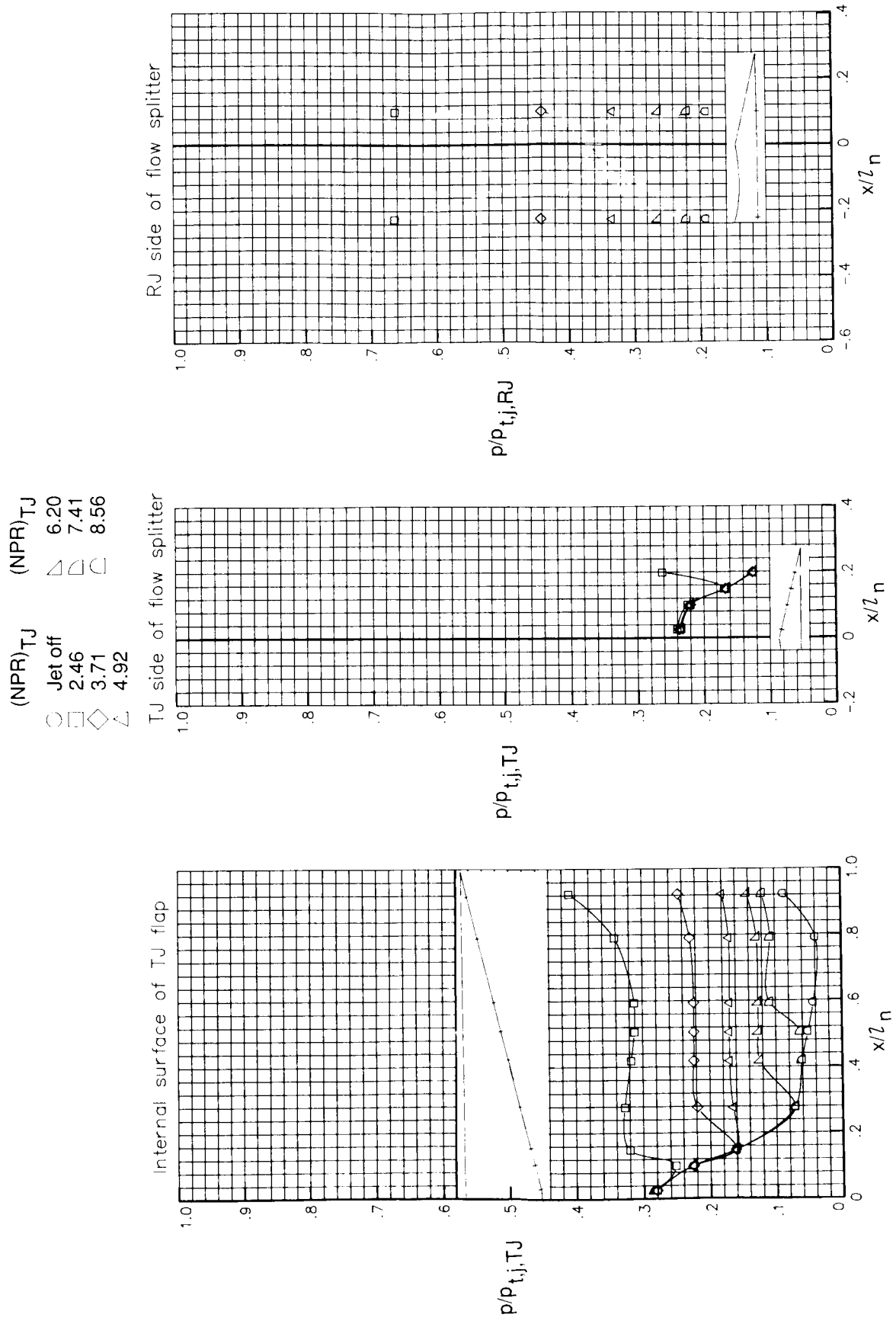(a) Concluded.

Figure 36. Continued.

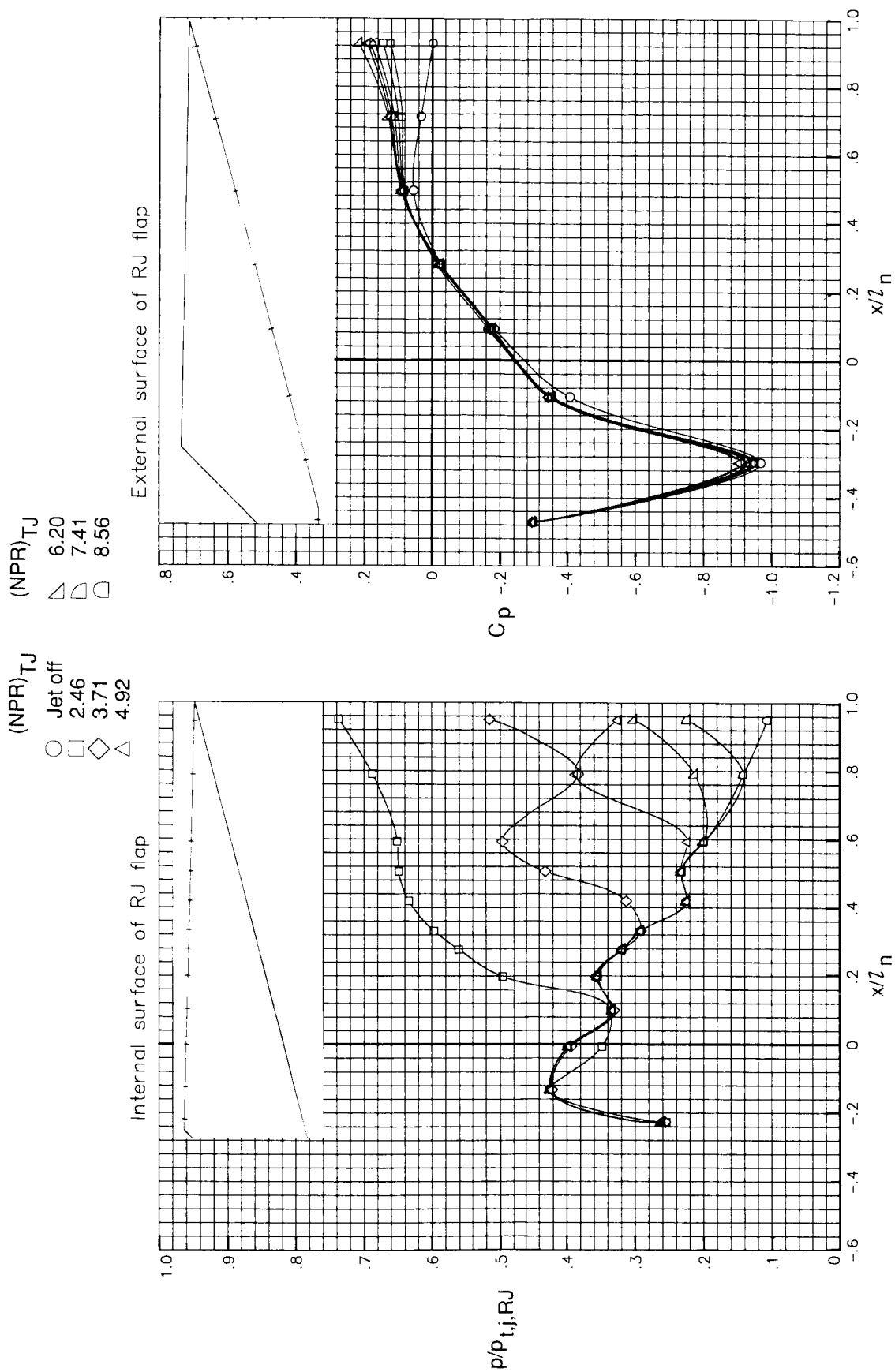(b) $M = 0.60$.

Figure 36. Continued.
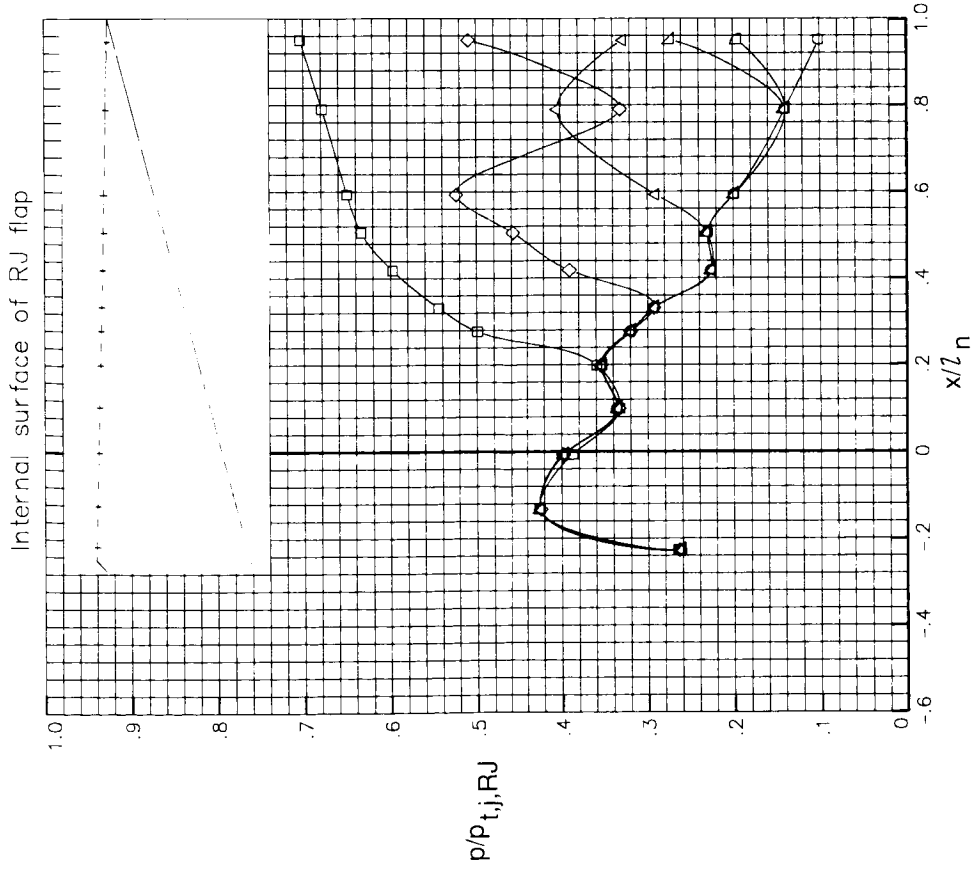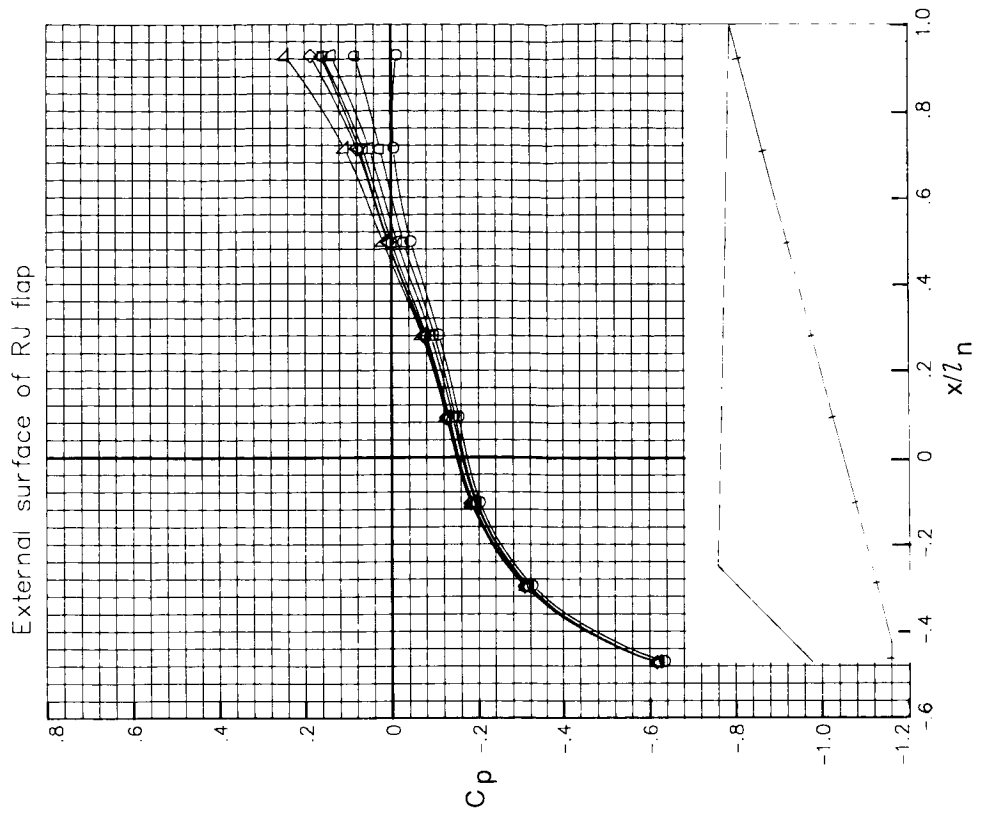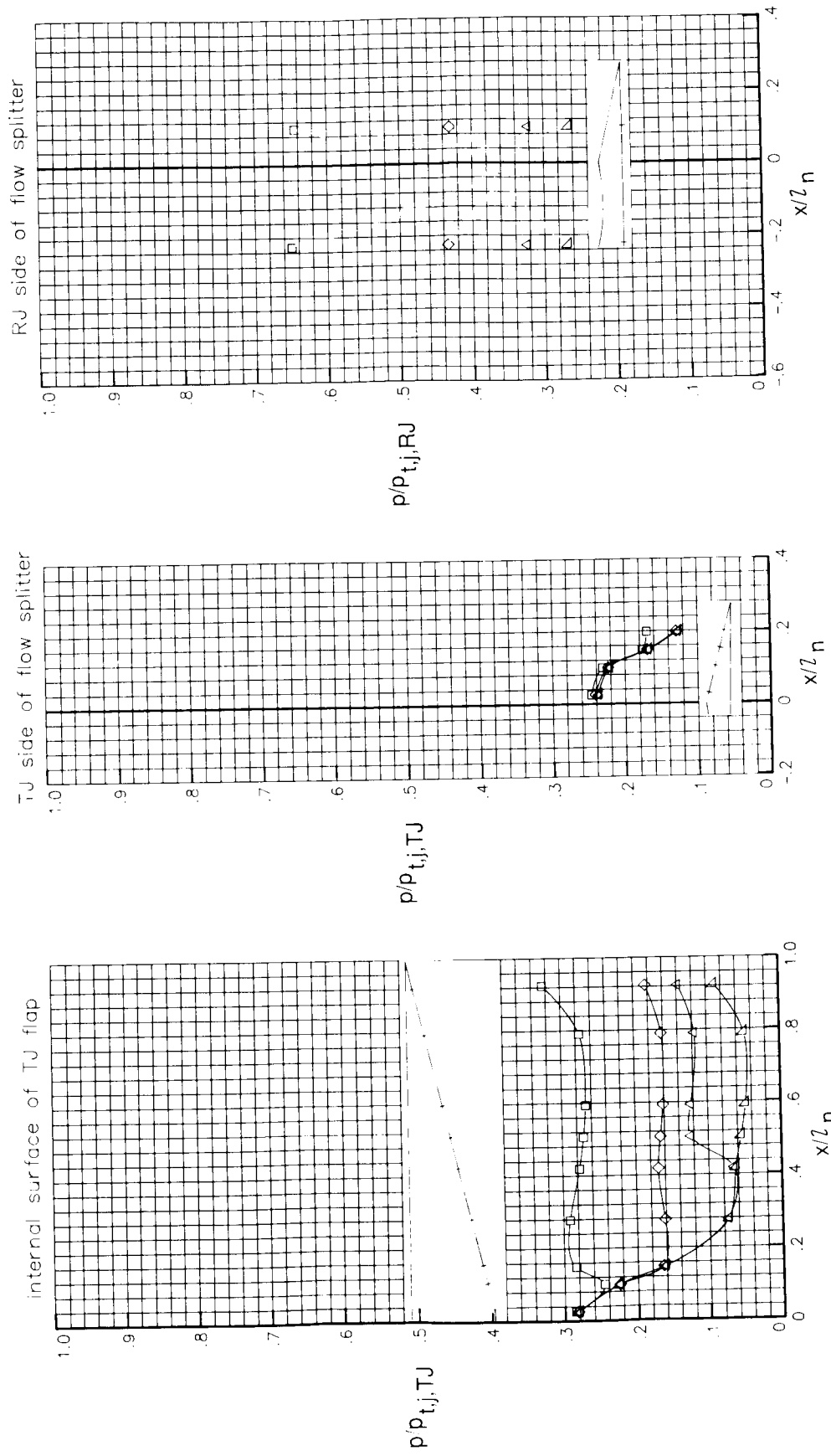
(b) Concluded.

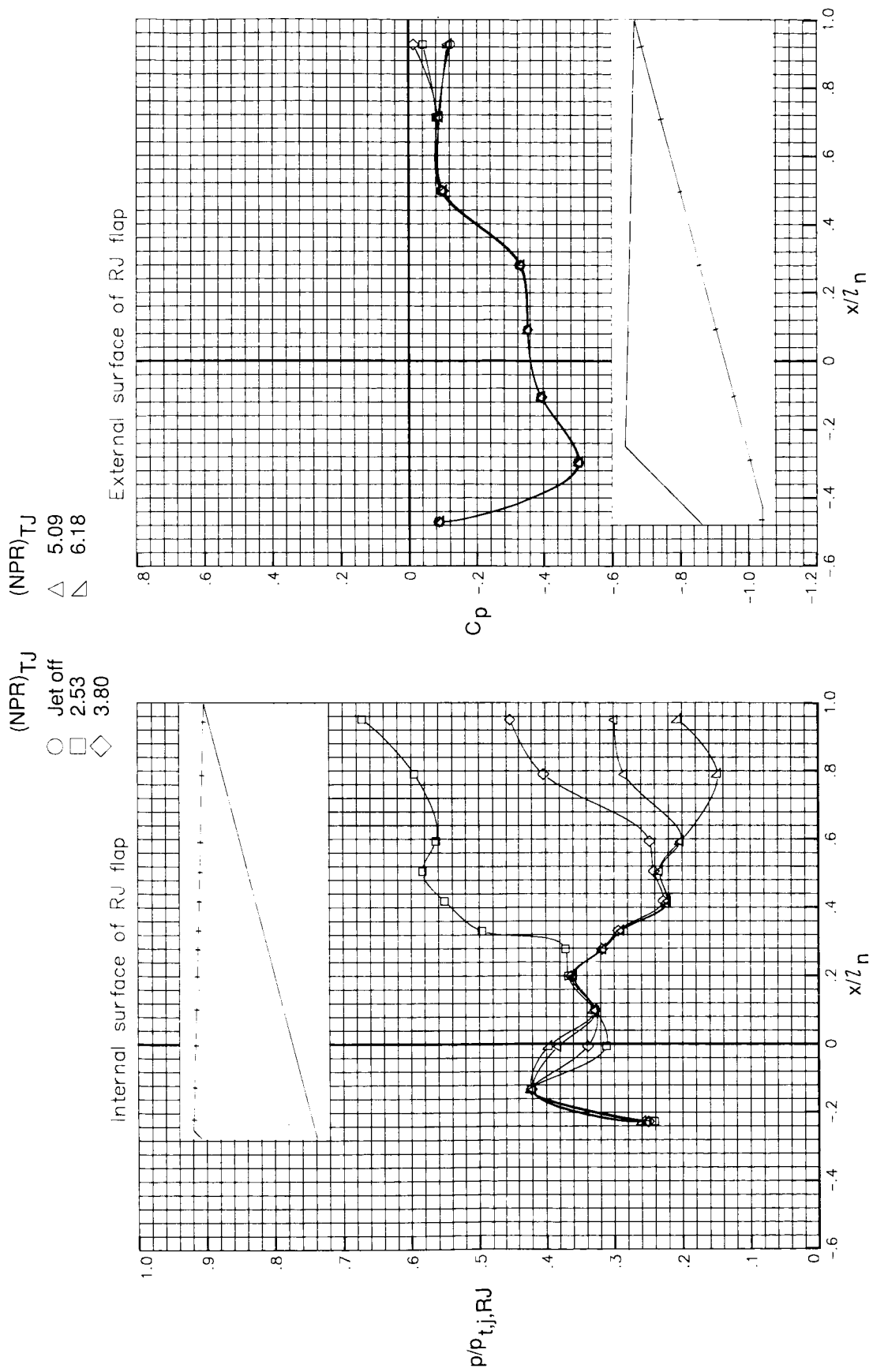Figure 36. Continued.

(c) $M = 0.90$.

Figure 36. Continued.
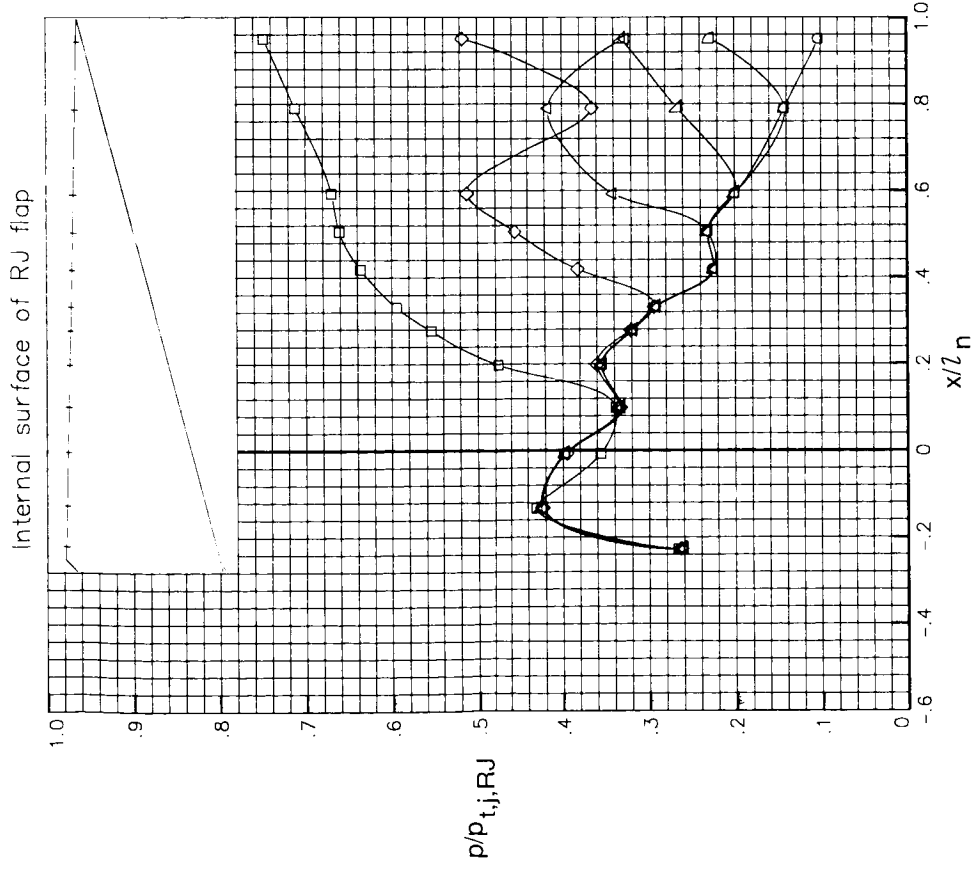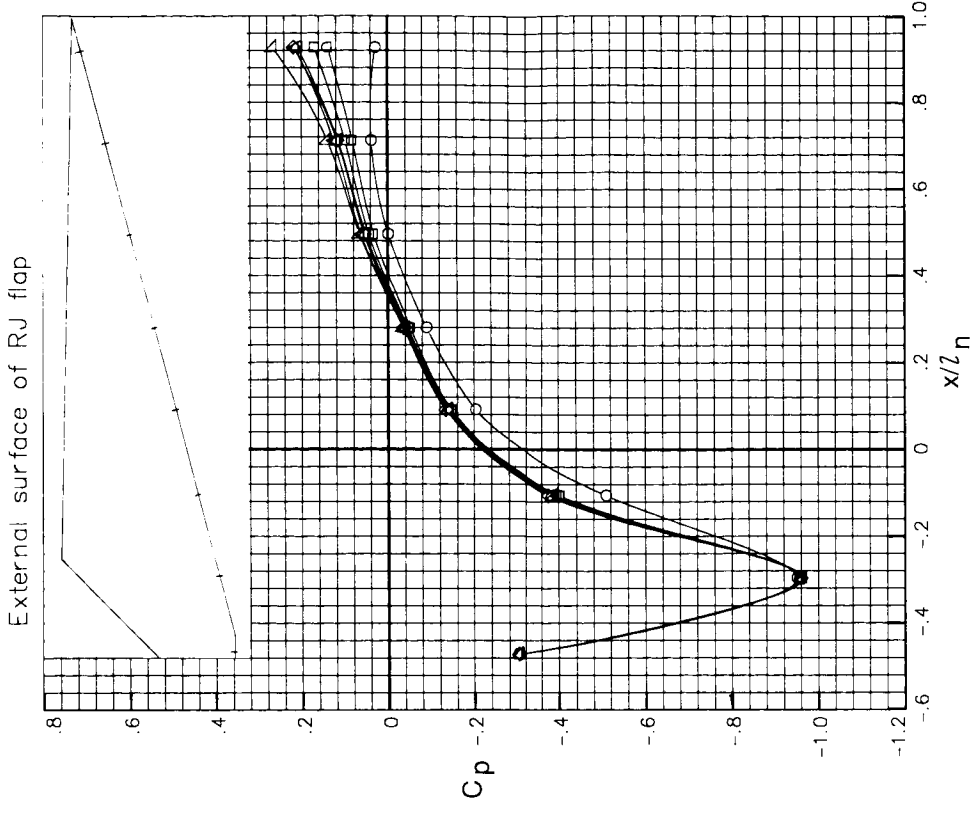
(c) Concluded.

Figure 36. Continued.
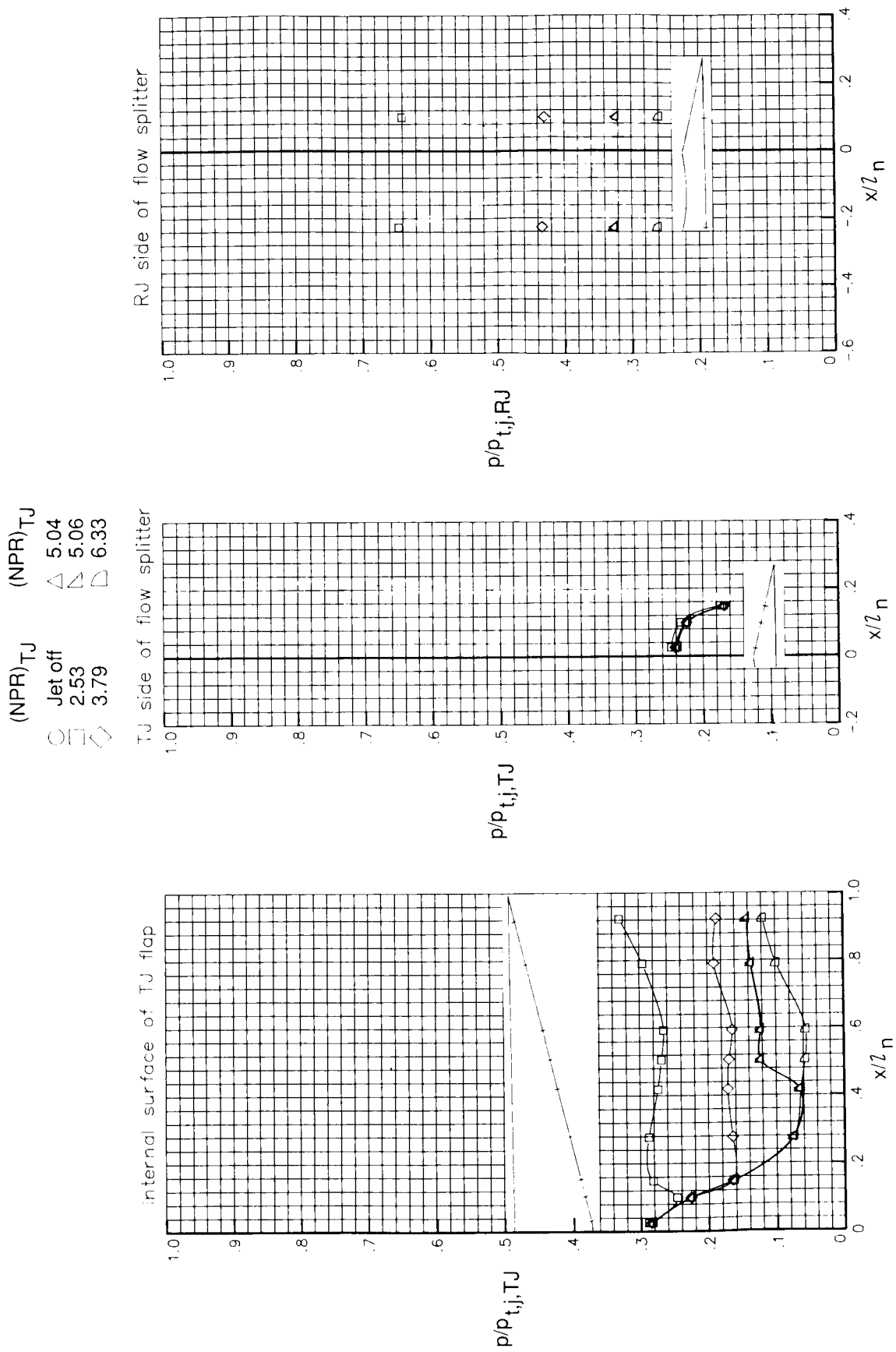
(d) $M = 1.20$.

Figure 36. Continued.
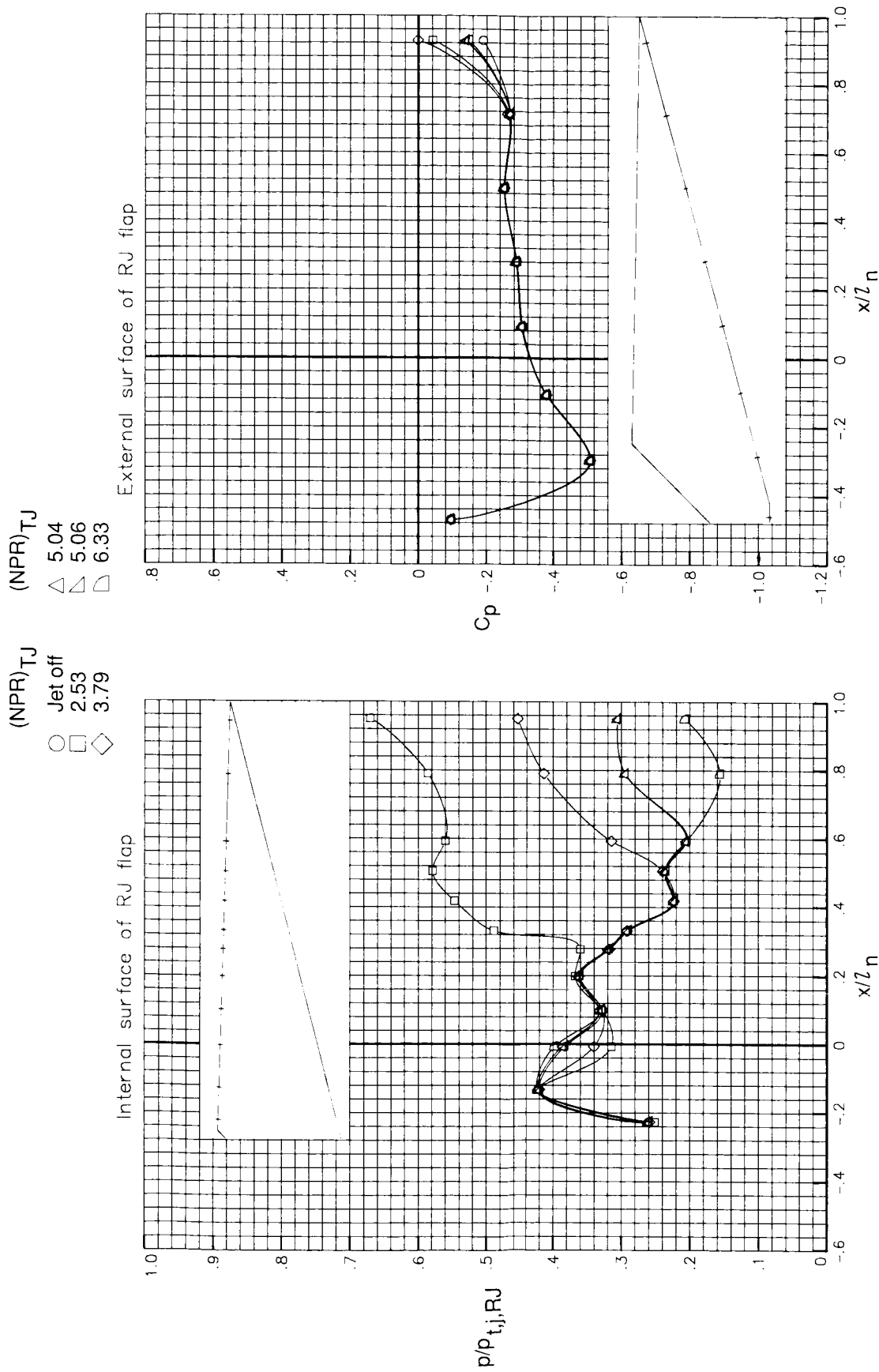
(d) Concluded.

Figure 36. Concluded.
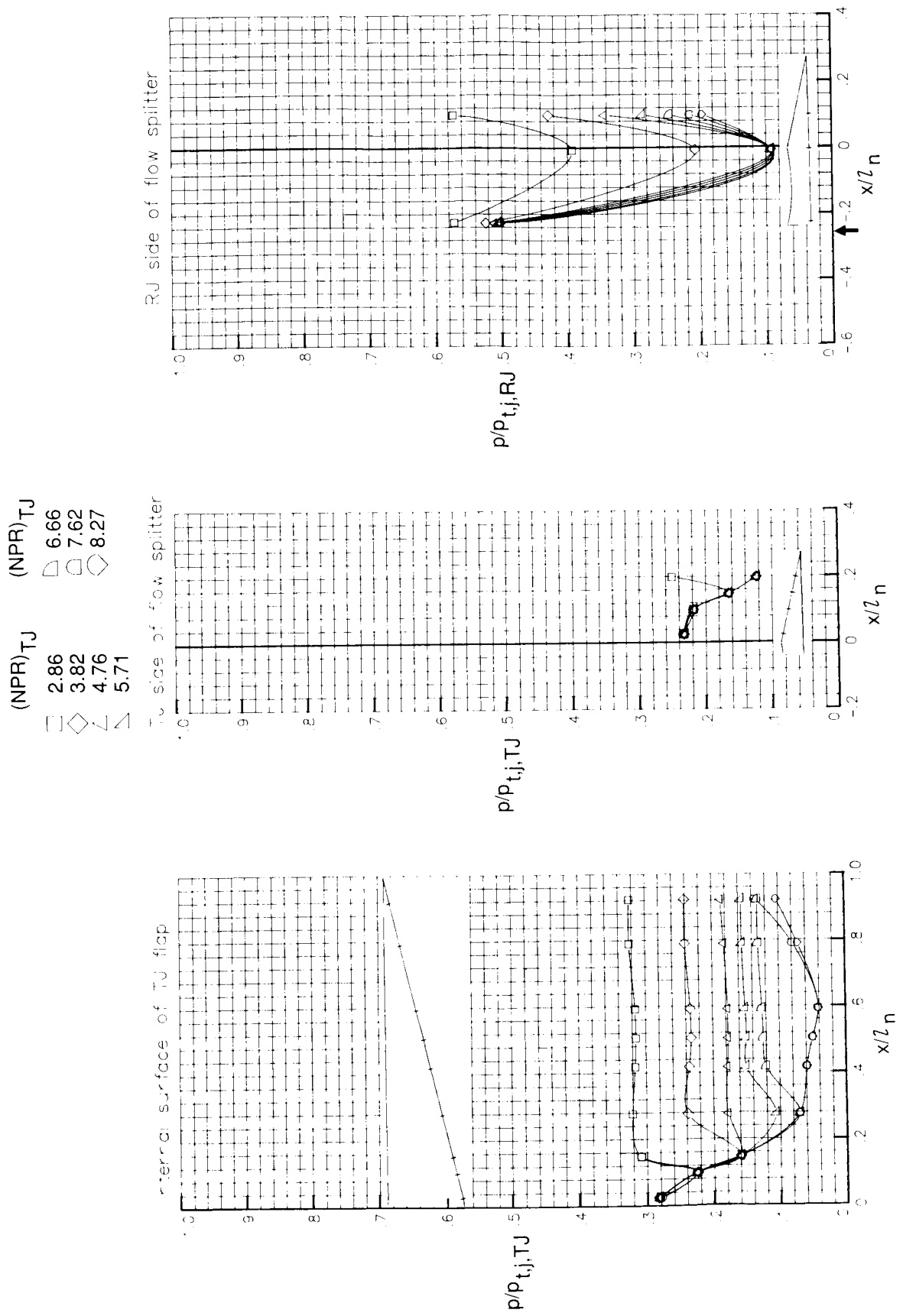
(a) $M = 0$. Arrow indicates RJ throat location.

Figure 37. Pressure ratio and pressure coefficient distributions of CCN with minimum ramjet throat area, cutback sidewalls. and ramjet flap 1.

(a) Concluded.

Figure 37. Continued.

RJ side of flow splitter

x/l_n

$p/p_{t,j,RJ}$

TJ side of flow splitter

x/l_n

$p/p_{t,j,TJ}$

$(NPR)_{TJ}$		$(NPR)_{TJ}$	
	Jet off		5.74
	2.87		6.69
	3.82		10.11
	4.77		

nternal surface of TJ flap

x/l_n

$p/p_{t,j,TJ}$
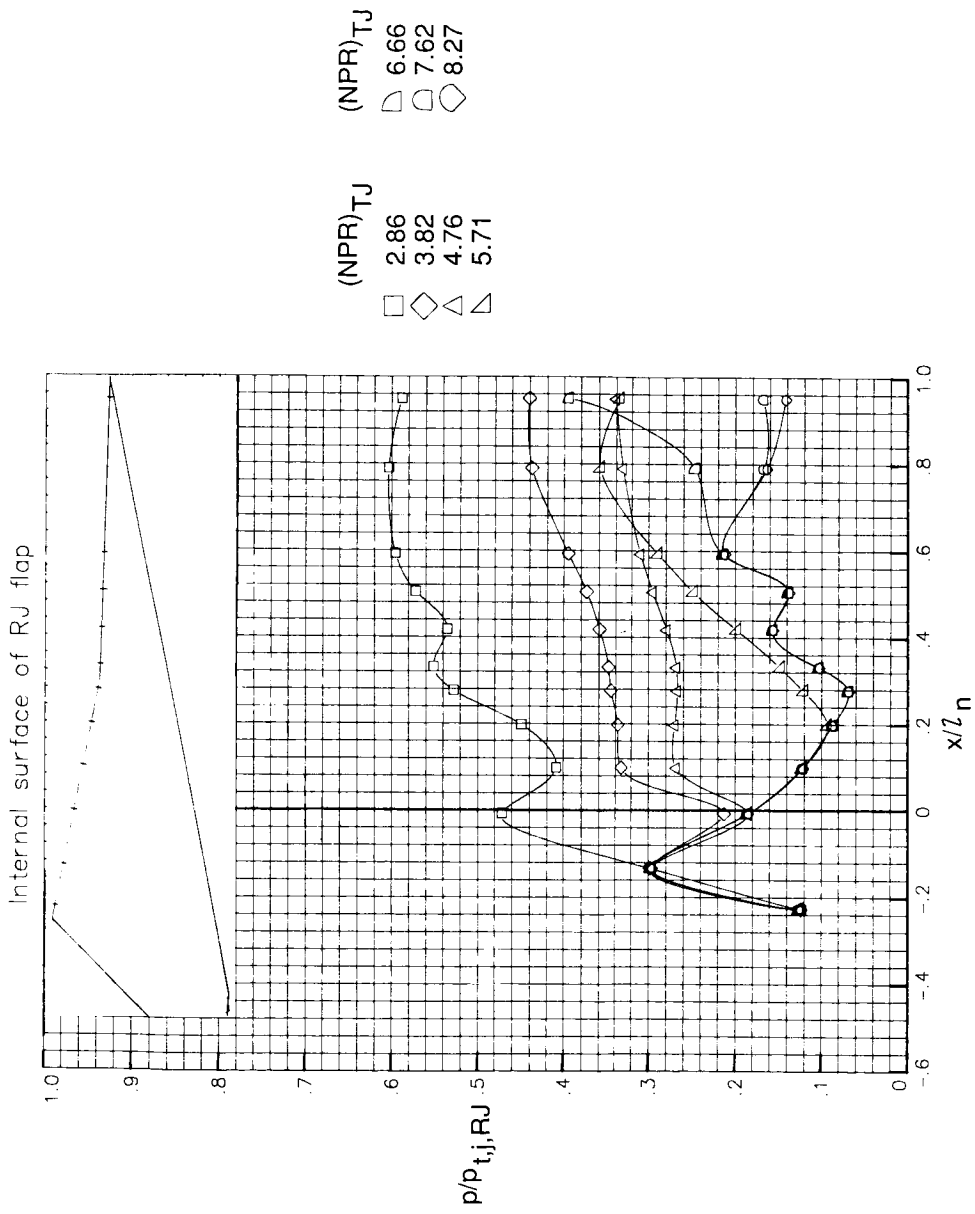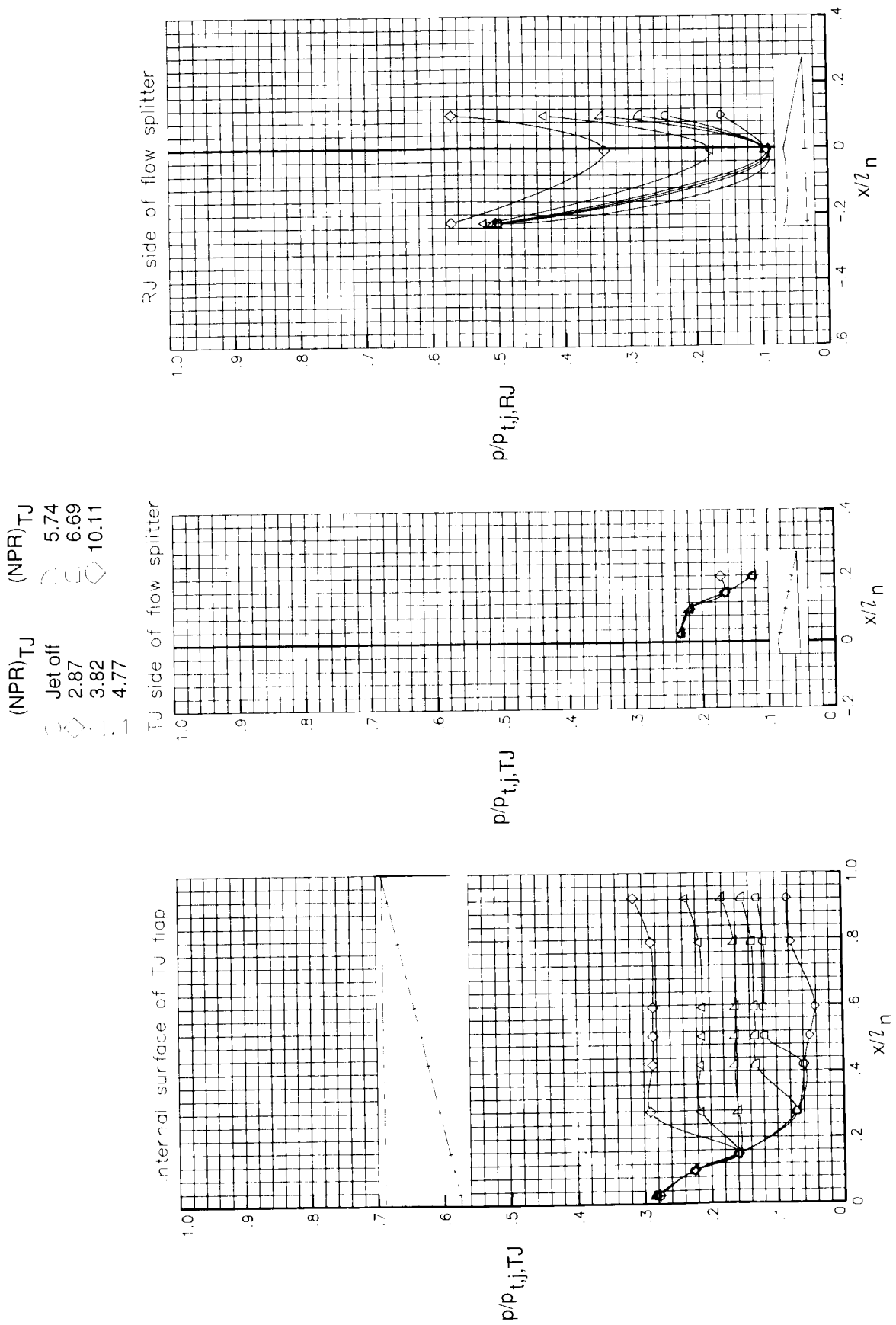
(b) $M = 0.60$.
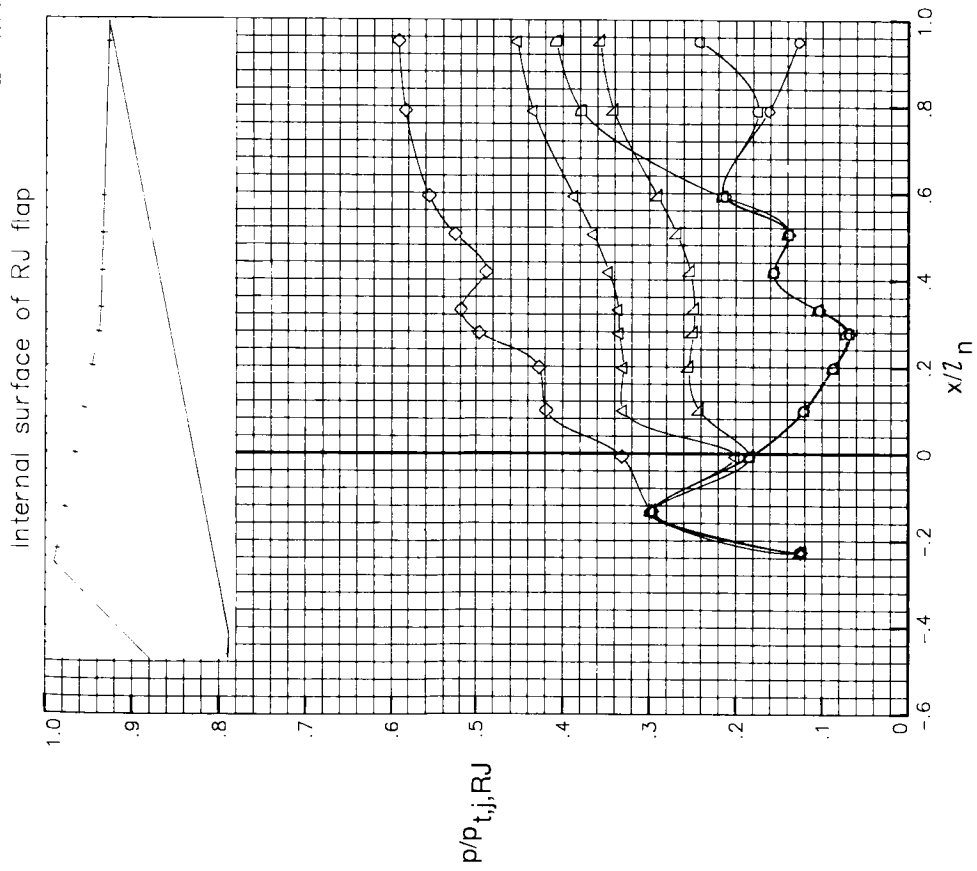
Figure 37. Continued.
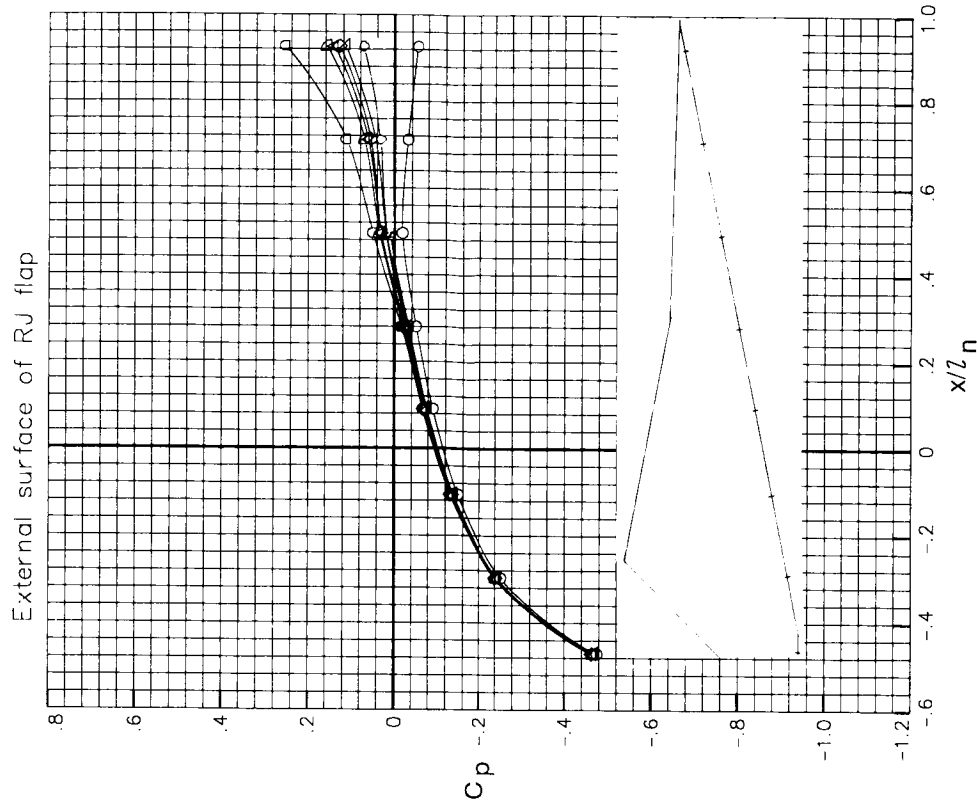
(b) Concluded.

Figure 37. Continued.

(c) $M = 0.90$.

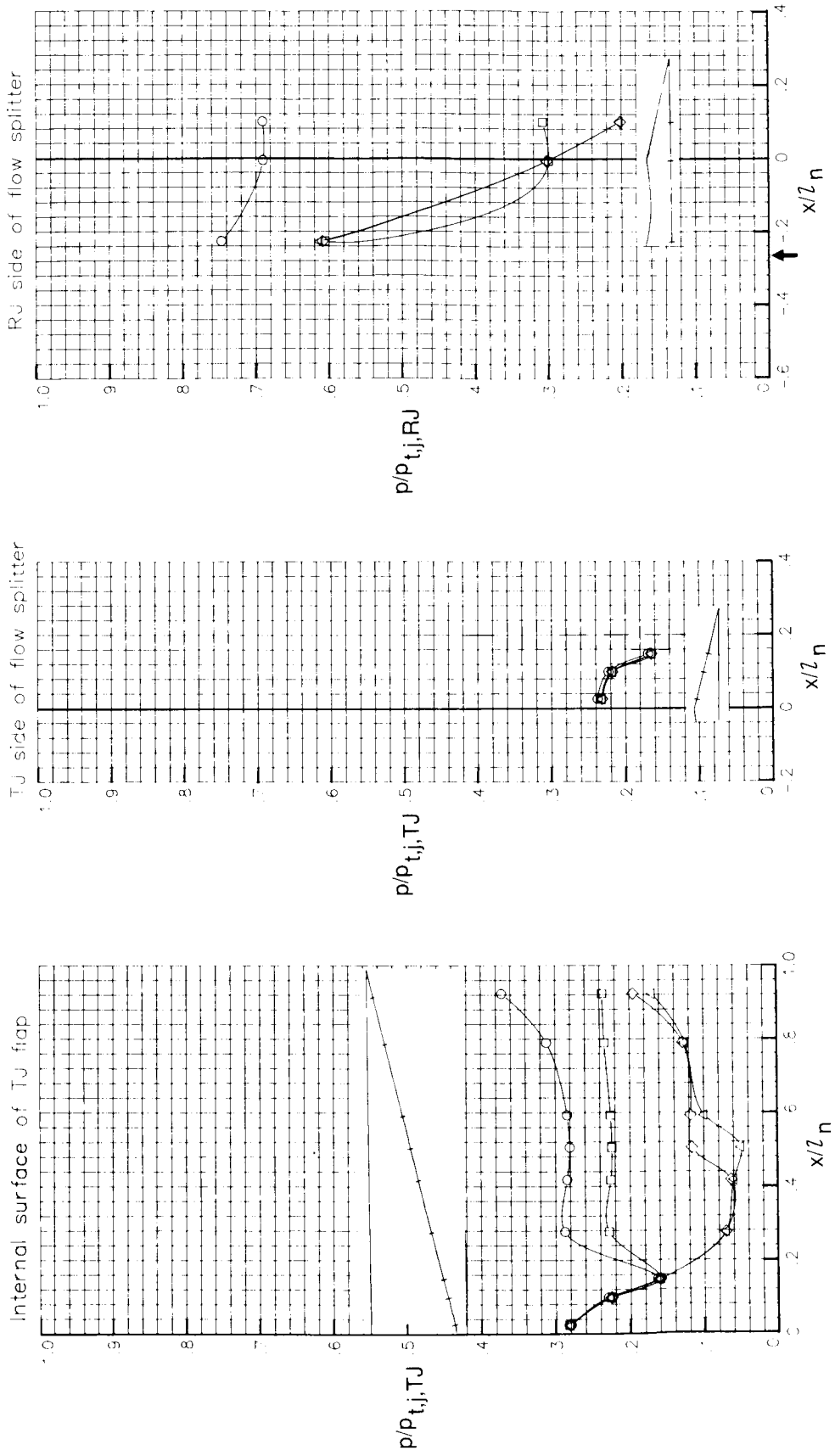Figure 37. Continued.
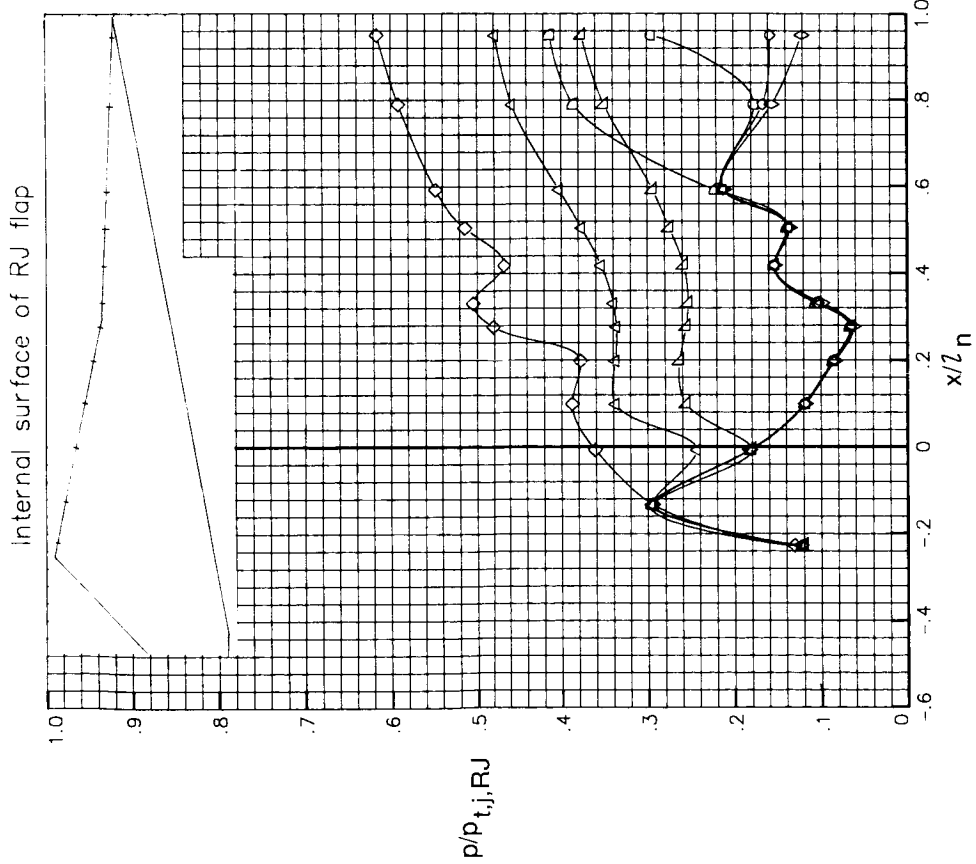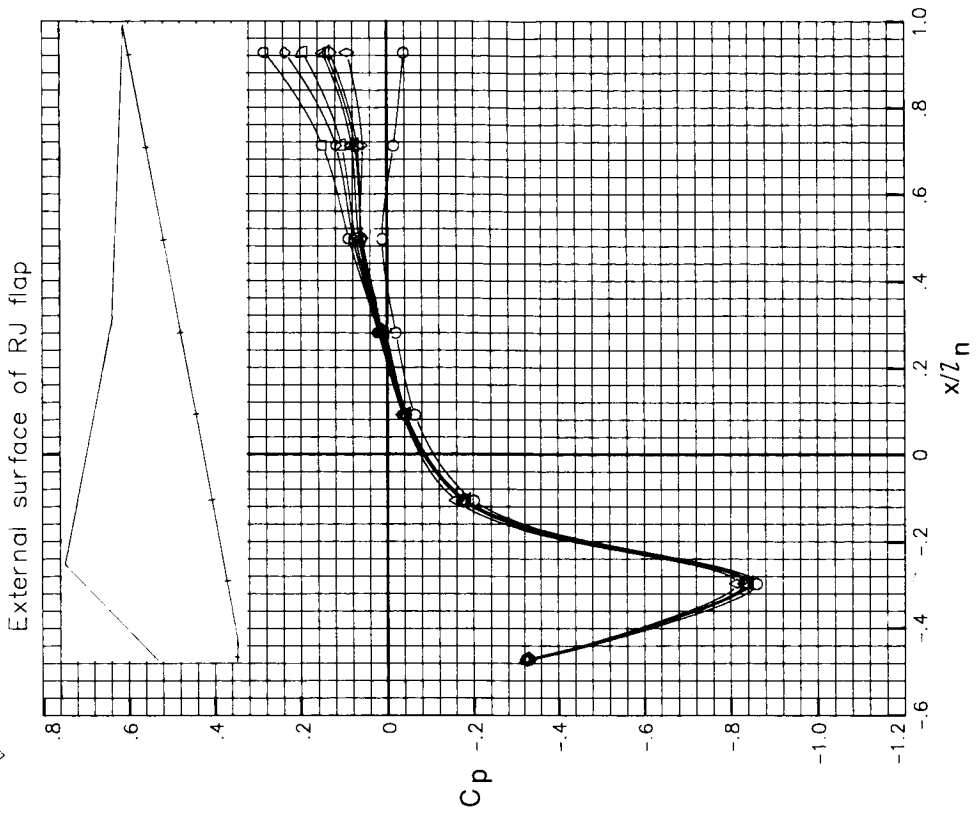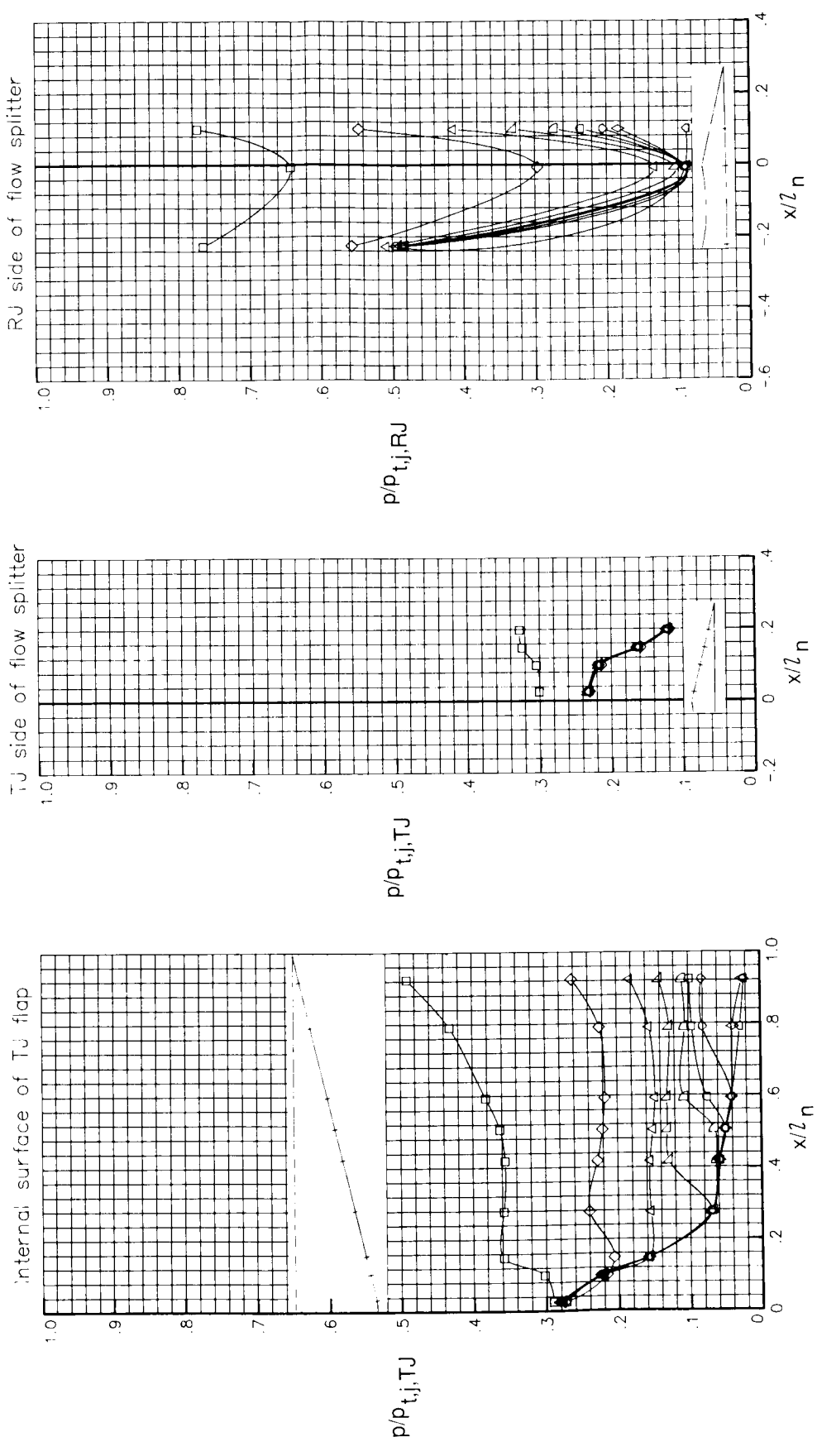
(c) Concluded.

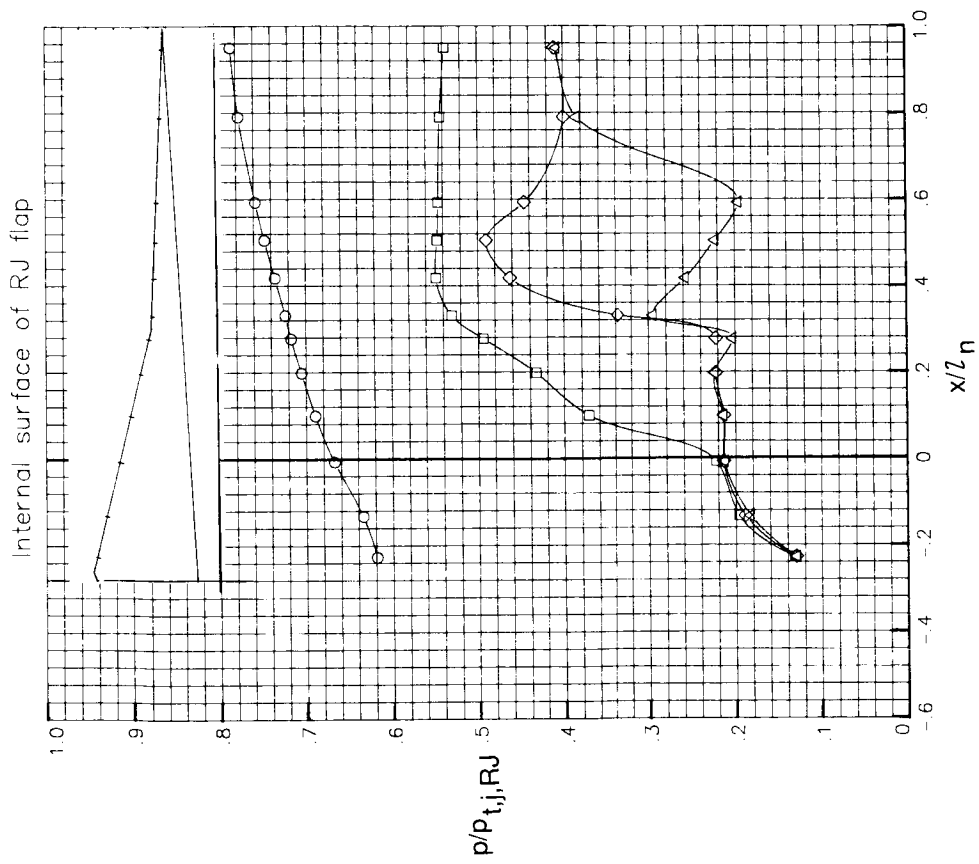Figure 37. Continued.

(d) $M = 1.20$.

Figure 37. Continued.

(d) Concluded.

Figure 37. Concluded.
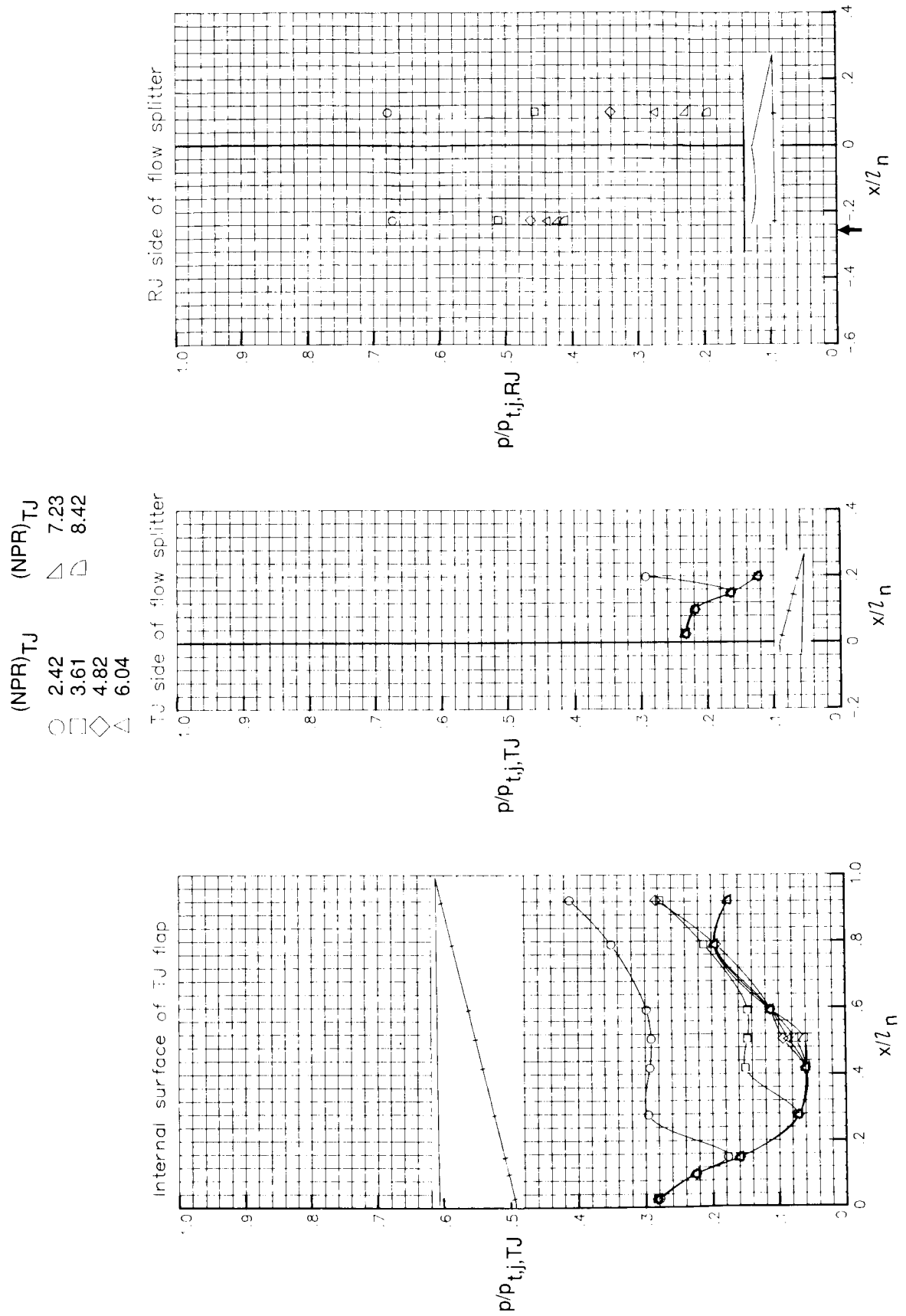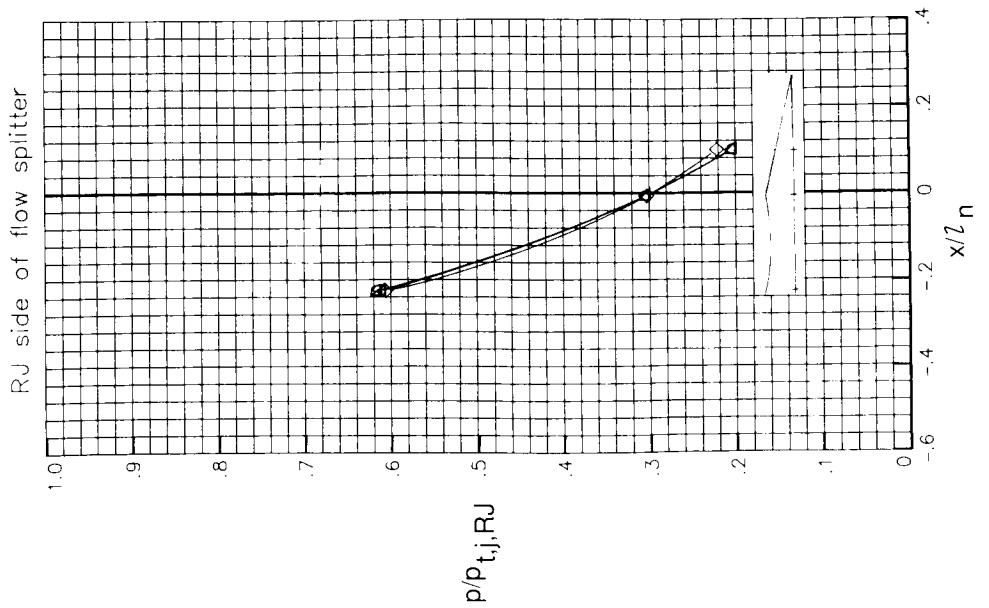
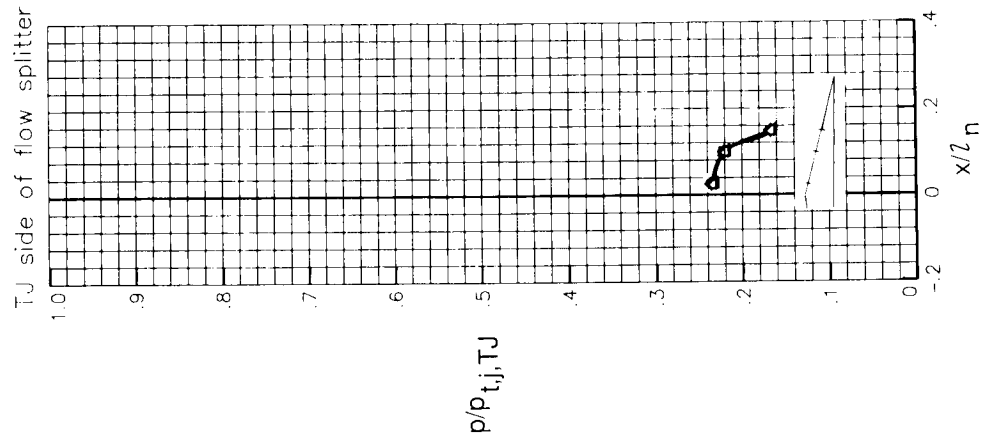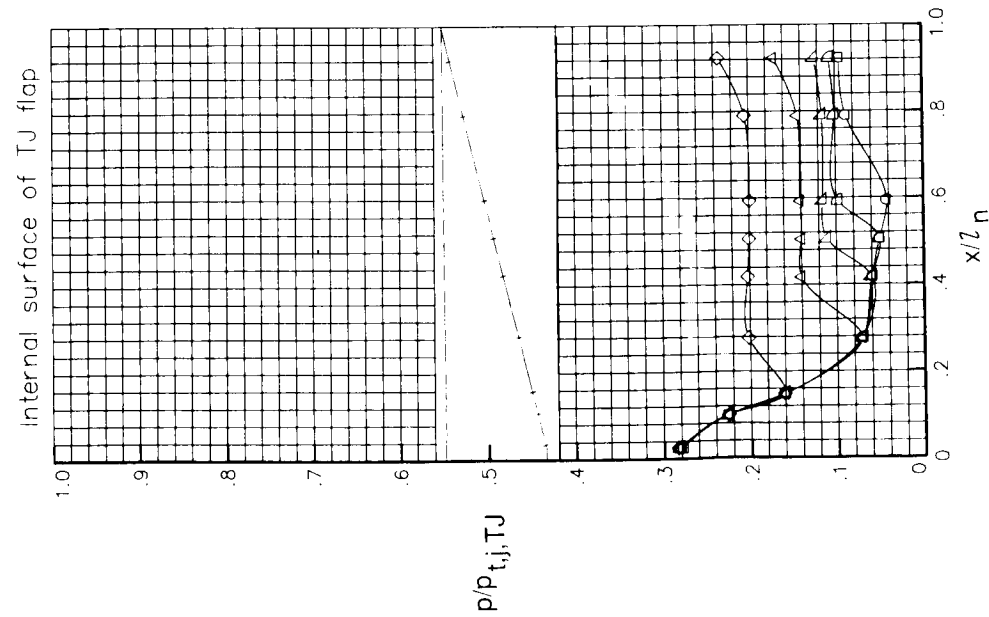(a) $M = 0$. Arrow indicates RJ throat location.

Figure 38. Pressure ratio and pressure coefficient distributions of CCN with minimum ramjet throat area, cutback sidewalls. and ramjet flap 2.
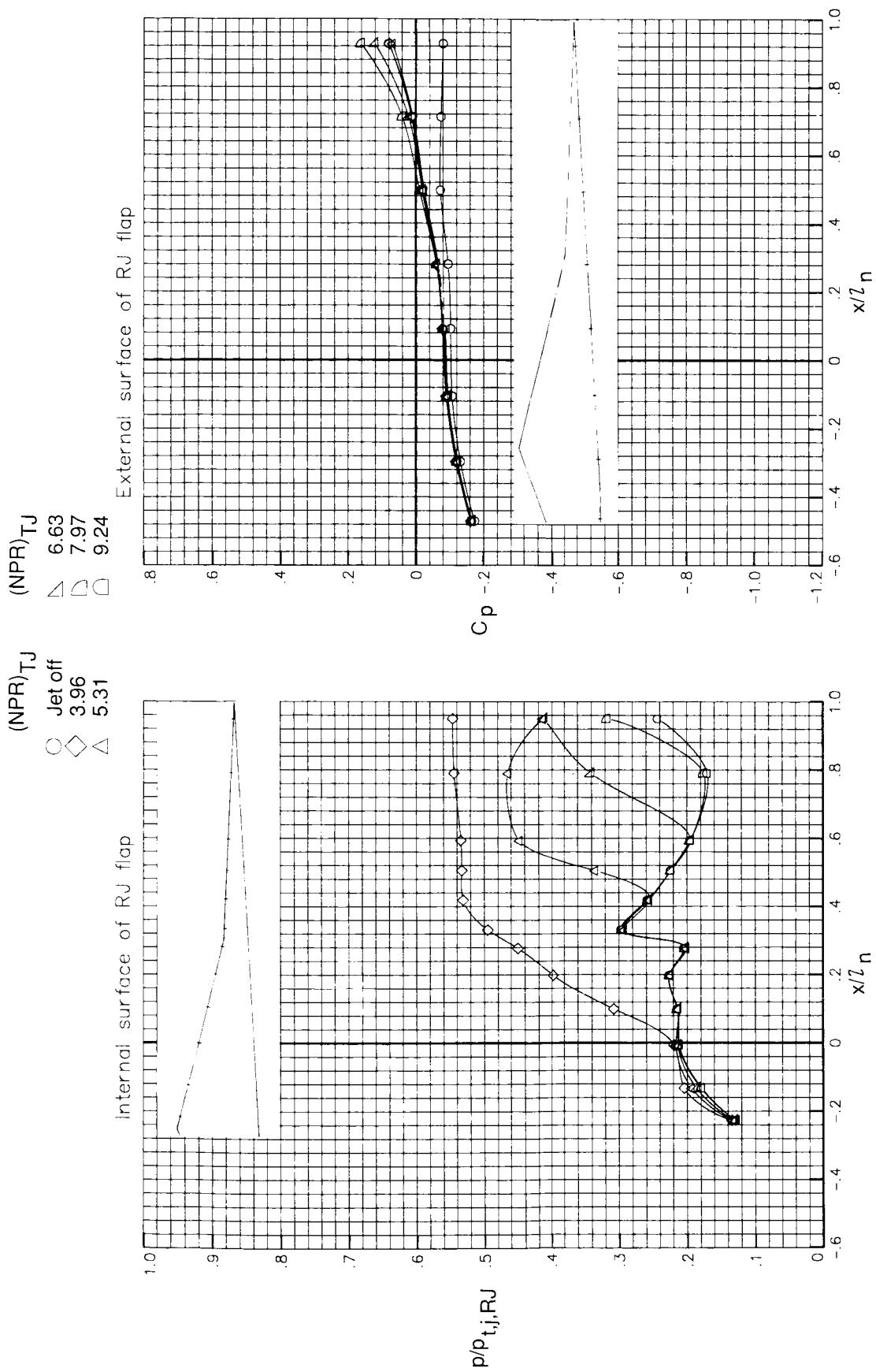
(a) Concluded.

Figure 38. Continued.

(b) $M = 0.60$.

Figure 38. Continued.

(NPR)$_{TJ}$

○ Jet off
□ 2.43
◇ 3.62
△ 4.84
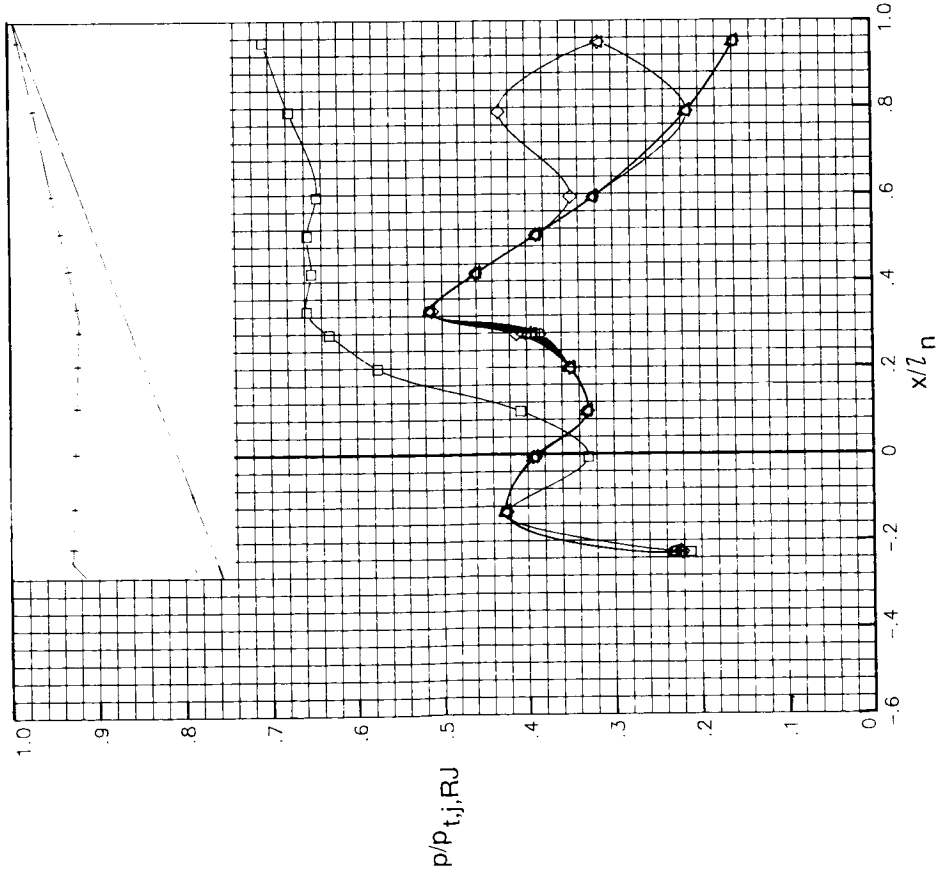
(NPR)$_{TJ}$

△ 6.04
◁ 7.25
◻ 8.49
◇ 9.86

Internal surface of RJ flap

External surface of RJ flap

(b) Concluded.

Figure 38. Continued.

123

RJ side of flow splitter

$p/p_{t,j,RJ}$

x/l_n

TJ side of flow splitter

$p/p_{t,j,TJ}$

x/l_n

internal surface of TJ flap

$p/p_{t,j,TJ}$

x/l_n
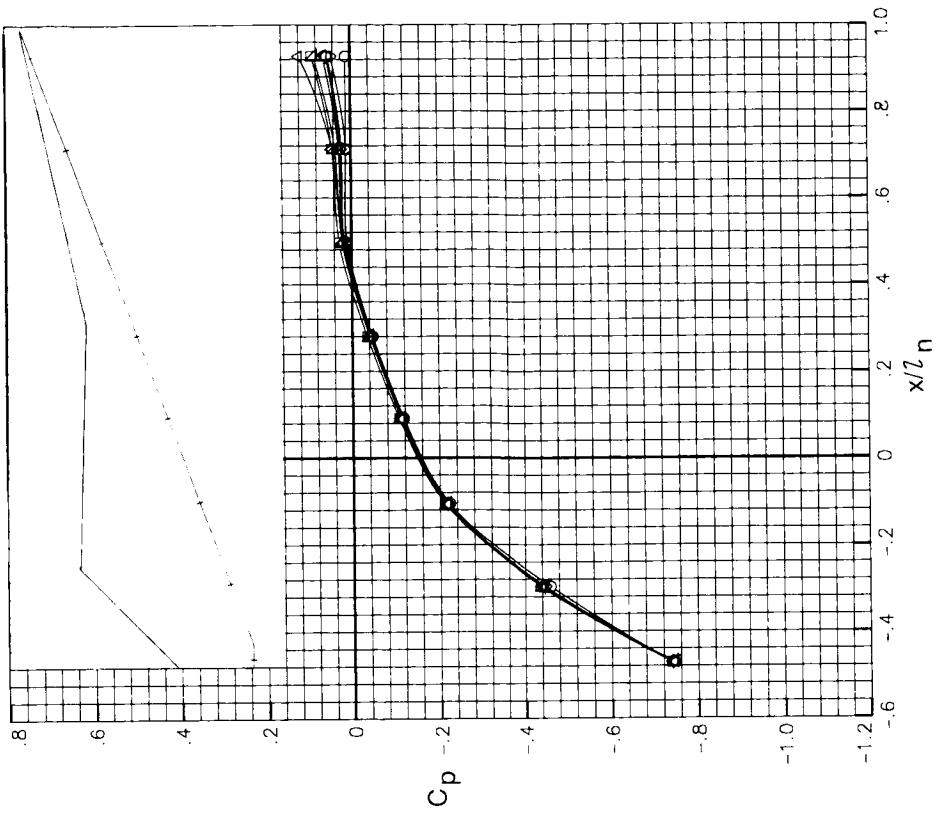
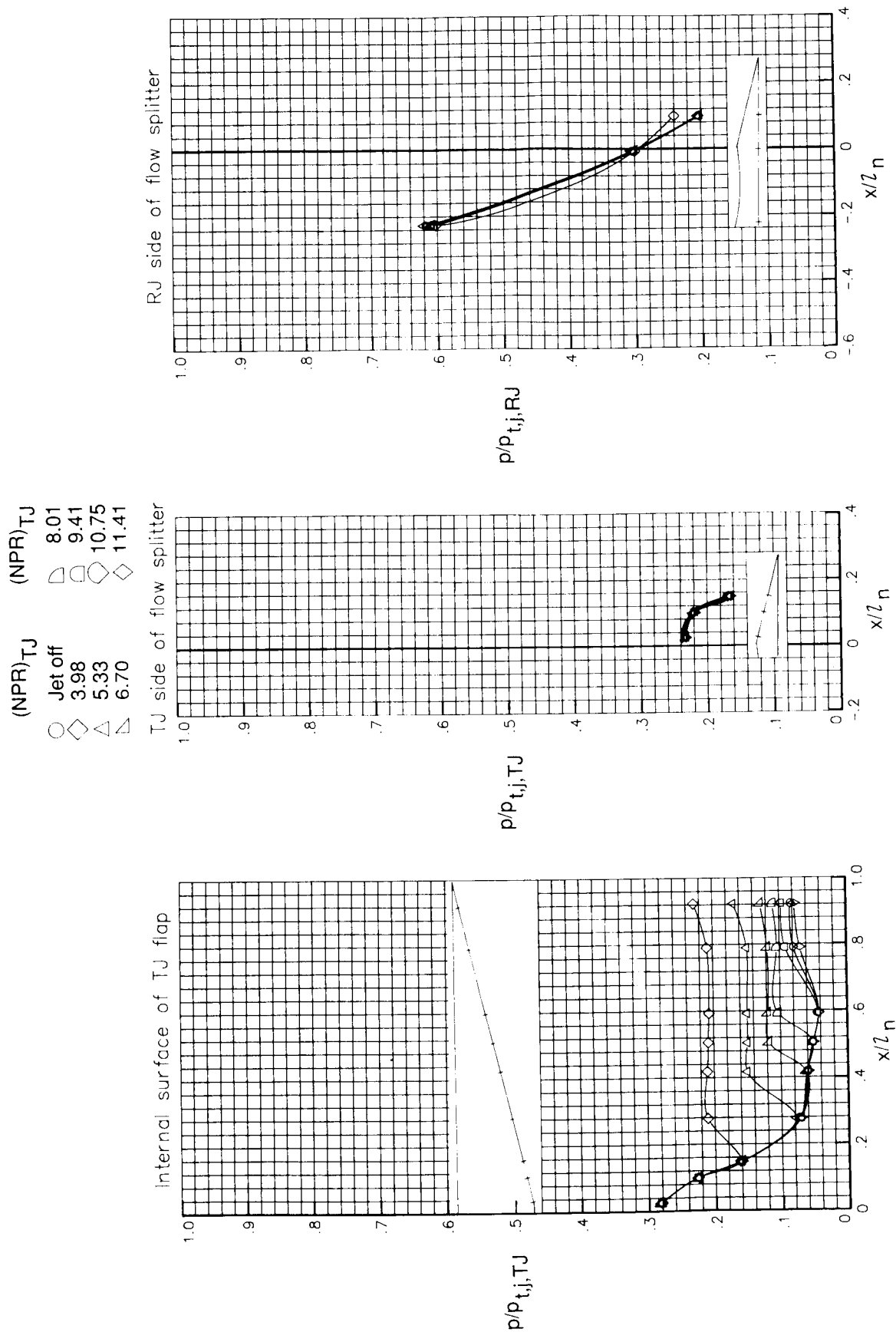| $(NPR)_{TJ}$		$(NPR)_{TJ}$	
○	Jet off	△	6.06
□	2.44	◷	7.26
◇	3.64	◖	8.49
△	4.85	◯	9.49
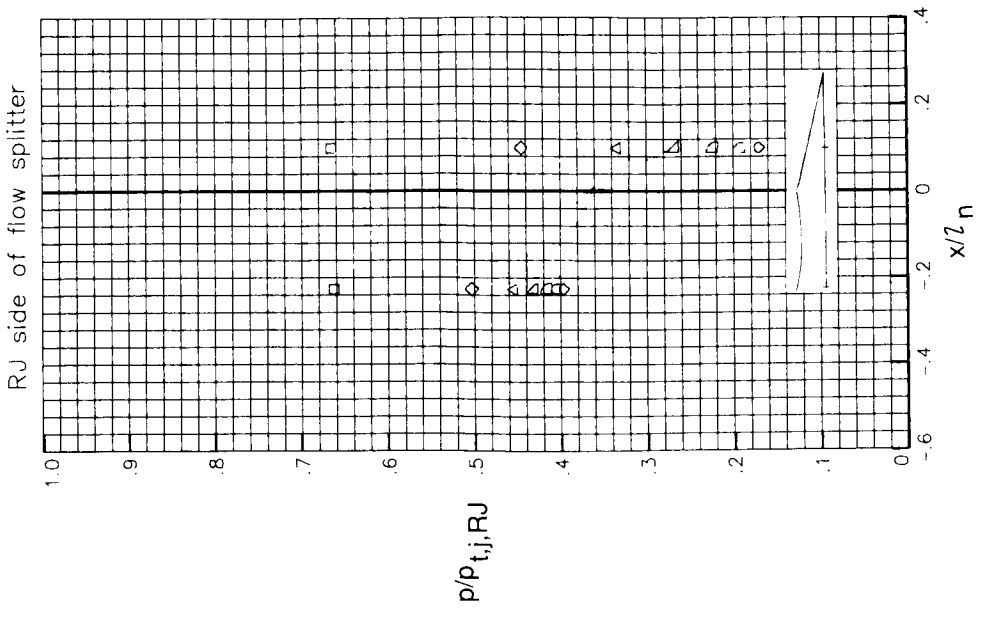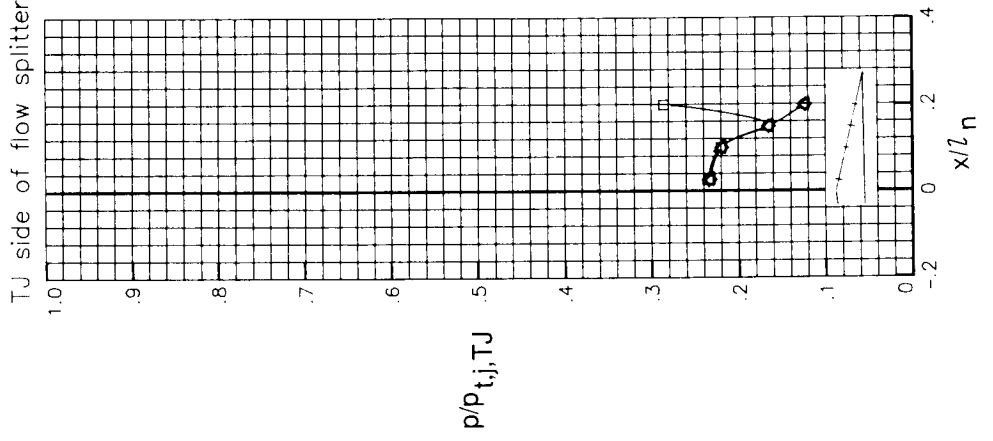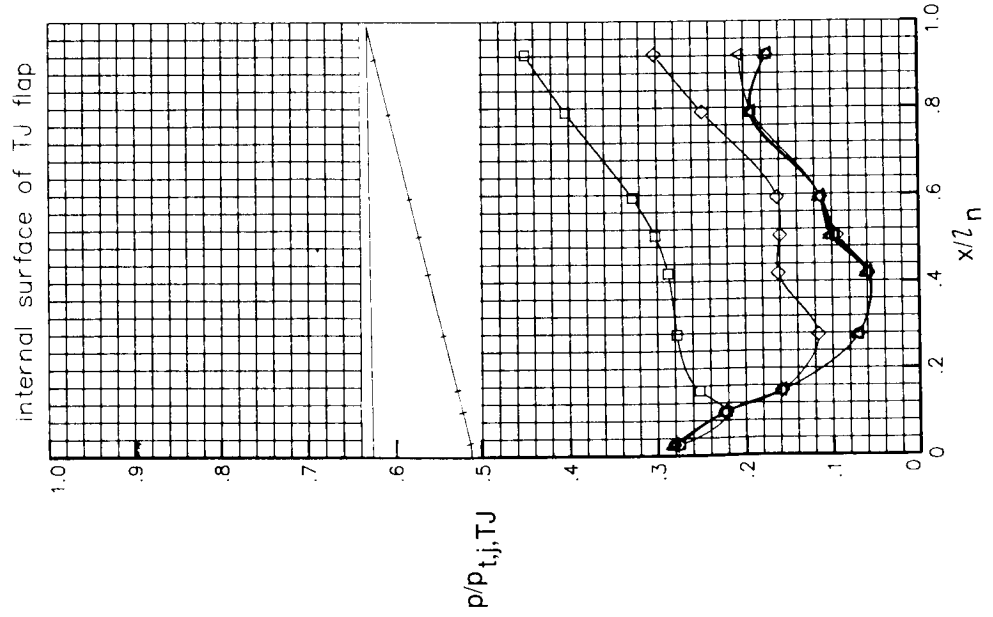
(c) $M = 0.90.$
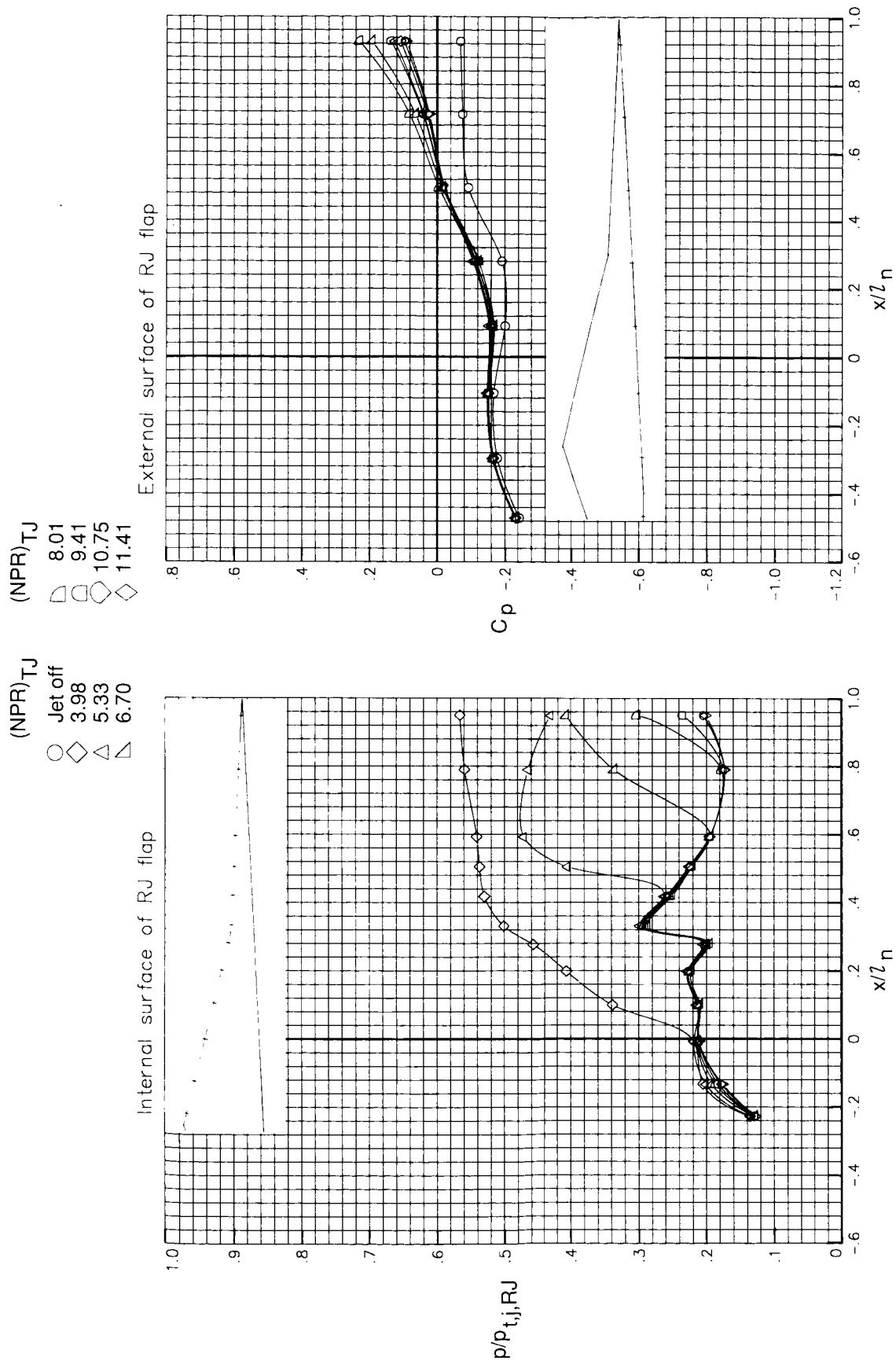
Figure 38. Continued.

(c) Concluded.

Figure 38. Continued.
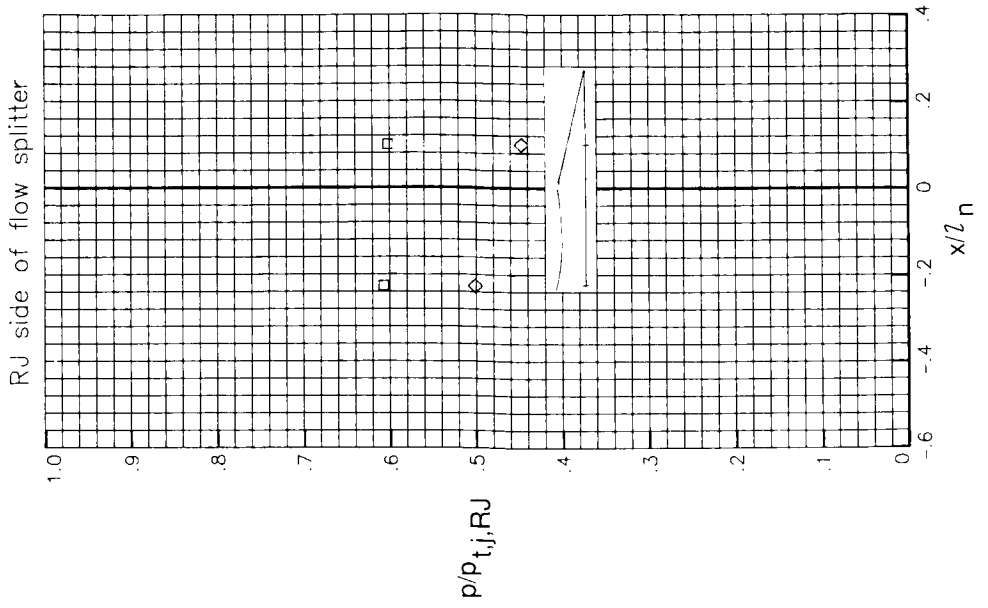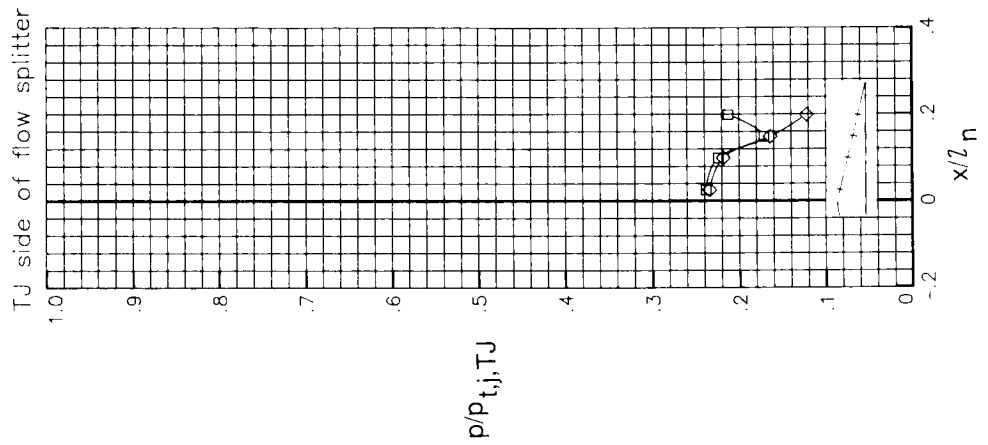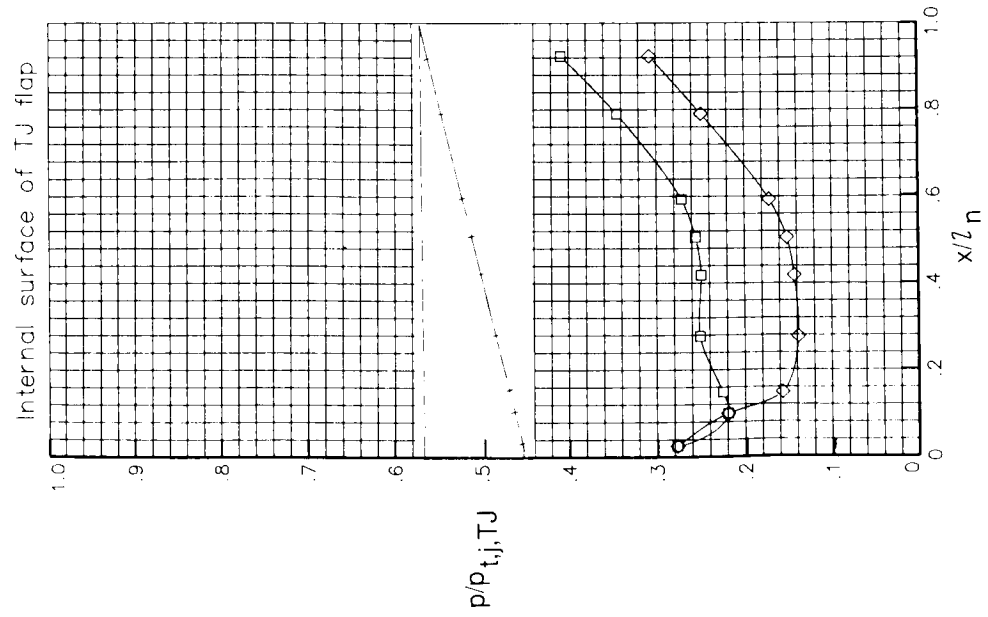
(d) $M = 1.20$.

Figure 38. Continued.
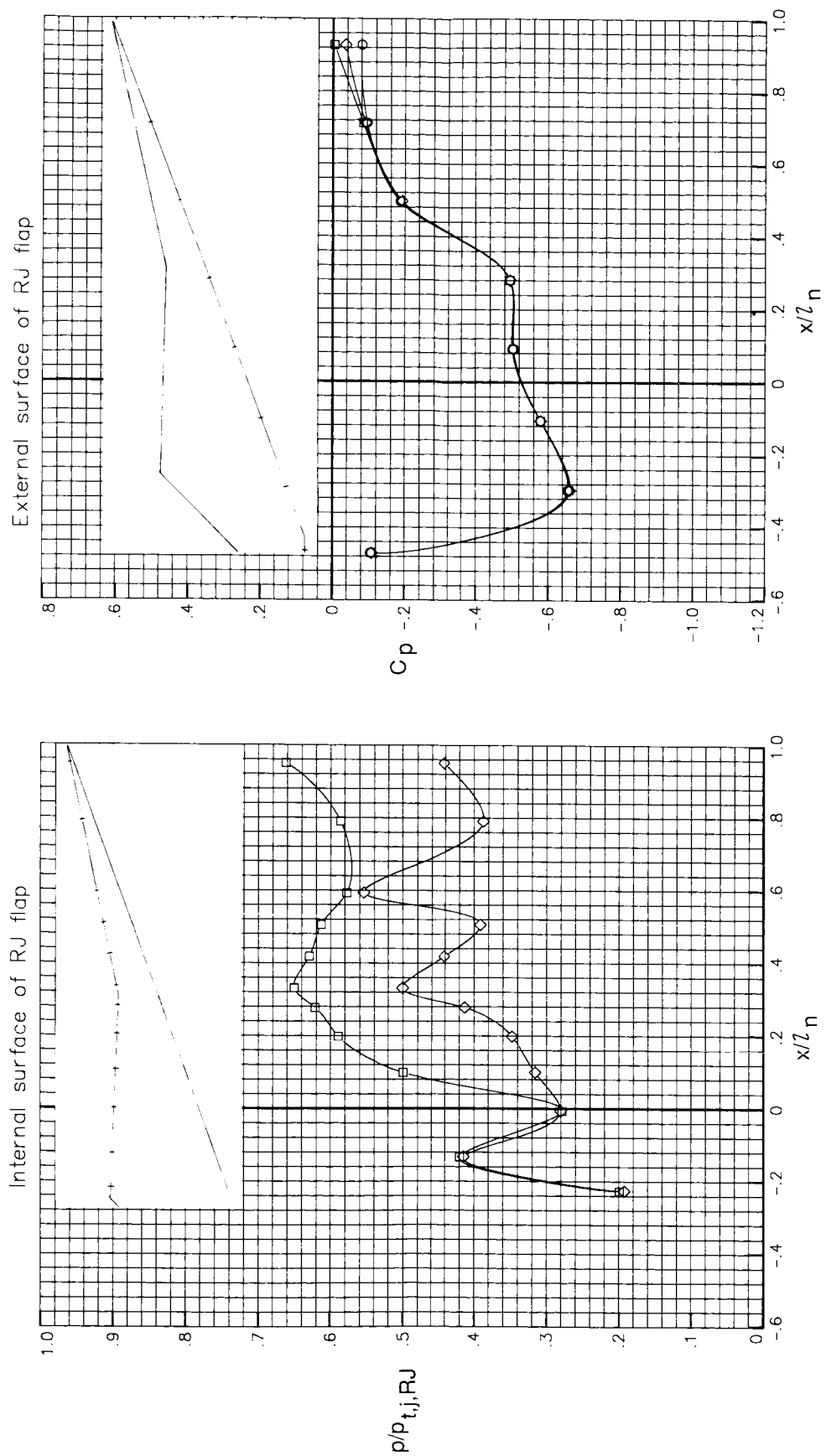
(d) Concluded.

Figure 38. Concluded.
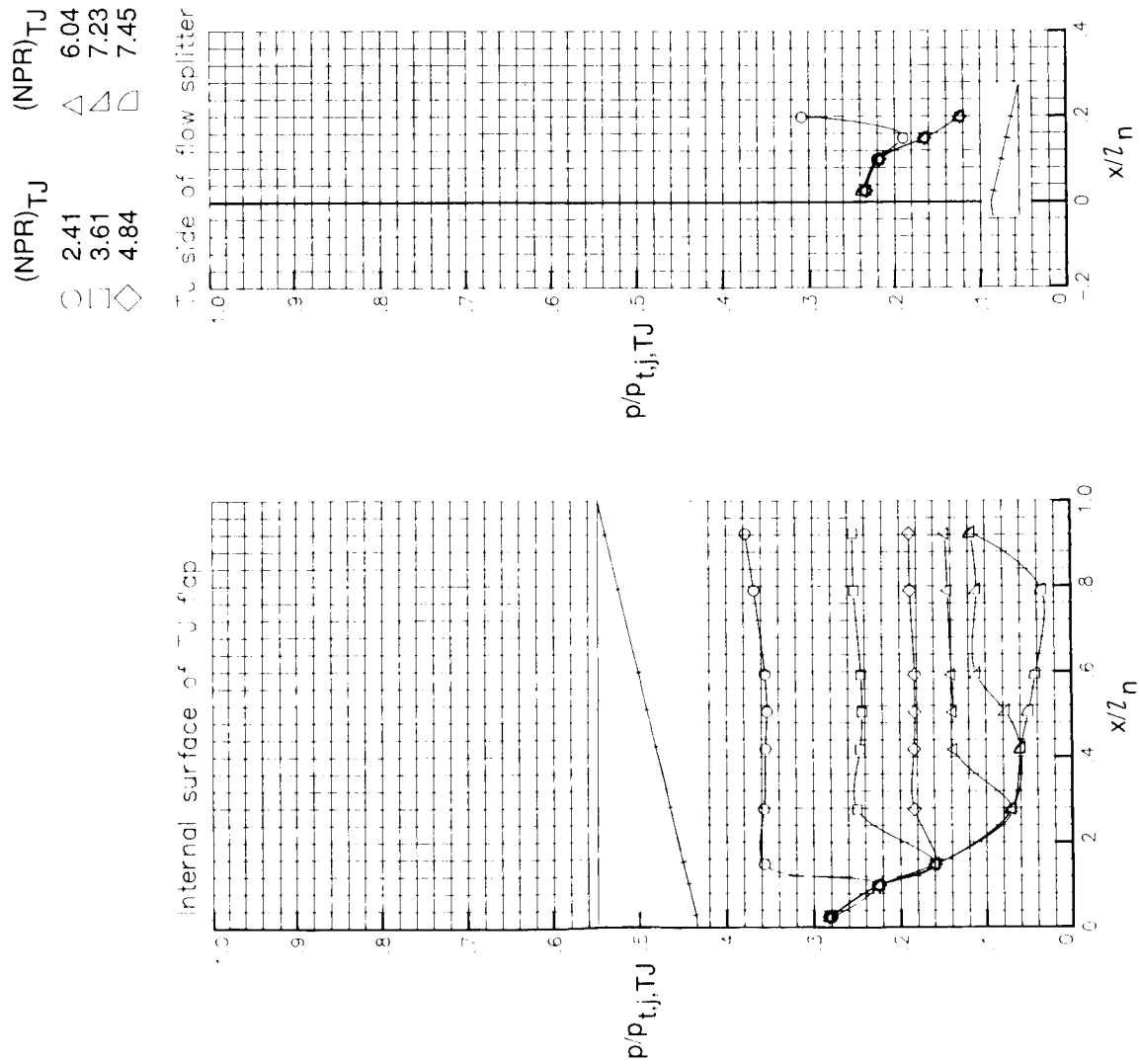
(a) $M = 0$. Arrow indicates RJ throat location.

Figure 39. Pressure ratio and pressure coefficient distributions of CCN with minimum ramjet throat area. cutback sidewalls. and ramjet flap 3.

128

Internal surface of RJ flap

$p/p_{t,j,RJ}$

x/l_n

$(NPR)_{TJ}$		$(NPR)_{TJ}$	
○	2.41	△	6.04
□	3.61	△	7.23
◇	4.84	◻	7.45

(a) Concluded.

Figure 39. Continued.
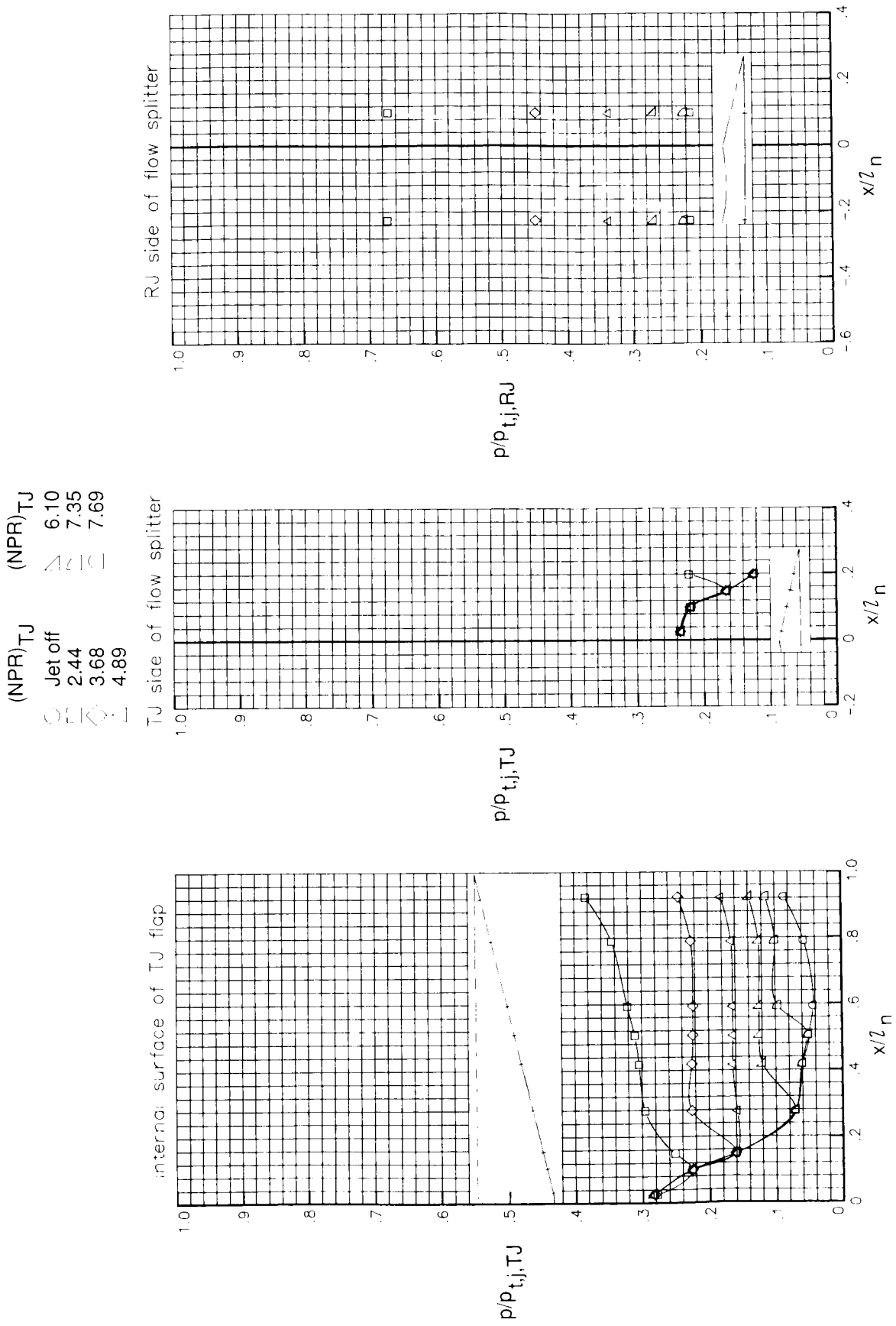
(b) $M = 0.60$.

Figure 39. Continued.

(b) Concluded.

Figure 39. Continued.

(c) $M = 0.90$.

Figure 39. Continued.

(c) Concluded.

Figure 39. Continued.
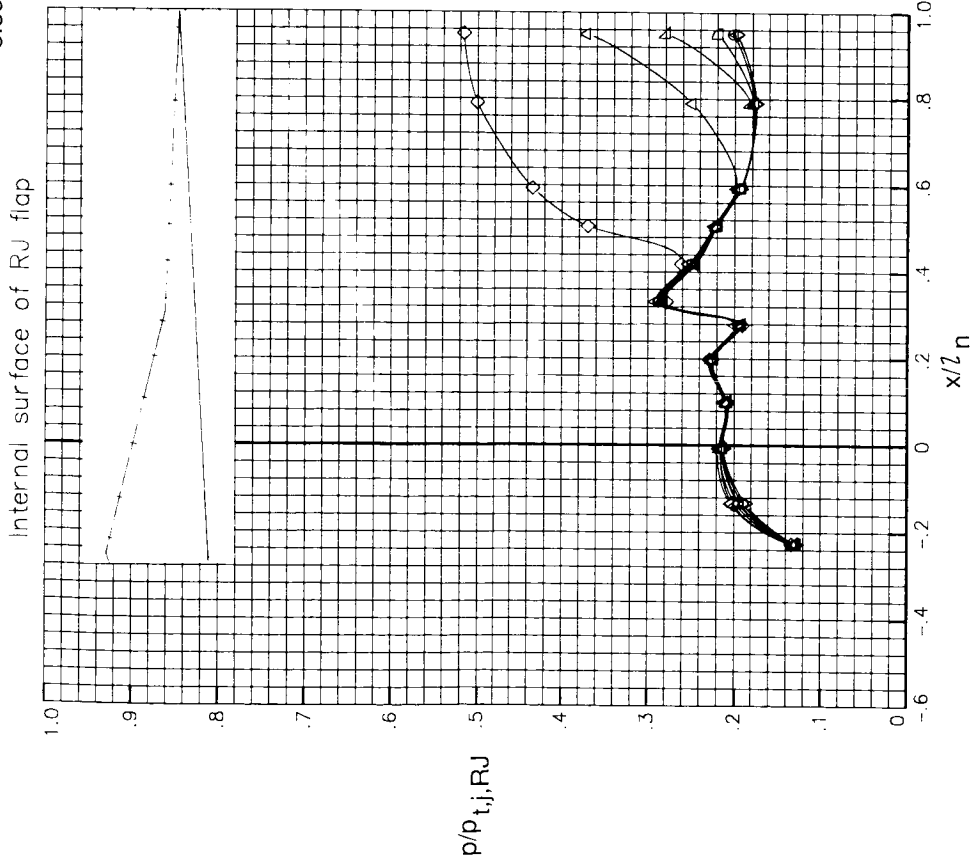
(d) $M = 1.20.$

Figure 39. Continued.
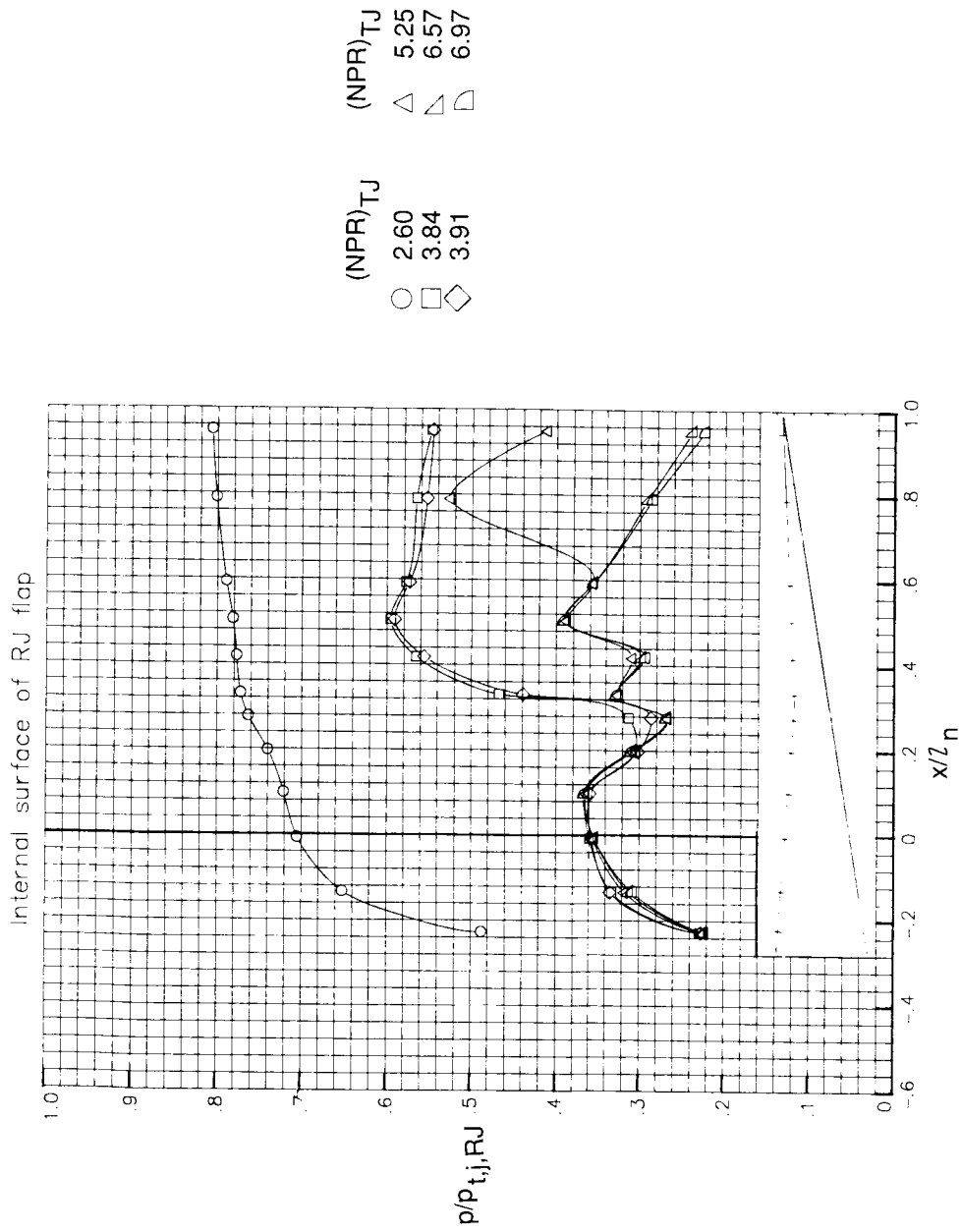
(d) Concluded.

Figure 39. Concluded.

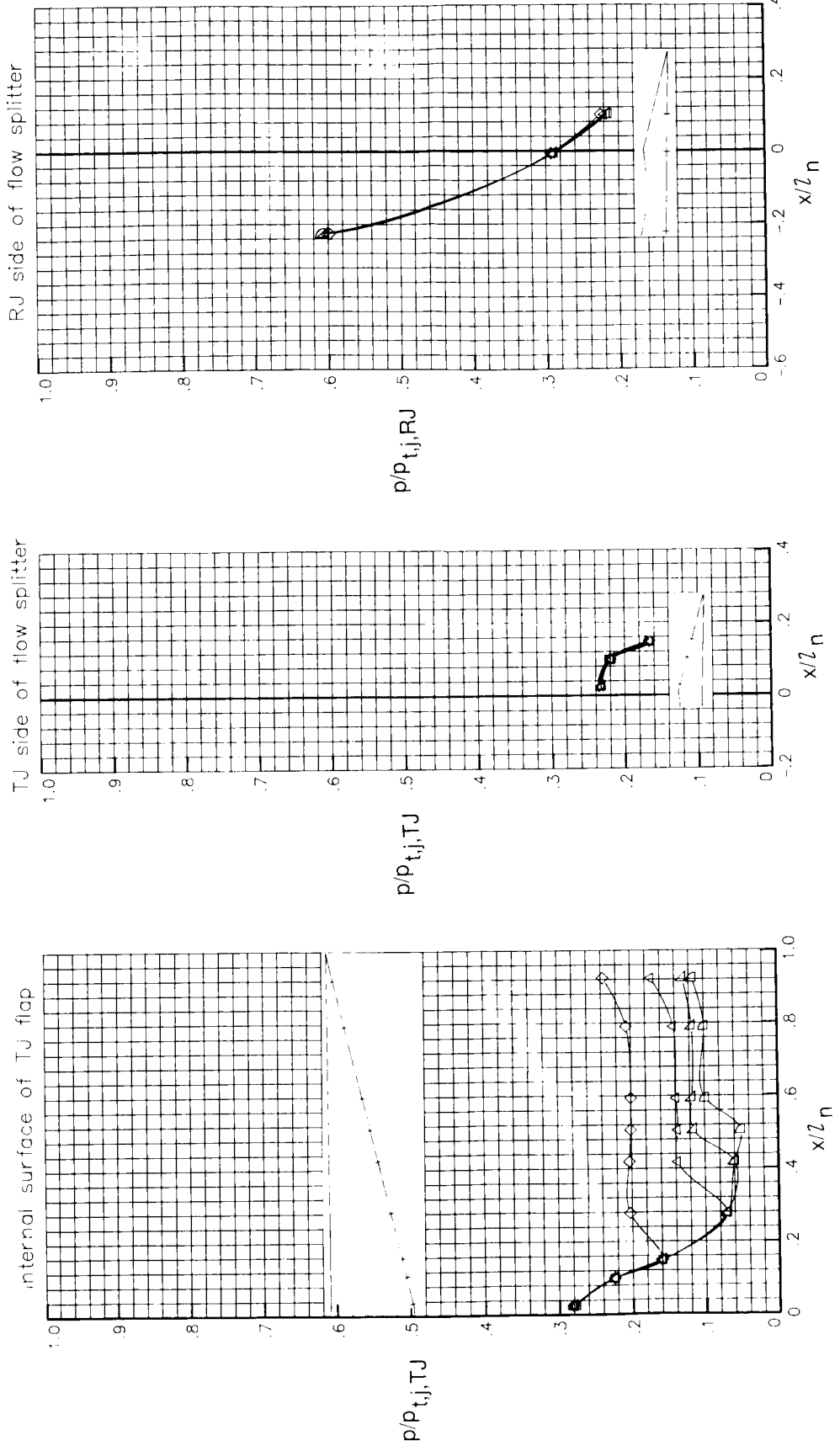(a) $M = 0$. Arrow indicates RJ throat location.

Figure 40. Pressure ratio and pressure coefficient distributions of CCN with maximum ramjet throat area, V-notch sidewalls, and ramjet flap 1.

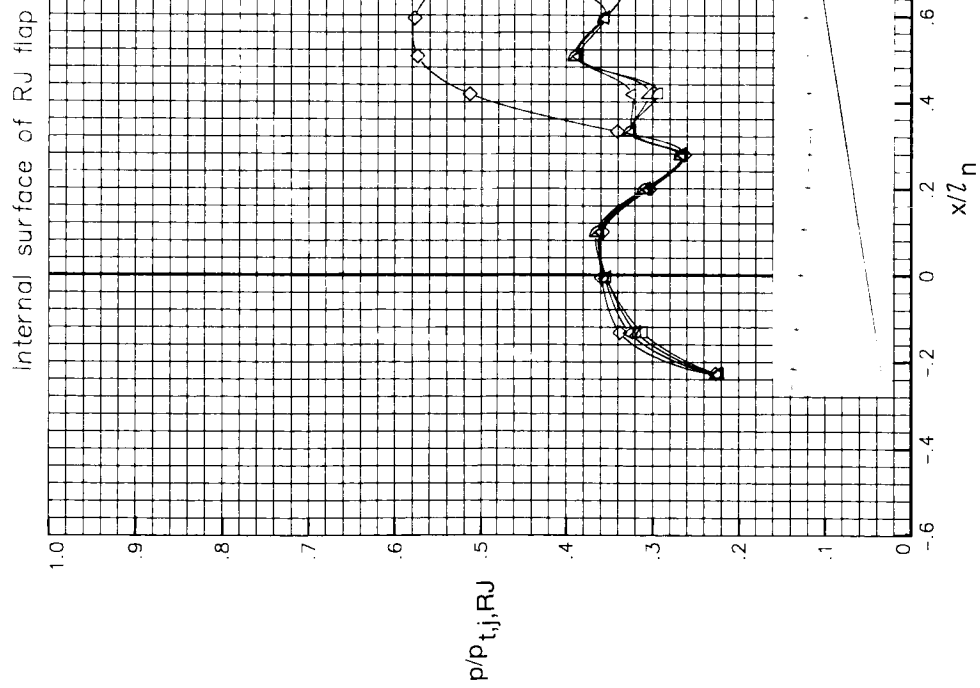(a) Concluded.

Figure 40. Continued.

(b) $M = 0.60$.

Figure 40. Continued.

(NPR)$_{TJ}$
○ Jet off
◇ 3.96
△ 5.31

(NPR)$_{TJ}$
△ 6.63
◁ 7.97
◐ 9.24

External surface of RJ flap

Internal surface of RJ flap

(b) Concluded.

Figure 40. Continued.

(c) $M = 0.90$.

Figure 40. Continued.

(c) Concluded.

Figure 40. Continued.

(d) $M = 1.20$.

Figure 40. Continued.
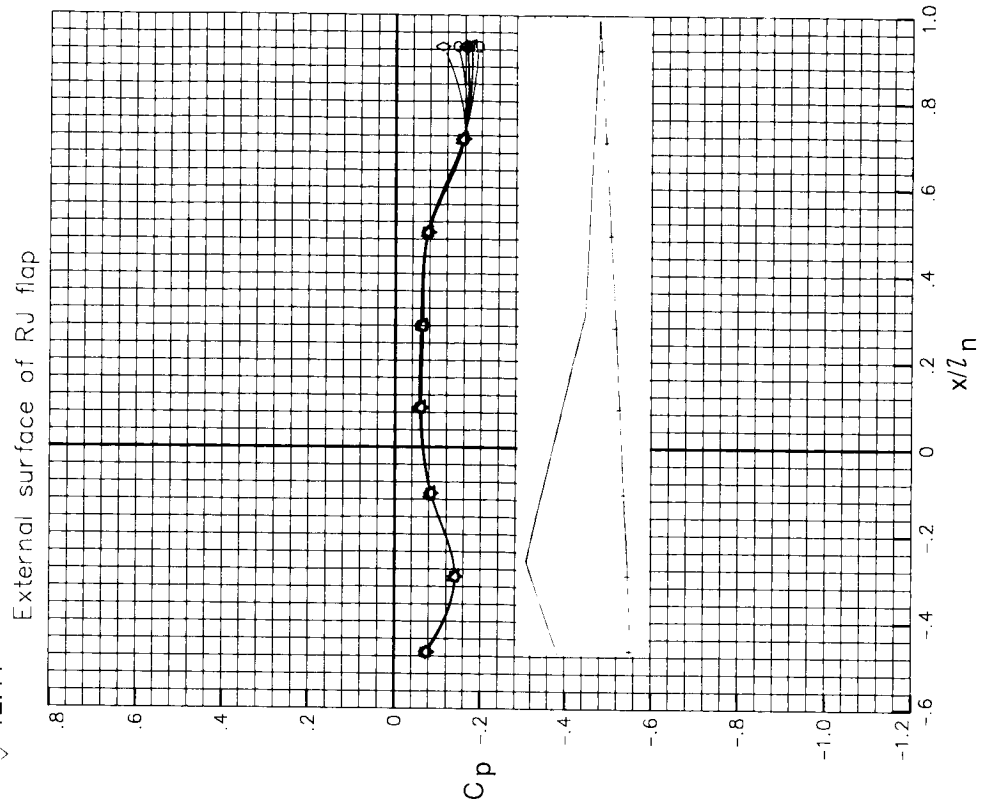
(d) Concluded.

Figure 40. Concluded.
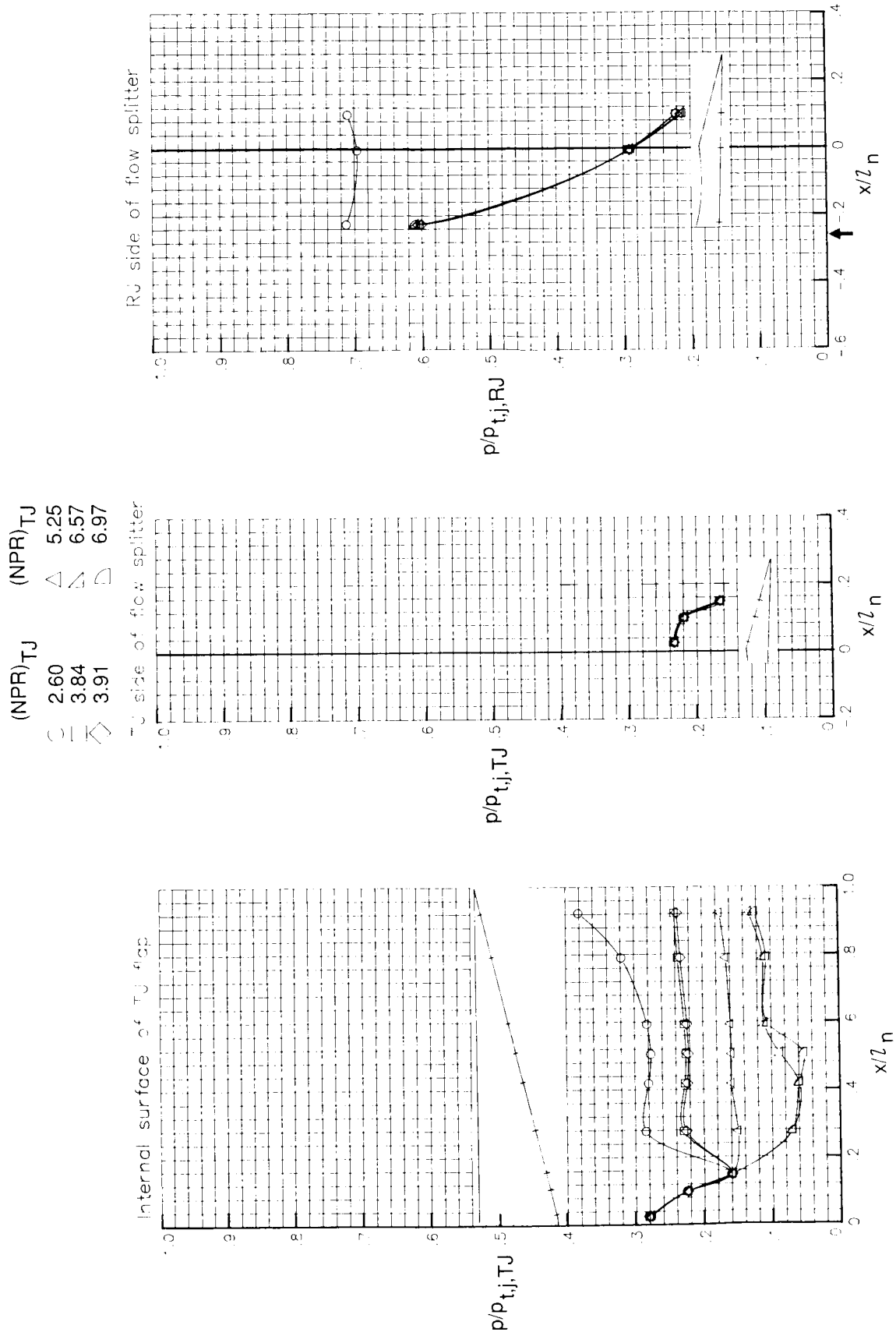
(a) $M = 0$. Arrow indicates RJ throat location.

Figure 41. Pressure ratio and pressure coefficient distributions of CCN with maximum ramjet throat area, V-notch sidewalls, and ramjet flap 2.

(a) Concluded.

Figure 41. Continued.

internal surface of TJ flap

$p/p_{t,j},TJ$

x/l_n

TJ side of flow splitter

$p/p_{t,j},TJ$

x/l_n

RJ side of flow splitter

$p/p_{t,j},RJ$

x/l_n

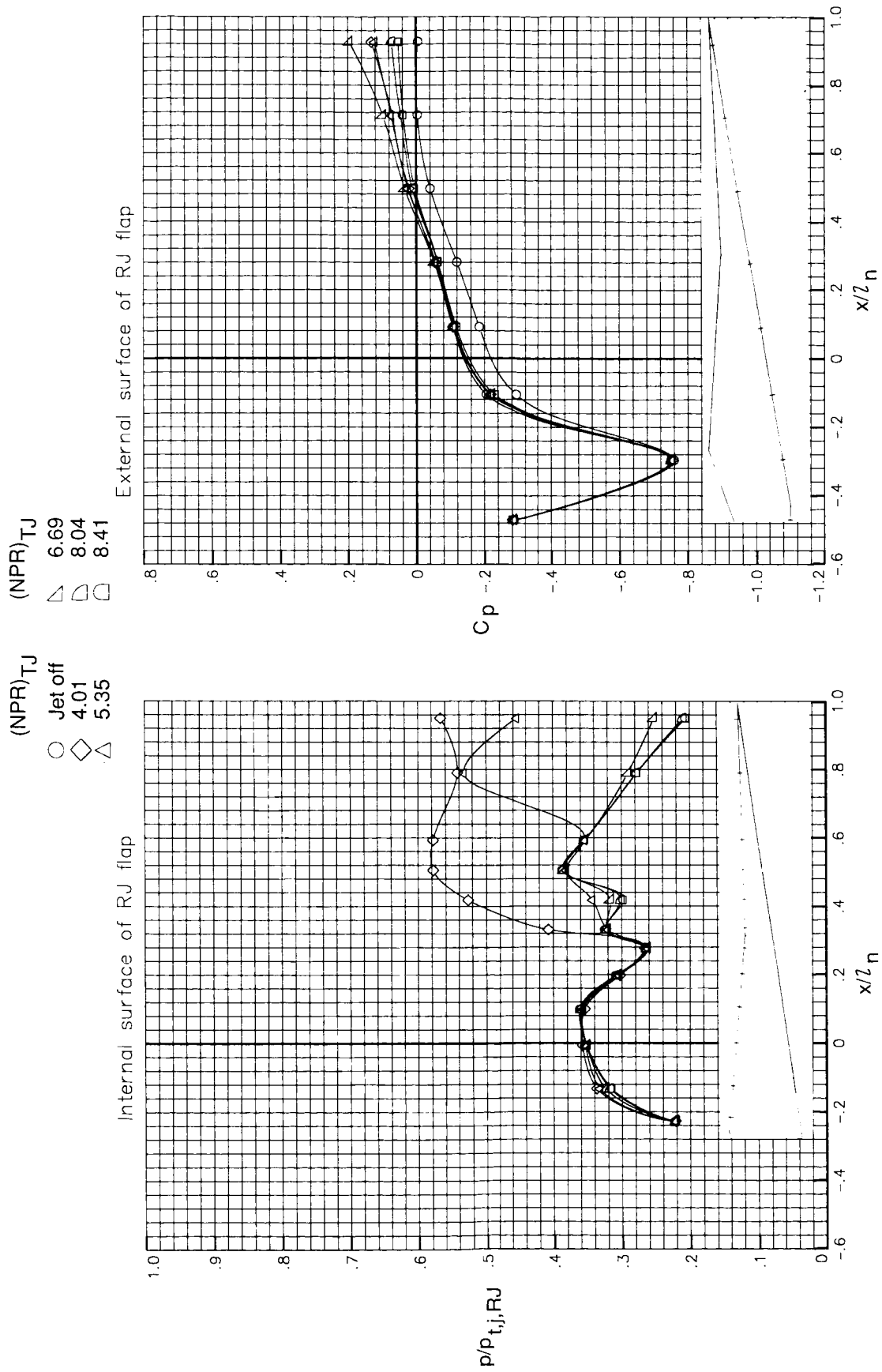| $(NPR)_{TJ}$	$(NPR)_{TJ}$
Jet off	6.64
3.95	7.66
5.31	

(b) $M = 0.60$.

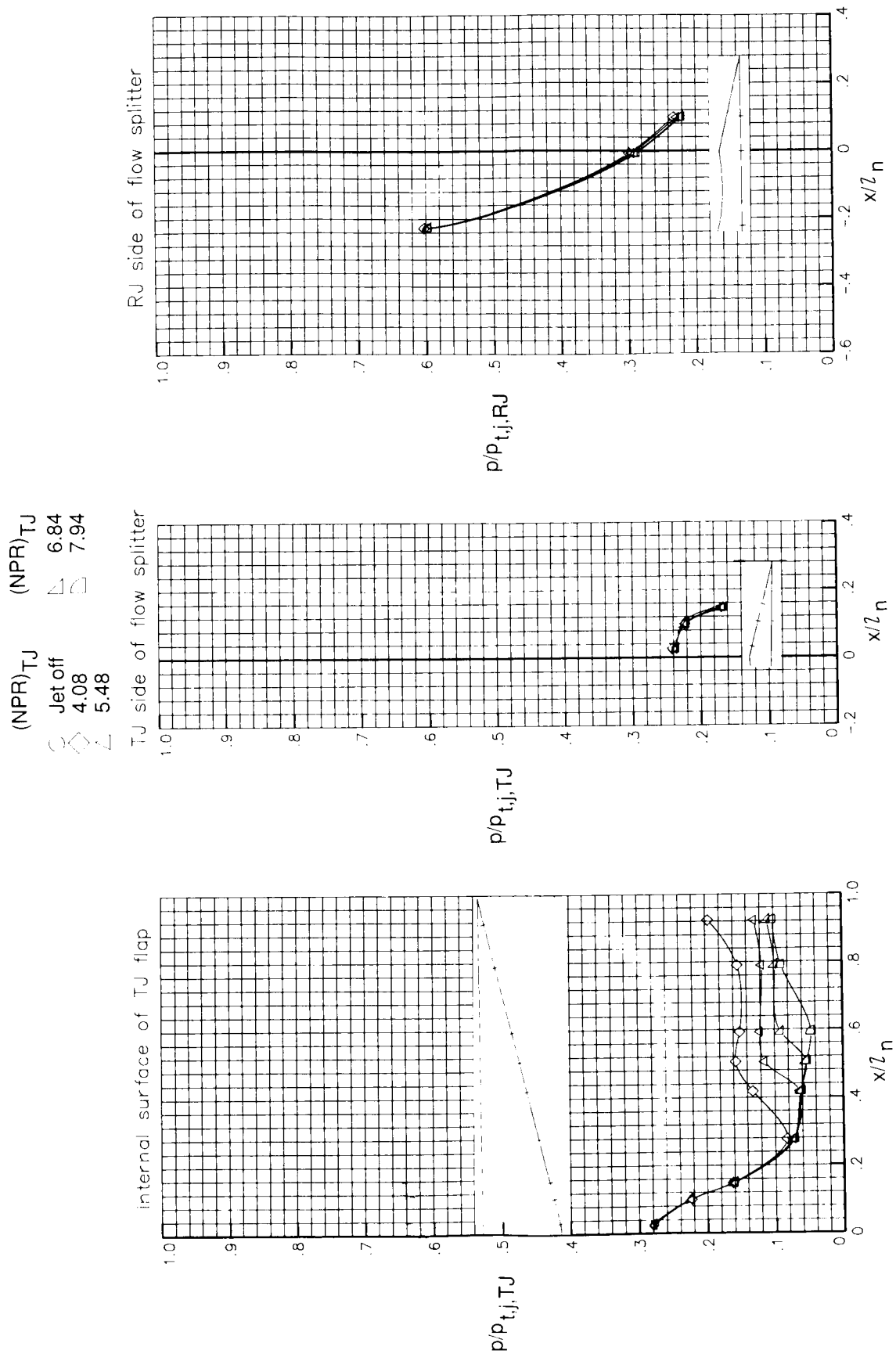Figure 41. Continued.
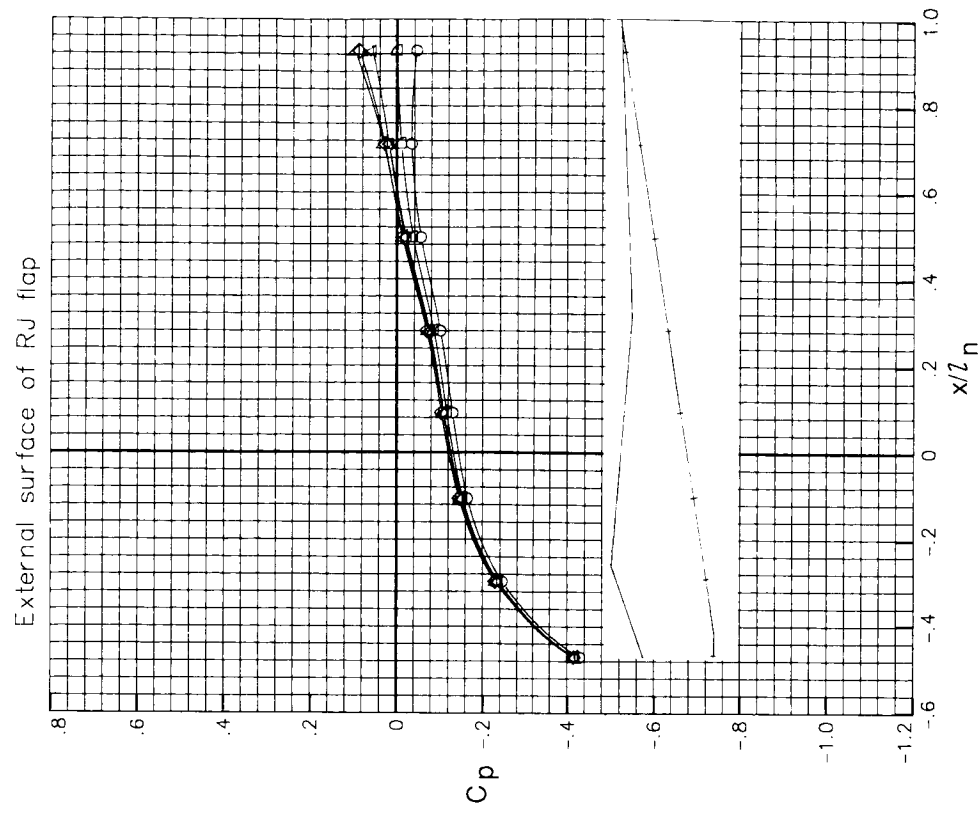
(b) Concluded.

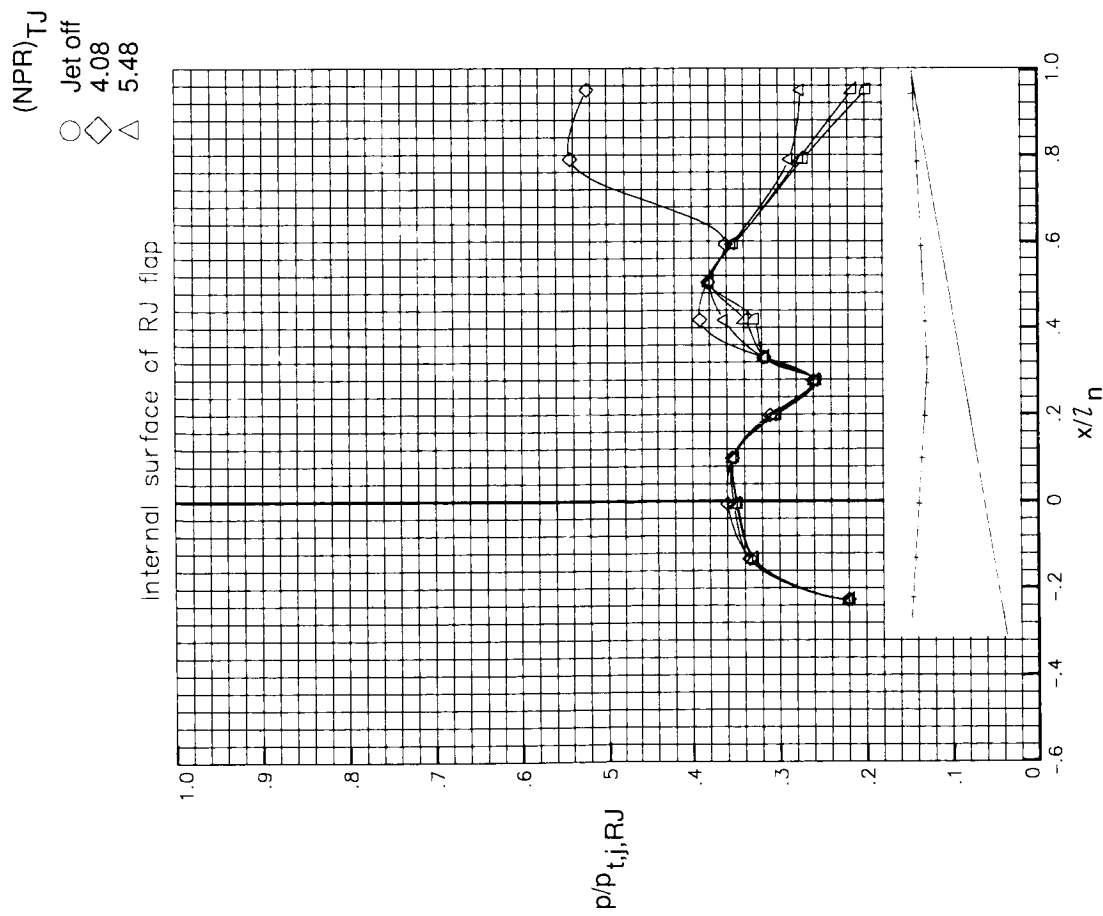Figure 41. Continued.
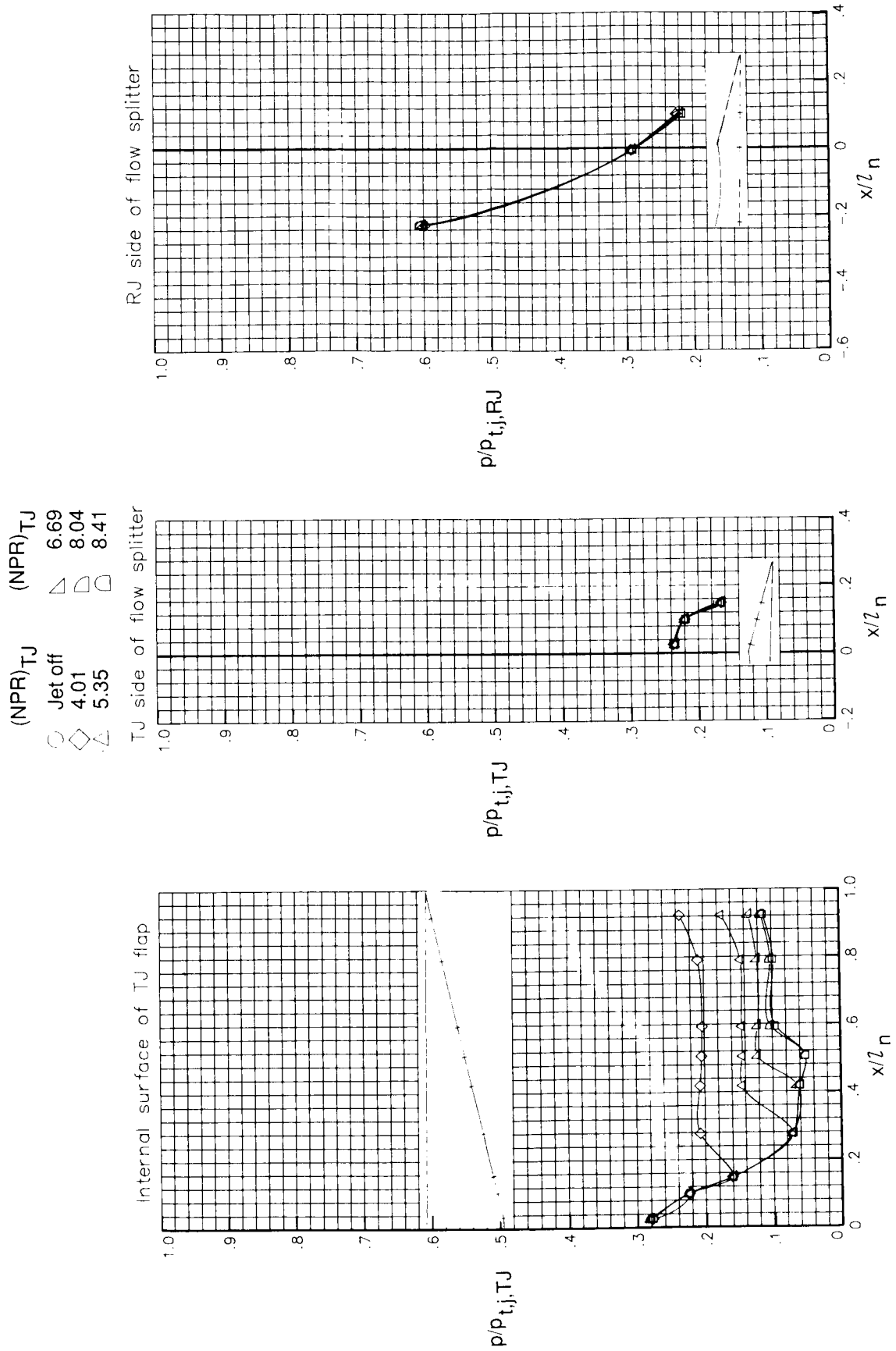
(c) $M = 0.90$.
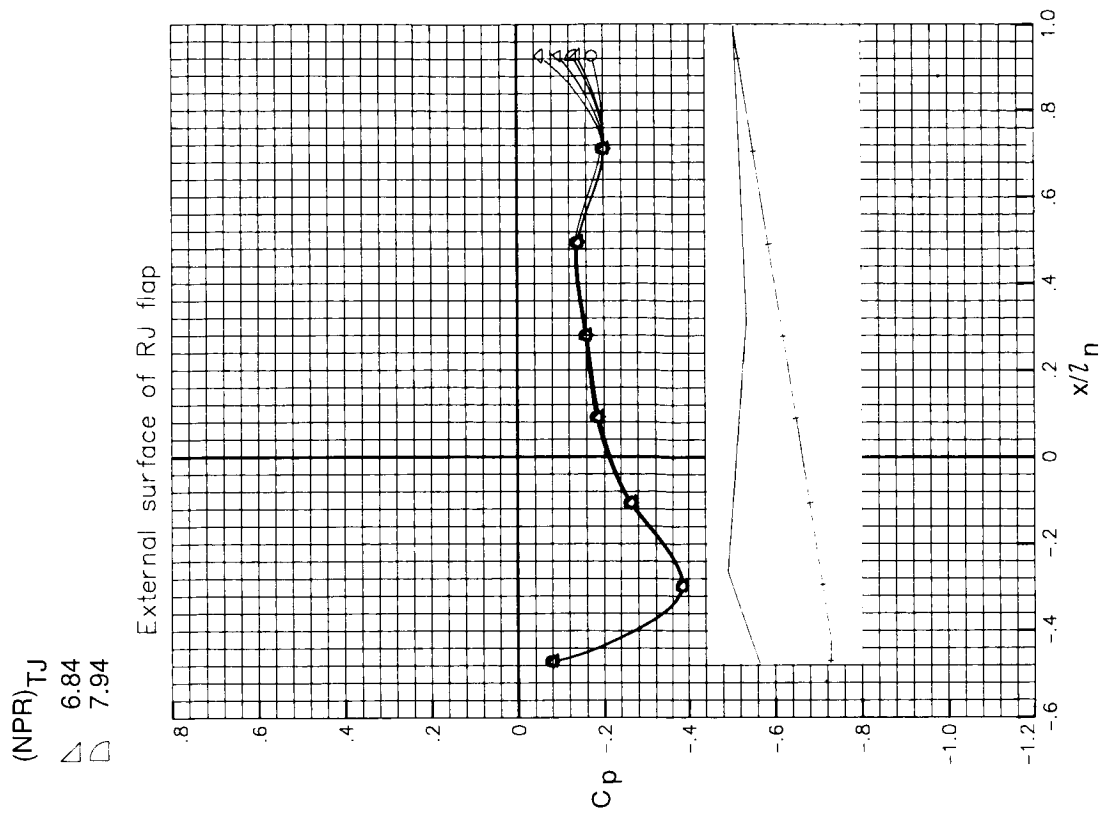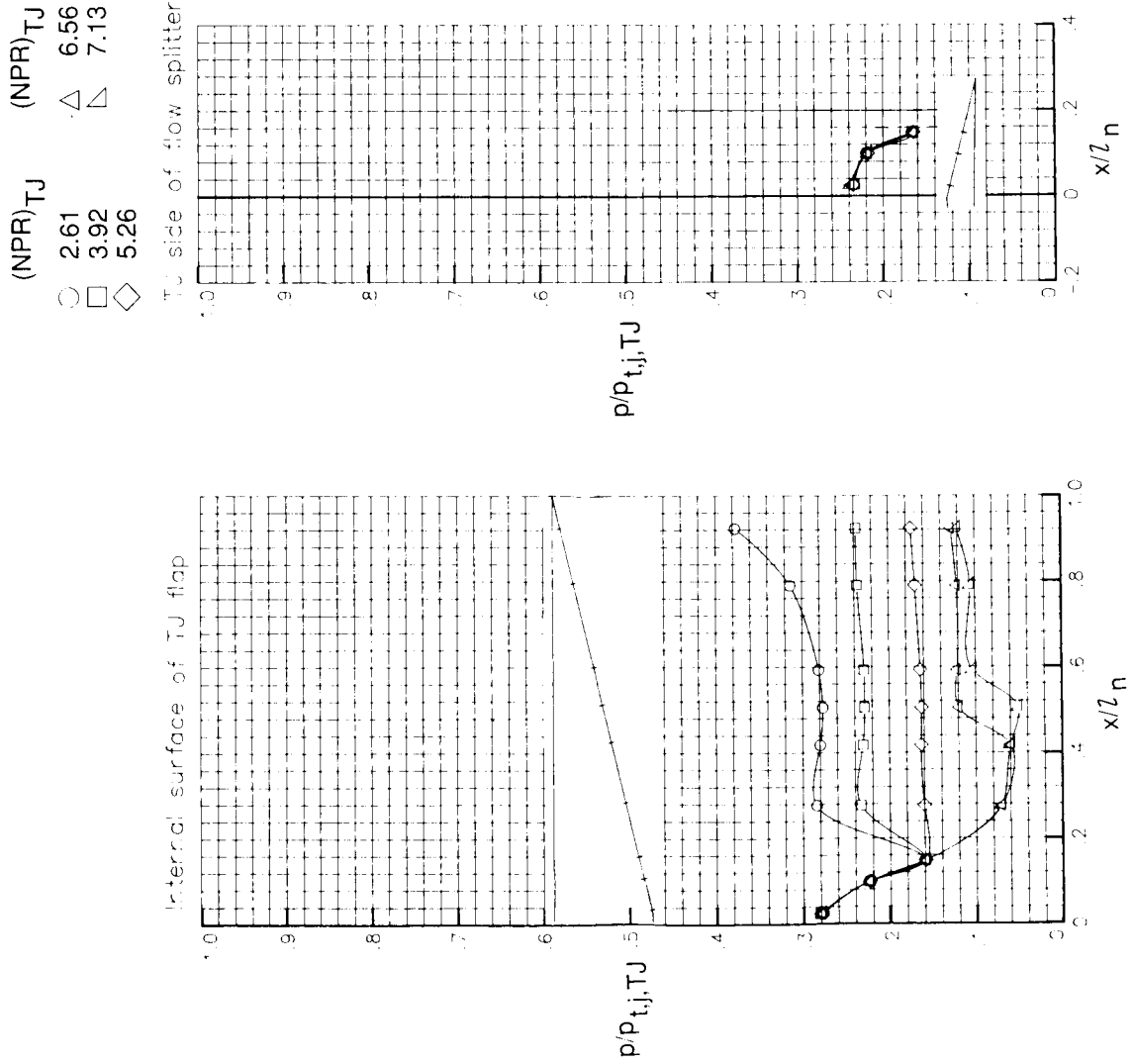
Figure 41. Continued.

(c) Concluded.

Figure 41. Continued.

(d) $M = 1.20.$

Figure 41. Continued.

(d) Concluded.

Figure 41. Concluded.

Figure 42. Pressure ratio and pressure coefficient distributions of CCN with maximum ramjet throat area, V-notch sidewalls, and ramjet flap 3.

(a) $M = 0$. Arrow indicates RJ throat location.

(a) Concluded.

Figure 42. Continued.

(b) $M = 0.60.$

Figure 42. Continued.
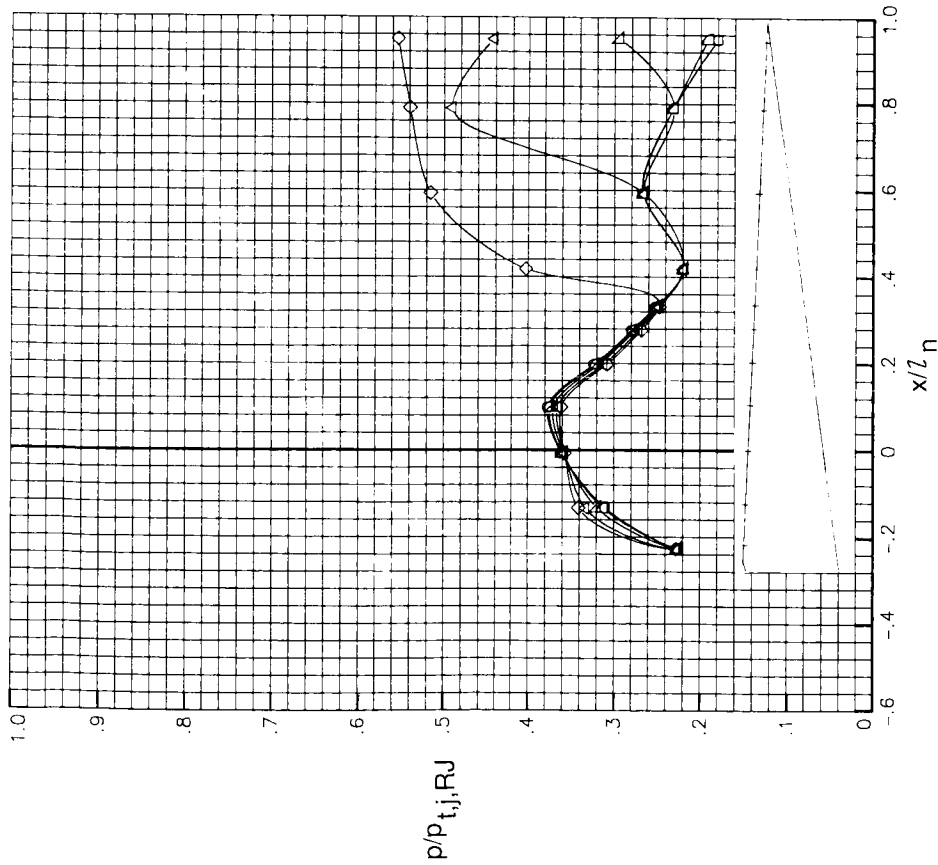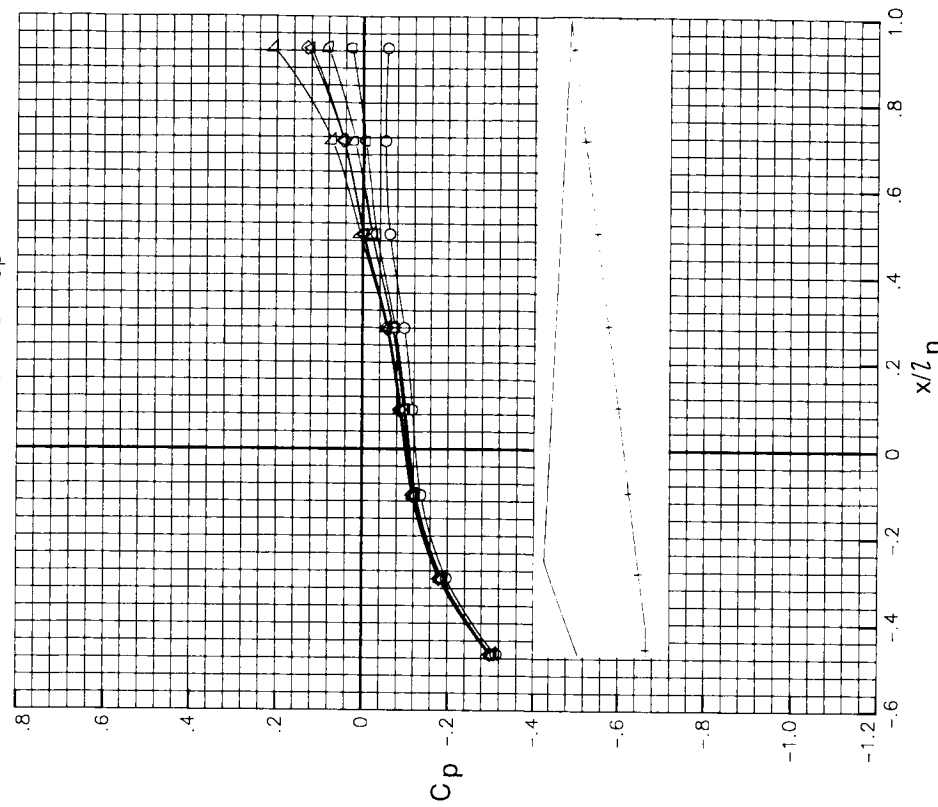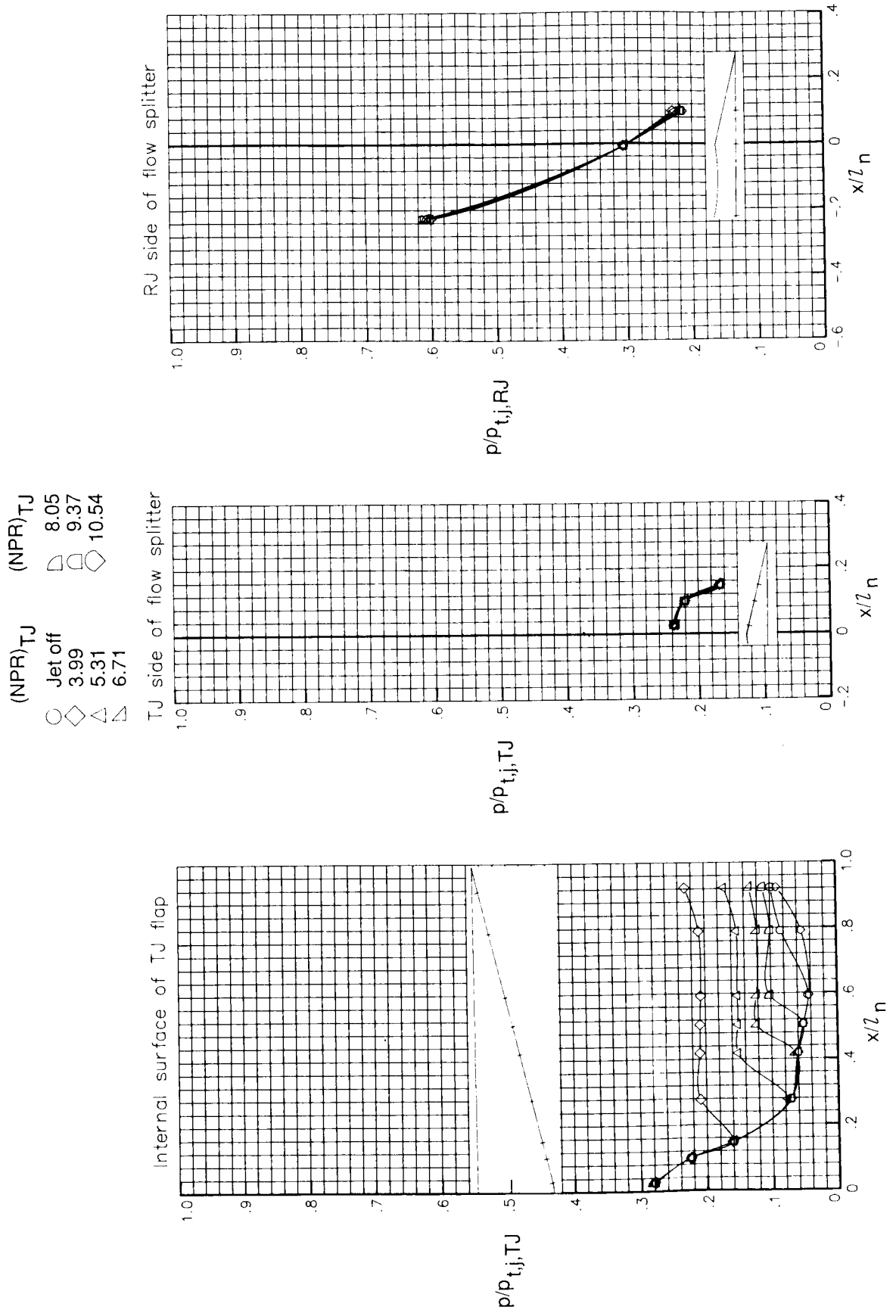
(b) Concluded.

Figure 42. Continued.

(c) $M = 0.90$.

Figure 42. Continued.
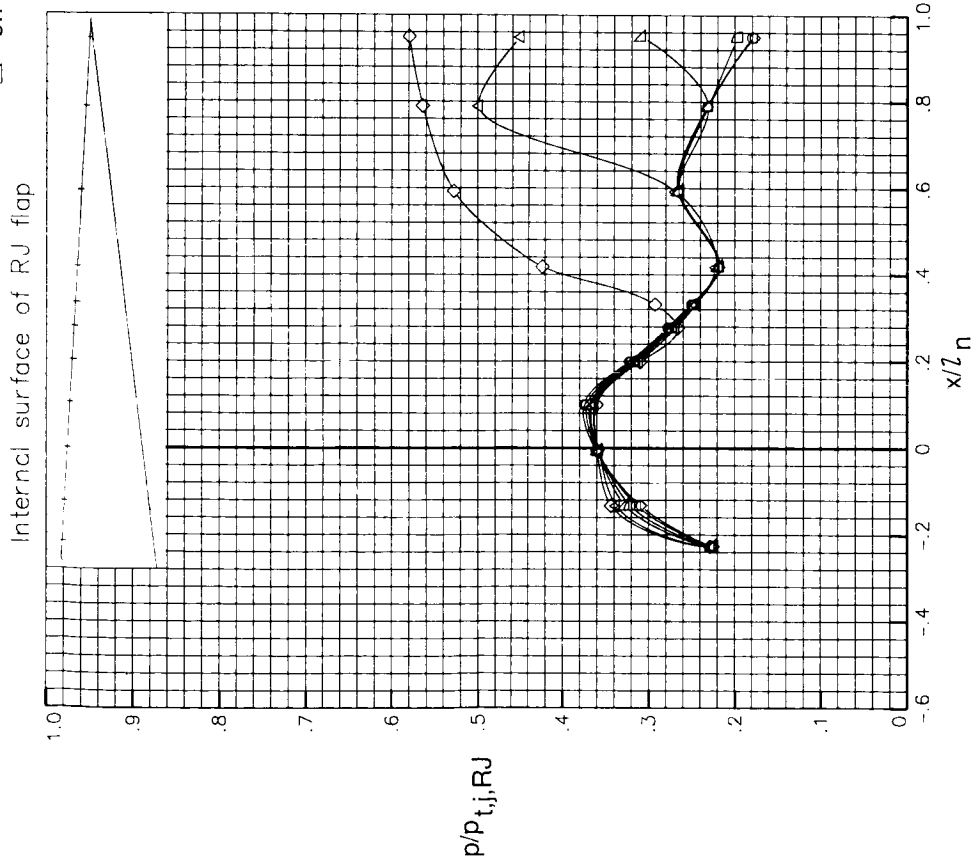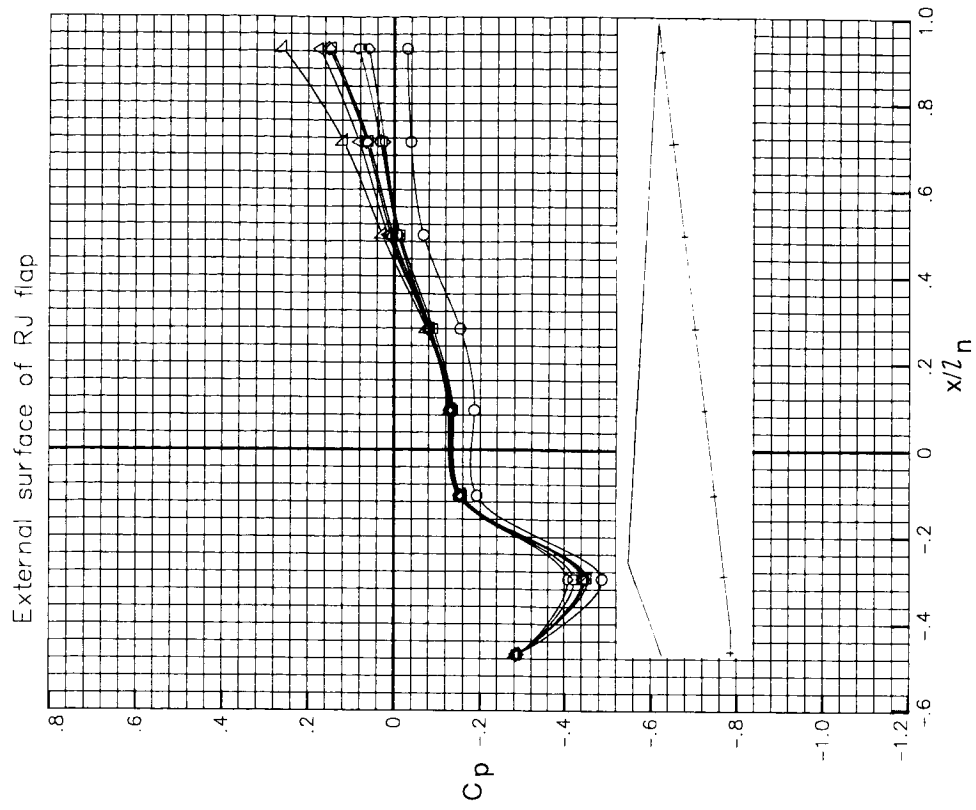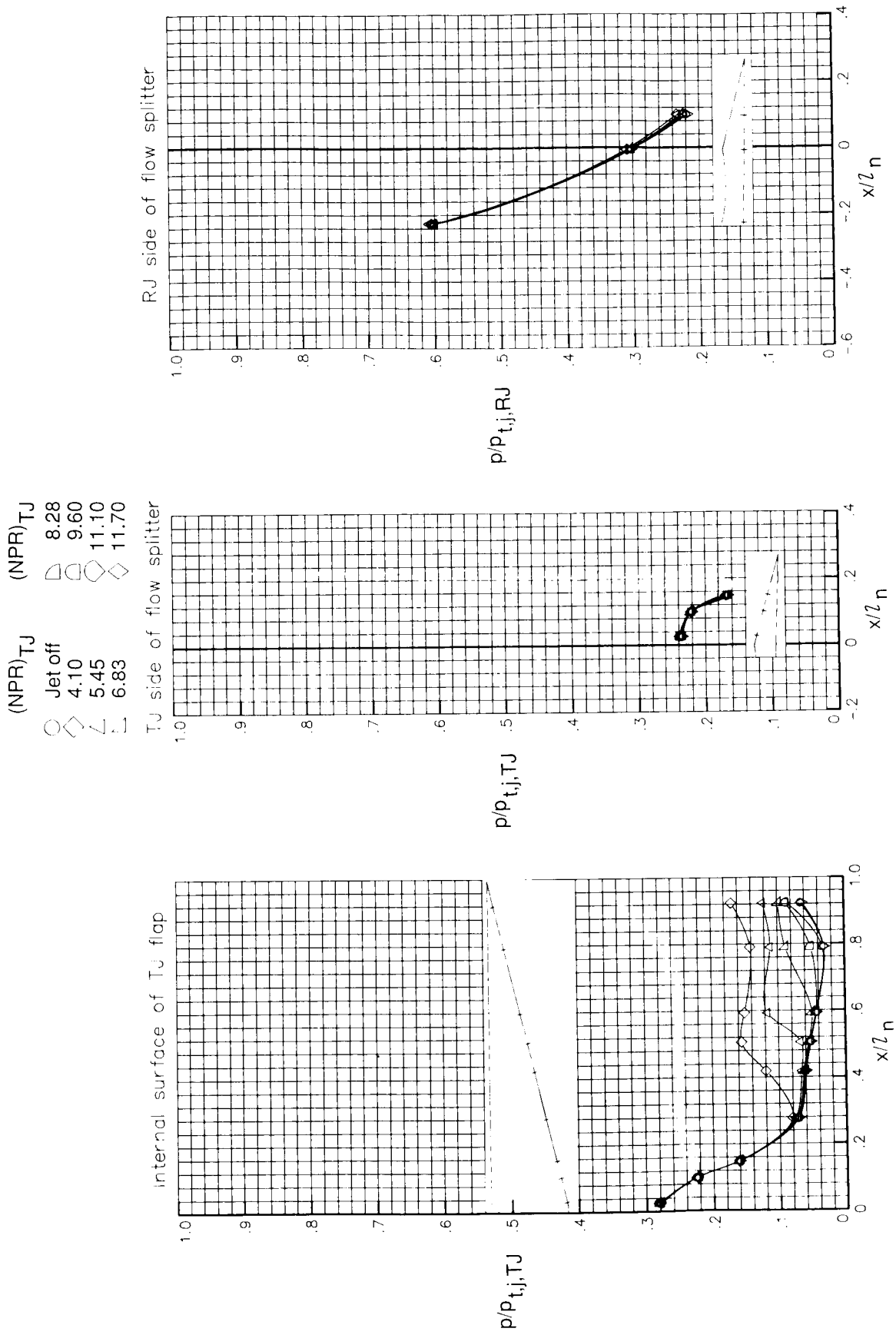
(c) Concluded. Figure 42. Continued.
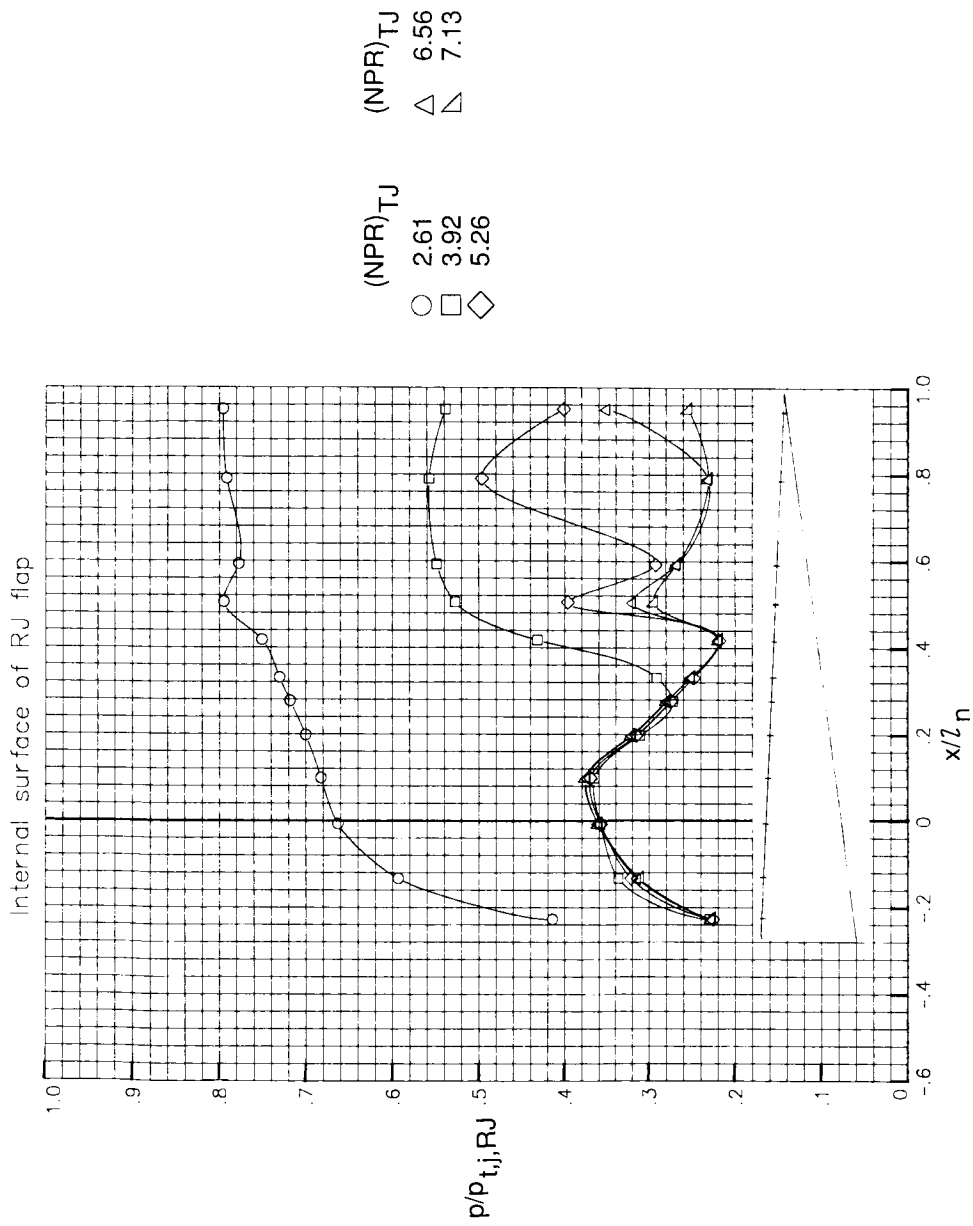
(d) $M = 1.20$.

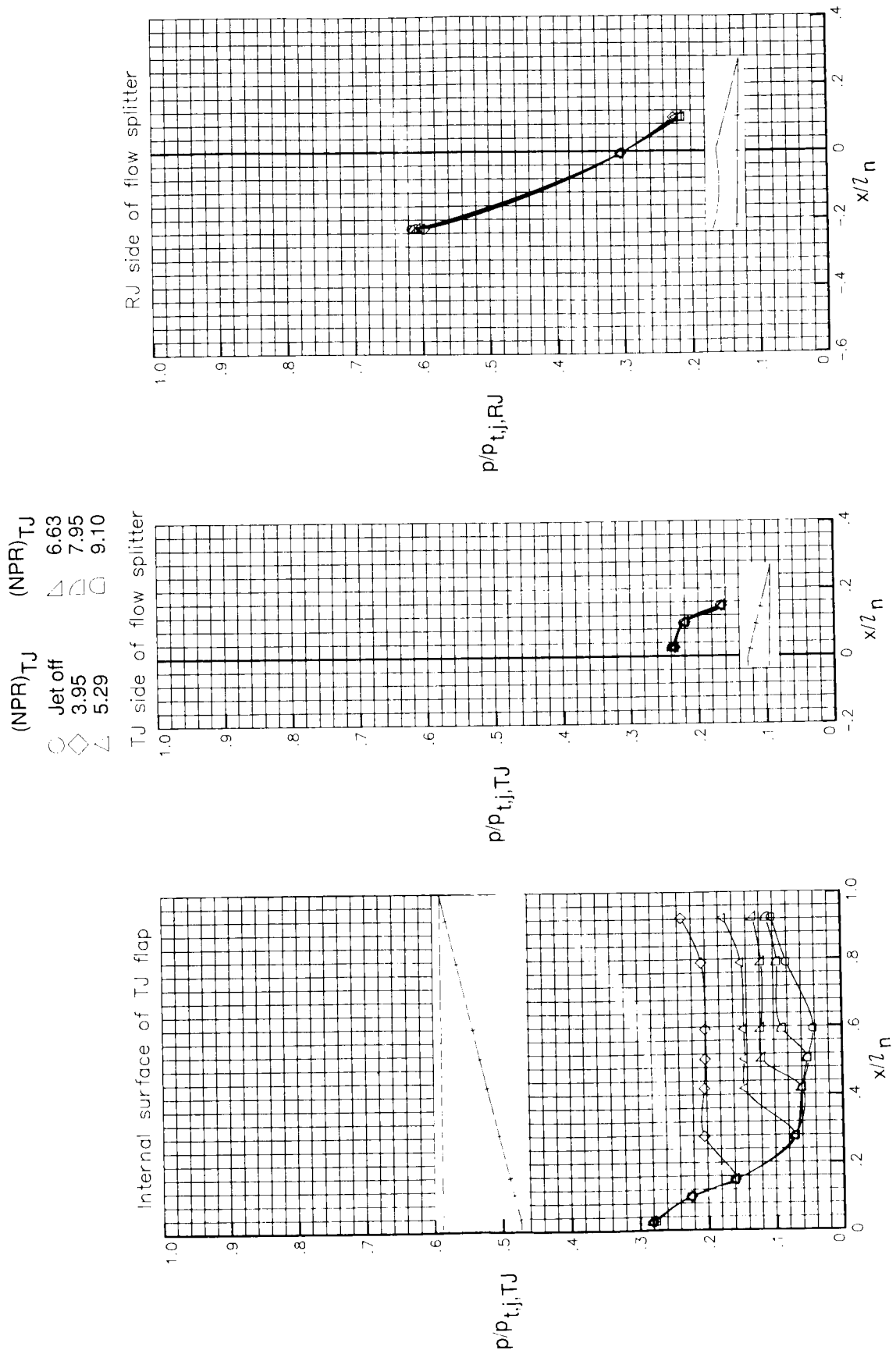Figure 42. Continued.
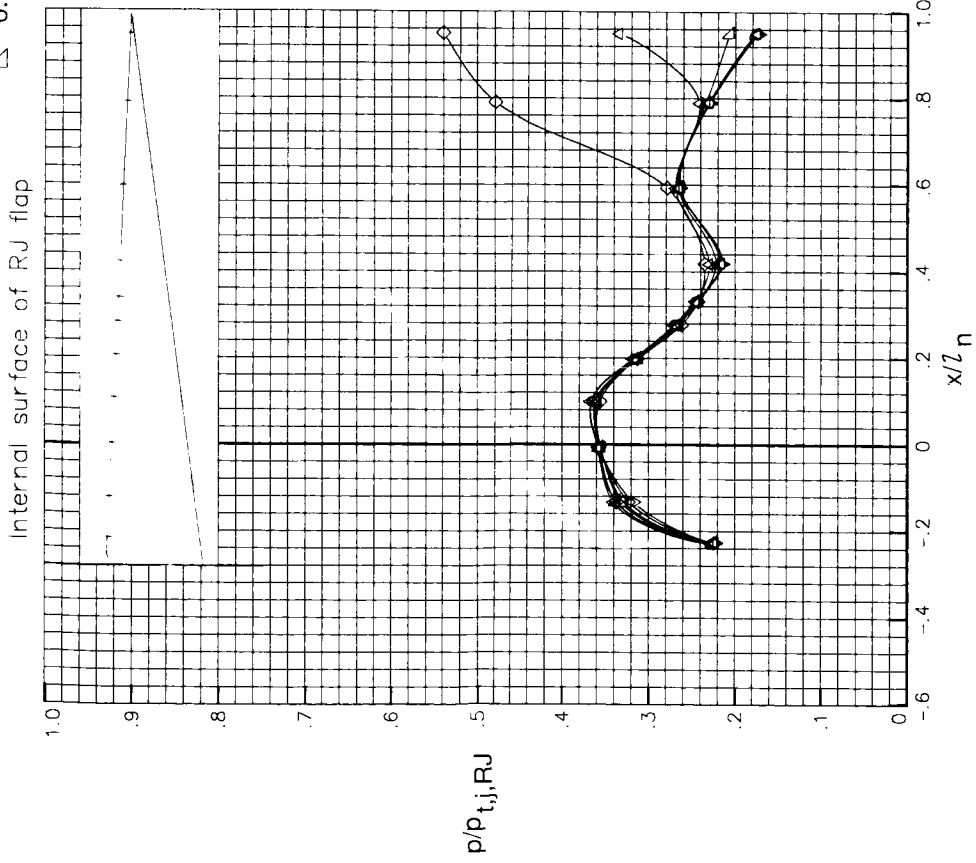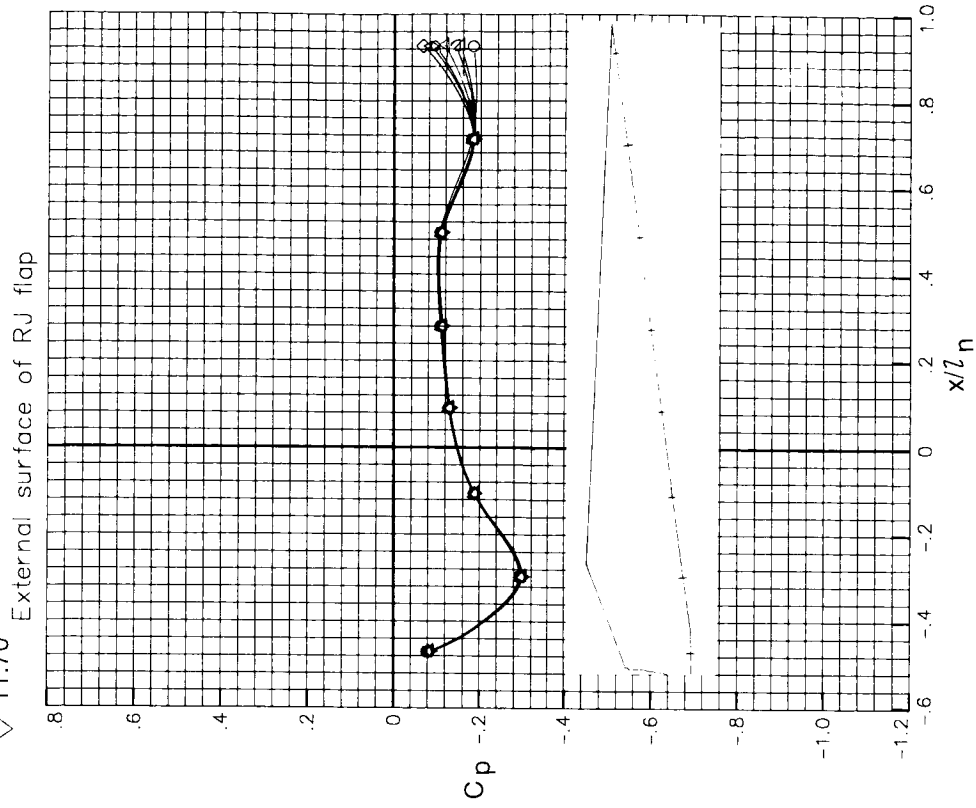
(d) Concluded.

Figure 42. Concluded.
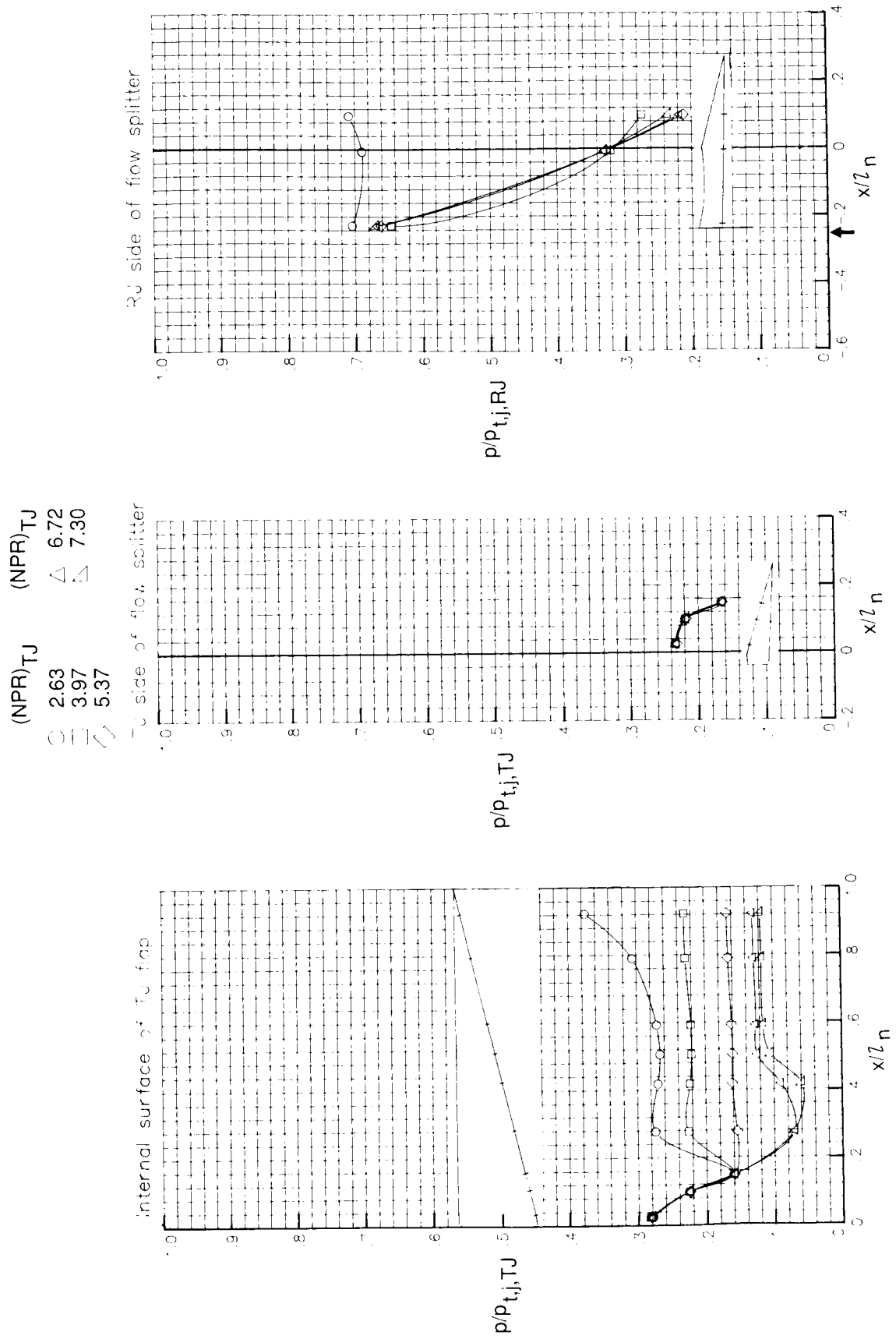
(a) $M = 0$. Arrow indicates RJ throat location.

Figure 43. Pressure ratio and pressure coefficient distributions of CCN with maximum ramjet throat area, cutback sidewalls, and ramjet flap 2.

Internal surface of RJ flap

(NPR)$_{TJ}$		(NPR)$_{TJ}$
○	2.63	△ 6.72
□	3.97	◁ 7.30
◇	5.37	

(a) Concluded.

Figure 43. Continued.

RJ side of flow splitter

$p/p_{tj,RJ}$

x/l_n

TJ side of flow splitter

$p/p_{tj,TJ}$

x/l_n

Internal surface of TJ flap

$p/p_{tj,TJ}$

x/l_n

$(NPR)_{TJ}$		$(NPR)_{TJ}$	
○	Jet off	△	6.79
◇	4.00	□	7.87
△	5.38		
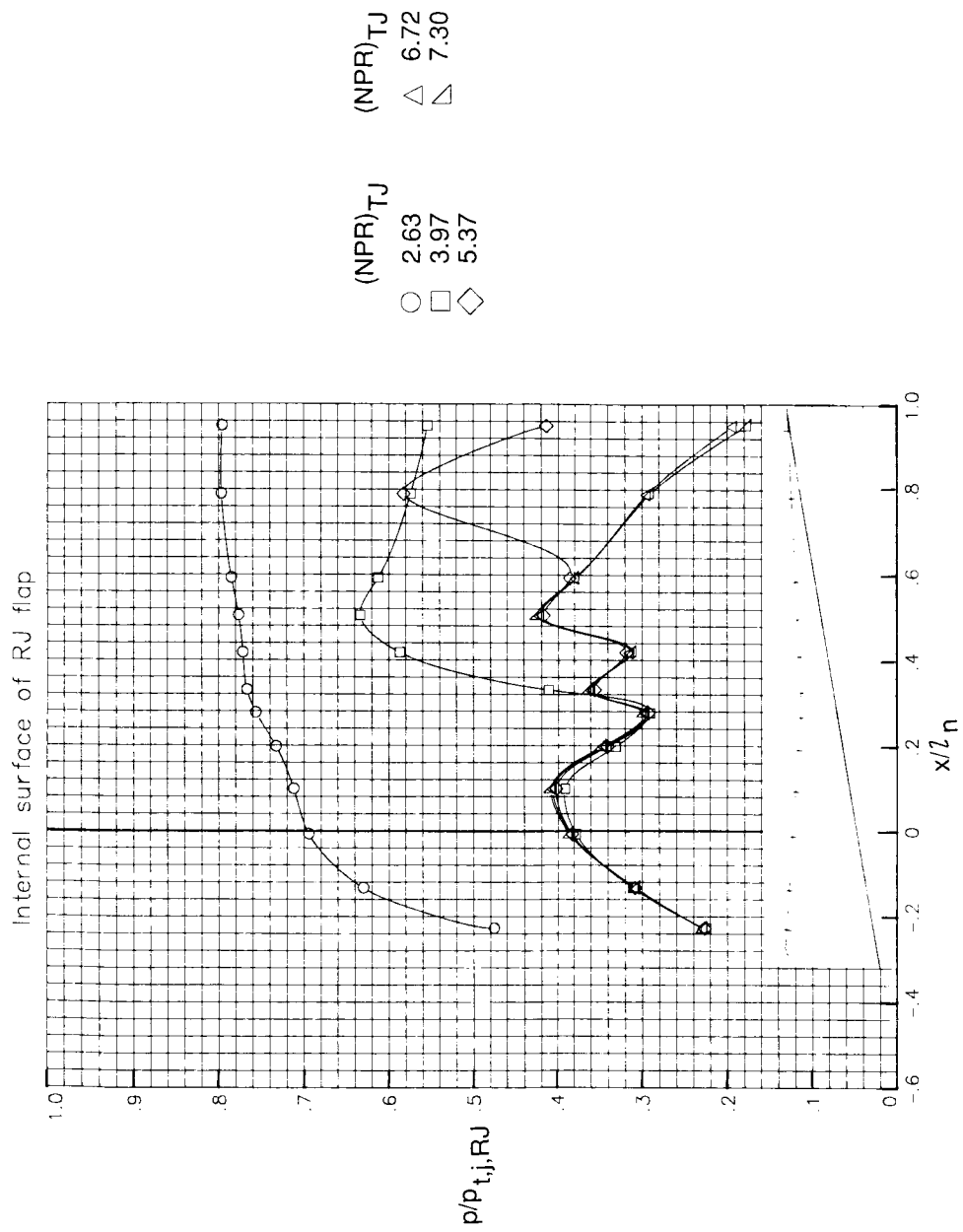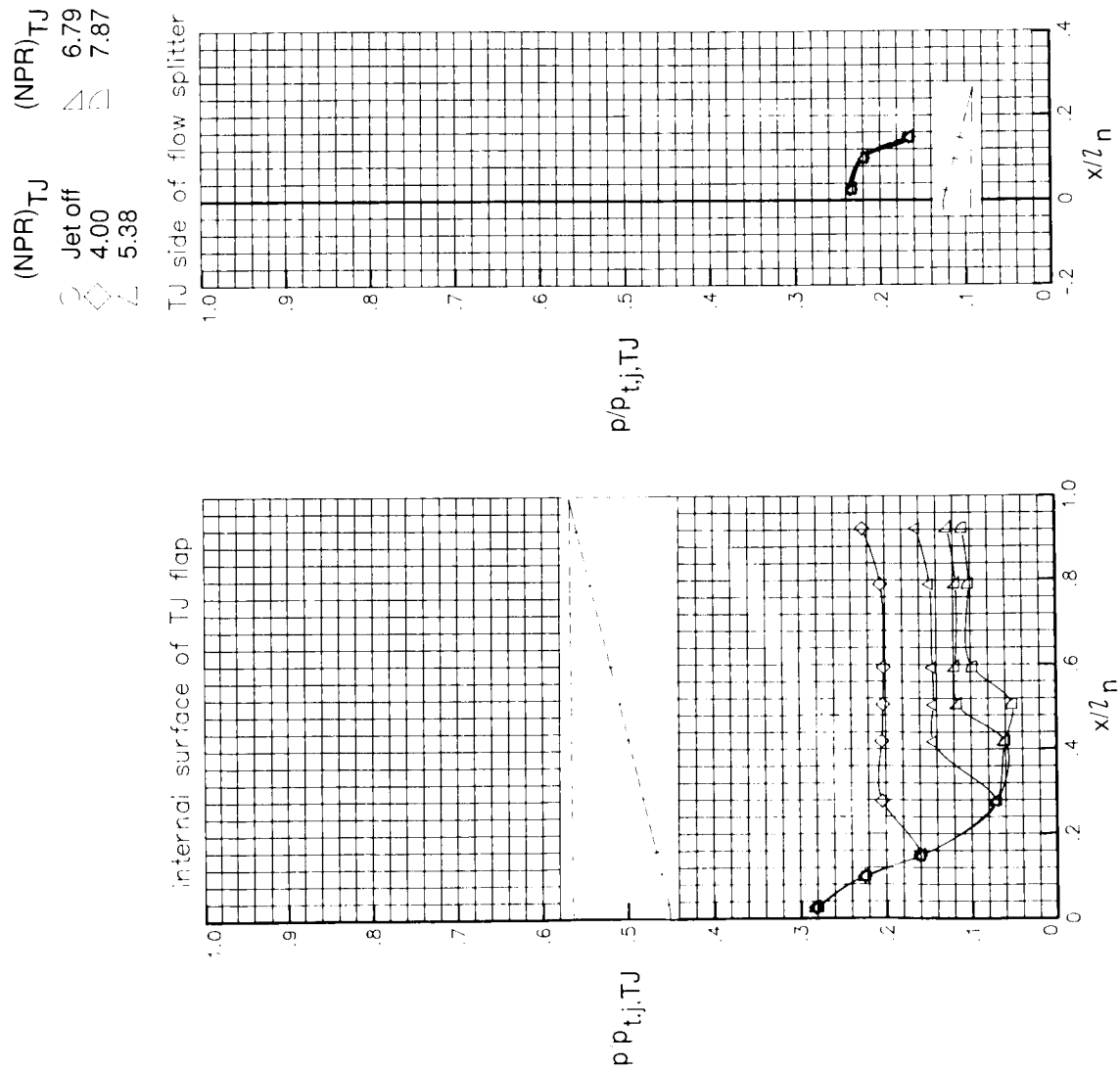
(b) $M = 0.60$.
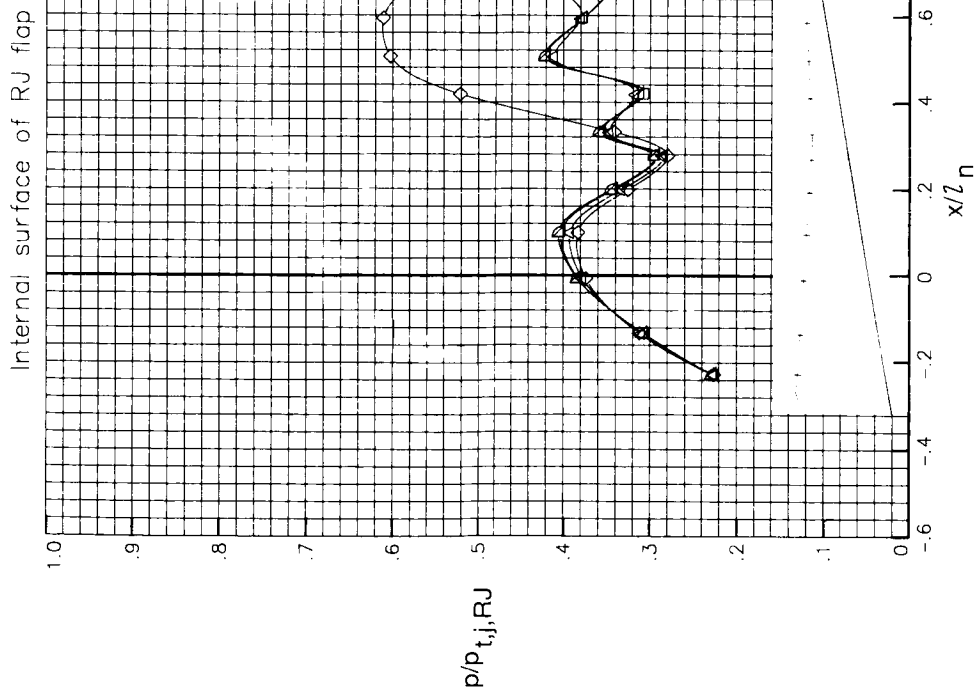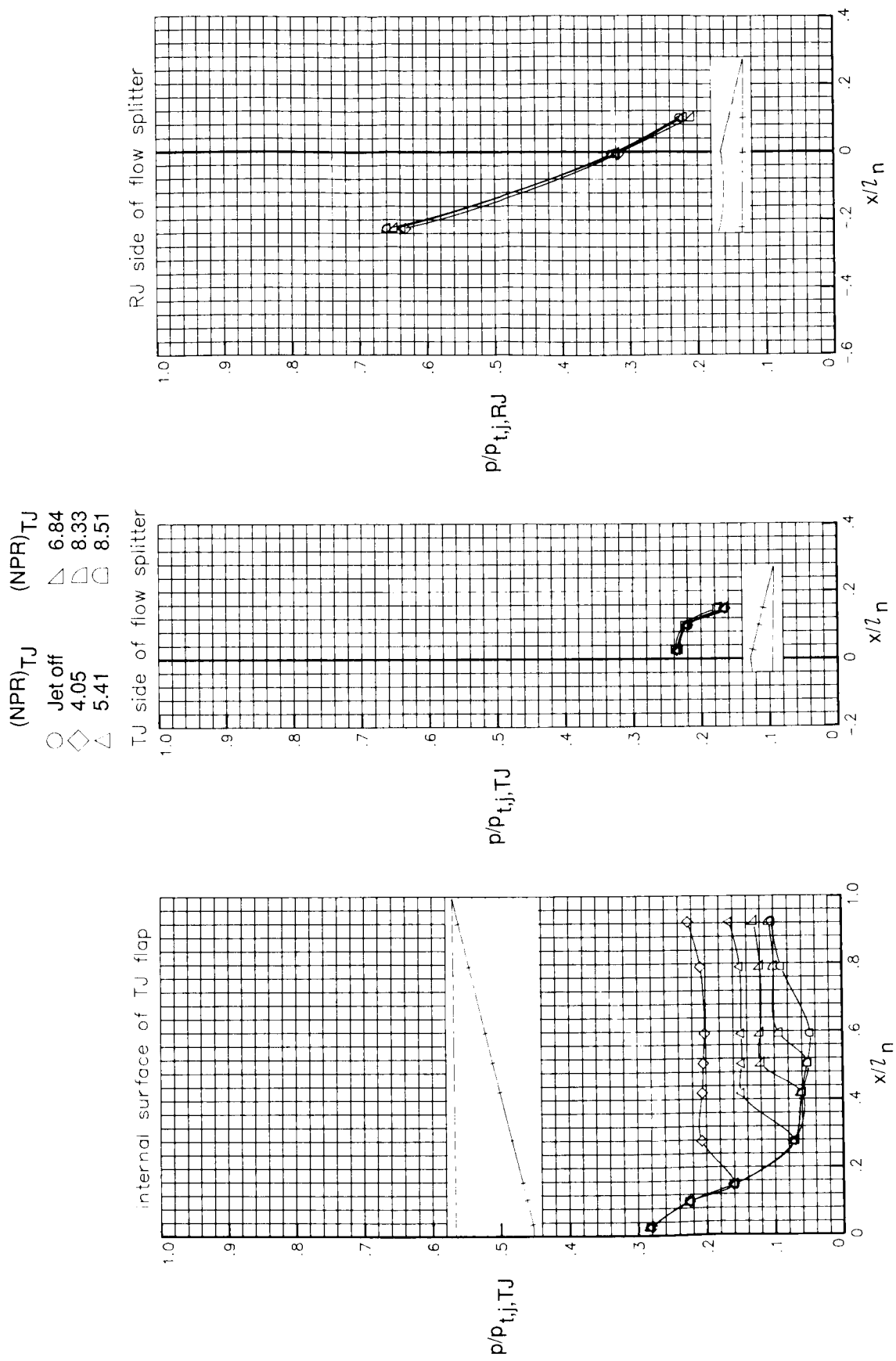
Figure 43. Continued.

(b) Concluded.

Figure 43. Continued.

(c) $M = 0.90$.

Figure 43. Continued.
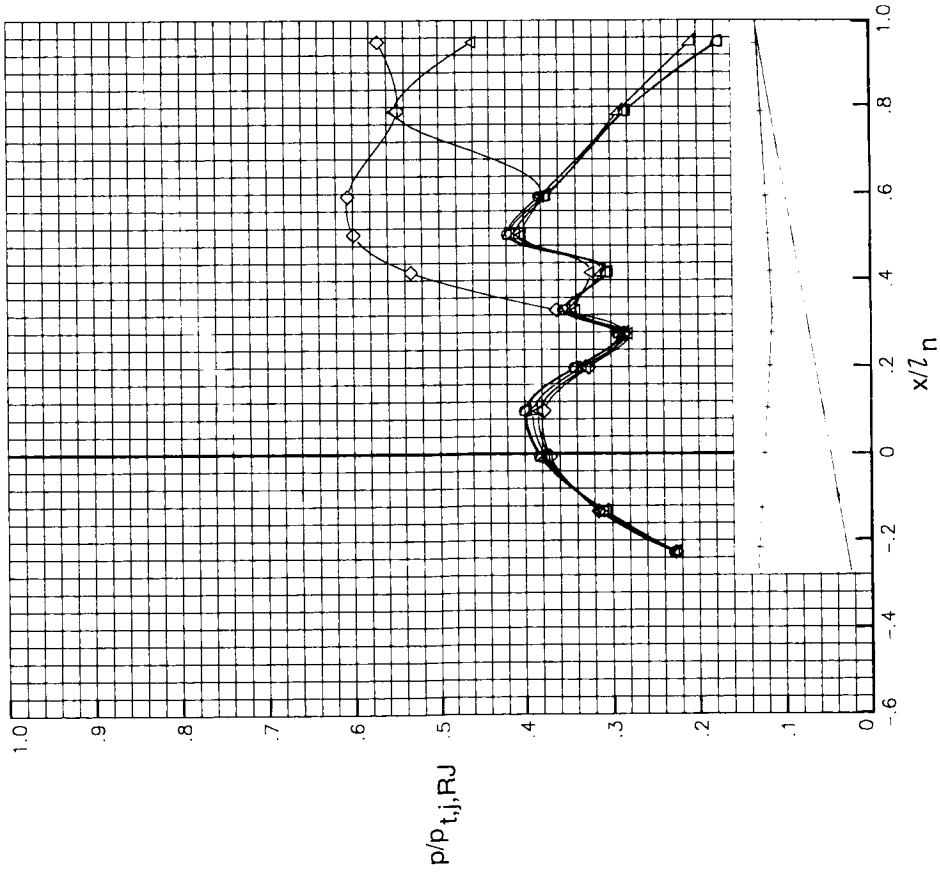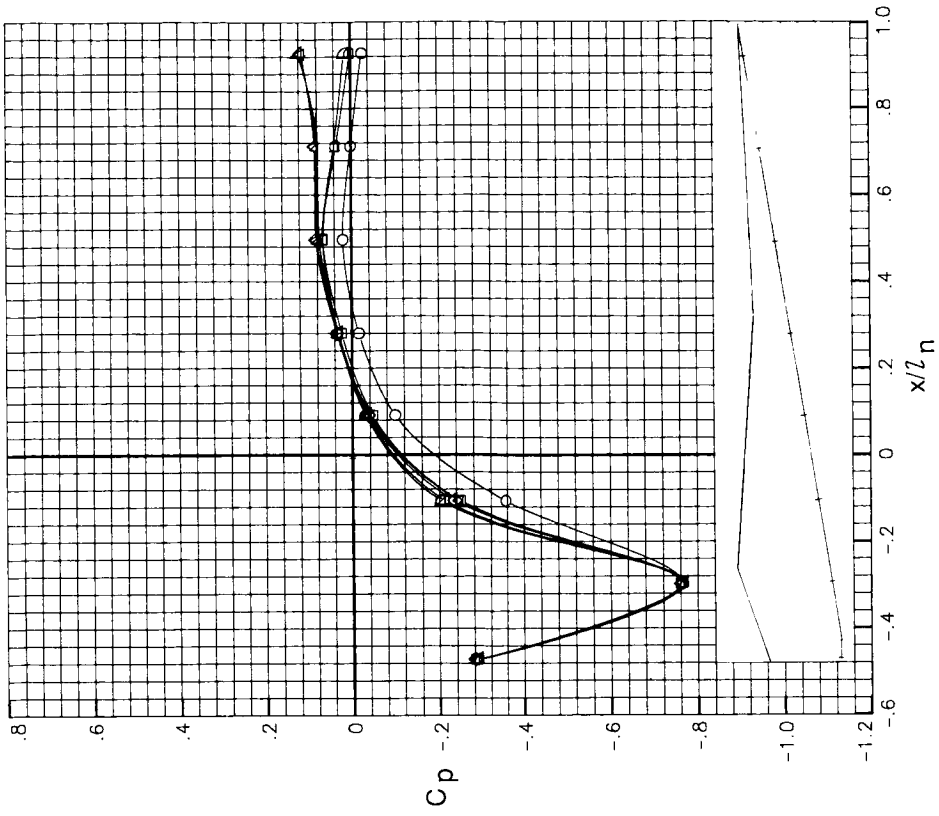
(c) Concluded.

Figure 43. Continued.
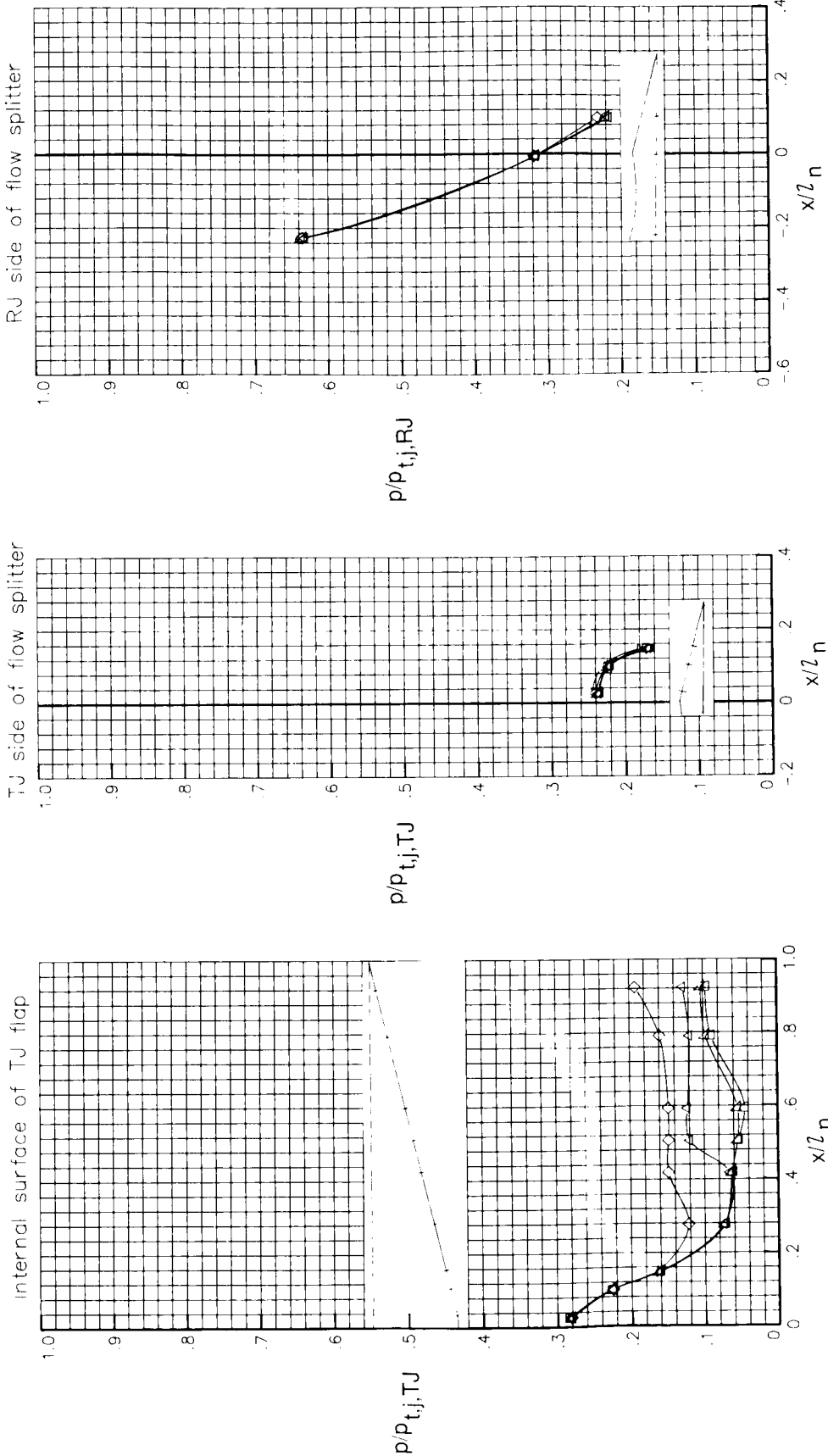
(d) $M = 1.20$.

Figure 43. Continued.

External surface of RJ flap

Internal surface of RJ flap

$(NPR)_{TJ}$

$(NPR)_{TJ}$

○ Jet off
◇ 4.15
△ 5.56

△ 6.98
◁ 7.67

x/l_n

x/l_n

C_p

$p/p_{t,j,RJ}$
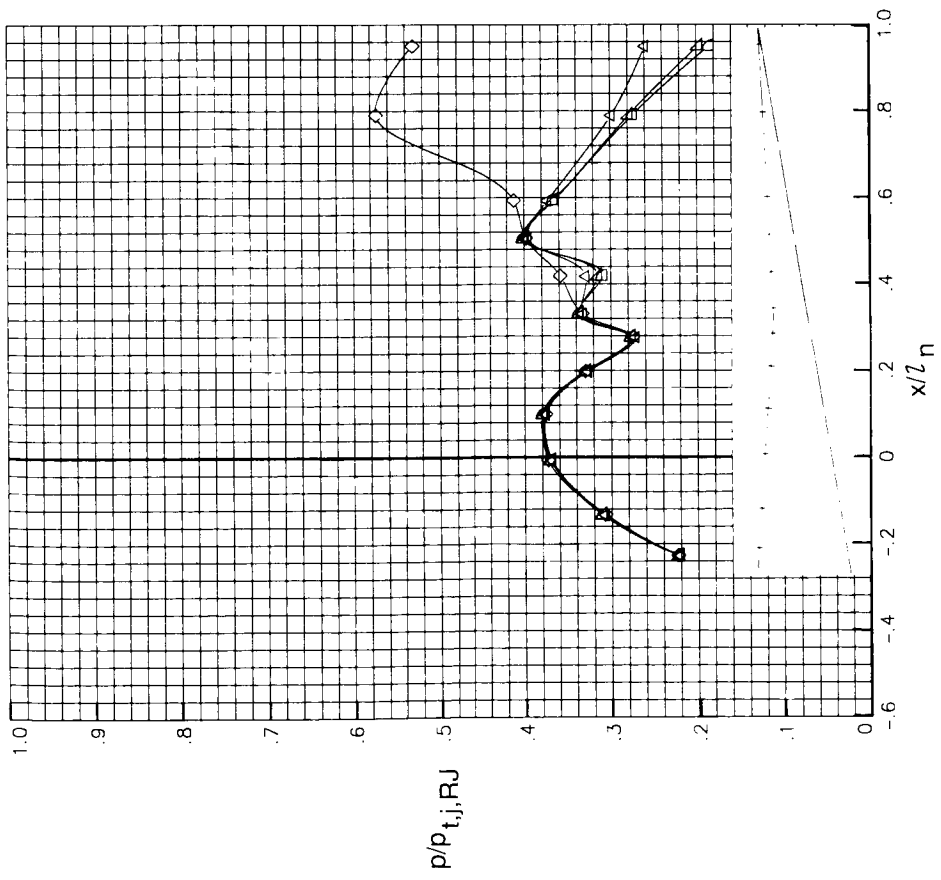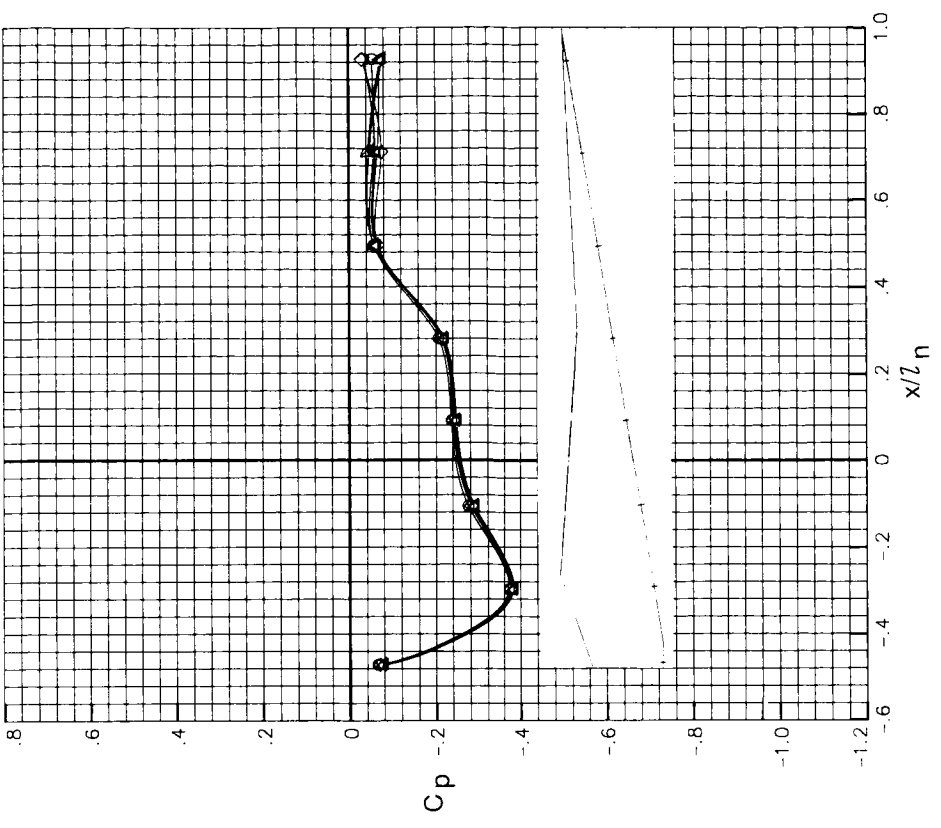
(d) Concluded.

Figure 43. Concluded.

TJ side of flow splitter   Internal surface of TJ flap

$M = 0$

$(NPR)_{TJ}$

□   4.91
◇   6.85
△   8.94
◁   11.08
▷   11.18

$M = 0.60$

$(NPR)_{TJ}$

□   3.09
◇   5.10
△   7.27
◁   9.29
▷   11.31
○   13.31
◇   14.13

$M = 0.90$

$(NPR)_{TJ}$

□   3.26
◇   5.15
△   7.32
◁   9.48
▷   11.45
○   13.42
◇   15.46
◇   18.52

$M = 1.20$

$(NPR)_{TJ}$

□   3.46
◇   5.44
△   7.88
◁   9.93
▷   11.95
○   13.86
◇   16.03
◇   17.87
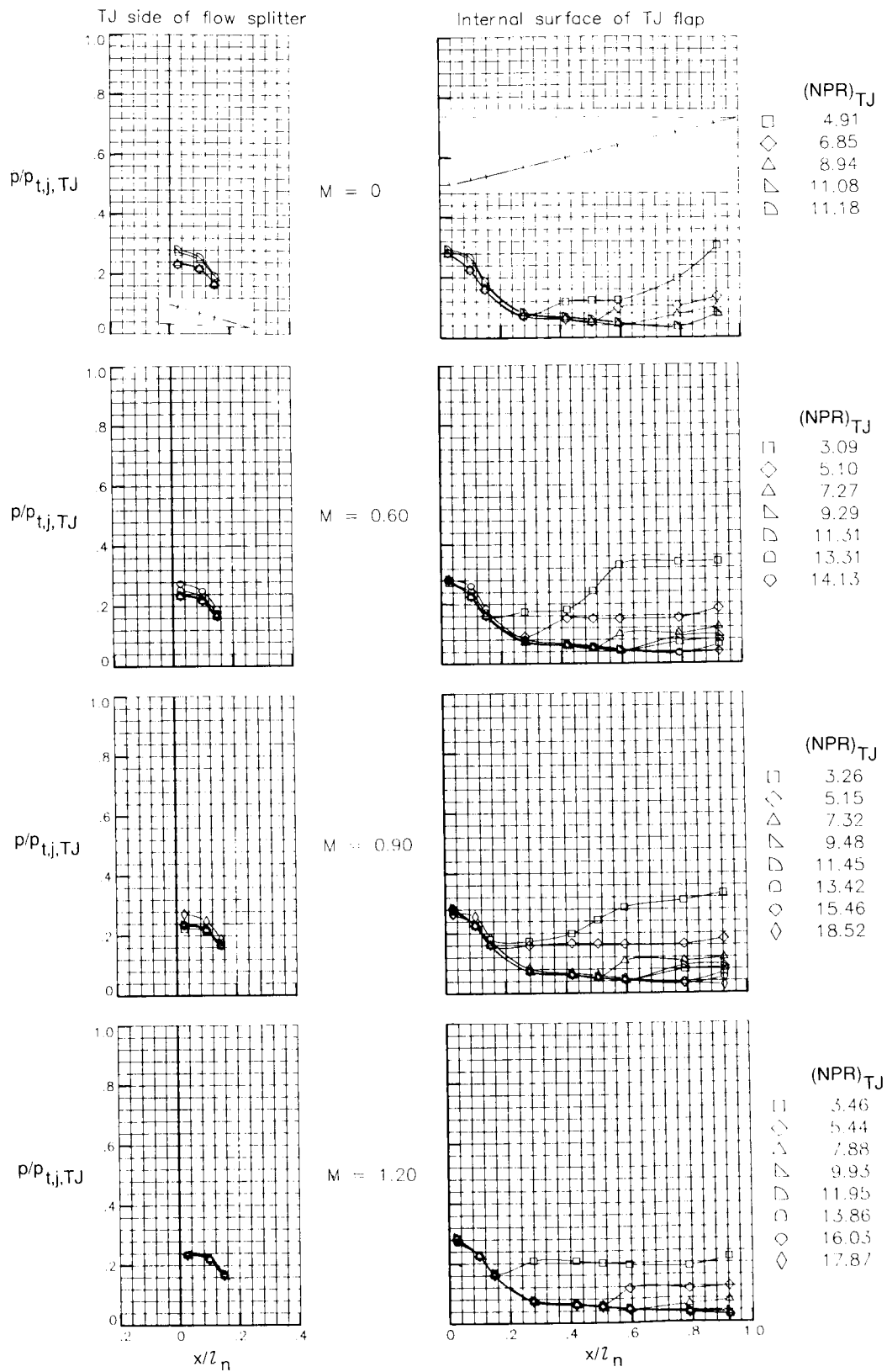
(a) Minimum ramjet throat area and V-notch sidewalls.

Figure 44. Pressure ratio and pressure coefficient distributions of CCN with blanked-off ramjet and ramjet flap 3.

168

TJ side of flow splitter

Internal surface of TJ flap

$p/p_{t,j,TJ}$

$M = 0$

$(NPR)_{TJ}$

□ 4.90
◇ 6.50
△ 6.89
◺ 9.37
▷ 10.19
◠ 10.21

$p/p_{t,j,TJ}$

$M = 0.60$

$(NPR)_{TJ}$

□ 3.06
◇ 5.12
△ 7.14
◺ 9.59
▷ 11.51
◠ 13.04

$p/p_{t,j,TJ}$

$M = 0.90$

$(NPR)_{TJ}$

□ 3.11
◇ 5.12
△ 7.18
◺ 9.72
▷ 11.66
◠ 13.65
◇ 17.07

$p/p_{t,j,TJ}$

$M = 1.20$

$(NPR)_{TJ}$

□ 3.47
◇ 5.51
△ 7.96
◺ 9.99
▷ 12.00
◠ 14.02
◇ 16.01
◇ 17.96
◠ 19.98

x/l_n

x/l_n

(b) Minimum ramjet throat area and cutback sidewalls.

Figure 44. Continued.

169

Internal surface of TJ flap

$p/p_{t,j,TJ}$ M = 0

$(NPR)_{TJ}$
□ 4.88
◇ 6.66

$p/p_{t,j,TJ}$ M = 0.60

$(NPR)_{TJ}$
□ 3.04
◇ 5.18
△ 7.15
◁ 9.05
◯ 11.20
◯ 13.10
◇ 14.13

$p/p_{t,j,TJ}$ M = 0.90

$(NPR)_{TJ}$
□ 3.05
◇ 5.16
△ 7.16
◁ 9.24
◯ 11.25
◯ 13.26
◯ 15.43
◇ 18.83

$p/p_{t,j,TJ}$ M = 1.20

$(NPR)_{TJ}$
□ 3.13
◇ 5.58
△ 7.67
◁ 9.86
◯ 11.92
◯ 14.10
◯ 16.17
◇ 18.22

x/l_n x/l_n

(c) Maximum ramjet throat area and V-notch sidewalls.

Figure 44. Continued.

TJ side of flow splitter

Internal surface of TJ flap

$p/p_{t,j,TJ}$ $M = 0$

$(NPR)_{TJ}$
□ 4.89
◇ 6.87
△ 8.86
◺ 10.74
◹ 11.08

$p/p_{t,j,TJ}$ $M = 0.60$

$(NPR)_{TJ}$
□ 3.06
◇ 5.08
△ 7.01
◺ 9.04
◹ 10.97
◷ 12.99
○ 14.14

$p/p_{t,j,TJ}$ $M = 0.90$

$(NPR)_{TJ}$
□ 3.10
◇ 5.16
△ 7.17
◺ 9.15
◹ 11.14
◷ 13.17
○ 15.28
◊ 18.65

$p/p_{t,j,TJ}$ $M = 1.20$

$(NPR)_{TJ}$
□ 3.43
◇ 5.51
△ 7.57
◺ 9.72
◹ 11.76
◷ 13.80
○ 15.84
◊ 18.00

x/l_n

x/l_n

(d) Maximum ramjet throat area and cutback sidewalls.

Figure 44. Concluded.

171

<table>
<tr><td colspan="2">NASA
National Aeronautics and
Space Administration</td><td>Report Documentation Page</td></tr>
</table>

1. Report No. NASA TP-2814	2. Government Accession No.	3. Recipient's Catalog No.
4. Title and Subtitle Aeropropulsive Characteristics of Isolated Combined Turbojet/ Ramjet Nozzles at Mach Numbers From 0 to 1.20		5. Report Date June 1988
		6. Performing Organization Code
7. Author(s) George T. Carson, Jr., and Milton Lamb		8. Performing Organization Report No. L-16390
9. Performing Organization Name and Address NASA Langley Research Center Hampton, VA 23665-5225		10. Work Unit No. 505-62-91-01
		11. Contract or Grant No.
12. Sponsoring Agency Name and Address National Aeronautics and Space Administration Washington, DC 20546-0001		13. Type of Report and Period Covered Technical Paper
		14. Sponsoring Agency Code

15. Supplementary Notes

16. Abstract

An investigation was conducted in the Langley 16-Foot Transonic Tunnel to determine the aeropropulsive performance characteristics (the aerodynamic quantities affected by propulsion) of 13 isolated combined turbojet/ramjet nozzle configurations. These configurations simulated the variable-geometry features of two nozzle designs designated as the multiple-expansion ramp nozzle (MERN) and the composite contour nozzle (CCN). Test data were obtained at static conditions and at Mach numbers of 0.60, 0.90, and 1.20 with jet exhaust simulated by high-pressure air. The results showed that the CCN had the higher performance over the Mach number range than the MERN, as indicated by the difference of thrust minus drag divided by ideal thrust. Increasing the ramjet throat area for the MERN resulted in an increase in performance that increased with Mach number. For the CCN at Mach numbers less than 1.20, increasing the ramjet throat area resulted in a loss in performance.

17. Key Words (Suggested by Authors(s)) Turbojet/ramjet Hypersonic air-breathing propulsion Nonaxisymmetric nozzles	18. Distribution Statement Unclassified - Unlimited Subject Category 02		
19. Security Classif.(of this report) Unclassified	20. Security Classif.(of this page) Unclassified	21. No. of Pages 172	22. Price A08

NASA FORM 1626 OCT 86

NASA-Langley, 1988

National Aeronautics and
Space Administration
Code NTT-4

Washington, D.C.
20546-0001

NASA